

國立交通大學

電子物理系

博士論文

直流離子濺鍍機於液晶配向的應用
及其配向特性之研究



Study on the Alignment Properties of Liquid Crystals on
the Surfaces treated by a Direct-Current Ion Sputter

研究生：吳信穎

指導教授：趙如蘋 教授

中華民國九十八年二月

直流離子濺鍍機於液晶配向的應用
及其配向特性之研究

Study on the Alignment Properties of Liquid Crystals on
the Surfaces treated by a Direct-Current Ion Sputter

研究生：吳信穎

Student : Hsin-Ying Wu

指導教授：趙如蘋

Advisor : Ru-Pin Pan



A Thesis

Submitted to Department of Electrophysics

College of Science

National Chiao Tung University

in Partial Fulfillment of the Requirements

for the Degree of

Doctor of Philosophy

in Electrophysics

Feb 2009

Hsinchu, Taiwan, Republic of China

中華民國九十八年二月

直流離子濺鍍機於液晶配向的應用 及其配向特性之研究

學生：吳信穎

指導教授：趙如蘋 博士

國立交通大學電子物理系

摘 要

液晶配向技術早已廣泛的應用在液晶顯示科技領域。在這段期間，由於傳統摩刷配向方法本身所具有的缺點限制了顯示相關技術品質的提昇，因此有許多新的配向技術陸續被開發出來。本論文係利用一台構造簡單的直流離子濺鍍機來產生離子源，以提供液晶配向處理之用。利用電漿放電的不同區域來進行表面處理，能提供不同的液晶配向效果。分別利用偏光顯微鏡與聚光干涉儀來鑒別所組合成之液晶盒的配向效果，並且進一步量測液晶盒的表面定向錨定強度與預傾角。此外，利用原子力/磁力顯微鏡、表面化學成分分析儀、紫外/可見光譜儀、超導量子干涉磁量儀及接觸角量測系統深入探討造成表面配向與預傾角的機制是本論文的研究重點。

首先，我們發現不同的離子束能量可以使液晶產生兩種配向效果，包括水平配向及垂直配向。經證實於高能量離子轟擊的狀況下，會在配向膜表面堆積一定量的氧化鐵。也因此，我們提出一種利用單步驟濺鍍所形成的薄膜來產生垂直配向方法。此種薄膜經由表面分析證實是由許多顆粒大小約三十奈米的粒子所組成，且表面具有磁化強度的異向性。由表面錨定強度與飽和磁化強度的比較結果，我們推測垂直配向的效果是起因於磁性薄膜所產生的磁場。因此我們假設一個簡單的表面模型，描述兩兩相鄰但所具備磁矩的方向相反的磁區所產生的磁場空間分布。經由與液晶間的力矩作用所產生的能量計算，進一步推得表面錨定能的大

小並與實驗量測值做比較。

此外，我們利用偏振紫外光照射與離子轟擊一種新型帶有含氟羰基側鏈的感光性配向膜。並觀察含氟側鏈的不同濃度對於液晶配向效果的影響。發現經由紫外光照射過的表面有明顯較大的預傾角。相反地，離子轟擊過後的表面所得到的預傾角很小。經由表面分析證實，含 CF_2 的側鏈結構含量的確在影響表面預傾角的大小上扮演重要的角色。此外，在經離子轟擊過後的表面發現含氧量的大幅增加，這也解釋了極性表面能的增加現象。在這份工作中，表面的極性力被證實是影響液晶預傾角的主要因素。

最後，我們利用輝光放電區對聚醯亞胺膜表面進行處理，同時濺鍍氧化鐵於其上。發現在所加偏壓低於七百伏特的條件下，所處理過的薄膜表面對液晶產生品質與穩定度皆不錯的水平配向效果。此外，預傾角能透過調變偏壓或處理時間來改變其大小。其產生預傾角的機制也在本論文探討的範疇內。



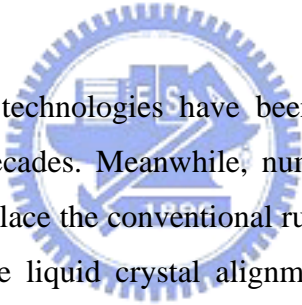
Study on the Alignment Properties of Liquid Crystals on the Surfaces treated by a Direct-Current Ion Sputter

Student: Hsin-Ying Wu

Advisor: Dr. Ru-Pin Pan

Department of Electrophysics
National Chiao Tung University

ABSTRACT



Liquid crystal alignment technologies have been widely used in liquid crystal display industry in the past decades. Meanwhile, numerous alignment methods have been intensely developed to replace the conventional rubbing method due to its intrinsic shortcoming. In this thesis, the liquid crystal alignments on surfaces treated by ion bombardments are achieved by utilizing a direct-current ion sputter with diode-type electrodes. Various conditions of plasma discharge offer a variety of alignment effects. The alignment effects of nematic liquid crystal on plasma/ion-treated surfaces are characterized using polarizing optical microscope and conoscope. The surface polar anchoring strength and pretilt angle have also been studied. Furthermore, the corresponding mechanisms of pretilt angle and alignment effect are studied using atomic/magnetic force microscope (AFM/MFM), x-ray photoelectron spectroscopy (XPS), ultraviolet-visible spectroscopy (UV-VIS), super conducting quantum interference device (SQUID), and apparatus of contact angle measurement.

First of all, we found that two alignment modes, homogeneous alignment and homeotropic alignment, can be induced by bombardments of ion accelerated by different electric bias. According to the discovery of iron oxide on the surface bombarded by high-energy ion, a method for homeotropic alignment of liquid crystals

using a one-step, ion beam sputtering on glass substrates is proposed. The surveyed surface morphology reveals that the films are composed of granular nanoparticles with dimensions around 30 nm. Anisotropy of magnetization is also found on the sputtered ferric films. Polar anchoring strength and saturation magnetization of the coated films of different thicknesses are compared with each other. Accordingly, we deduce that the homeotropic alignment is achieved probably due to the orientation of the diamagnetic nematogenic molecules in the magnetic field caused by the γ -Fe₂O₃ ferrimagnetic thin films. Therefore, a simple model of alternatively distributed magnetic moments with opposite direction is proposed. The profile of magnetic field strength near the surface is then evaluated and taken into the calculation of polar anchoring strength.

Besides, surface treatments accomplished through the ultraviolet irradiation and ion bombardment on a newly developed copolymer materials with fluorinated carbonyl groups of different mole fraction and their effects on liquid crystal surface alignments have been studied. The surface alignment with high pretilt angle is achieved by the ultraviolet treatment. The induced pretilt angle by ion bombardments on this photo-reactive polymer film, however, is relatively small. It is confirmed that the content of CF₂ grafted side chains plays a dominant role while determining the pretilt angle. A significant increase of oxygen content has also been found to be responsible for the increase of polar surface free energy in ion bombardments. Consequently, the polar force contributed to the surface tension has been proved to dominate the induced pretilt angle.

Finally, we demonstrate that the polyimide surfaces are treated by oblique plasma irradiation with simultaneous coating of maghemite nanoparticles. Homogeneous alignments of liquid crystals with good quality and reliability are obtained on the polyimide surfaces treated with plasma energy lower than 700 V. The pretilt angle can be controlled by different plasma energies and treating time. The mechanism in determining the pretilt angle has also been discussed.

誌 謝

轉眼間，博士班的研究生涯即將進入尾聲，非常感謝我的指導老師 趙如蘋 教授在這段過程中，適時的給予指導與鼓勵，讓我受益匪淺。老師的包容在研究上讓我有足夠的空間來自由發揮，才能夠讓我擁有今天這些成果。過程中所獲得的滿足與喜悅也是支撐我走完這段路的動力。謝謝老師！在這邊，也感謝這幾年來給實驗室帶來歡笑的學弟妹們，以及你們在實驗上的幫忙。

最後，僅將這份成果獻給我親愛的父母與女友，你們的善體人意讓我無後顧之憂，才能平穩地走過這一切。有你們真好，謝謝你們！！

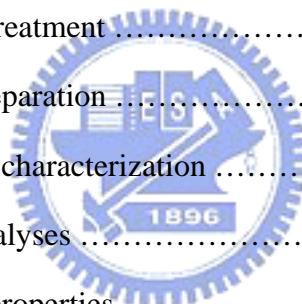


信穎

Table of Contents

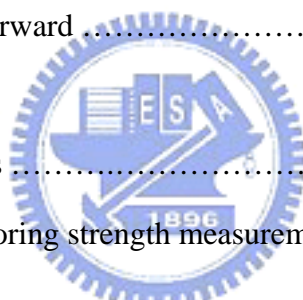
| | | |
|--|-------|-------|
| 中文摘要 | | i |
| Abstract | | iii |
| 誌謝 | | v |
| Table of Contents | | vi |
| List of Figures | | x |
| List of Tables | | xviii |
| 1. Introduction | | 1 |
| 1.1 Background | | 1 |
| 1.1.1 Photoalignment | | 1 |
| 1.1.2 Oblique Evaporation | | 2 |
| 1.1.3 Ion Beam Alignment | | 3 |
| 1.1.4 Alignment mechanism | | 3 |
| 1.2 Overview of this thesis | | 4 |
| References | | 6 |
| 2. Controllable Alignment Modes of Nematic Liquid Crystals on Argon Ion Beam Bombarded Polyimide Films | | 8 |
| 2.1 Overview | | 8 |
| 2.2 Ion beam treatment | | 8 |
| 2.2.1 Ion source | | 8 |
| 2.2.2 Ion beam conditions | | 9 |
| 2.3 Experiments | | 9 |
| 2.3.1 Sample preparation | | 10 |
| 2.3.2 Alignment characterization | | 10 |
| 2.3.3 Surface analyses | | 10 |
| 2.4 Results and discussion | | 12 |

| | | |
|------------|---|-----|
| 2.4.1 | Alignment characterization | 12 |
| 2.4.2 | Surface morphologies | 13 |
| 2.4.3 | XPS analyses | 14 |
| 2.5 | Concluding remarks | 18 |
| References | | 20 |
| Figures | | 22 |
| Tables | | 47 |
| 3. | Liquid Crystalline alignment on the Ion Beam Sputtered Magnetic Thin Film | 50 |
| 3.1 | Overview | 50 |
| 3.2 | Experiments | 50 |
| 3.2.1 | Ion beam treatment | 51 |
| 3.2.2 | Sample preparation | 51 |
| 3.2.3 | Alignment characterization | 51 |
| 3.2.4 | Surface analyses | 52 |
| 3.2.5 | Magnetic properties | 52 |
| 3.3 | Results and discussion | 52 |
| 3.3.1 | Film characterization | 53 |
| 3.3.2 | Alignment characterization | 53 |
| 3.3.3 | Magnetic properties | 54 |
| 3.3.4 | Surface morphology | 56 |
| 3.3.5 | Theoretical analyses | 57 |
| 3.4 | Concluding remarks | 60 |
| References | | 62 |
| Figures | | 63 |
| Tables | | 102 |



| | |
|---|-----|
| 4. Liquid Crystal Alignments on the Fluorinated Copolymer Films Treated by Ion Beam Bombardment and Ultraviolet Irradiation | 103 |
| 4.1 Overview | 103 |
| 4.2 Experiments | 103 |
| 4.2.1 Surface treatments | 104 |
| 4.2.2 Sample preparation | 105 |
| 4.2.3 Alignment characterization | 105 |
| 4.2.4 Surface analyses | 105 |
| 4.3 Results and discussion | 106 |
| 4.3.1 Alignment characterization | 106 |
| 4.3.2 XPS analyses | 106 |
| 4.3.3 Surface free energy | 108 |
| 4.3.4 Depth-dependence of fluorine content | 109 |
| 4.4 Concluding remarks | 110 |
| References | 112 |
| Figures | 113 |
| Tables | 128 |
| | |
| 5. Tilt Alignment of Liquid Crystals on the Polyimide Surface Treated by Plasma Irradiation with Simultaneous Coating of Magnetic Nanoparticles | 130 |
| 5.1 Overview | 130 |
| 5.2 Experiments | 130 |
| 5.2.1 Plasma beam treatment | 130 |
| 5.2.2 Sample preparation | 131 |
| 5.2.3 Alignment characterization | 131 |
| 5.2.4 Surface analyses | 131 |
| 5.3 Results and discussion | 132 |

| | | |
|------------------|--|-----|
| 5.3.1 | Alignment characterization | 132 |
| 5.3.2 | Surface morphologies | 132 |
| 5.3.3 | Surface energy | 133 |
| 5.3.4 | XPS analyses | 134 |
| 5.4 | Concluding remarks | 136 |
| References | | 138 |
| Figures | | 139 |
| Tables | | 151 |
| 6. | Concluding Remarks | 152 |
| 6.1 | Looking back | 152 |
| 6.2 | Looking forward | 154 |
| Appendix A | Ion sources | 156 |
| Appendix B | Polar anchoring strength measurement | 162 |
| Appendix C | Simulation of magnetic field distribution | 171 |
| Appendix D | Estimation of the magnetic field strength for liquid crystal alignment | 178 |
| Curriculum Vitae | | |



List of Figures

| | | |
|---------------|--|----|
| Figure 2.2.1 | Structural view of the DC ion-beam sputter operated in coating mode | 20 |
| Figure 2.2.2 | Sketch of argon ion-beam bombardment: (a) The space distribution of glow discharge in a diode sputter operated in etching mode, and (b) the arrangement of glass substrates in the sputter | 20 |
| Figure 2.3.1 | Procedures of cleaning process | 21 |
| Figure 2.3.2 | A Shirley background computed from a Fe 2p spectrum | 21 |
| Figure 2.4.1 | The POM photographs of NLC 5CB cells treated by different ion beam conditions: (a) homogeneous alignment, and (b) homeotropic alignment. (Inset: conoscopic pattern)..... | 22 |
| Figure 2.4.2 | Pretilt angle vs. the ion beam bombarding time with V_b of 560 V (top) and 1120 V (bottom) | 22 |
| Figure 2.4.3 | Polar anchoring strength W_p of 5CB cells determined for (a) various τ with $\theta_{ion}=60^\circ$ and (b) various θ_{ion} with $\tau=8$ min for all with $V_b=560$ V | 23 |
| Figure 2.4.4 | AFM images of the PI films treated for different τ : (a) As-deposited, (b) 6 min, (c) 14 min, and (d) 30 min with ion energy $V_b =560$ V. The films here give homogeneous alignments | 23 |
| Figure 2.4.5 | Roughness of the surfaces treated with ion energy $V_b=560$ V for various τ | 24 |
| Figure 2.4.6 | AFM images of the PI films treated by different ion energies: (a) 560 V, (b) 840 V, and (c) 1120 V with $\tau=5$ min | 25 |
| Figure 2.4.7 | Primary structure of polyimide | 26 |
| Figure 2.4.8 | Survey spectra for the untreated and ion-beam treated PI films with various V_b , $\tau=5$ min, $\theta_{ion}=60^\circ$, and $J_{ion}=255 \mu A/cm^2$ | 26 |
| Figure 2.4.9 | Multiplex spectra for the untreated and ion-beam treated PI films with various V_b , $\tau=5$ min, $\theta_{ion}=60^\circ$, and $J_{ion}=255 \mu A/cm^2$ | 27 |
| Figure 2.4.10 | Deconvolution of the (a) C_{1s} and (b) O_{1s} spectra of the untreated and treated PI films with $V_b=1120$ V | 28 |
| Figure 2.4.11 | Fraction of the components contributing to the (a) C_{1s} and (b) O_{1s} core-level spectra of untreated and ion-beam treated PI films as a function of V_b | 29 |

| | | |
|---------------|---|----|
| Figure 2.4.12 | Survey spectra for the untreated and ion-beam treated PI films with different τ , $V_b=560$ V, $\theta_{ion}=60^\circ$, and $J_{ion}=255$ $\mu\text{A}/\text{cm}^2$ | 30 |
| Figure 2.4.13 | Multiplex spectra for the untreated and ion-beam treated PI films with different τ , $V_b=560$ V, $\theta_{ion}=60^\circ$, and $J_{ion}=255$ $\mu\text{A}/\text{cm}^2$ | 31 |
| Figure 2.4.14 | Deconvolution of the (a) C_{1s} and (b) O_{1s} spectra for the untreated and treated PI films with $\tau=8$ min | 32 |
| Figure 2.4.15 | Fraction of the components contributing to the (a) C_{1s} and (b) O_{1s} core-level spectra of untreated and ion-beam treated PI films as a function of τ | 33 |
| Figure 2.4.16 | Survey spectra for the untreated and ion-beam treated PI films with different θ_{ion} , $V_b=840$ V, $J_{ion}=458$ $\mu\text{A}/\text{cm}^2$, and $\tau=5$ min | 34 |
| Figure 2.4.17 | Multiplex spectra for the untreated and ion-beam treated PI films with different θ_{ion} , $V_b=840$ V, $J_{ion}=458$ $\mu\text{A}/\text{cm}^2$, and $\tau=5$ min | 35 |
| Figure 2.4.18 | Deconvolution of the C_{1s} spectra of the treated PI films with θ_{ion} of 40° , 60° , and 80° | 36 |
| Figure 2.4.19 | Deconvolution of the O_{1s} spectra of the treated PI films with θ_{ion} of 40° , 60° , and 80° | 37 |
| Figure 2.4.20 | Fraction of the components contributing to the (a) C_{1s} and (b) O_{1s} core-level spectra of untreated and ion-beam treated PI films as a function of θ_{ion} | 38 |
| Figure 2.4.21 | Survey spectra scanned with x-ray monochromatic sources of the Mg $\text{K}\alpha$ and Al $\text{K}\alpha$ lines for the PI surface treated with $V_b=1120$ V, $\theta_{ion}=60^\circ$, $J_{ion}=255$ $\mu\text{A}/\text{cm}^2$, and $\tau=5$ min | 39 |
| Figure 2.4.22 | The Fe 2p spectrum in multiplex mode of the film treated by $V_b=1120$ V, $J_{ion}=255$ $\mu\text{A}/\text{cm}^2$, $\theta_{ion}=60^\circ$, and $\tau=5$ min | 40 |
| Figure 2.4.23 | Deconvolution of the Fe 2p _{3/2} spectrum of (a) IB-etched PI film and (b) IB-etched ITO film with ion beam condition: $V_b=1120$ V, $J_{ion}=255$ $\mu\text{A}/\text{cm}^2$, $\theta_{ion}=60^\circ$, and $\tau=5$ min | 41 |
| Figure 2.4.24 | Photographs of an ion beam treated NLC cell placed between crossed-polarizers. The left side of the substrates was covered with fused silica plate while being ion-beam treated. The V_b and τ are 560 V and 20 min, respectively | 42 |
| Figure 3.2.1 | Procedures of etching process for the patterned-ITO | 58 |
| Figure 3.2.2 | Schematic structure of a LC cell | 59 |

| | | |
|---------------|---|----|
| Figure 3.3.1 | Deconvolution of the Fe 2p _{3/2} spectra of ITO-coated substrates treated in (a) etching mode and (b) coating mode with ion beam condition: $V_b=1120$ V, $J_{ion}=255$ $\mu\text{A}/\text{cm}^2$, incidence angle of (a) 60° and (b) 0°, and treating time of 5 min. (c) Deconvolution of the O 1s spectrum of ITO-coated substrates treated in coating mode with the same energy, current density, and treating time. The incidence angle is 0° | 60 |
| Figure 3.3.2 | The UV/VIS absorbance spectrum of iron oxide thin film with ion condition: $V_b=1120$ V, $J_{ion}=255$ $\mu\text{A}/\text{cm}^2$, incidence angle of 0°, and coating time of 20 min. Inset: the optical constants of hematite ($\alpha\text{-Fe}_2\text{O}_3$) | 61 |
| Figure 3.3.3 | The UV/VIS transmittance spectra of $\gamma\text{-Fe}_2\text{O}_3$ films with different thickness of 63.6, 106, 212, 424, and 636 nm | 62 |
| Figure 3.3.4 | (a) Top-view and (b) tilt-view of the MLC-6608 cells with $\gamma\text{-Fe}_2\text{O}_3$ and DMOAP coating under crossed-polarizers; (c) top-view (without polarizers) and (d) tilt-view of the 5CB cells coated with different thickness of $\gamma\text{-Fe}_2\text{O}_3$ films. Inset: the conoscopic pattern of the MLC-6608 cells with $\gamma\text{-Fe}_2\text{O}_3$ coating... | 63 |
| Figure 3.3.5 | Normalized phase retardation of MLC-6608 cells at different applied voltage. Inset: the measured curves of transmittance versus applied voltage | 64 |
| Figure 3.3.6 | Temperature dependence of the magnetization measured in the direction parallel to the surface for the iron oxide film with thickness of 636 nm in an applied field of 300 Oe | 65 |
| Figure 3.3.7 | Magnetization curves for a $\gamma\text{-Fe}_2\text{O}_3$ film with thickness of 636 nm at T=10 K and 300 K in the magnetic field parallel to the film surface | 66 |
| Figure 3.3.8 | Hysteresis loops measured in the direction (a) perpendicular and (b) parallel to the surfaces for sputtered $\gamma\text{-Fe}_2\text{O}_3$ films with thickness of 212 nm (◆), 424 nm (●), and 636 nm (▲) | 67 |
| Figure 3.3.9 | Thickness-dependence on (a) M_s and (b) M_{net} of the $\gamma\text{-Fe}_2\text{O}_3$ films. The vertical and horizontal components of M are labeled as (▲) and (●), respectively | 68 |
| Figure 3.3.10 | Polar anchoring strength W_p and the saturation magnetization M_s as a function of $\gamma\text{-Fe}_2\text{O}_3$ film thickness | 69 |
| Figure 3.3.11 | Hysteresis loops measured for an as-sputtered $\gamma\text{-Fe}_2\text{O}_3$ film (—●—) and a thermally-treated $\gamma\text{-Fe}_2\text{O}_3$ film (—○—) with thickness of 212 nm. Two randomly directions on each film are selected for measurements | 70 |
| Figure 3.3.12 | Hysteresis loops measured in the direction parallel to the surface (a) for as-sputtered $\gamma\text{-Fe}_2\text{O}_3$ films with thickness of 106 and 424 nm and (b) a 106 nm-thick $\gamma\text{-Fe}_2\text{O}_3$ film with thermal treatment at 573 K for 2 hours | 71 |

| | | |
|---------------|--|----|
| Figure 3.3.13 | AFM images taken at three different positions on the γ -Fe ₂ O ₃ film surface with thickness of 42.4 nm | 72 |
| Figure 3.3.14 | AFM images taken at three different positions on the γ -Fe ₂ O ₃ film surface with thickness of 106 nm | 73 |
| Figure 3.3.15 | AFM images taken at three different positions on the γ -Fe ₂ O ₃ film surface with thickness of 212 nm | 74 |
| Figure 3.3.16 | AFM images taken at three different positions on the γ -Fe ₂ O ₃ film surface with thickness of 424 nm | 75 |
| Figure 3.3.17 | AFM images taken at three different positions on the γ -Fe ₂ O ₃ film surface with thickness of 848 nm | 76 |
| Figure 3.3.18 | AFM images taken at three different positions on the annealed γ -Fe ₂ O ₃ film surface with thickness of 42.4 nm | 77 |
| Figure 3.3.19 | AFM images taken at three different positions on the annealed γ -Fe ₂ O ₃ film surface with thickness of 106 nm | 78 |
| Figure 3.3.20 | AFM images taken at three different positions on the annealed γ -Fe ₂ O ₃ film surface with thickness of 212 nm | 79 |
| Figure 3.3.21 | AFM images taken at three different positions on the annealed γ -Fe ₂ O ₃ film surface with thickness of 424 nm | 80 |
| Figure 3.3.22 | AFM images taken at three different positions on the annealed γ -Fe ₂ O ₃ film surface with thickness of 848 nm | 81 |
| Figure 3.3.23 | Surface morphology image of as-sputtered γ -Fe ₂ O ₃ film with thickness of 169.6 nm: (a) Top-view image; (b) top-view phase image; (c) three-dimensional image | 82 |
| Figure 3.3.24 | Surface morphology of a γ -Fe ₂ O ₃ film with thickness of 169.6 nm: (a) Three-dimensional image; (b) top-view phase image; (c) surface profiles for particle size analyses | 83 |
| Figure 3.3.25 | Thickness-dependence of particle size for as-sputtered (●) and annealed (○) γ -Fe ₂ O ₃ films | 84 |
| Figure 3.3.26 | AFM images taken at two different positions on the γ -Fe ₂ O ₃ film surface with coating time of 2 min and beam energy of 840 V | 85 |
| Figure 3.3.27 | AFM images taken at three different positions on the γ -Fe ₂ O ₃ film surface with coating time of 10 min and beam energy of 840 V | 86 |
| Figure 3.3.28 | AFM images taken at two different positions on the annealed γ -Fe ₂ O ₃ film surface with coating time of 2 min and beam energy of 840 V | 87 |
| Figure 3.3.29 | AFM images taken at three different positions on the annealed γ -Fe ₂ O ₃ film surface with coating time of 10 min and beam energy of 840 V | 88 |
| Figure 3.3.30 | AFM images taken at two different positions on the γ -Fe ₂ O ₃ film surface with coating time of 2 min and beam energy of 1400 V | 89 |

| | | |
|---------------|---|-----|
| Figure 3.3.31 | AFM images taken at three different positions on the γ -Fe ₂ O ₃ film surface with coating time of 10 min and beam energy of 1400 V .. | 90 |
| Figure 3.3.32 | AFM images taken at two different positions on the annealed γ -Fe ₂ O ₃ film surface with coating time of 2 min and beam energy of 1400 V | 91 |
| Figure 3.3.33 | AFM images taken at three different positions on the annealed γ -Fe ₂ O ₃ film surface with coating time of 10 min and beam energy of 1400 V | 92 |
| Figure 3.3.34 | Thickness-dependence of size of particle for as-sputtered (solid) and annealed (open) γ -Fe ₂ O ₃ films coated by beam energies of 840 V (circle) and 1400 V (triangle) | 93 |
| Figure 3.3.35 | SEM images taken for γ -Fe ₂ O ₃ films with thickness of (a) 106 nm (60,000X), (b) 318 nm (60,000X), and (c) 636 nm (60,000X), and γ -Fe ₂ O ₃ films with thickness of (d) 212 nm (190,000X), (e) 424 nm (22,000X) and (f) 424 nm (85,000X) for 60-second thermal annealing | 94 |
| Figure 3.3.36 | A simple model describing the spatial distribution of the induced magnetic field by the γ -Fe ₂ O ₃ film: (a) imaginary surface structure; (b) H _m (x, y) at z=5 nm; (c) H _m (x, y) at z=20 nm; (d) H _m (z) at different (x, y) | 95 |
| Figure 3.3.37 | Surveyed images for γ -Fe ₂ O ₃ film with 212 nm thick by (a) AFM and (b) MFM | 96 |
| Figure 4.1.1 | Chemical structure of the fluorinated polymer MAPHM-F8..... | 109 |
| Figure 4.2.1 | Schematic diagram of the LPUVL irradiation system..... | 109 |
| Figure 4.3.1 | Photographs of 5CB cells taken with crossed polarizers in the dark state. The cells are aligned with surface-treated x_0 , $x_{0.5}$, and $x_{0.67}$ films by LPUVL irradiation and IB bombardment | 110 |
| Figure 4.3.2 | Pretilt angle of LC cells with MAPHM-F8 films, X ₀ (▲), X _{1/2} (●), and X _{2/3} (■), treated by LPUVL irradiations and IB bombardments for different exposure times | 111 |
| Figure 4.3.3 | Survey spectra for the untreated and IB-treated X _{2/3} films with different bombarding times | 112 |
| Figure 4.3.4 | Survey spectra for the untreated and LPUVL-irradiated X _{2/3} films with different exposure times | 113 |
| Figure 4.3.5 | Variation of chemical composition of the (a) X _{1/2} and (b) X _{2/3} film surfaces treated by LPUVL irradiation and IB bombardment with respect to the treating time for elements: C (■), O (●), N (▲), F (▼), and Fe (◆) | 114 |
| Figure 4.3.6 | XPS spectra for X _{2/3} films treated by both noncontact methods with different exposure times. The C _{1s} spectra for (a) LPUVL-irradiated films and (b) IB bombarded films and (c) the F _{1s} spectrum for LPUVL-irradiated films | 115 |

| | | |
|---------------|--|-----|
| Figure 4.3.7 | Logarithm scaled pretilt angle as a function of CF ₂ /C ratio for the LPUVL (●) and IB (▲) treatments | 116 |
| Figure 4.3.8 | Surface energies of MAPHM-F8 films including X ₀ (■), X _{1/2} (●), and X _{2/3} (▲) treated by LPUVL irradiations and IB bombardments for different treating times | 117 |
| Figure 4.3.9 | Pretilt angle (circle) and atomic ratio of oxygen content (triangle) as a function of surface energy for all the samples treated by LPUVL irradiation (open) and IB bombardment (solid) with different treating times | 118 |
| Figure 4.3.10 | Total surface energy γ_s (circle), polar surface energy γ_s^p (triangle), and dispersion surface energy γ_s^d (square) are plotted as a function of pretilt angle in logarithm scale for all the samples treated by LPUVL irradiation (open) and IB bombardment (solid) with different treating times | 119 |
| Figure 4.3.11 | Depth-dependencies of C (■), O (●), N (▲) and F (▼) contents in the LPUVL-irradiated X _{2/3} films with treating time: (a) 1 min and (b) 10 min | 120 |
| Figure 4.3.12 | Depth-dependencies of (a) F and (b) CF ₂ contents in the LPUVL-irradiated X _{2/3} films with treating time of 1 min (▲) and 10 min (●) | 121 |
| Figure 4.3.13 | (a) Number of F8 monomer assumed in each layer and (b) the evaluated fluorine content for the as-deposited film (▲) and films treated by LPUVL-irradiation for 1 min (●) and 10 min (◆) | 122 |
| Figure 4.3.14 | Stability of pretilt angle on the X ₀ (square), X _{1/2} (circle), X _{2/3} (triangle) films treated by LPUVL-irradiation for 1 min (solid) and 10 min (open) | 123 |
| Figure 5.2.1 | Spatial distribution of glow discharge in the diode-type ion beam system operated in the coating mode | 135 |
| Figure 5.3.1 | The POM photographs of LC cells treated by different V _b : 420 V and 560 V for 20 min | 135 |
| Figure 5.3.2 | Pretilt angle θ_p is plotted as a function of (a) τ for 5CB cells with surfaces treated by plasma beam with different V _b : 420 V (■), 560 V (●), and 700 V (▲) and (b) V _b for 10 min treatments | 136 |
| Figure 5.3.3 | Surface roughness of the PI films treated with different (a) τ for V _b of 420 V (▲) and 560 V (●), and (b) V _b with $\tau=10$ min | 137 |
| Figure 5.3.4 | SEM photographs of the PI film surfaces treated with different (a) V _b for $\tau=10$ min and (b) τ for V _b of 420 V and 560 V | 138 |

| | | |
|---------------|---|-----|
| Figure 5.3.5 | Size of aggregation on the PI surfaces treated by V_b of 420 V (●) and 560 V (▲) is plotted as a function of τ | 139 |
| Figure 5.3.6 | Pretilt angle is plotted as a function of the size of aggregation for V_b of 420 V (●) and 560 V (▲) | 140 |
| Figure 5.3.7 | Surface energy is plotted with treating time for V_b of (a) 420 V and (b) 560 V | 141 |
| Figure 5.3.8 | Surface energies of the PI films treated with different V_b for 10 min | 142 |
| Figure 5.3.9 | Content of C (■), O (●), N (▲), and Fe (▼) are plotted as a function of (a) τ with the bias of 560 V and (b) V_b for 20 min irradiation | 143 |
| Figure 5.3.10 | Composition of O1s core level signal as a function of (a) τ with the bias of 560 V and (b) V_b for 20 min irradiation | 144 |
| Figure 5.3.11 | Relation between the dispersive surface energy and the content of C-O-Fe bond for surfaces treated by different V_b and τ | 145 |
| Figure 5.3.12 | Modes of ligand coordination to the iron oxide surface and modes of coordination through COOH groups | 146 |
| Figure A1 | Schematic drawing of ion beam system utilized in (a) Chaudhari <i>et al.</i> 's, (b) Hwang <i>et al.</i> 's, and (c) Gwag <i>et al.</i> 's works | 157 |
| Figure A2 | The normal glow discharge in neon in a 50 cm tube at pressure of 1 torr | 158 |
| Figure A3 | Schematic representation of self-sustained plasma induced in a planar diode | 159 |
| Figure A4 | Potential distribution in a dc glow discharge process | 160 |
| Figure B1 | Schematic representation of the displacement of component angles | 162 |
| Figure B2 | Experimental setup for measuring the optical transmittance of the LC cell: P1 and P2, polarizers; PD1 and PD2, photo-detectors; BS, beam splitter; DMM, digital multi-meter; Lock-in, Lock-in amplifier. (The light source is a He-Ne laser with wavelength 632.8nm and the two polarizers are Glan-Thompson type) | 164 |
| Figure B3 | The extreme values of intensity measured as a function of the applied voltage. The sample is IB-aligned (DC voltage of 560 V, current density of 255 $\mu\text{A}/\text{cm}^2$, irradiation time of 8 min, and angle of incidence of 60° with thickness of LC layer being 32.4 μm | 165 |
| Figure B4 | Dependence of $(V - V')R/R_{max}$ plotted against $(V - V')$. The solid line represents the best linear fit to the data (a) from 34.0 V to 88.8 V and yields $W_p = 6.6 \times 10^{-4} \text{ J/m}^2$ of a rubbed 5CB cell and (b) 20.2 V to 60.0 V and yields $W_p = 3.2 \times 10^{-4} \text{ J/m}^2$ of an ion-beam bombarded 5CB cell with condition of 560 V, 255 | |

| | | |
|-----------|--|-----|
| | $\mu\text{A}/\text{cm}^2$, 60° and 90 sec for ion energy, current density, angle of incidence and treating time, respectively | 166 |
| Figure B5 | Voltage-dependent capacitance of a VA cell filled with MLC-6608 | 168 |
| Figure B6 | Illustration of the (a) intercept extrapolation method and (b) slope fitting method. A MLC-6608 cell aligned by $\gamma\text{-Fe}_2\text{O}_3$ film with thickness of 212 nm is used as an example | 169 |
| Figure C1 | Equivalent current-loops of squarely-arrayed magnetic domains ... | 171 |
| Figure C2 | Z-dependence of $H_z(x, y, z)$ | 174 |
| Figure C3 | Z-dependence of $H_x(x, y, z)$ | 175 |
| Figure C4 | X-dependence of (a) H_x and (b) H_z components at the position of ($y=L, z=2$ nm) | 176 |
| Figure C5 | X-dependence of (a) H_x and (b) H_z components at the position of ($y=L, z=5$ nm) | 177 |
| Figure D1 | Schematic drawing of director distribution of a LC cell | 178 |
| Figure D2 | Field-dependence of director distribution in a LC cell aligned with $W_p=2\times 10^{-4}$ J/m ² | 179 |
| Figure D3 | A close look at director distribution in nearby region of surface in a LC cell aligned with $W_p=2\times 10^{-4}$ J/m ² | 180 |
| Figure D4 | Schematic drawing of LC director distribution in surface region... | 181 |
| Figure D5 | Director distribution $\phi(z)$ in SR at $H=0.5$ T | 182 |
| Figure D6 | $W_v(z)$ in SR evaluated for two strength of H : 0.35 and 0.50 T | 182 |
| Figure D7 | $W_v(z)$ in SR at $H=0.5$ T with three different W_p | 183 |
| Figure D8 | Director distribution $\phi(z)$ in SR with $\xi=4$ nm at $H=0.5$ T for (a) $H_m(z)$ and (b) $1300\times H_m(z)$ | 184 |

List of Tables

| | | |
|-------------|---|-----|
| Table 2.4.1 | Intensities a_0 of chemical bonds convoluted to the C_{1s} spectrum of surfaces treated by different energies of ion beam | 47 |
| Table 2.4.2 | Intensities a_0 of chemical bonds convoluted to the O_{1s} spectrum of surfaces treated by different energies of ion beam | 47 |
| Table 2.4.3 | Intensities a_0 of chemical bonds convoluted to the C_{1s} spectrum of surfaces treated by different bombarding time | 48 |
| Table 2.4.4 | Intensities a_0 of chemical bonds convoluted to the O_{1s} spectrum of surfaces treated by different bombarding time | 48 |
| Table 2.4.5 | Intensities a_0 of chemical bonds convoluted to the C_{1s} spectrum of surfaces treated by different angle of incidence | 49 |
| Table 2.4.6 | Intensities a_0 of chemical bonds convoluted to the O_{1s} spectrum of surfaces treated by different angle of incidence | 49 |
| Table 3.3.1 | Comparison of polar anchoring strength of the γ - Fe_2O_3 and DMOAP films | 102 |
| Table 3.3.2 | Horizontal and vertical components of the magnetization induced by the γ - Fe_2O_3 films with different thickness. (Unit: emu/g) | 102 |
| Table 3.3.3 | Magnetization of the γ - Fe_2O_3 films with or without thermal annealing. (Unit: emu/g) | 102 |
| Table 4.3.1 | Intensities a_0 of chemical bonds convoluted to the C_{1s} spectrum of X_0 surfaces treated by LPUVL irradiations and IB bombardments | 128 |
| Table 4.3.2 | Intensities a_0 of chemical bonds convoluted to the C_{1s} spectrum of $X_{1/2}$ surfaces treated by LPUVL irradiations and IB bombardments | 128 |
| Table 4.3.3 | Intensities a_0 of chemical bonds convoluted to the C_{1s} spectrum of $X_{2/3}$ surfaces treated by LPUVL irradiations and IB bombardments | 129 |
| Table 5.3.1 | Intensities a_0 of chemical bonds convoluted to the O_{1s} spectrum of surfaces treated by diode plasma with $V_b=560$ V for various τ ... | 151 |
| Table 5.3.2 | Intensities a_0 of chemical bonds convoluted to the O_{1s} spectrum of surfaces treated by different V_b for 20 min | 151 |
| Table D1 | Boundary condition θ_0 and θ_0' at $H=0.5$ T | 181 |

Chapter 1

Introduction

1.1 Background

The applications of liquid crystals (LCs) in optical devices have been widely investigated for decades due to their anisotropic electrical permittivity and magnetic susceptibility [1]. Especially in the area of information display, nematic liquid crystals (NLCs) have received considerable attention due to its promising electro-optical properties. Furthermore, surface alignments of liquid crystals are essential in liquid crystal displays (LCDs). It determines the boundary condition for the molecular orientation at the surface. Currently, the mechanical rubbing is the most conventional method of surface alignment due to its low cost and reliable alignment ability. As a polymer with convincing thermal and mechanical properties, the polyimide (PI) is so far the most favorable alignment material in the conventional rubbing method owing to its high transparency, superior adhesion and chemical stability [2]. However, the mechanical rubbing method which employs a velvet rubbing process on the PI-coated substrate has some drawbacks such as leaving debris and electrostatic charges on the rubbed surfaces. Also, it becomes increasingly difficult to maintain uniformity as the substrate size of LCD gets larger rapidly in industry. Multi-domain or high pretilt angle alignment cannot be easily achieved either.

In order to enhance the qualities of LC products, several contact-free alignment methods such as the photoalignment [3-15], oblique evaporation [16-20] and ion beam alignment [21-27] techniques have been vastly investigated in the past decades. Besides, intense studies have been carried out to develop the alignment materials suitable for each alternative method. These techniques and the related alignment mechanisms are introduced in the following sections.

1.1.1 Photoalignment

In 1991, Gibbons et al. first reported a method for LC alignment that uses

polarized laser light in visible range [3]. A rewritable ability was also discovered by subsequently illuminating the silicone PI copolymer doped with a diazodiamine dye. So far, three kinds of photoreactive polymers have been extensively studied as the photoalignment layer including photo-decomposable polymers [6-9], photocrosslinkable polymers [4,10-12], and photo-isomerizable polymers [13-15]. The corresponding photoreactions have been confirmed as the selective degradation, dimerization reaction (or crosslinking), and isomerization mechanism. Either a parallel or a perpendicular aligning direction can be obtained in these treatments depending on the type of polymer or reaction mechanism. It is worth noticing that the photoreaction of the PI has received considerable attention because of its being widely used in LCDs industries already [6,9,15]. However, long exposure time or high dosage of ultraviolet (UV) irradiation is required to achieve significant effect of surface alignment due to the low photoreactive efficiency of PI.

1.1.2 Oblique evaporation

In 1972, Janning demonstrated a promising method to align LCs using the silicon monoxide or gold film obliquely deposited on the substrates [16]. The angular deposit causes the film to grow in a preferred direction. Only a very thin film with thickness of 70 Å is required for surface alignment. It is interesting that various deposited materials show different results. For example, a copper will give homeotropic alignment, while chromium, platinum, and aluminum align LC to the direction of deposit. In 1980, Uchida et al. investigated the relationship between the pretilt angle and the evaporation conditions including the incidence angle and film thickness [19]. They proposed two methods of varying the pretilt angle in the range of 0° to 30° from the homeotropic alignment. In 1982, Hiroshima proposed another evaporation procedure to obtain a wide tilt range of 0° to 60° from surface normal [20]. Without change of incidence angle, the azimuth of SiO beam changes continuously during deposition. The tilt angle can be controlled by choosing the azimuthal distribution of deposition.

In the oblique evaporation process, a micro columnar structure is realized on the substrate surface due to the self shadowing effect. This columnar structure agrees with the growth process of the surface structure model suggested by van de Waterbeemd [21].

The relationship among the surface topology and LC orientation could be explained well by the columnar structure model proposed by Goodman-van de Waterbeemd [22]. At a deposition angle of ca. 50°, homogeneous alignment with a 0° pretilt angle is realized due to the formed grooves perpendicular to the incidence plane of beam.

1.1.3 Ion beam alignment

In 1998, Chaudhari et al. from IBM research group found that the LCs can be aligned on the PI surface exposed to a low energy and neutral argon ion beam [23]. They also successfully realized this non-contact alignment technology by integrating low energy ion beam equipments and diamond-like carbon (DLC) thin films into LCD manufacturing processes [24]. In 2001, Stöhr et al. demonstrated that the anisotropical changes of carbon double or triple bonds caused by ion bombardment are responsible for introducing the surface orientational anisotropy [26]. That means any amorphous carbon layer with directional nature of sp^2 and sp bonds can induce the alignment of LCs. Besides carbon, also a great variety of other materials, such as SiN_x , SiC , SiO_2 , Al_2O_3 , CeO_2 , SnO_2 , $ZnTiO_2$ and $InTiO_2$ can be used as alignment materials.

Over the past few years, several studies devoted to ion-beam bombarded DLC and PI films have also been reported [27-29]. One of the most remarkable results is that the homeotropic alignments can be obtained by using fluorinated DLC thin films as the alignment layer and the pretilt angle can also be controlled by choosing different ion-beam parameters or the concentration of fluorine doped in DLC films [29]. In addition, both homogeneous and homeotropic alignments can be obtained with the same kind of organic alignment layers bombarded by ion beams with different energies [27,28]. This remarkable ability of controlling the alignment modes makes the ion-beam alignment method potentially useful in LC-based applications, especially in LCDs industry.

1.1.4 Alignment mechanism

For a conventional rubbing method, the preferential alignment of polyimide chain segments along the rubbing direction is formed. The epitaxial effects are suggested responsible for the LC alignment [30]. Another mechanism suggested by Berreman is

that the LC molecules prefer to align with the microgrooves created by rubbing process, so as to the total surface free energy is reduced [31]. However, LC alignment also occurs on surfaces of disordered polymers. Most recently, Stöhr et al.'s results suggest that LC alignment only requires a statistically significant preferential bond orientation at the polymer surface, without the necessity of crystalline or quasi-crystalline order [32]. A general directional interaction model was proposed in which the LC direction is guided by a π orbital interaction between the LC molecules and the anisotropic polymer surface. Even materials without translational order, i.e. amorphous materials, may have orientational order because of the strong directional nature of unsaturated carbon bonds [33]. Rubbing, UV irradiation, and ion beam bombardment are examples of methods that can produce orientational order.

1.2 Overview of this thesis

In this thesis, the content is divided into four subjects related to the ion beam alignment techniques. The first coming, in Chap. 2, is titled as the “controllable alignment modes of nematic liquid crystals on argon ion beam bombarded polyimide films”. We will demonstrate that the polyimide surface treated by argon ion beams can give both homogeneous and homeotropic alignments with the same ion beam apparatus but varying the energy of ion beam and the bombarding time.

In Chap. 3, demonstration of a method for liquid crystal surface alignment by using a one-step, ion beam sputtering on glass substrates is followed with the identification of the unexpectedly coated material, i.e. iron-oxide. In subsequent two chapters, two alignment methods of inducing high pretilt angle are presented. In Chap. 4, surface treatments accomplished through the ultraviolet irradiation and ion beam bombardment on the newly developed copolymer materials with fluorinated carbonyl groups of different mole fraction and their effects on liquid crystal surface alignments have been studied. In Chap. 5, the polyimide surfaces are treated by oblique plasma beam irradiation with simultaneous coating of maghemite nanoparticles. For each of them, the mechanism in determining the pretilt angle has also been discussed.

Finally, we will summarize the remarks concluded in each work and point out the

possible directions of future work.



References

1. P. G. deGennes and J. Prost, *The Physics of Liquid Crystals*, 2nd ed. (Oxford, New York, 1993), pp. 117-139.
2. M. K. Ghosh and K. L. Mittal, *Polyimides: Fundamentals and Applications*, (Marcel Dekker, New York, 1996).
3. W. M. Gibbons, P. J. Shannon, S. T. Sun, and B. J. Swetlin, *Nature* 351, 49 (1991).
4. M. Schadt, K. Schmitt, V. Kozinkov, and V. Chigrinov, *Jpn. J. Appl. Phys.* 31, 2155 (1992).
5. J. Chen, D. L. Johnson, P. J. Bos, X. Wang, and J. L. West, *Phys. Rev. E* 54, 1599 (1996).
6. J. Lu, S. V. Deshpande, E. Gulari, J. Kanicki, and W. L. Warren, *J. Appl. Phys.* 80, 5028 (1996).
7. S. Gong, J. Kanicki, L. Ma, and J. Z. Z. Zhong, *Jpn. J. Appl. Phys.* 38, 5996 (1999).
8. M. Nishikawa, T. Kosa, and J. L. West, *Jpn. J. Appl. Phys.* 38, L334 (1999).
9. M. Nishikawa, J. L. West, and Yu. Reznikov, *Liq. Cryst.* 26, 575 (1999).
10. M. Schadt, H. Seiberle, and A. Schuster, *Nature* 381, 212 (1996).
11. Y. Iimura, S. Kobayashi, T. Hashimoto, T. Sugiyama, and K. Katoh, *IEICE Trans. Electron* E79-C, 1040 (1996).
12. G. P. Bryan-Brown, and I. C. Sage, *Liq. Cryst.* 20, 825 (1996).
13. H. Akiyama, K. Kudo, and K. Ichimura, *Macromol. Rapid Commun.* 16, 35 (1995).
14. T. Ikeda and A. Kanazawa, *Bull. Chem. Soc. Jpn.* 73, 1715 (2000).
15. B. Park, Y. Jung, H. H. Choi, H. K. Hwang, Y. Kim, S. Lee, S. H. Jang, M. A. Kakimoto, and H. Takezoe, *Jpn. J. Appl. Phys.* 37, 5663 (1998).
16. J. L. Janning, *Appl. Phys. Lett.* 21, 173 (1972).
17. W. Urbach, M. Boix, and E. Guyon, *Appl. Phys. Lett.* 25, 479 (1974).
18. D. Armitage, *J. Appl. Phys.* 51, 2552 (1980).
19. T. Uchida, M. Ohgawara, and M. Wada, *Jpn. J. Appl. Phys.* 19, 2127 (1980).
20. K. Hiroshima, *Jpn. J. Appl. Phys.* 21, L761 (1982).
21. J. G. W. van de Waterbeemd and G. W. van Oosterhout, *Philips Res. Rep.* 22, 375 (1967).
22. L. A. Goodman, J. T. McGinn, C. H. Anderson and F. Digeronimo, *IEEE Trans. Electron Devices* ED-24, 795 (1977).
23. P. Chaudhari, J. Lacey, S. C. Alan Lien, and J. L. Speidell, *Jpn. J. Appl. Phys.* 37, L55 (1998).
24. P. Chaudhari et al., *Nature* 411, 56 (2001).

25. J. P. Doyle et al., *Nuclear Instruments and Methods in Physics Research B* 206, 467 (2003).
26. J. Stöhr, M. G. Samant, J. Lüning, A. C. Callegari, P. Chaudhari, J. P. Doyle, J. A. Lacey, S. A. Lien, S. Purushothaman, and J. L. Speidell, *Science* 292, 2299 (2001).
27. S. H. Lee, K. H. Park, J. S. Gwag, T. H. Yoon, and J. C. Kim, *Jpn. J. Appl. Phys.* 42, 5127 (2003).
28. J. S. Gwag, K. H. Park, J. L. Lee, J. C. Kim, and T. H. Yoon, *Jpn. J. Appl. Phys.* 44, 1875 (2005).
29. H. J. Ahn, S. J. Rho, K. C. Kim, J. B. Kim, B. H. Hwang, C. J. Park, and H. K. Baik, *Jpn. J. Appl. Phys.* 44, 4092 (2005).
30. J. M. Geary, J. W. Goodby, A. R. Kmetz, and J. S. Patel, *J. Appl. Phys.* 62, 4100 (1987).
31. Dwight W. Berreman, *Phys. Rev. Lett.* 28, 1683 (1972).
32. J. Stöhr, et al., *Macromolecules* 31, 1942 (1998).
33. R. H. Hurt, Z.-Y. Chen, *Phys. Today* 53, 39 (2000).



Chapter 2

Controllable Alignment Modes of Nematic Liquid Crystals on Argon Ion Beam Bombarded Polyimide Films

2.1 Overview

In this work, we study the alignment properties of nematic liquid crystal (NLC) on the polyimide (PI) films treated by argon ion beams with various energies and bombarding times by using a commercial diode sputter as the ion beam source. The structural design and operating principle of a diode type ion sputter will be described in detail in Sec. 2.2. We find that there exist two alignment modes, homeotropic and homogeneous alignments, which can be controlled by varying the energy of ion beams and the bombarding time. The pretilt angle is measured as a function of the bombarding time. We have also studied the surface morphology change of the PI films by using atomic force microscope (AFM) and the chemical change by using the surface sensitive x-ray photoelectron spectroscopy (XPS). The alignment mechanism is then discussed depending on the results of AFM and XPS in Sec. 2.4.

2.2 Ion beam treatment

It is entirely different from the usage of an independent ion source (Kaufman type) in Chaudhari et al.'s excellent work [1,2] that a diode type source is adopted in our studies. More details about these two types of ion sources are introduced in Appendix A. The ion beam conditions used in this study are then addressed in Sec. 2.2.2.

2.2.1 Ion source

In this research, a direct-current (DC) ion sputter (model IB-2 from EIKO Engineering Co., Ltd.) has been used for ion-beam treatment on PI surface. A schematic structure is plotted in Fig. 2.2.1. A cylindrical vacuum chamber with diameter of 130

mm and height of 100 mm is connected to a direct drive oil rotary vacuum pump (GVD-101, ULVAC) through the exhaust pipeline. The ultimate pressure of 15 mTorr can be achieved. The working gas, argon, is introduced into the chamber through a gas inlet equipped with a precision micro gas control valve. The clearance between the electrodes is 35 mm. The diameters of upper and lower electrodes are 50 mm and 52 mm, respectively. This ion-beam sputter can be used either as a coating or etching device, depending on the polarity of the voltage. Its operational principles are the same as those of a diode sputter as described in Sec. 2.2.2.

2.2.2 Ion beam conditions

The etching mode is selected in this work. Figure 2.2.2(a) shows the spatial distribution of glow discharge in our ion coater under the etching mode. The cathode dark space has the most energetic ions and provides the main region for ion-beam treatment. Limited to the scale of bombarding area mentioned above, the size of substrates has to be controlled such that they are totally immersed in this region as shown in Figure 2.2.2(b). The arrows indicate the direction of incident ion beam. In our system, the incidence angle θ_{ion} , bombarding time τ , current density J_{ion} and the energy of ions are all controllable. The energy of ions can be varied by changing the DC bias between electrodes. It is difficult to quantitate the real ion energy in our diode plasma system; therefore, a DC bias is used instead and labeled as V_b . It should be noticed that the sample stages with different angles are insulated from the lower electrode. Before each ion-beam process, the chamber is pumped down to a base pressure of 30 mTorr and then argon gas is fed into the chamber to a target pressure. To obtain the required ion current density, the total pressure of the chamber has to be adjusted between 50 and 180 mTorr when the applied dc voltage is changed.

2.3 Experiments

The indium-tin-oxide coated glasses with size of 20 mm × 10 mm are used as the substrates. Before polymer coating, each substrate have to be cleaned using a standard process shown in the flowchart of Fig. 2.3.1.

2.3.1 Sample preparation

After cleaning, the substrates are spin coated with the polyimide SE-130B (Nissan Chemical Industries, Ltd.), which is commonly used as an alignment agent in super twisted nematic LCD. The spin rate is 2000 rpm for the first 15 seconds and 4000 rpm for the 25 seconds afterward. The substrates are then pre-baked at 70°C for 15 minutes and cured at 180°C for another one hour. This thermal treatment process is chosen according to the company's instruction for achieving a pretilt angle of 3° by conventional rubbing method. Two substrates are bombarded in ion beam chamber simultaneously and then combined with a 23 μm Mylar spacer in between with anti-parallel alignment direction to form an empty cell. The nematic liquid crystal 4'-n-pentyl-4-cyanobiphenyl (5CB, Merck) with a nematic range between 24.0°C and 35.3°C is filled into the empty cell for alignment characterization.

2.3.2 Alignment characterization

After annealing, the alignment modes of the LC cells are characterized with conoscope and polarizing optical microscope (POM). The pretilt angle of 5CB molecules near the surface is measured by using the "crystal rotation method" [3]. The experimental determination of polar anchoring strength is also carried out using the high-electric-field methods [4-6]. The process for measurement and theoretical analysis has been described in detail in Appendix B.

2.3.3 Surface analyses

In addition, the surface morphologies of ion-beam treated PI films are characterized by using a DINS3a atomic force microscope with tapping mode. To study the possible reactions caused by ion-beam bombardment, the compositions of chemical bonds of the polyimide film after ion-beam treatment at various conditions are also analyzed by using XPS (PHI-1600 from Physical Electronics, Inc.). For XPS, a PHI dual-anode x-ray monochromatic source for the x-ray irradiation of Mg K α (1253.6 eV) and Al K α (1486.6 eV) and a PHI 10-360 precision energy analyzer are used. Only the Mg K α line is used in this work unless it is mentioned otherwise. The incident angle of the x-ray is 36° from the sample normal and the photoelectrons are detected at the angle

of 45° from the sample normal. The base pressure during acquisition is below 5.0×10^{-9} Torr. The anode voltage is set at 15 kV (x-ray power 250 W).

Due to the surface charging effect, the measured binding energy (BE) of targeting core level of element will be shifted by *ca* 5 eV to a higher value in this work. The C1s photoelectrons are those most generally adopted for referencing purposes [7]. A binding energy of 284.7 ± 0.2 eV is used for this level in this work. Furthermore, if results from different laboratories are to be compared, the spectrometers should be properly calibrated [8]. After the correction of binding energy scale, the Shirley background [9] is subtracted from the XPS spectrum I of each element by using the packaged software MultiPak (version 8.0, ULVAC-PHI, Inc.). The essential feature of the Shirley algorithm is the iterative determination of a background using the areas marked A_1 and A_2 in Fig. 2.3.2 to compute the background intensity at BE :

$$S(BE) = B_2 + (B_1 - B_2) \frac{A_2(BE)}{A_1(BE) + A_2(BE)}$$

where A_1 and A_2 represent the enclosed areas by the spectrum and background curves. Clearly, $S(BE)$ is initially unknown, therefore, the calculation of a Shirley background from spectral data is an iterative procedure. That is, the integrated areas A_1 and A_2 for each point on the $S(BE)$ have to be initially determined using an approximation to $S(BE)$, then repeat the process using the evaluated $S(BE)$ as input to improve the computed values for A_1 and A_2 to achieve being self-consistent eventually.

After background subtraction, a deconvolution is carried out by fitting the spectra to multiple peaks I_i whereas each are described as a Gaussian-Lorentzian sum function, i.e.

$$I_i(BE) = 2a_0 \left\{ \frac{a_3 \sqrt{\ln 2}}{a_2 \sqrt{\pi}} \exp \left[-4 \ln 2 \left(\frac{BE - a_1}{a_2} \right)^2 \right] + \frac{1 - a_3}{\pi a_2 \left[1 + 4 \left(\frac{BE - a_1}{a_2} \right)^2 \right]} \right\}$$

where $I_i(BE)$ is the intensity of i -th component with peak center at BE which is given by a_1 , a_0 is the area of peak, a_2 is the full width at half maximum of peak and a_3 is the mixing ratio (1 for pure Gaussian, 0 for pure Lorentzian). In the process of deconvolution using the commercial software PeakFit (version 4.11, SYSTAT Software Inc.), parameters a_2 and a_3 are shared between each component peaks. According to the

BE specified in the literatures by which a_1 is initially given for each considered bonding, a_0 , a_2 and a_3 are then obtained after best fitting of experimental data whereas a_1 is usually slightly different from the given value.

After multiple-peaks fitting, the ratio of chemical composition is further evaluated using the fitted parameter a_0 of each component peak. For instance, assume n peaks are convoluted to the core-level signal of element; each fitted a_0 of them is labeled as A_i . Therefore, the total intensity A of considered spectrum should be equal to the sum of each component signal, i.e. $A = \sum_{i=1}^n A_i$. Moreover, the composition ratio of each chemical bond related to the considered element j then can be simply obtained by

$$R_{i,j} = \left(\frac{A_{i,j}}{\sum_{i=1}^n A_{i,j}} \right) \times 100 (\%).$$

If m number of elements is considered, moreover, the ratio of each component element C_j can be evaluated by

$$C_j = \left(\frac{\sum_{i=1}^n A_{i,j}}{\sum_{j=1}^m \sum_{i=1}^n A_{i,j}} \right) \times 100 (\%)$$

2.4 Results and discussion

2.4.1 Alignment characterization

We have observed both of the homeotropic and homogeneous alignments with the ion bombarded films. Figure 2.4.1 shows the POM photographs of 5CB cells put in between the two crossed polarizers. The substrates treated by argon ion beam with various energies exhibit good alignment qualities. In Fig. 2.4.1(a), the homogeneous alignment of 5CB is obtained by using substrates bombarded with the following ion beam condition: the DC bias of 560 V and bombarding time of 40 min. The working pressure is 120 mTorr. The easy axis of 5CB lies in the incidence plane of ion beam and tilts toward the direction of incident ion beam. These alignment properties agree with the results reported by an IBM group [1]. In Fig. 2.4.1(b), we show the homeotropic alignment obtained with another set of ion beam condition: the DC bias of 1120V and bombarding time of 7 min. The working pressure is 50 mTorr. The conoscopic pattern shown in the inset further indicates that the cell is homeotropically aligned.

The measured pretilt angles for two DC biases are shown in Fig. 2.4.2 with respect

to the bombarding time. In the case of homogeneous alignment ($V_b=560$ V), the pretilt angle approaches to a maximum value about 6.43° and then decreases with the increasing bombarding time. However, the pretilt angle of the homeotropic cell ($V_b=1120$ V) is determined as 90° and remains almost the same while increasing the bombarding time.

The polar anchoring strength W_p of 5CB cells are also determined as a function of bombarding time and angle of incidence with $V_b=560$ V. Figure 2.4.3(a) shows an optimized W_p of *ca* 1.6×10^{-3} J/m² is found for the surfaces bombarded for 6 to 8 min. It is followed with an abrupt drop of W_p for surfaces bombarded with duration longer than 8 min. We believe that the etching ability of ion bombardment is responsible for this resultant behavior. In Fig. 2.4.3(b), an angle-dependency of W_p shows that lower values are found in the range of 40° to 60° .

2.4.2 Surface morphologies

To investigate the possible alignment mechanism for liquid crystals on treated PI films, the surface topology are surveyed using AFM. A series of roughness with respect to different bombarding time and applied bias of 560 V is measured. All the treated substrates induce the homogeneous alignments. As seen in Fig. 2.4.4, the surface morphology becomes rough as bombarding time increases. The mean roughness of the surfaces treated for 0, 6, 14, 30 min is 0.2 nm, 1.7 nm, 1.8 nm, and 3.6 nm, respectively. Figure 2.4.5 shows a linear fit of roughness versus bombarding time. Compare the results here with the measured pretilt angle, no strong connection between them is found.

Figure 2.4.6 also shows the AFM images of the PI surfaces but bombarded by various ion energies. The mean roughness of the surfaces treated with V_b of 560 V, 840 V, and 1120 V is 1.2 nm, 1.4 nm, and 0.3 nm respectively. Obviously, the roughness of PI surface bombarded by high energy ion ($V_b=1120$ V) is much smaller than it is by lower energy treatment. It is expected because the higher energy ions have better etching ability and reduces the roughness more. Accordingly, there is not a straightforward relation between the alignment modes and surface topologies induced by ion beam bombardment with different ion energy either.

Although the generation of micro-scaled directional grooves is one of the major alignment mechanisms for conventional rubbing method, the groove structures are not found on the ion-beam treated surfaces. Therefore, the mechanism for aligning liquid crystals is predominately related to the intermolecular interactions.

2.4.3 XPS analyses

The XPS is used to further investigate the changes of chemical bonds on ion-beam treated SE-130B films which possess the typical chemical structure of PI drawn in Fig. 2.4.7 [10-12]. A series of conditions including different ion energies, incidence angles, and bombarding times are chosen for comparison in the ion-beam bombardments. We will begin with the issue of ion beam energy.

Four kinds of samples treated by ion beam bombardments with various V_b , bombarding time of 5 min, incidence angle of 60° , and current density of $255 \mu\text{A}/\text{cm}^2$ are scanned in survey mode with the step size of 1 eV and the analyzer pass energy of 117.4 eV. The survey spectra shown in Fig. 2.4.8 reveal that a significant amount of iron appears on the treated surface with ion beam energy higher than 560 V. The Fe 2p and Fe 3p core-level signals are located in the ranges of 705-735 eV and 53-60 eV, respectively [13]. We speculate that this iron contamination comes from the electrodes of ion beam system. More discussions on these unexpected results will be given later on. In addition, the Si_{2s} signal probably comes from the glass substrate. Figure 2.4.9 shows the core-level 1s signals of carbon (C), oxygen (O), and nitrogen (N) elements scanned in multiplex mode with the step size of 0.2 eV and the analyzer pass energy of 23.5 eV. As we can see, the signals of C_{1s} and N_{1s} are dramatically reduced by increasing the ion beam energy in the treatments. However, the peak position of O_{1s} signal moves to a lower binding energy. And the increase of peak intensity indicates that the extra bonds have been newly formed. The deconvolutions are further carried out for C_{1s} and O_{1s} signals and their fitting results are plotted in Fig. 2.4.10.

For core-level C_{1s} signal, it is composed of five main signals, C-C/C-H (284.56 eV), C-N (285.68 eV), C-O-C (286.29 eV), N-C=O (288.6 eV) and O-C=O (287.4 eV), and a signal contributed from the shakeup satellite at $\text{BE}=291.30$ eV described in [10]. The shakeup satellites are usually shown on the higher BE side of the core-level spectra

of aromatic and unsaturated polymer [14,15]. As shown in Fig. 2.4.10(a), a significant decrease of signal from C-C/C-H, C-N, and C-O-C bonds are found in the high-energy ion beam treatments. The intensity of shakeup satellite also disappears after ion beam treatment with energy of 1120 V. This indicates that the aromatic components like benzene ring and pyrrolidine are destroyed by ion beam bombardments. Similar trend of variation for carbonyl group is also found in O_{1s} spectra as shown in Fig. 2.4.10(b). It should be noticed that two bonds, C-O-Fe (531.1 eV) and Fe_2O_3 (529.77 eV), related to the iron element are newly formed on the surfaces after high energy ion-beam treatments. Their appearances cause the movement of envelope of spectrum to a lower BE side.

To quantitate the variation of signals, the intensity of each chemical bond convoluted to a core-level spectrum is obtained by the integration of its fitted curve, i.e. the mentioned Gaussian-Lorentzian sum function in Sec. 2.3.3, and summarized in Table 2.4.1 and Table 2.4.2. Besides, the integrated intensity is further divided by the overall intensity of the corresponding spectrum to obtain the composition ratio. Figure 2.4.10 shows the composition of each bond as a function of ion beam energy. We can find out that the shakeup satellite in Fig. 2.4.11(a) is gradually reduced with the raise of ion beam energy. In addition, the iron-related bonds appear to become larger as the ion energy increases, as shown in Fig. 2.4.11(b). In Table 2.4.1 and Table 2.4.2, another chemical reaction should be noticed is that the re-oxidization of the dangling bonds occurs after the ion beam bombardments. It causes the increase of oxygen content. However, most contribution is made from the formation of iron oxide on the treated surface for the cases with the ion energy higher than 560 V.

Furthermore, the impact of different bombarding times of the ion beam treatments with ion energy of 560 V, incidence angle of 60° , and current density of $255 \mu A/cm^2$ on the chemical bonding of treated surface is discussed as well. Figure 2.4.12 shows the survey spectra of PI surfaces treated for different bombarding times, 0 min, 2 min, and 8 min. It is not surprising that the iron content is raised by an increase in length of bombarding time. Figure 2.4.13 shows the raw spectra of C_{1s} , O_{1s} , and N_{1s} scanned in the multiplex mode. The deconvoluted signals of C-O-C and C-C/C-H bonds are obviously attenuated for 8 min treatment, as seen in Fig. 2.4.14(a). No significant

reduction but a movement to a lower BE of signal is found for shakeup satellites. The same behavior as remarked before is also observed in the O_{1s} spectrum, as shown in Fig. 2.4.14(b). The intensities of chemical bonds convoluted to the C_{1s} and O_{1s} spectra are also organized in Table 2.4.3 and Table 2.4.4. The decrease of intensity of C-N bond means that a part of the backbones of PI are broken into pieces; meanwhile, the dangling bonds react with oxygen to form the carbonyl groups, N-C=O and O-C=O. Similar results can also be concluded in Fig. 2.4.15(a). Moreover, a dramatic increase of the content of Fe_2O_3 and C-O-Fe bonds after ion beam bombardment is reconfirmed in Fig. 2.4.15(b).

Next, ion beam conditions of ion energy of 840 V, current density of $458 \mu A/cm^2$, bombarding time of 5 min and different angles of incidence are discussed. The survey spectra of surfaces treated with incidence angle of 40° , 60° , and 80° are shown in Fig. 2.4.16. All the bombarded surfaces have the iron contamination without exception. The relative intensities of the fine scanned spectra shown in Fig. 2.4.17 suggest that a smaller angle of incidence offers a better etching ability. Deconvolutions of C_{1s} and O_{1s} spectra have been accomplished further and shown in Fig. 2.4.18 and Fig. 2.4.19. The fitted intensity of each chemical bond is listed in Table 2.4.5 and Table 2.4.6. We can find out that the best etching effect is given by incidence angle of 60° ; on the other hand, more iron contaminations are also found. A similar remark can be concluded according to the calculated composition ratio as shown in Fig. 2.4.20.

Now, we turn to look deeply into how the iron element leads to the homeotropic alignment of liquid crystal. As it has been noticed above that the iron element could be found in the sample if treated by ion beam with energy higher than 560 eV. Figure 2.4.21 shows two survey spectra scanned by using the Mg $K\alpha$ and Al $K\alpha$ lines as the x-ray monochromatic sources for the PI surface treated by beam energy of 1120 V, incidence angle of 60° , beam current density of $255 \mu A/cm^2$, and treating time of 5 min. It should be mentioned that the BE of auger signals remain the same no matter what the x-ray source is. The survey spectrum by Al $K\alpha$ line has been shifted about +230 eV for comparison with that by Mg $K\alpha$ line. In other words, a shift of BE about -230 eV for primary signals of the O_{1s} and Fe_{2p3} levels when x-ray source is changed from Mg $K\alpha$ to Al $K\alpha$ line reveals that these unexpected signals are the auger signals of iron, Fe

LMM [16]. For a detail study of the Fe peaks, the multiplex mode scanning of Fe 2p region on the high energy IB-treated surface is carried out. The spectrum is shown in Fig. 2.4.22. According to the literatures [17,18], the shake-up satellite line at 718.2 eV is characteristic of Fe³⁺ in Fe₂O₃. Further, the narrow peak at 710.4 eV of the Fe 2p spectrum indicates that no Fe²⁺ iron oxidation state exists. In other words, the possibility of forming Fe₃O₄ (magnetite) in the film can be excluded. The film should be composed of the Fe³⁺ oxides, Fe₂O₃ only. The spectrum of the IB-etched ITO film reveals the same profile. Structurally, however, there are four possible types of Fe₂O₃. Two of them, α -Fe₂O₃ (hematite) and γ -Fe₂O₃ (maghemite) are common and widespread in soils [19]. Of the two, only the γ -Fe₂O₃ has permanent magnetic moments.

An interesting result that the homeotropic alignment is still achieved even on a clean substrate without PI coating after the high-energy IB treatment was discovered in addition. To further identify the coated films, the XPS Fe 2p_{3/2} signals of IB-etched PI and ITO films are analyzed in detail as shown in Fig. 2.4.23(a) and Fig. 2.4.23(b), respectively. The measured XPS data are smoothed and the Shirley background is subtracted. Then a deconvolution is done by fitting the spectra to multiple Gaussian peaks. The Fe 2p_{3/2} envelope of the measured spectra is well fitted by using peaks constrained to the multiplets calculated for the iron compound γ -Fe₂O₃ by Gupta and Sen [20]. The splitting of four Fe³⁺ 2p_{3/2} multiplet peaks with binding energies at 709.8, 710.8, 711.8, and 713.0 eV in Fig. 2.4.23 are due to the inclusion of electrostatic interactions and spin-orbit coupling in theoretical calculation [21]. The presence of satellite peak has been ascribed to the shake-up processes [22]. We conclude, therefore, that the treated substrate is coated with an iron oxide of γ -Fe₂O₃.

It is well known that the LC molecules can be reorientated by electric and magnetic field due to their anisotropic electrical permittivity and magnetic susceptibility [23]. The mechanism of homeotropic LC alignment might be ascribed to the magnetic field induced by the γ -Fe₂O₃ or/and the intermolecular interactions at the liquid-crystalline-maghemite interface.

Finally, another issue concerned in this work is that the bond-breaking effects of PI films to the LC alignment induced by ion beams here are similar to that induced by polarized ultraviolet (UV) light irradiation [24,25]. They are both attributed to the

intermolecular interactions between the liquid crystals and the unbroken polyimide chains. To confirm that the alignment in this work is indeed induced by ion beam rather than the UV irradiation in the ion beam chamber, we have formed a cell with substrates partially covered by a fused silica plate while performing the ion-beam treatment. At the covered area the UV light can transmit through the silica plate while the ion beam is blocked. The pictures of this cell between crossed-polarizers are shown in Fig. 2.4.24, only the uncovered area (right hand side) shows good alignment. Since no alignment effect appears in the untreated area (left hand side), we can conclude that the alignment effects are not caused by the UV light from plasma discharge.

2.5 Concluding remarks

We have demonstrated that both homeotropic and homogeneous alignments can be obtained with the same ion beam apparatus and polyimide by varying the ion beam energy or the bombarding time. Both of the homeotropic and homogeneous cells have uniform and high contrast under the crossed polarizer. AFM images of polyimide surfaces treated by ion beams show no microgroove structure but only with roughness changing with bombarding time and ion-beam energy. There is no strong connection between the measured pretilt angle and the roughness. The XPS results show that the main structures including the C-N, C-O-C bonds, and the aromatic rings of PI films are significantly destroyed in the ion beam bombardments and the formation of N-C=O bonds is considered as the neutralization of dangling bonds when exposed to the air. We deduce that the anisotropic destruction to the aromatic groups of PI film dominate the alignment mechanism, as mentioned in Stöhr et al.'s works [26]. The alignment effects are attributed to the intermolecular interactions between the liquid crystals and the unbroken polyimide chains, or more precisely, the benzene rings [27]. Besides, an unexpected contamination of iron element is detected on the bombarded PI film surface. No matter the ion beam condition of how long or what angle the PI film treated with, ion beam energy higher than 560 V always makes it happen. Even the substrate without PI coating is treated by high-energy IB treatments. A homeotropic alignment of LC can be achieved as well. Through the XPS analyses, we have confirmed that the coated

material is an iron oxide of $\gamma\text{-Fe}_2\text{O}_3$ which has intrinsic magnetism. As a result, we speculate that the magnetic field induced by $\gamma\text{-Fe}_2\text{O}_3$ or/and the intermolecular interaction at the liquid-crystalline-maghemite interface give rise to the resultant homeotropic alignment of LC. Moreover, the possibility of UV light induced alignment effect has been excluded in our ion beam treatment process.



References

1. P. Chaudhari, J. Lacey, S. C. Alan Lien, and J. L. Speidell, *Jpn. J. Appl. Phys.* 37, L55 (1998).
2. P. Chaudhari et al., *Nature* 411, 56 (2001).
3. T. J. Scheffer and J. Nehring, *J. Appl. Phys.* 48 (5), 1783 (1977).
4. H. Yokoyama and H. A. van Sprang, *J. Appl. Phys.* 57, 4520 (1985).
5. Yu. A. Nastishin, R. D. Polak, S. V. Shiyanovskii, V. H. Bodnar, and O. D. Lavrentovich, *J. Appl. Phys.* 86, 4199 (1999).
6. Yu. A. Nastishin, R. D. Polak, S. V. Shiyanovskii, and O. D. Lavrentovich, *Appl. Phys. Lett.* 75, 202 (1999).
7. M. P. Seah, in *Practical Surface Analysis*, edited by D. Briggs and M. P. Seah, 2nd ed. (Wiley, Chichester, 1990), Vol. 1, pp. 541-544.
8. M. P. Seah, *Surf. Interface Anal.* 14, 488 (1989).
9. D. A. Shirley, *Phys. Rev. B* 5, 4709 (1972).
10. D. Wolany, T. Fladung, L. Duda, J. W. Lee, T. Gantenfort, L. Wiedmann, and A. Benninghoven, *Surf. Interface Anal.* 27, 609 (1999).
11. A. M. Ektessabi and S. Hakamata, *Thin Solid Films* 377-378, 621 (2000).
12. 遠藤秀幸, 袋裕善, 「液晶配向處理方法」, 中華民國專利 086102577, 民國八十六年.
13. M. Descostes, F. Mercier, N. Thromat, C. Beaucaire, and M. Gautier-Soyer, *Appl. Surf. Sci.* 165, 288 (2000).
14. G. Beamson and D. Briggs, *High Resolution XPS of Organic Polymers: The Scienta ESCA300 Database*, (Wiley, Chichester, 1992), p. 37.
15. D. Briggs and J. C. Rivière, in *Practical Surface Analysis*, edited by D. Briggs and M. P. Seah, 2nd ed. (Wiley, Chichester, 1990), Vol. 1, pp. 130-131.
16. D. Briggs and J. C. Rivière, in *Practical Surface Analysis*, edited by D. Briggs and M. P. Seah, 2nd ed. (Wiley, Chichester, 1990), Vol. 1, pp. 117-119.
17. C. R. Brundle, T. J. Chuang, and K. Wandelt, *Surf. Sci.* 68, 459 (1977).
18. Y. Gao and S. A. Chambers, *J. Cryst. Growth* 174, 446 (1997).
19. R. M. Cornell and U. Schwertmann, *The Iron Oxides: Structures, Properties, Reactions, Occurrences, and Uses*, 2nd ed. (Wiley-VCH, Weinheim, 2003), Chap. 1, pp. 1-7.
20. R. P. Gupta and S. K. Sen, *Phys. Rev. B* 10, 71 (1974).
21. A. P. Grosvenor, B. A. Kobe, M. C. Biesinger, and N. S. McIntyre, *Surf. Interface Anal.* 36, 1564 (2004).
22. L. Yin, I. Adler, T. Tsang, L. J. Matienzo, and S. O. Grim, *Chem. Phys. Lett.* 24, 81 (1974).

23. P. G. deGennes and J. Prost, *The Physics of Liquid Crystals*, 2nd ed. (Oxford, New York, 1993), pp. 117-139.
24. J. Lu, S. V. Deshpande, E. Gulari, J. Kanicki, and W. L. Warren, *J. Appl. Phys.* 80 (9), 5028 (1996).
25. M. Oh-e, D. Kim, and Y. R. Shen, *J. Chem. Phys.* 115, 5582 (2001).
26. J. Stöhr, M. G. Samant, J. Lüning, A. C. Callegari, P. Chaudhari, J. P. Doyle, J. A. Lacey, S. A. Lien, S. Purushothaman, and J. L. Speidell, *Science* 292, 2299 (2001).
27. J. Stöhr and M. G. Samant, *J. Electr. Spectrosc. Relat. Phenom.* 98, 189 (1999).



Figures

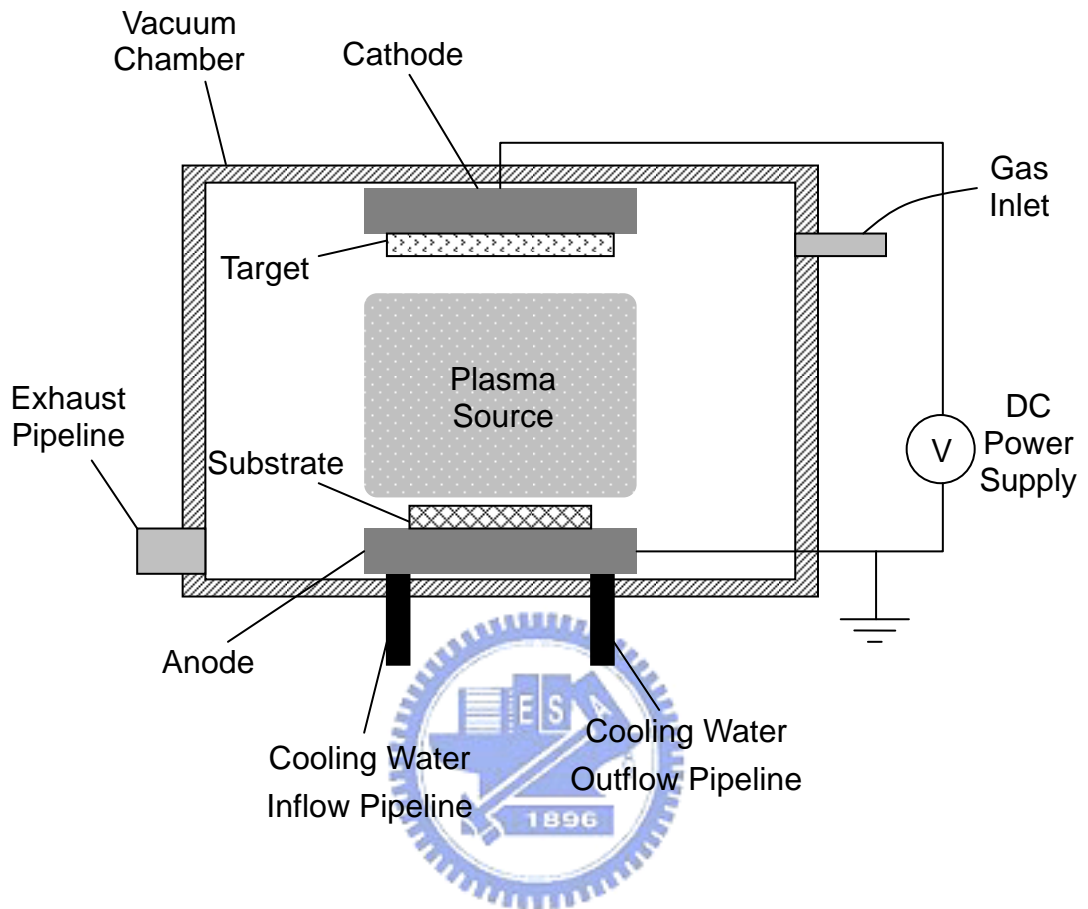


Figure 2.2.1 Structural view of the DC ion-beam sputter operated in coating mode.

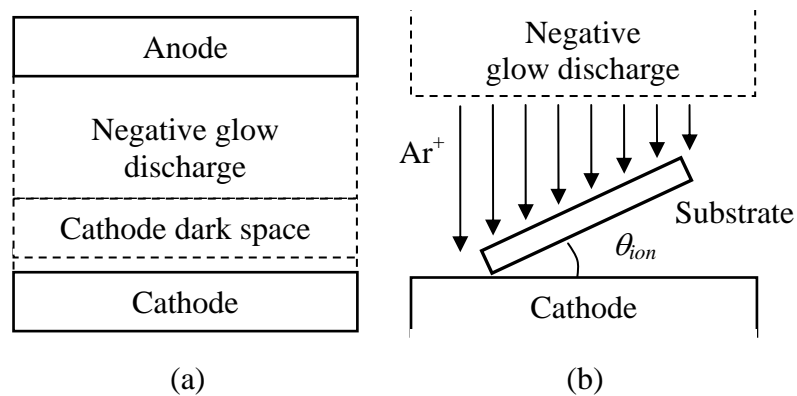


Figure 2.2.2 Sketch of argon ion-beam bombardment: (a) The space distribution of glow discharge in a diode sputter operated in etching mode, and (b) the arrangement of glass substrates in the sputter.

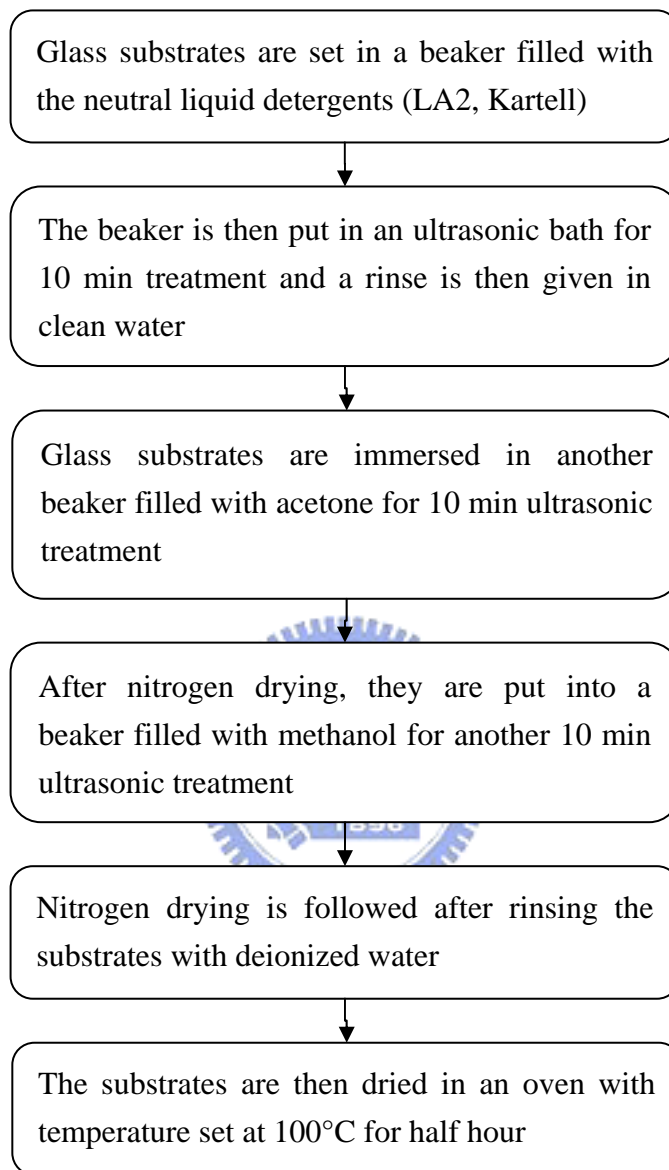


Figure 2.3.1 Procedures of cleaning process.

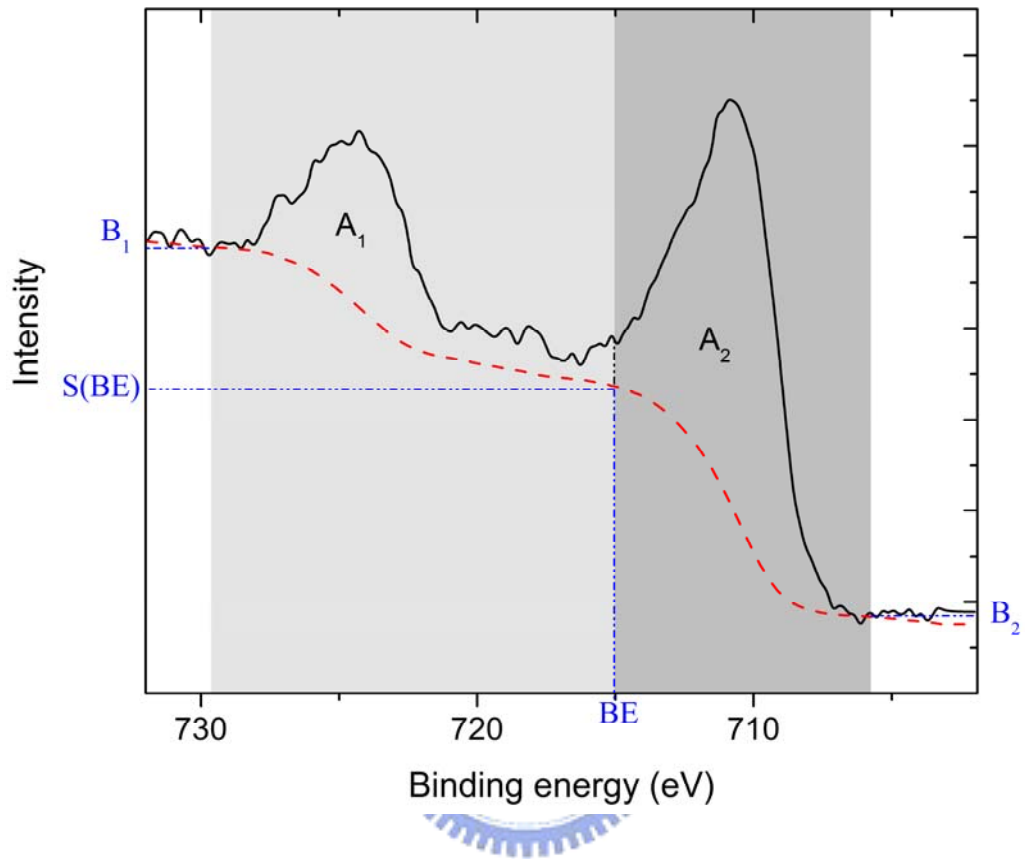


Figure 2.3.2 A Shirley background computed from a Fe 2p spectrum.

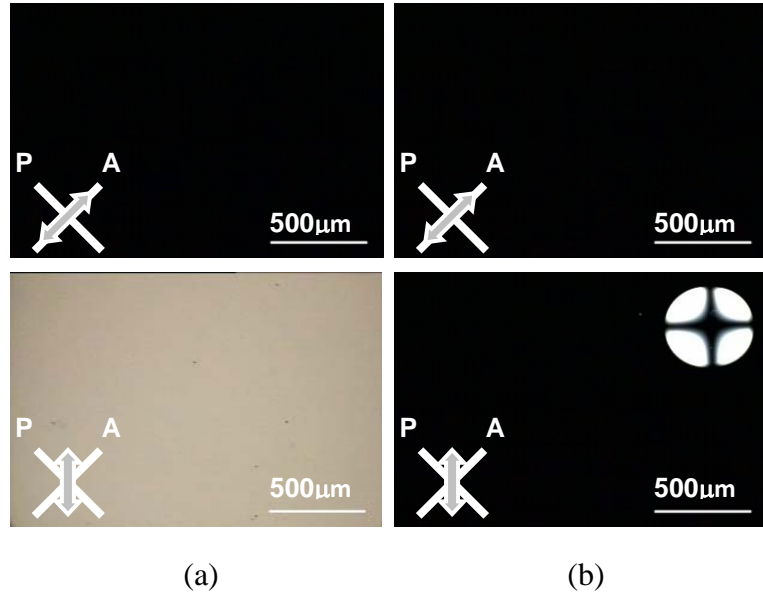


Figure 2.4.1 The POM photographs of NLC 5CB cells treated by different ion beam conditions: (a) homogeneous alignment, and (b) homeotropic alignment. (Inset: conoscopic pattern)

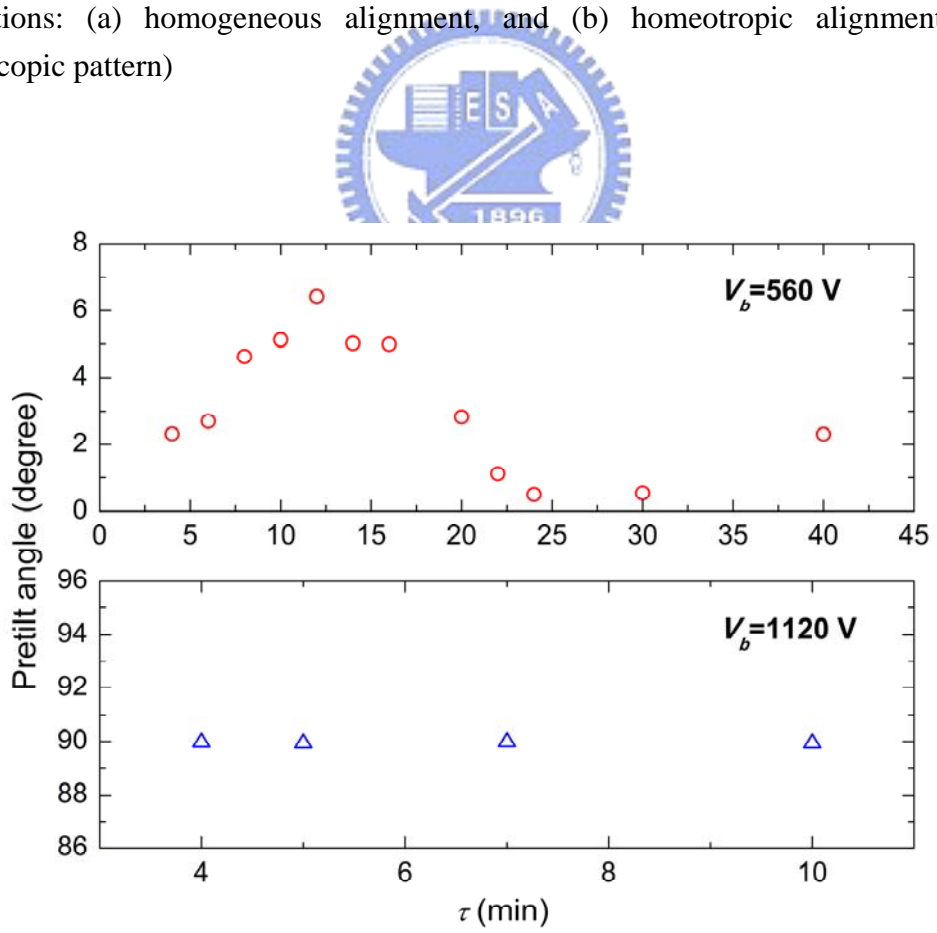
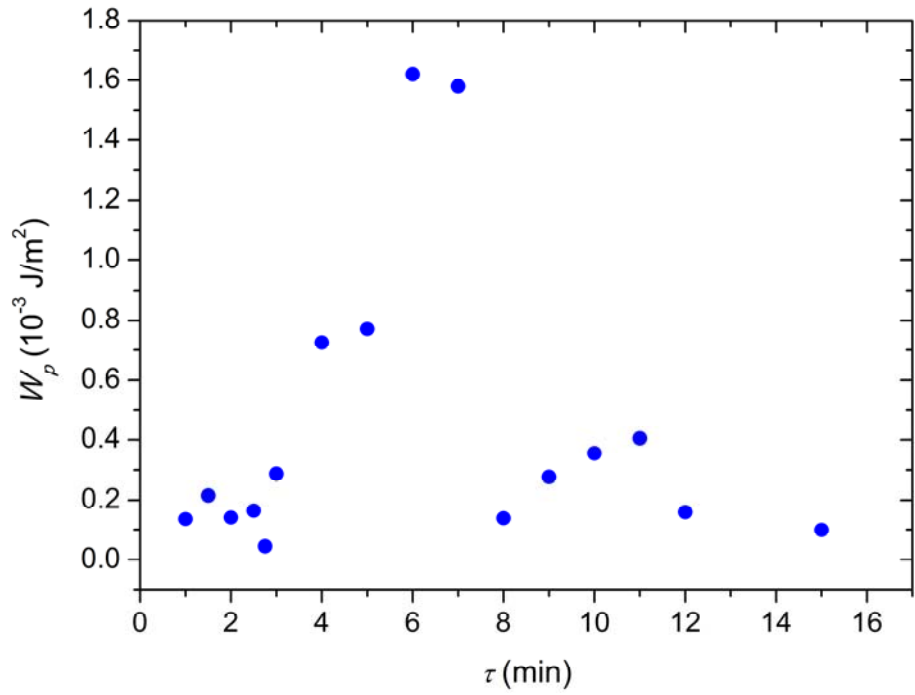
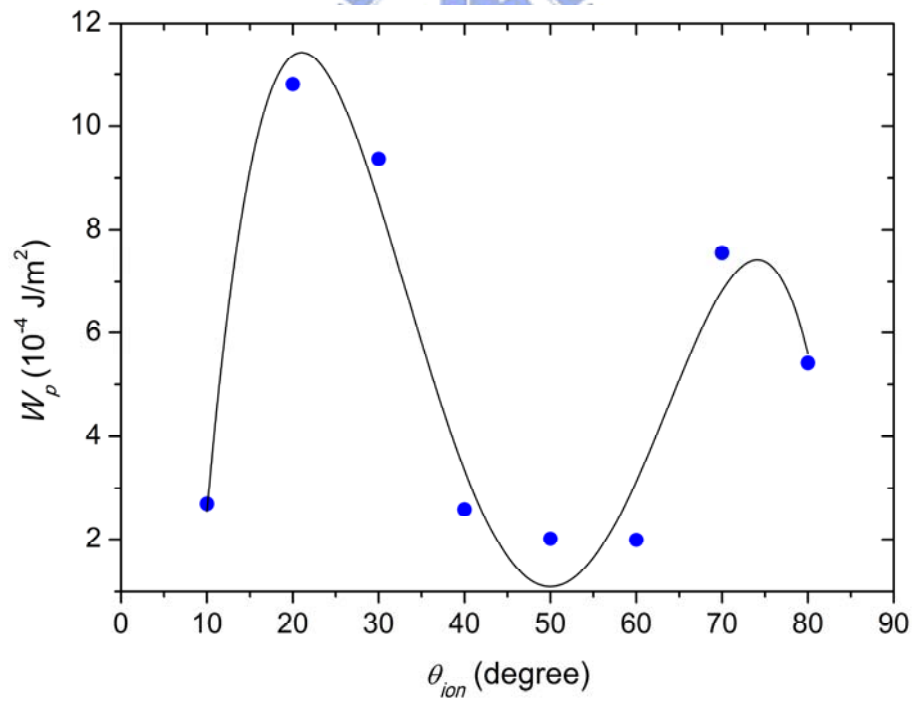


Figure 2.4.2 Pretilt angle vs. the ion beam bombarding time with V_b of 560 V (top) and 1120 V (bottom).



(a)



(b)

Figure 2.4.3 Polar anchoring strength W_p of 5CB cells determined for (a) various τ with $\theta_{ion}=60^\circ$ and (b) various θ_{ion} with $\tau=8$ min for all with $V_b=560$ V.

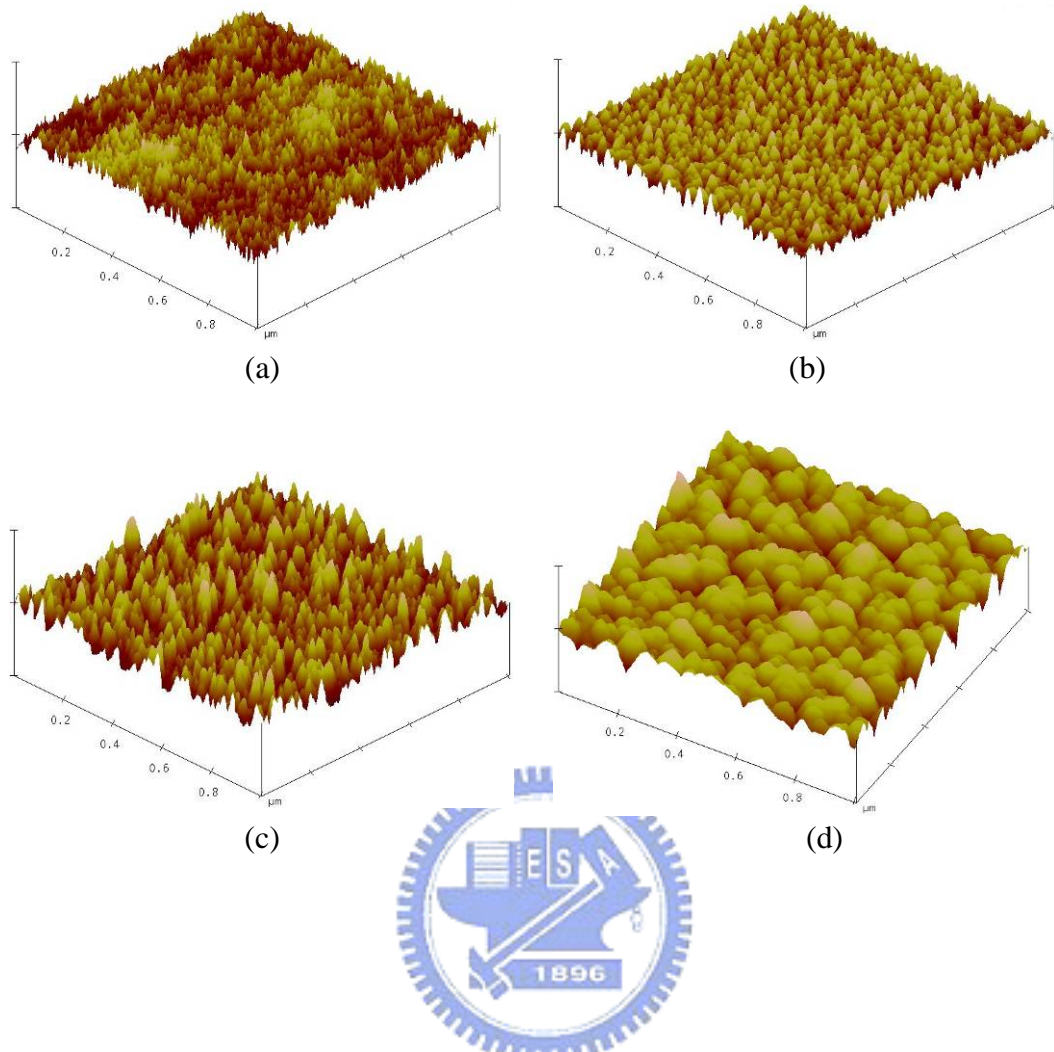


Figure 2.4.4 AFM images of the PI films treated for different τ (a) As-deposited, (b) 6 min, (c) 14 min, and (d) 30 min with $V_b=560$ V. The films here give homogeneous alignments.

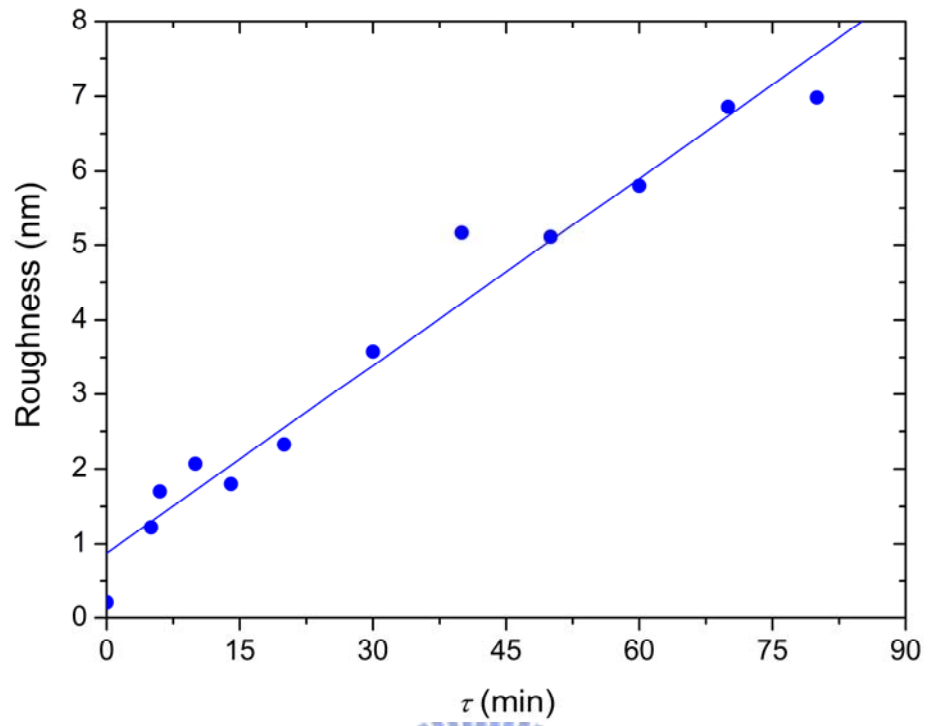


Figure 2.4.5 Roughness of the surfaces treated with $V_b=560$ V for various τ .



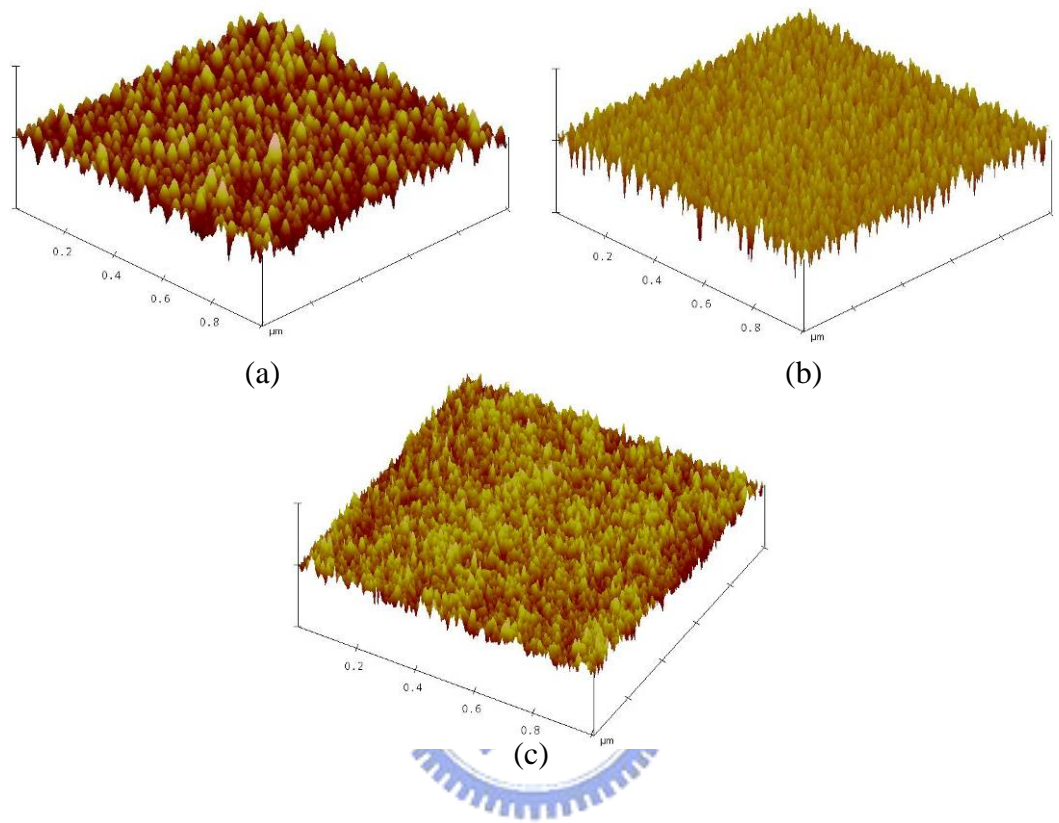


Figure 2.4.6 AFM images of the PI films treated by different ion energies: (a) 560 V, (b) 840 V, and (c) 1120 V with $\tau=5$ min.

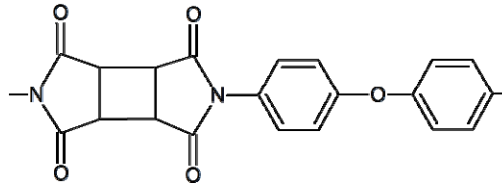


Figure 2.4.7 Primary structure of polyimide.

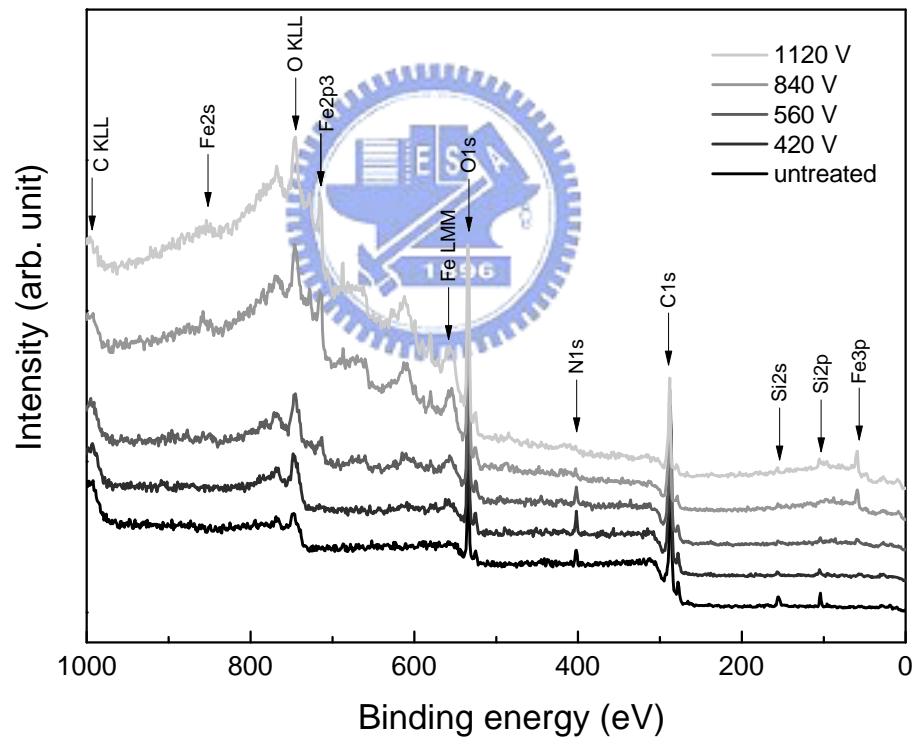


Figure 2.4.8 Survey spectra for the untreated and ion-beam treated PI films with various V_b , $\tau=5$ min, $\theta_{ion}=60^\circ$, and $J_{ion}=255 \mu\text{A}/\text{cm}^2$.

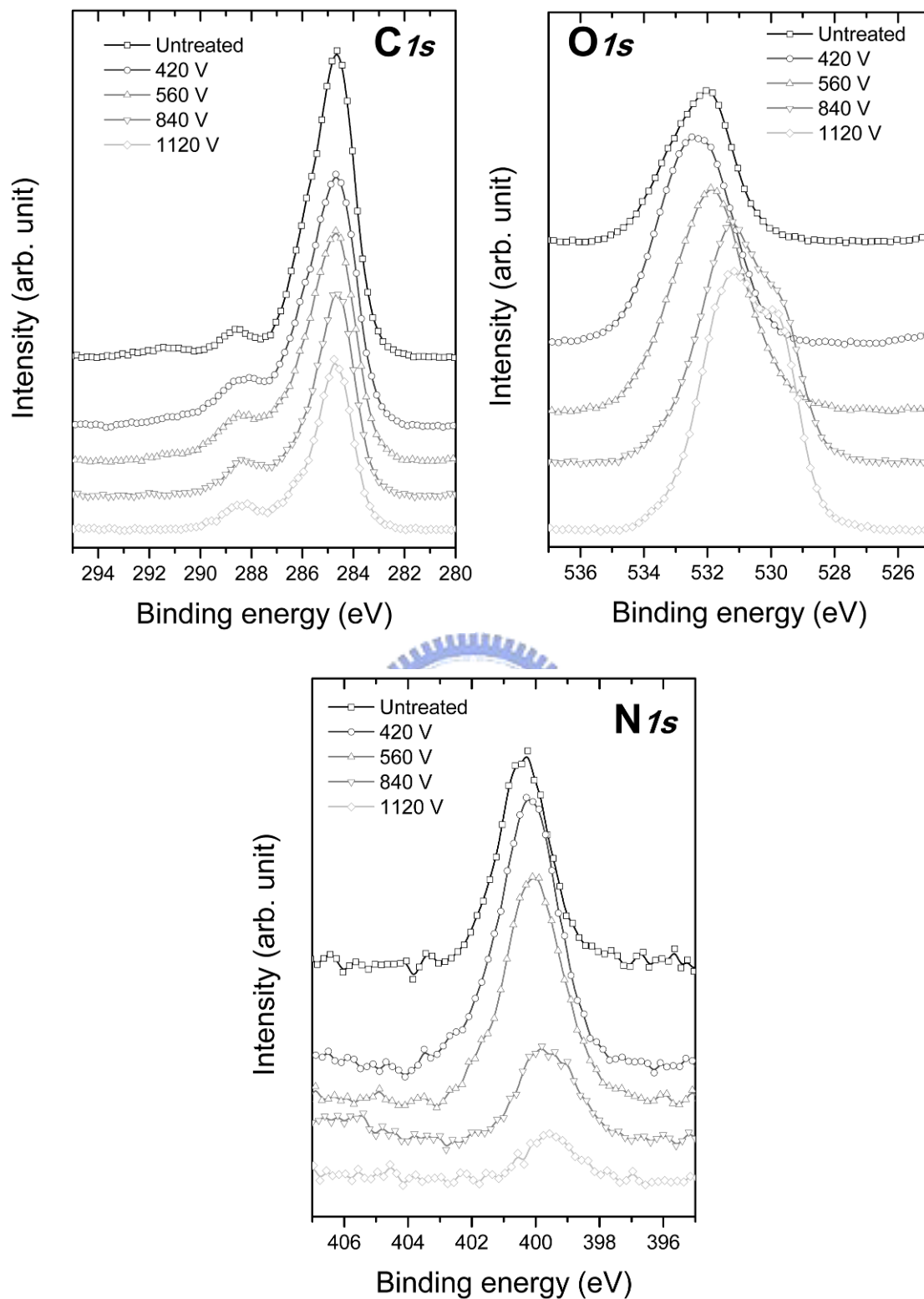
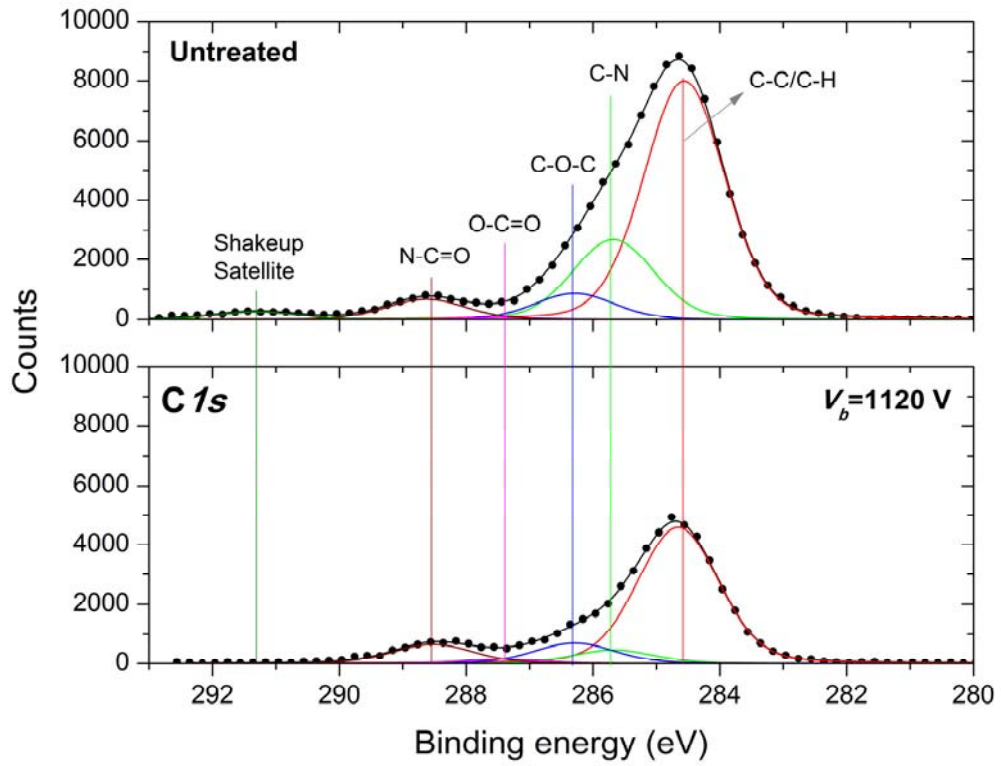
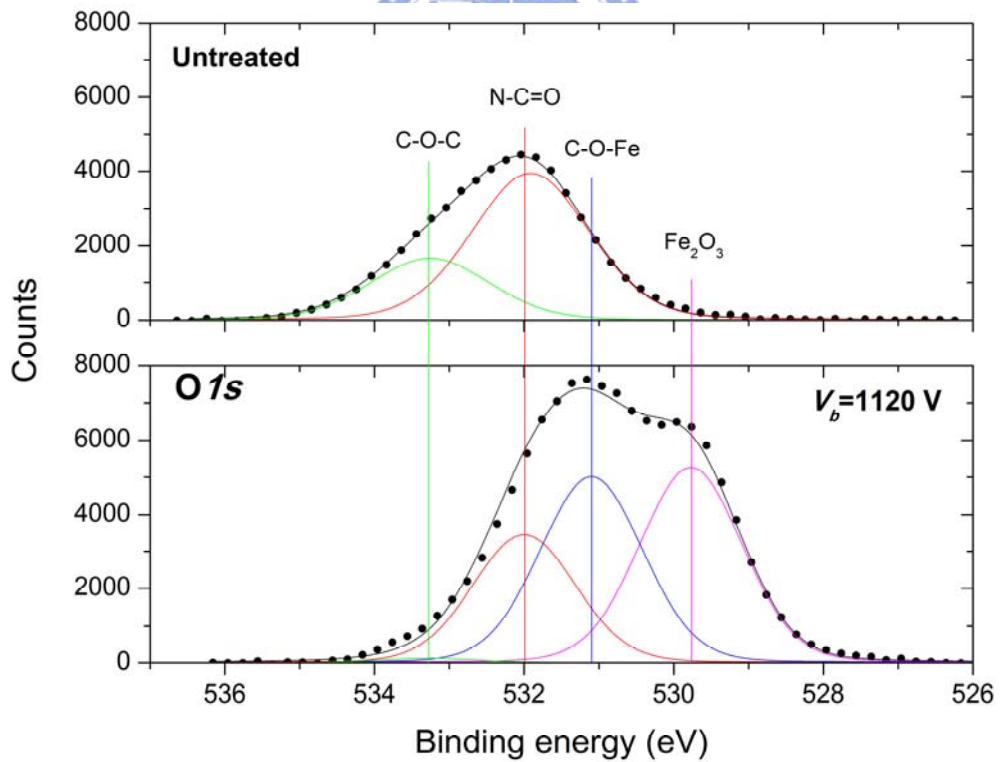


Figure 2.4.9 Multiplex spectra for the untreated and ion-beam treated PI films with various V_b , $\tau=5$ min, $\theta_{ion}=60^\circ$, and $J_{ion}=255 \mu\text{A}/\text{cm}^2$.

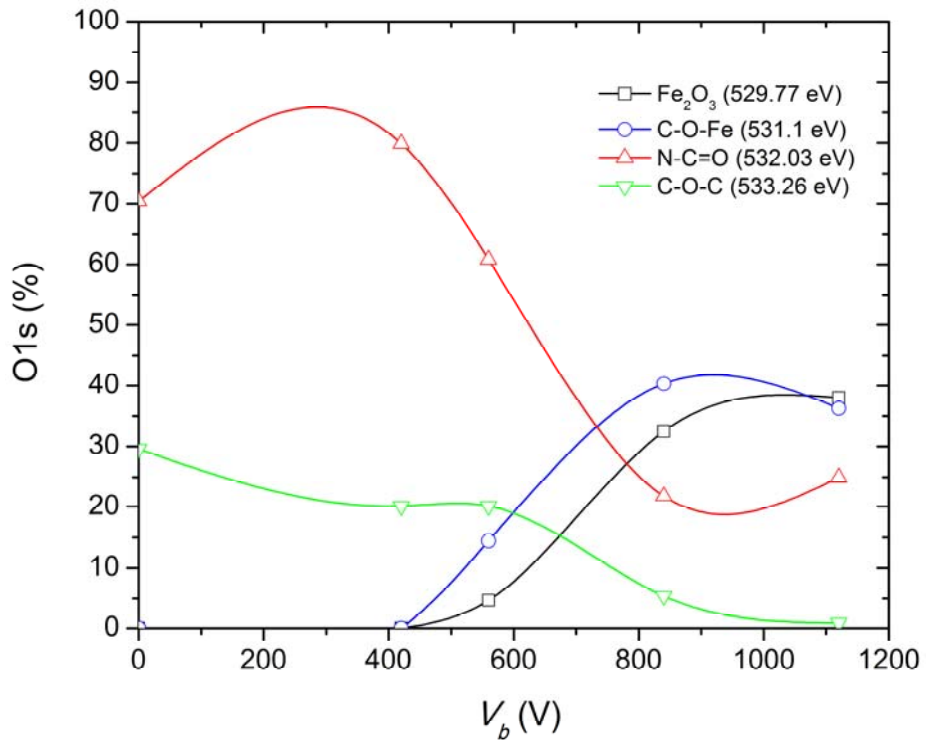
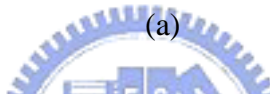
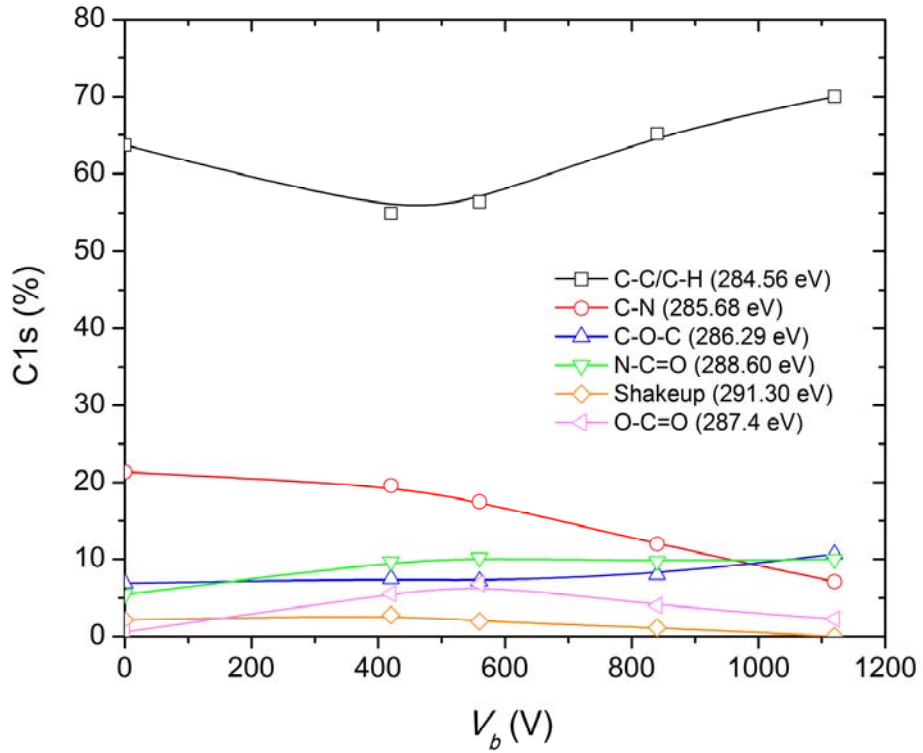


(a)



(b)

Figure 2.4.10 Deconvolution of the (a) C_{1s} and (b) O_{1s} spectra of the untreated and treated PI films with $V_b = 1120$ V.



(b)

Figure 2.4.11 Fraction of the components contributing to the (a) C_{1s} and (b) O_{1s} core-level spectra of untreated and ion-beam treated PI films as a function of V_b.

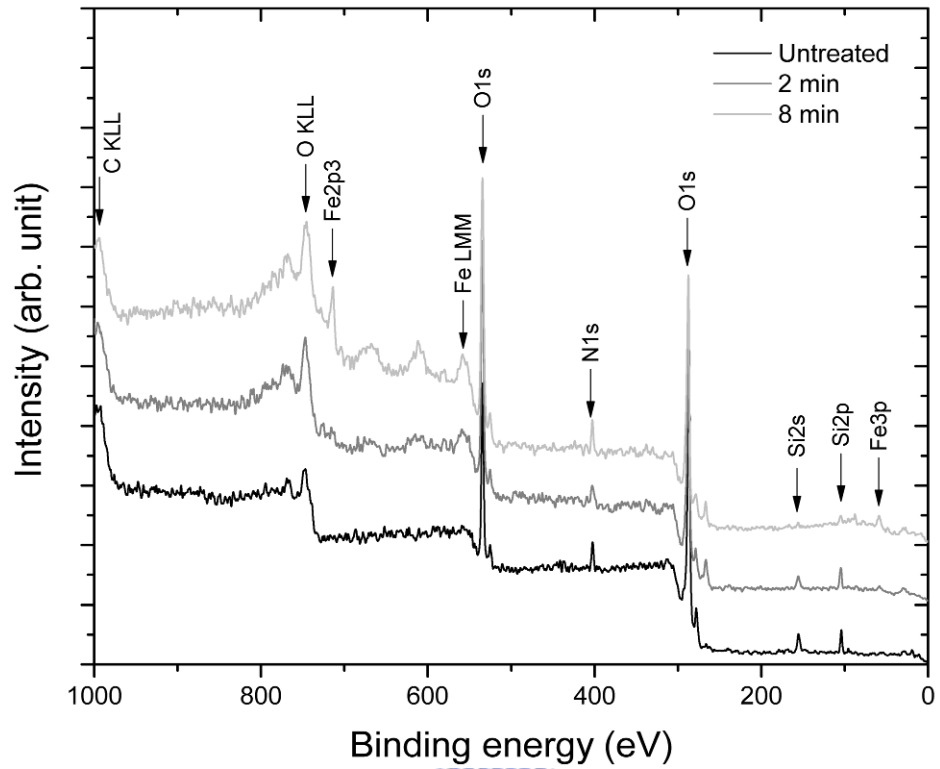


Figure 2.4.12 Survey spectra for the untreated and ion-beam treated PI films with different τ , $V_b=560$ V, $\theta_{ion}=60^\circ$, and $J_{ion}=255 \mu\text{A}/\text{cm}^2$.



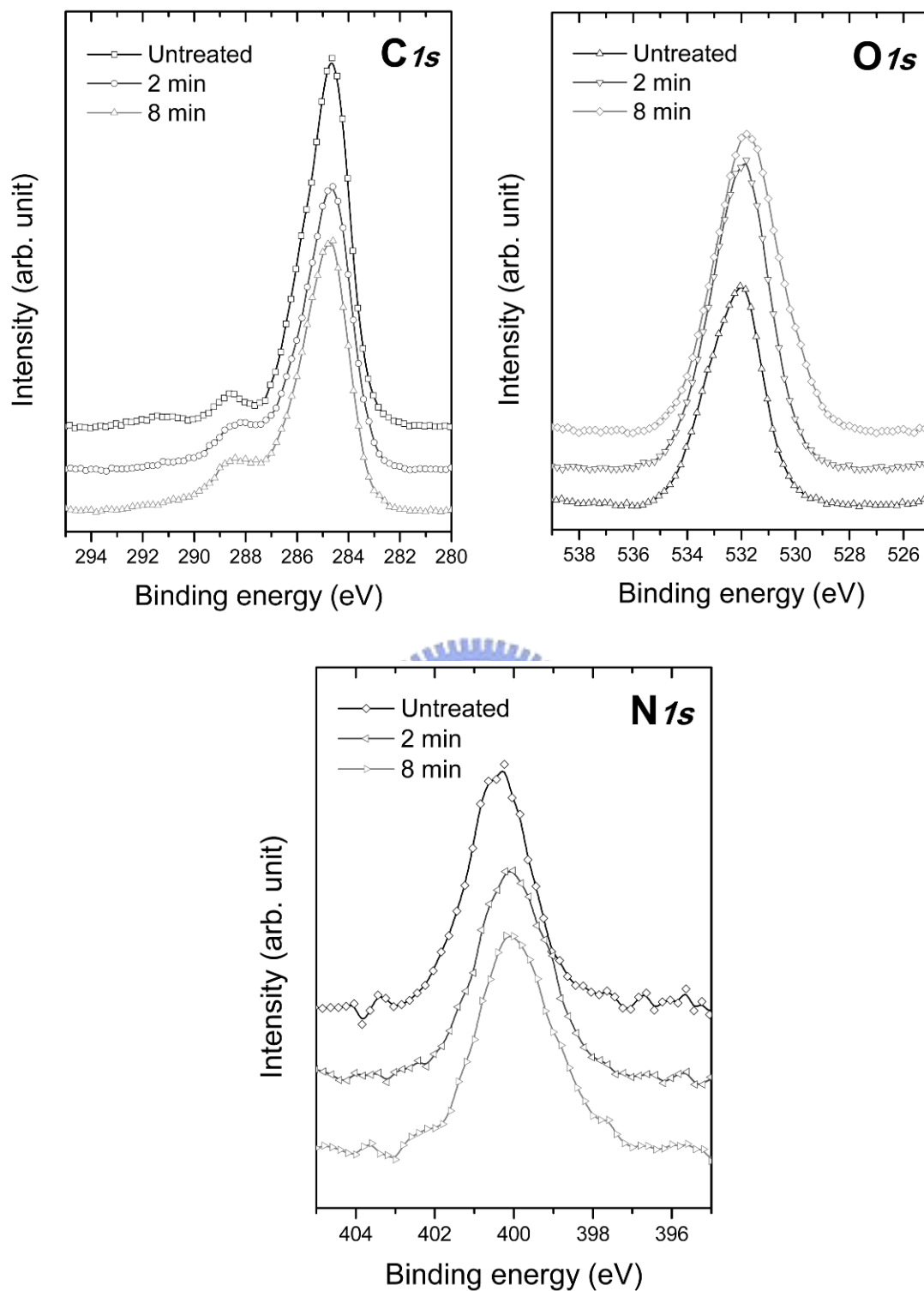
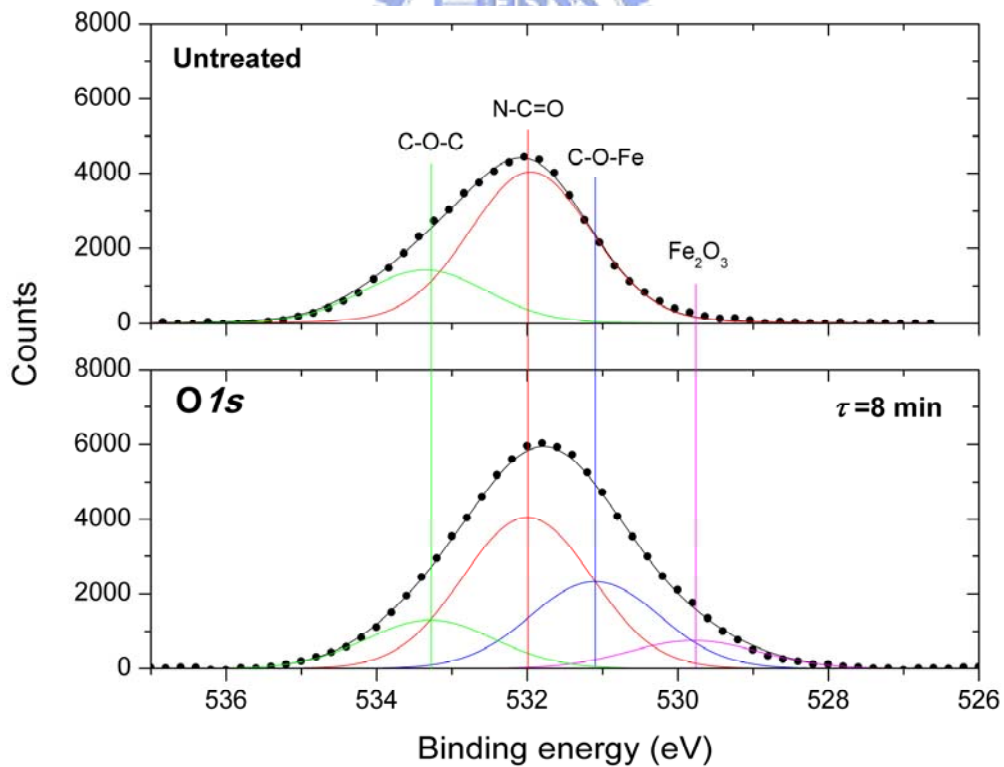
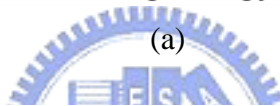
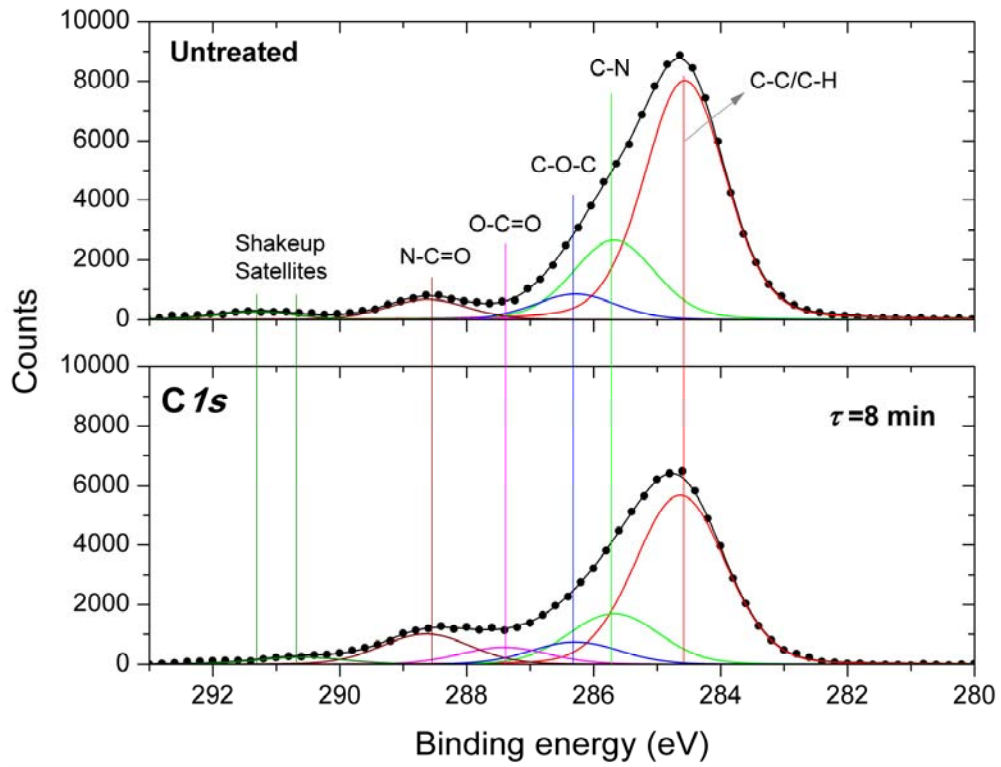


Figure 2.4.13 Multiplex spectra for the untreated and ion-beam treated PI films with different τ , $V_b=560$ V, $\theta_{ion}=60^\circ$, and $J_{ion}=255$ $\mu\text{A}/\text{cm}^2$.



(b)

Figure 2.4.14 Deconvolution of the (a) C_{1s} and (b) O_{1s} spectra for the untreated and treated PI films with $\tau = 8$ min.

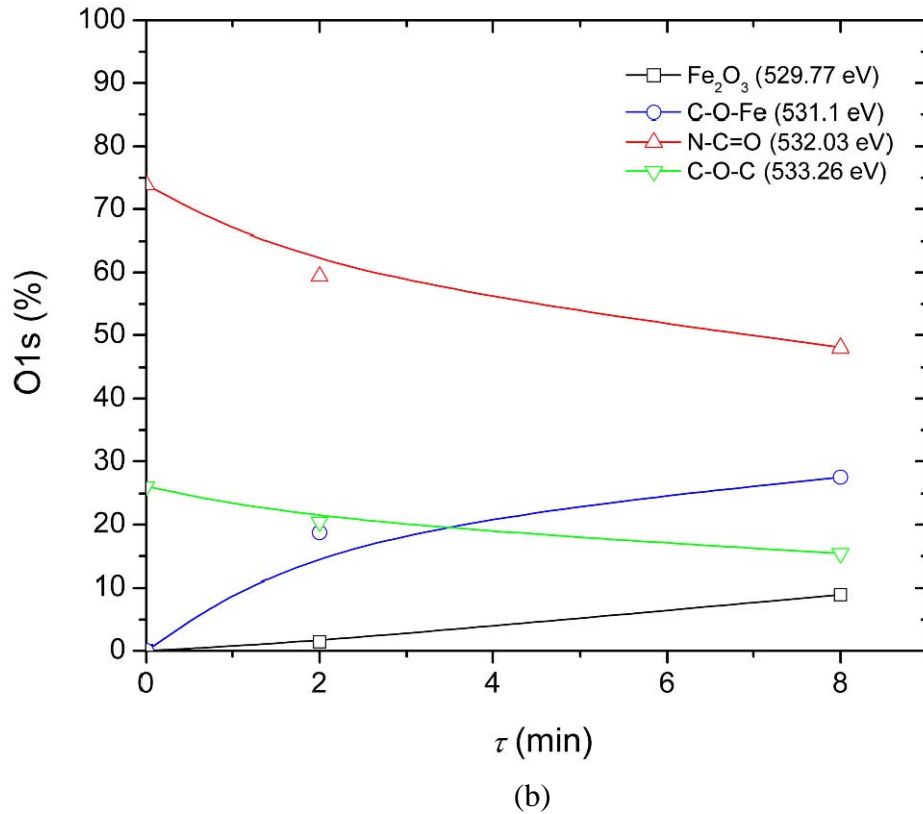
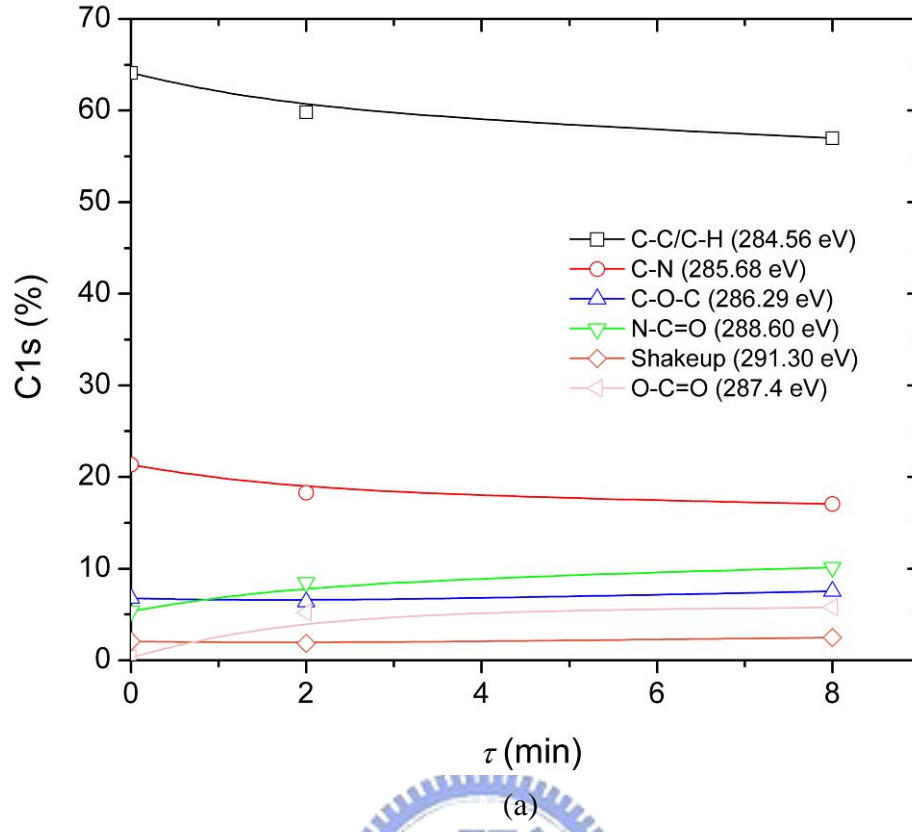


Figure 2.4.15 Fraction of the components contributing to the (a) C_{1s} and (b) O_{1s} core-level spectra of untreated and ion-beam treated PI films as a function of τ .

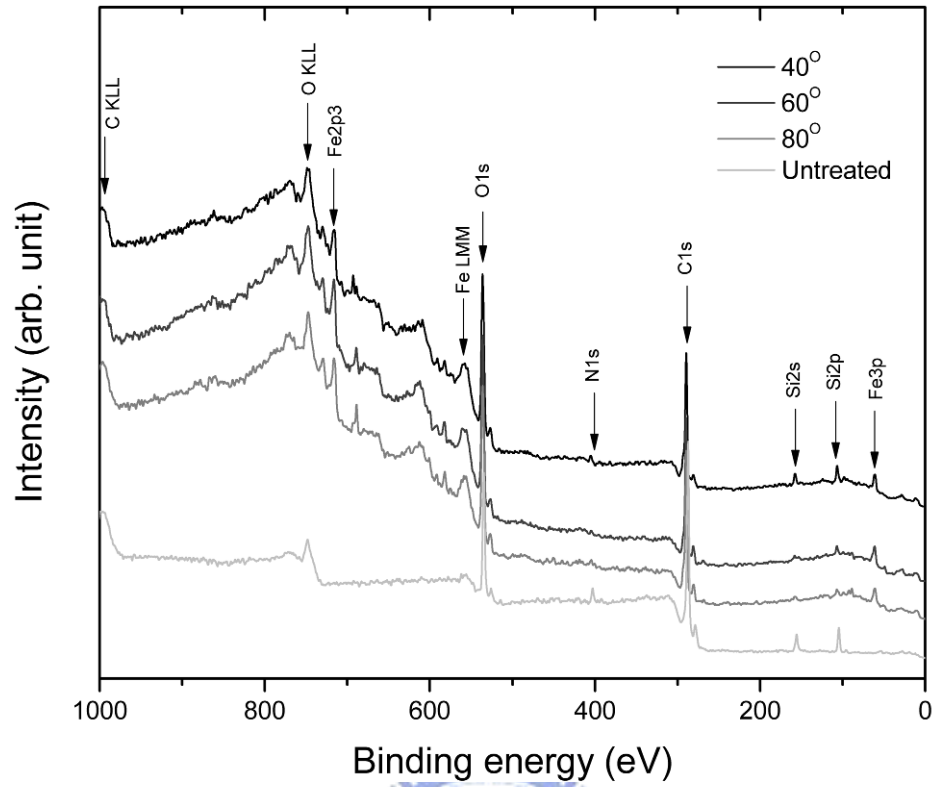
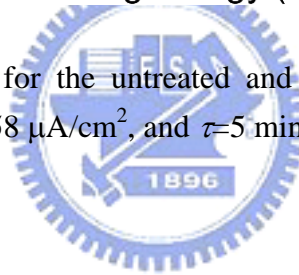


Figure 2.4.16 Survey spectra for the untreated and ion-beam treated PI films with different θ_{ion} , $V_b=840$ V, $J_{ion}=458 \mu\text{A}/\text{cm}^2$, and $\tau=5$ min.



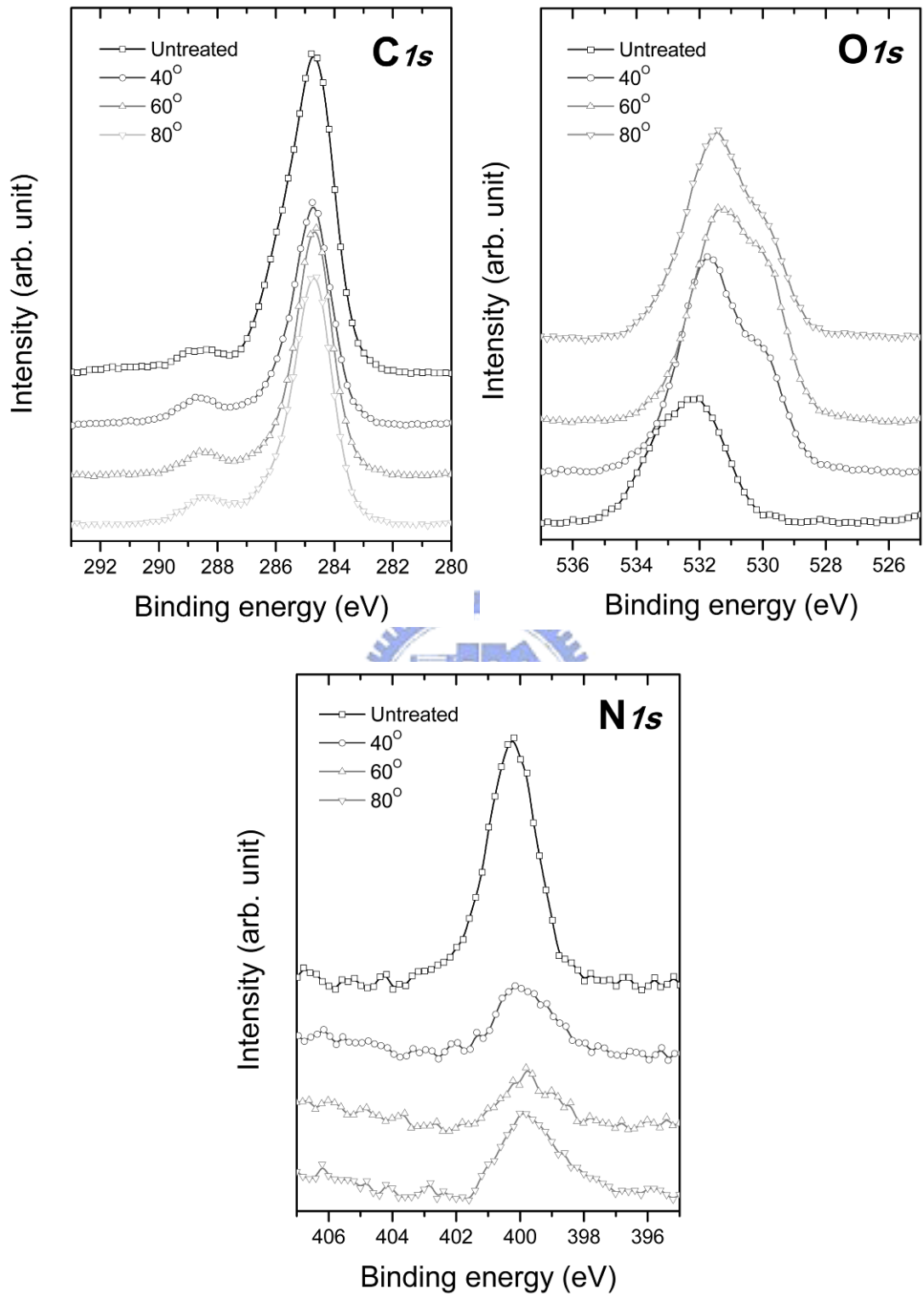


Figure 2.4.17 Multiplex spectra for the untreated and ion-beam treated PI films with different θ_{ion} , $V_b=840$ V, $J_{ion}=458 \mu\text{A}/\text{cm}^2$, and $\tau=5$ min.

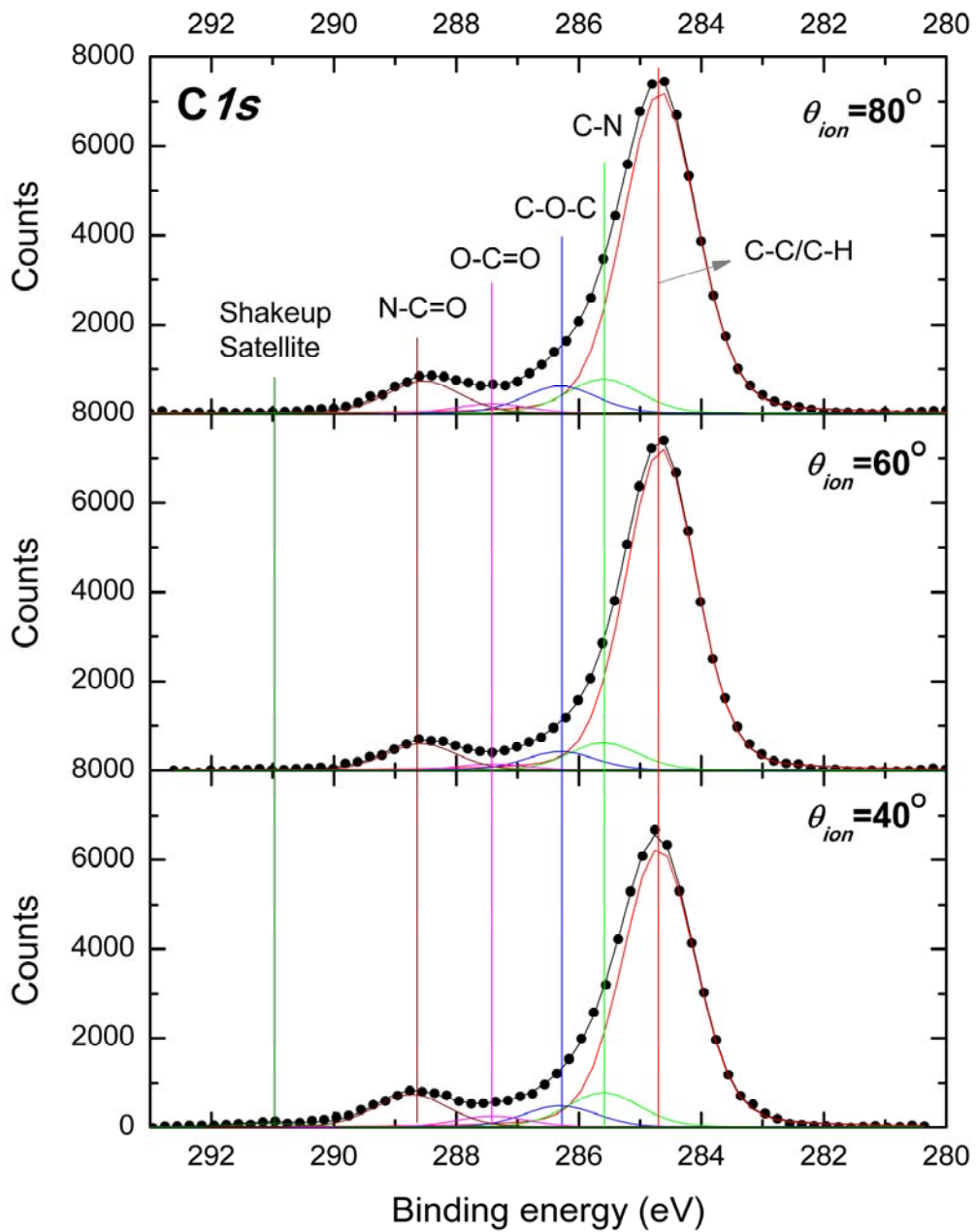


Figure 2.4.18 Deconvolution of the C_{1s} spectra of the treated PI films with θ_{ion} of 40° , 60° , and 80° .

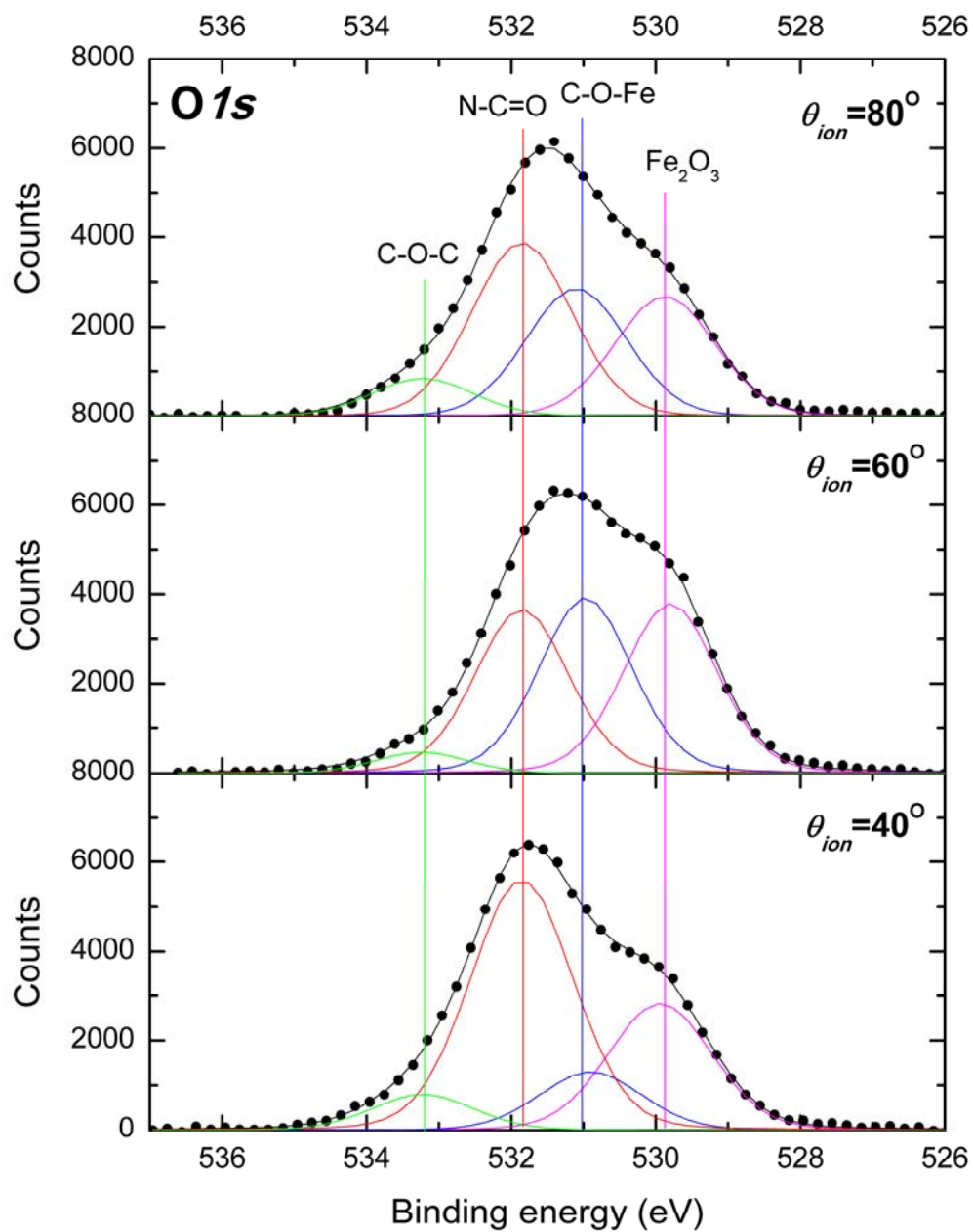
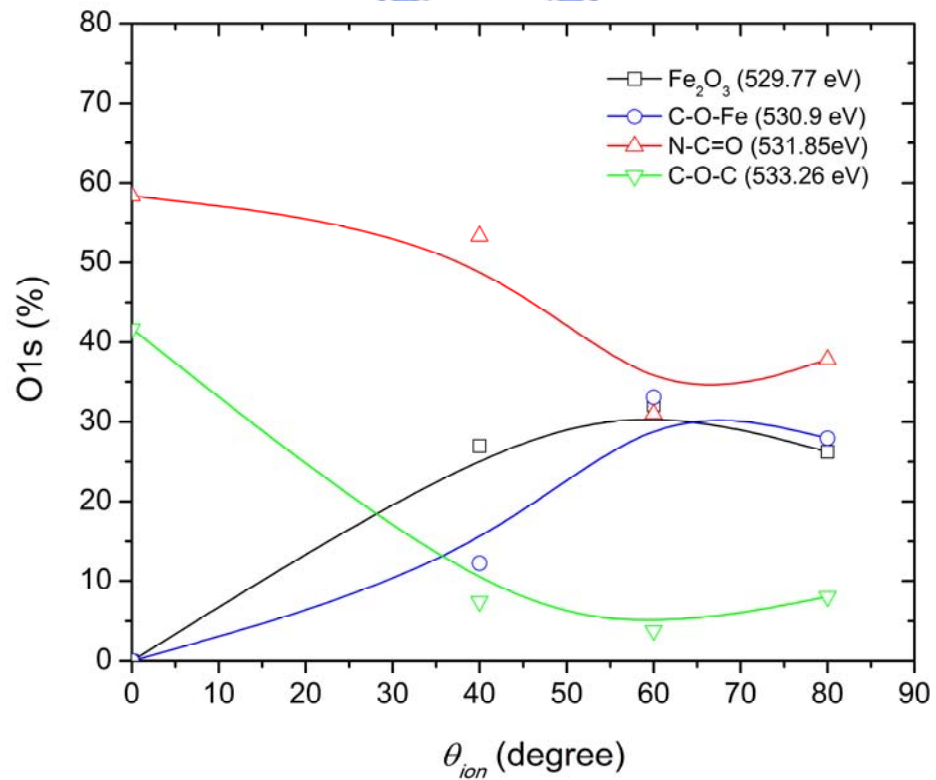
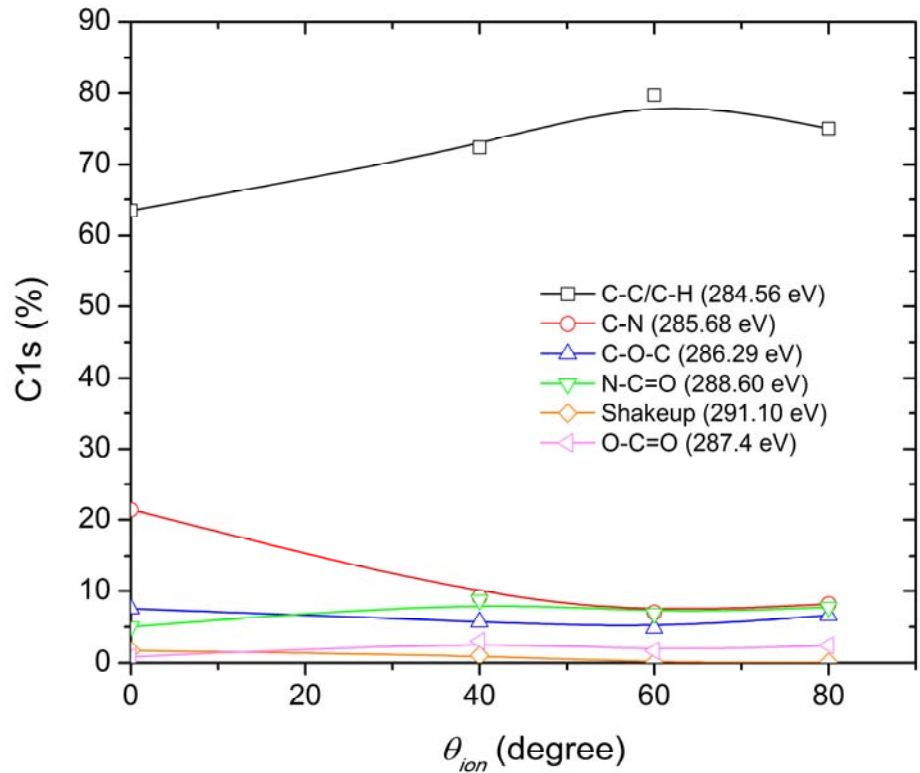


Figure 2.4.19 Deconvolution of the O_{1s} spectra of the treated PI films with θ_{ion} of 40° , 60° , and 80° .



(b)

Figure 2.4.20 Fraction of the components contributing to the (a) C_{1s} and (b) O_{1s} core-level spectra of untreated and ion-beam treated PI films as a function of θ_{ion} .

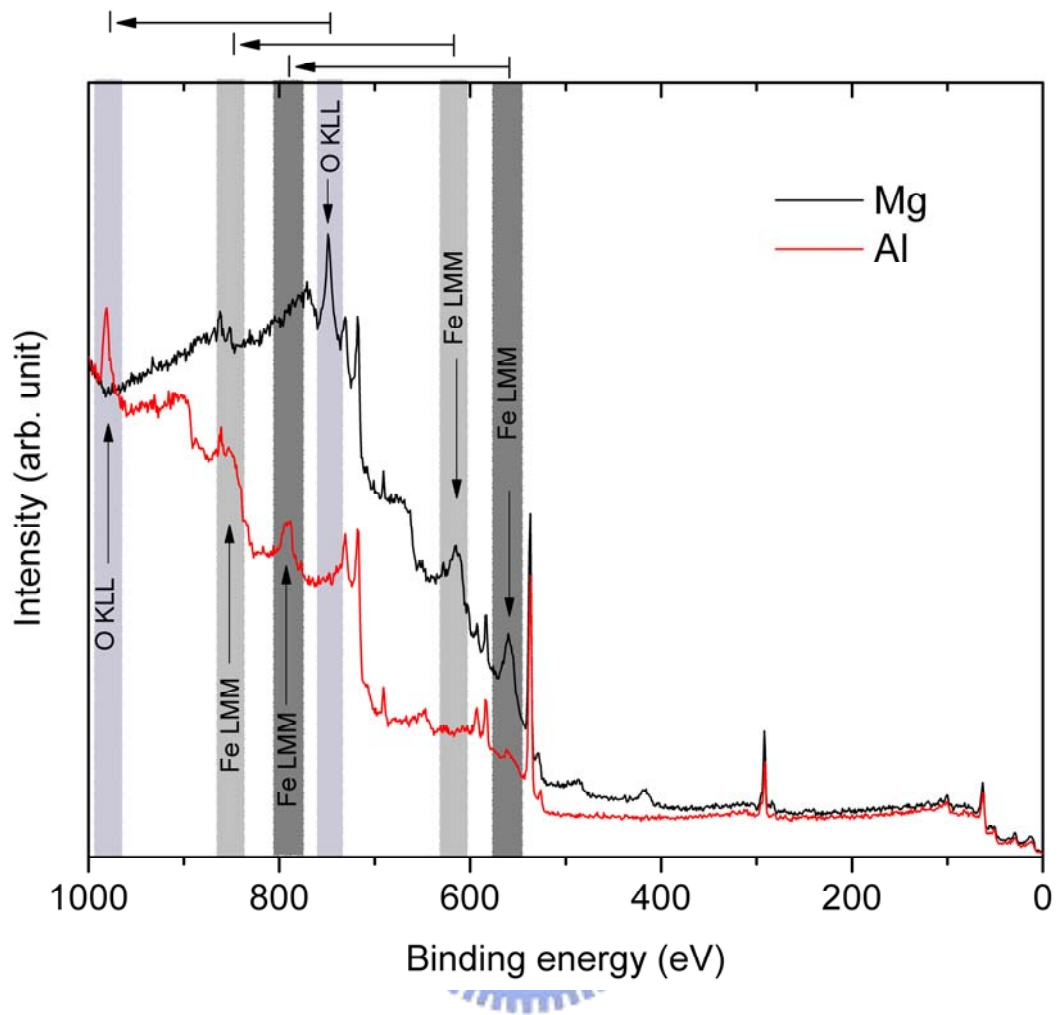


Figure 2.4.21 Survey spectra scanned with x-ray monochromatic sources of the Mg $K\alpha$ and Al $K\alpha$ lines for the PI surface treated with $V_b=1120$ V, $\theta_{ion}=60^\circ$, $J_{ion}=255 \mu\text{A}/\text{cm}^2$, and $\tau=5$ min.

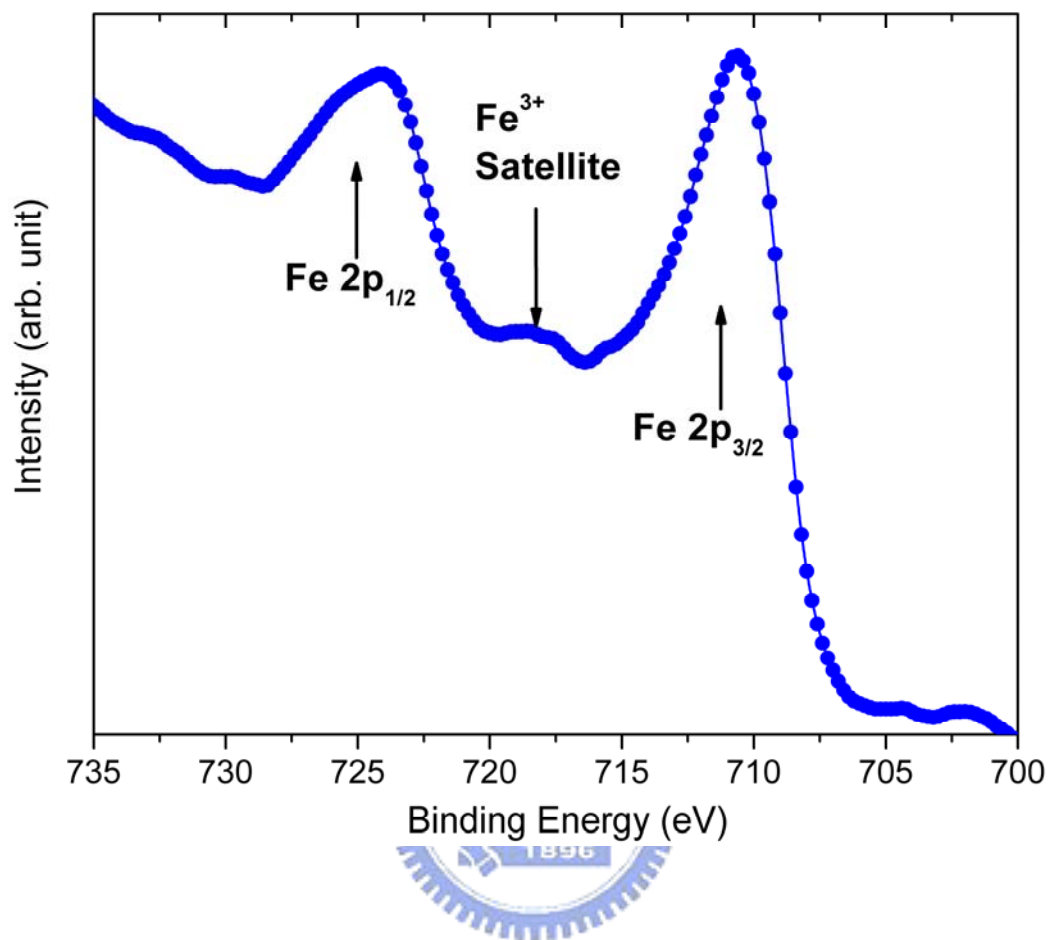


Figure 2.4.22 The Fe 2p spectrum in multiplex mode of the film treated by $V_b=1120$ V, $J_{ion}=255 \mu\text{A}/\text{cm}^2$, $\theta_{ion}=60^\circ$, and $\tau=5$ min.

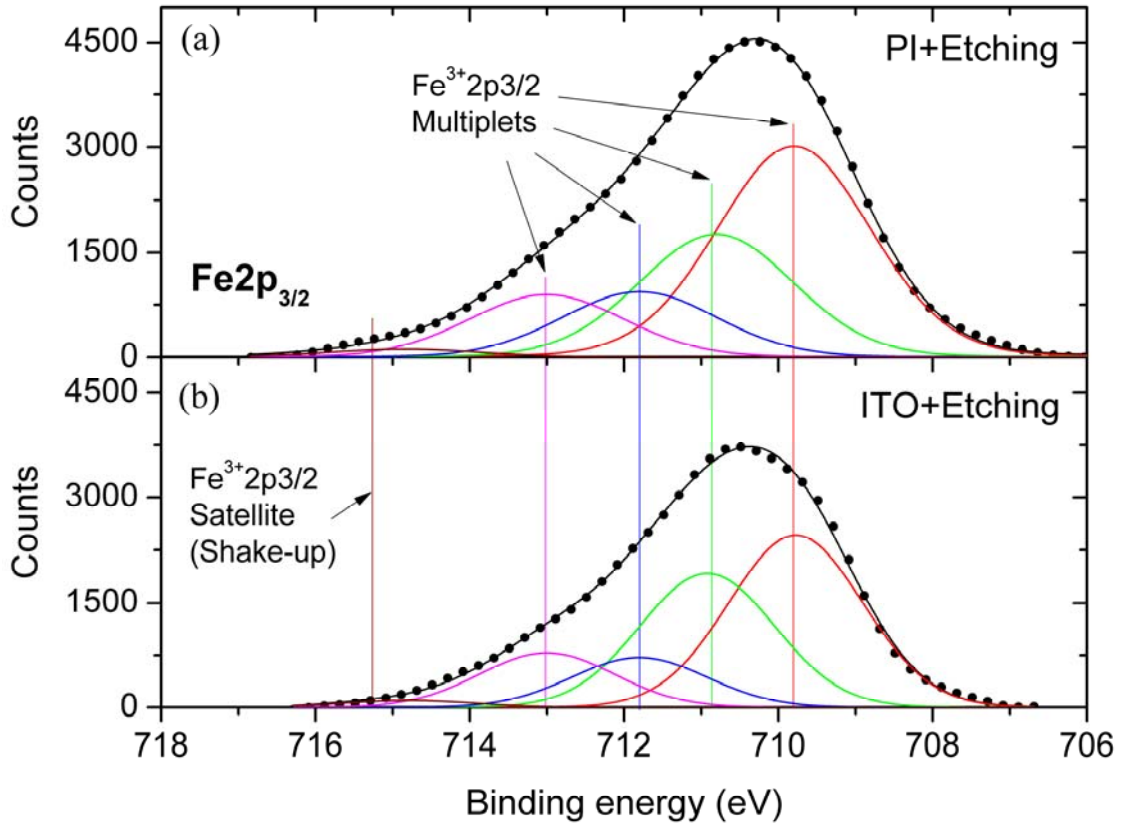


Figure 2.4.23 Deconvolution of the Fe 2p_{3/2} spectrum of (a) IB-etched PI film and (b) IB-etched ITO film with ion beam condition: $V_b=1120$ V, $J_{ion}=255$ $\mu\text{A}/\text{cm}^2$, $\theta_{ion}=60^\circ$, and $\tau=5$ min.

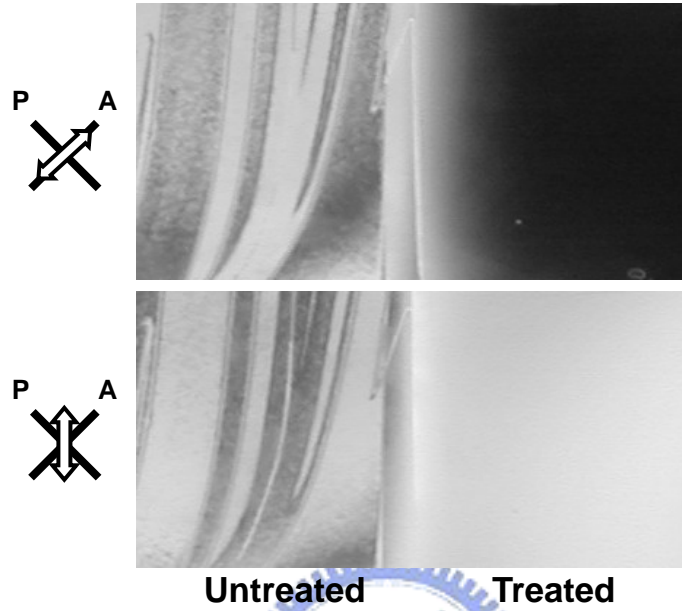


Figure 2.4.24 Photographs of an ion beam treated NLC cell placed between crossed-polarizers. The left side of the substrates was covered with fused silica plate while being ion-beam treated. The V_b and τ are 560 V and 20 min, respectively.

Tables

Table 2.4.1 Intensities a_0 of chemical bonds convoluted to the C_{1s} spectrum of surfaces treated by different energies of ion beam.

| | Untreated | 420 V | 560 V | 840 V | 1120 V |
|---------|-----------|---------|---------|---------|---------|
| a_2 | 1.4747 | 1.6456 | 1.6680 | 1.4932 | 1.4789 |
| a_3 | 0.7744 | 0.8490 | 0.8545 | 0.7983 | 0.7364 |
| C-C/C-H | 13780 | 11890 | 10980 | 9487.5 | 8039.1 |
| C-N | 4614.4 | 4244.0 | 3406.2 | 1740.6 | 812.8 |
| C-O-C | 1497.9 | 1623.3 | 1396.4 | 1166.6 | 1226.1 |
| N-C=O | 1170.2 | 2104.1 | 1981.2 | 1418.1 | 1148.7 |
| O-C=O | 112.9 | 1194.7 | 1327.7 | 580.3 | 256.7 |
| Shakeup | 458.1 | 599.2 | 372.1 | 159.6 | 0 |
| Total | 21633.5 | 21655.3 | 19463.6 | 14552.7 | 11483.4 |

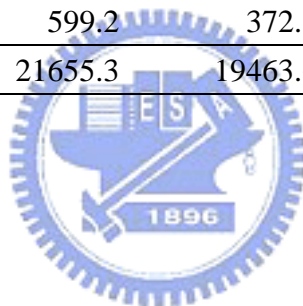


Table 2.4.2 Intensities a_0 of chemical bonds convoluted to the O_{1s} spectrum of surfaces treated by different energies of ion beam.

| | Untreated | 420 V | 560 V | 840 V | 1120 V |
|--------------------------------|-----------|---------|---------|---------|---------|
| a_2 | 1.8367 | 2.4928 | 1.9908 | 1.5508 | 1.5957 |
| a_3 | 0.8086 | 0.9719 | 0.9035 | 0.7976 | 0.8473 |
| N-C=O | 8305.8 | 14260 | 11790 | 5044.3 | 6258.9 |
| C-O-C | 3488.9 | 3591.5 | 3894.4 | 1239.7 | 225.1 |
| C-O-Fe | 0 | 0 | 2796.2 | 9322.4 | 9089.2 |
| Fe ₂ O ₃ | 0 | 0 | 896.7 | 7509.4 | 9531.9 |
| Total | 11794.7 | 17851.5 | 19377.3 | 23115.9 | 25105.1 |

Table 2.4.3 Intensities a_0 of chemical bonds convoluted to the C_{1s} spectrum of surfaces treated by different bombarding time.

| | Untreated | 2 min | 8 min |
|---------|-----------|---------|---------|
| a_2 | 1.4755 | 1.6520 | 1.6440 |
| a_3 | 0.7298 | 0.9029 | 0.8543 |
| C-C/C-H | 14060 | 11190 | 10580 |
| C-N | 4677.5 | 3417.7 | 3162.5 |
| C-O-C | 1484.6 | 1194.8 | 1403.0 |
| N-C=O | 1178.3 | 1590.0 | 1883.2 |
| O-C=O | 70.6 | 976.3 | 1069.1 |
| Shakeup | 455.6 | 341.1 | 460.2 |
| Total | 21926.6 | 18710.0 | 18558.0 |



Table 2.4.4 Intensities a_0 of chemical bonds convoluted to the O_{1s} spectrum of surfaces treated by different bombarding time.

| | Untreated | 2 min | 8 min |
|--------------------------------|-----------|---------|---------|
| a_2 | 1.9048 | 1.8695 | 1.9983 |
| a_3 | 0.8572 | 0.9169 | 1.0000 |
| N-C=O | 8666.9 | 10050 | 8687.6 |
| C-O-C | 3062.1 | 3461.4 | 2787.8 |
| C-O-Fe | 0 | 3176.1 | 4994.1 |
| Fe ₂ O ₃ | 0 | 238.5 | 1622.0 |
| Total | 11729.0 | 16926.0 | 18091.5 |

Table 2.4.5 Intensities a_0 of chemical bonds convoluted to the C_{1s} spectrum of surfaces treated by different angle of incidence.

| | Untreated | 40° | 60° | 80° |
|---------|-----------|---------|---------|---------|
| a_2 | 1.4325 | 1.4039 | 1.3563 | 1.4199 |
| a_3 | 0.7129 | 0.7152 | 0.7221 | 0.7142 |
| C-C/C-H | 14700 | 10290 | 11440 | 12020 |
| C-N | 4965.0 | 1299.5 | 1001.0 | 1312.0 |
| C-O-C | 1742.9 | 810.7 | 689.5 | 1054.4 |
| N-C=O | 1167.6 | 1237.9 | 978.8 | 1240.2 |
| O-C=O | 195.7 | 426.3 | 236.7 | 382.8 |
| Shakeup | 403.3 | 144.8 | 3.7 | 15.4 |
| Total | 23174.6 | 14209.2 | 14349.6 | 16024.8 |



Table 2.4.6 Intensities a_0 of chemical bonds convoluted to the O_{1s} spectrum of surfaces treated by different angle of incidence.

| | Untreated | 40° | 60° | 80° |
|--------------------------------|-----------|---------|---------|---------|
| a_2 | 1.8638 | 1.6731 | 1.5127 | 1.6284 |
| a_3 | 0.8134 | 0.8337 | 0.8024 | 0.9372 |
| N-C=O | 6354.7 | 10540 | 6321.3 | 6845.6 |
| C-O-C | 4534.2 | 1472.1 | 777.0 | 1454.0 |
| C-O-Fe | 0 | 2419.3 | 6748.8 | 5057.1 |
| Fe ₂ O ₃ | 0 | 5327.2 | 6535.9 | 4747.8 |
| Total | 10888.9 | 19758.5 | 20382.9 | 18104.5 |

Chapter 3

Liquid Crystalline Alignment on the Ion Beam Sputtered Magnetic Thin Film

3.1 Overview

It is well known that the liquid crystal (LC) molecules can be reorientated by electric and magnetic field due to their anisotropic electrical permittivity and magnetic susceptibility [1]. In Sec. 2.4.3, we speculate that the homeotropic alignment of LC on the sputtered γ -Fe₂O₃ film is probably due to the induced magnetic field from surface or/and the intermolecular interaction at the liquid-crystalline-maghemite interface. In this chapter, a homeotropic LC alignment using a uniformly coated γ -Fe₂O₃ film without pre-coating of polyimide (PI) on the substrate is demonstrated. Besides, its polar anchoring strength (PAS) is compared with that of LC cell aligned by *N,N*-dimethyl-*N*-octadecyl-3-aminopropyltrimethoxysilyl chloride (DMOAP) coating. To verify our speculation on the alignment mechanism, systematic analyses by using x-ray photoemission spectroscopy (XPS), atomic/magnetic force microscope (AFM/MFM), ultraviolet-visible spectroscopy (UV/VIS), and super conducting quantum interference device (SQUID) data are necessary; the details will be given in Sec. 3.2. The surveyed surface morphology reveals that the films are amorphous and composed of nanoparticles with dimensions around 30 nm. The magnetization anisotropy of the sputtered magnetic films is analyzed. The PAS of the coated films with different thicknesses are measured and compared with their saturation magnetization. A simple model of alternatively distributed magnetic moments with opposite direction is proposed. The profile of magnetic field strength near the surface is then calculated to compare with the measured alignment strength.

3.2 Experiments

The indium-tin-oxide (ITO) coated glasses with different sizes are used as the

substrates. Before iron-oxide coating, each substrate have to be cleaned out using a standard process shown in the flowchart of Fig. 2.3.1. For measuring the PAS, the ITO layer has to be etched into a certain pattern before substrate cleaning. The etching process is shown in the flowchart of Fig. 3.2.1.

3.2.1 Ion beam treatment

A direct-current (DC) ion sputter (model IB-2 from EIKO Engineering Co., Ltd.) has been used for ion-beam (IB) sputtering. Its specification has already been described in Sec. 2.2.1; therefore, we will not go through that again. Throughout this work, the coating mode is selected, that means the bottom electrode, on which the sample substrates are set, acts as an anode. The target material is mounted on the cathode for sputtering. A plate of stainless steel and an iron foil (Puratronic, 99.995 %) are chosen as the iron sources. The substrates are horizontally laid on the anode while sputtering with applied bias V_b higher than 700 V and ion current density J_{ion} of 255 $\mu\text{A}/\text{cm}^2$. In this work, the ion current density remains the same. For sputtering with V_b of 1120 V, the coating rate of 21.2 nm/min is determined by ellipsometry.

3.2.2 Sample preparation

Two identically substrates coated at the same time are assembled with a Mylar spacer of specific thickness in between to form an empty cell. A schematic structure is drawn in Fig. 3.2.2. The thickness of spacer is chosen in the range from 6 μm to 50 μm to satisfy the requirements for the measuring methods. Various Merck nematic LC (NLC) such as *4'-n-pentyl-4-cyanobiphenyl* (5CB) and MLC-6608 are then filled into the empty cells for alignment characterization. The dielectric anisotropy ($\Delta\epsilon$) of the former is positive while the later is negative.

3.2.3 Alignment characterization

After annealing, the alignment modes of the LC cells are characterized with conoscope and polarizing optical microscope (POM). The pretilt angle and thickness of LC layer are simultaneously obtained by crystal rotation method [2]. To investigate the relation between the polar anchoring strength and the thickness of ferric films, the experimental determination of polar anchoring strength is carried out by using the

external field methods [3,4].

3.2.4 Surface analyses

In addition, the superficial distribution of the magnetization and morphology on the film surface are investigated by the scanning probe microscope (SPM) unit system (SPA-300HV, SII NanoTechnology Inc.) operated in dynamic force mode AFM (DFM/AFM). Besides, the MFM function could be obtained when the probe of SPM has a hard magnetic coating on it. To confirm that the type of iron-oxide sputtered in coating mode is the same as that is obtained in etching mode, the compositions of chemical bonds are analyzed by using x-ray photoemission spectroscopy (XPS, PHI-1600 from Physical Electronics, Inc.). More description about the XPS we used has been given in Sec. 2.3.3. Only the Mg K α line is used in this work.

3.2.5 Magnetic properties

We have also measured the magnetization of the sputtered films to verify its magnetic properties. A superconducting quantum interference device (SQUID, MPMS-XL7, Quantum Design) equipped with a superconducting magnet with maximum strength of 70 kOe has been used for this measurement. The typical sensitivity of the magnetization measurement is better than 1×10^{-8} emu ($H < 2.5$ kOe).

3.3 Results and discussion

In a previous work already described in Chap. 2, we found a significant amount of iron-oxide is sputtered on the PI-coated substrate and even the one without PI coating while treated by the high-energy ion beam (HEIB) bombardments. The type of iron-oxide has been identified as the maghemite (γ -Fe₂O₃) which has intrinsic magnetism through the XPS analyses. The magnetic field induced by γ -Fe₂O₃ or/and the intermolecular interaction at the liquid-crystalline-maghemite interface are deduced to be responsible for the resultant homeotropic LC alignment. However, the fundamental interaction at the LC-maghemite interface is not clear yet; more evidences are required to prove this speculation. In the following section, we will characterize the iron-oxide film obtained IB-sputtering in coating mode first.

3.3.1 Film characterization

The deconvoluted $\text{Fe}_{2p_{3/2}}$ spectra of ITO-coated substrates treated in etching mode and coating mode are plotted in Fig. 3.3.1(a) and Fig. 3.3.1(b), respectively. The splitting of four $\text{Fe}^{3+} 2p_{3/2}$ multiplet peaks with binding energies at 709.8, 710.8, 711.8, and 713.0 eV in Fig. 2.4.22 are due to the inclusion of electrostatic interactions and spin-orbit coupling in theoretical calculation [5]. Despite of different incidence angles and operating mode, no significant difference is found in their $\text{Fe}_{2p_{3/2}}$ spectra. A higher intensity found in Fig. 3.3.1(b) is possibly due to a larger area of electrode exposed to the HEIB bombardments. The O_{1s} spectrum has also been deconvoluted into three component signals of bonds, C-C=O (532.4 eV), C-O-Fe (531.1 eV), and Fe_2O_3 (529.6 eV). Two bonds related to the iron element shown in Fig. 3.3.1(c) indicate that the surface is primarily covered with the iron-oxide molecules of Fe_2O_3 type.

Furthermore, the UV/VIS absorbance spectrum of an iron-oxide film sputtered in coating mode is plotted in Fig. 3.3.2 which coincides with the results reported in literatures [6,7]. The spectrum shows a better transparency in the visible spectral region and no typical absorption peak shown in the inset of Fig. 3.3.2 for $\alpha\text{-Fe}_2\text{O}_3$ (hematite) in the UV region from 300 nm to 380 nm [8,9]. These results also support our assertion that the coated iron oxide films are of the particular allotropic form, i.e. $\gamma\text{-Fe}_2\text{O}_3$. In Fig. 3.3.3, the UV/VIS transmittance spectra of $\gamma\text{-Fe}_2\text{O}_3$ films with different thickness of 63.6, 106, 212, 424, and 636 nm are measured. Good quality of homeotropic LC alignment is promised on all these film surfaces. We should notice that a transmittance better than 90 % can be obtained in the visible band if the film thickness is smaller than 212 nm. This advantage makes the $\gamma\text{-Fe}_2\text{O}_3$ film potentially useful for the application of liquid crystal display.

3.3.2 Alignment characterization

Base on these points, we have investigated the relation between the surface anchoring strength and the magnetization of $\gamma\text{-Fe}_2\text{O}_3$ film. For the purpose of measuring PAS, the NLC cells with homeotropic alignment are prepared and shown in Fig. 3.3.4. The alignment qualities of $\gamma\text{-Fe}_2\text{O}_3$ film are as good as those given by DMOAP films. Figure 3.3.4(a) shows the optical behavior and uniformities of the MLC-6608 sample

with a picture of these cells under crossed polarizers; the inset is a conoscopic picture. In Fig 3.3.4(b), we show the picture of the same samples but tilted from the polarizer plane. The homeotropic alignment of NLC is confirmed with these pictures. It should be noticed as well that the ITO coated glass substrate with the $\gamma\text{-Fe}_2\text{O}_3$ film coating is not totally transparent in the visible band. The cells without polarizers reveal the color of light brown, as seen in Fig. 3.3.4(c), which becomes dark brown for a thick coating. However, the measured transmittance of a $\gamma\text{-Fe}_2\text{O}_3$ film with thickness of 212 nm is higher than 90%. The alignment effects of 5CB on the $\gamma\text{-Fe}_2\text{O}_3$ films are also demonstrated with the tilt-view of the samples as shown in Fig. 3.3.4(d).

The electro-optical (EO) responses of the MLC-6608 cells with $\gamma\text{-Fe}_2\text{O}_3$ and DMOAP coating are measured under crossed polarizers and shown in Fig. 3.3.5. The phase retardation R is transformed from the transmittance T and normalized by the maximum phase retardation R_{\max} which is calculated with the measured thickness and pretilt angle of the NLC cell. The measured T-V curves are stable and reproducible.

Furthermore, the PAS can be derived from theoretical analyses on this EO response [4]. The extracted polar anchoring strength, W_p , as a function of coating time is summarized in Table 3.3.1. For the MLC-6608 cells with the coating time of 10, 20, and 30 min, their W_p are 1.1×10^{-4} , 7.9×10^{-5} , and 4.8×10^{-5} J/m², respectively. For cells coated by $\gamma\text{-Fe}_2\text{O}_3$ films with thickness of 212 and 424 nm have the W_p stronger than 7.1×10^{-5} J/m² measured for the cell with DMOAP coating. Furthermore, the comparison of W_p of 5CB on these two alignment layers is also carried out. The W_p is obtained by using the magnetic field method [3]. The measured results are 2.0×10^{-4} and 3.4×10^{-5} J/m² for 10 min $\gamma\text{-Fe}_2\text{O}_3$ and DMOAP coating, respectively. The description of process for measuring the PAS is given in Appendix B.

3.3.3 Magnetic properties

The total magnetization (M) of a $\gamma\text{-Fe}_2\text{O}_3$ film with thickness of 636 nm is measured as a function of temperature (T) from 75 to 350 K in an applied field of 300 Oe. A raw data of M with unit emu is then transformed into the one with unit emu/g by using the density of 4.87 g/cm^3 , assuming that all Fe is oxidized in the $\gamma\text{-Fe}_2\text{O}_3$ phase [10]. The measured M-T curve is shown in the inset of Fig. 3.3.6. This curve shows a

minimum that corresponds to the compensation temperature, a typical feature of ferrimagnetism [11]. The Curie temperature reported in the literature for $\gamma\text{-Fe}_2\text{O}_3$ is in the range from 820 to 986 K [12]. This is well above our measuring temperature and the operating temperature of common LC devices. The characteristic hysteresis loops expected for ferrimagnetic films are obtained at 10 K and 300 K. These are shown in Fig. 3.3.7 after correction for the diamagnetic component at high field due to the quartz substrate. We note that the magnetization of our sample is measured with the magnetic field parallel to the film surface. So far, these evidences have supported again that the coated compound is $\gamma\text{-Fe}_2\text{O}_3$.

Next, how the film thickness affects its magnetic property? To investigate this issue, three $\gamma\text{-Fe}_2\text{O}_3$ films with different thicknesses of 212 nm, 424 nm, and 636 nm are prepared. It should be noticed that all the following SQUID results are measured at a temperature of 300 K. For SQUID measurements, two sizes of samples required for measuring vertical and horizontal magnetizations are $2.5\text{ mm} \times 2.5\text{ mm}$ and $5.0\text{ mm} \times 5.0\text{ mm}$, respectively. The net magnetization M_{net} of each sample is recorded before applying any external field H while doing the M-H curve measurements. As shown in Fig. 3.3.8, the vertical component of magnetization $M (\perp)$ is larger than horizontal component $M (//)$. For both components, the saturation magnetization M_s and zero-field magnetization are getting larger while decreasing the thickness of $\gamma\text{-Fe}_2\text{O}_3$ film. The measured M_s and M_{net} are summarized in Table 3.3.2 and plotted against the film thickness in Fig. 3.3.9(a) and Fig. 3.3.9(b), respectively. A decreasing trend with thickness is found for both M_s and M_{net} . For example, the $M_s (\perp)$ have been obtained as 0.94 emu/g, 0.26 emu/g, and 0.16 emu/g for film thickness of 212 nm, 424 nm, and 636 nm, respectively. Besides, the orientation of induced magnetization of $\gamma\text{-Fe}_2\text{O}_3$ film apparently prefers to be out of plane. Let us compare the determined W_p of the $\gamma\text{-Fe}_2\text{O}_3$ film listed in Table 3.3.1 with the saturation magnetization M_s of the corresponding film thickness. Figure 3.3.10 shows a strong connection exists between them. As a result, we strongly deduce that the magnetic field induced by the magnetic moment of ferrite film dominates the alignment mechanism. A theoretical estimation of polar anchoring strength basing on a simple surface model has been carried out to verify this point of view in the following Sec. 3.3.5.

Before ending this section, another interesting issue should be addressed. What will happen to the ferrite film after thermal annealing? To answer this question, the as-sputtered γ -Fe₂O₃ films with thickness of 106 nm and 212 nm are thermal treated at 573 K for two hours. Figure 3.3.11 shows the change of M-H curve for 212 nm-thick γ -Fe₂O₃ film after annealing. Despite the magnetization has not been saturated yet, we still can find out that the measured maximum magnetization at H=3 kOe becomes at least 40 times larger than that is without annealing, as indicated in Table 3.3.3. Besides, the anisotropy of magnetization has been found in the surface plane no matter whether the film is annealed or not. Even for a thinner film with thickness of 106 nm, the growths of M_s , M_{net} , and coercivity are revealed after thermal annealing, as shown in Fig. 3.3.12(b). Therefore, the field strength higher than 3 kOe is required for measuring the M_s . Without an exception, a similar decreasing trend of M_s with film thickness has also been obtained in Fig. 3.3.12(a). The M_s is determined as 2.51 emu/g and 0.23 emu/g for film thickness of 106 nm and 424 nm, respectively.

3.3.4 Surface morphology

The surface morphologies of the sputtered γ -Fe₂O₃ films are investigated by using a SPM. Surveyed morphologies of surfaces with several coating conditions are presented. Figures 3.3.13, 3.3.14, 3.3.15, 3.3.16, and 3.3.17 show the morphologies of γ -Fe₂O₃ films with thicknesses of 42.4 nm, 106 nm, 212 nm, 424 nm, and 848 nm, respectively. For DFM, an additional phase measurement could be simultaneously accomplished with the survey of surface morphology. The phase variation offers a qualitative analysis about the hardness and viscosity distribution of the scanned surface. The DFM images of right hand side in Figs. 3.3.13-3.3.17 show the recorded phase. For each sample, we randomly pick at least three positions for image scan, as shown in each figure. After thermal annealing at 573 K for two hours, AFM images show no significant change is found on the morphology of treated surfaces, as taken in Figs. 3.3.18-3.3.22.

Figures 3.3.23 and 3.3.24 show the surveyed morphology of a γ -Fe₂O₃ film with thickness of 169.6 nm. Furthermore, three paths have been randomly chosen for the particle size analysis, as marked in Fig. 3.3.24(b). Their surface profiles are shown in

Fig. 3.3.24(c). The mean size of the particles composed of γ -Fe₂O₃ material is 30±5 nm. The same method is used to analyze other γ -Fe₂O₃ films with different thicknesses and plot the results in Fig. 3.3.25. We found that the size of particles is not significantly influenced by film thickness and even the extra thermal treatment.

A similar result, moreover, is obtained for γ -Fe₂O₃ films coated with V_b of 840 V and 1400 V, as seen in Figs. 3.3.26-3.3.33. The analyzed size of particle is plotted with respect to the coating time in Fig. 3.3.34. Accordingly, we could conclude that the size of particles cannot be effectively controlled by the coating time and beam energy. Even the films are thermally treated, no significant change in size of particle is found.

The photographs taken by the scanning electron microscope (SEM) for the sputtered γ -Fe₂O₃ films with different thicknesses are shown in Fig. 3.3.35. A stacking of nanoparticles is revealed to form the ferrite film, as clearly seen in Fig. 3.3.35(d).

3.3.5 Theoretical analyses

Accordingly, we propose a simple model to explain how the magnetic field is induced and affects the orientation of NLC near the surface. For simplicity, a surface structure composed of the square domains with equal size and magnetization as illustrated in Fig. 3.3.36(a) is considered. The average directions of magnetic moments for neighboring domains are opposite to each other. The characteristic of this model is that the induced z-component magnetic field H_m decays rapidly as being away from the surface and the component field lying in the x-y plane is relatively small over the most domain area except for the nearby region of domain boundary. According to the measured saturation magnetization of 212 nm thick γ -Fe₂O₃ film and the particle mean size as mentioned above, the size and magnetization of each square domain are 30 nm and 0.94 emu/g, respectively, in this model. The total magnetic moment \mathbf{m} of 8.73×10^{-19} Am² for each domain is then calculated. It is well known that a magnetic moment \mathbf{m} could be equivalently represented by IS where S is the area enclosed by the route of current I . Therefore, we could evaluate the induced magnetic field simply using the Biot-Savart law. The detail of calculation for induced magnetic-field distribution and the revealed properties have been represented in Appendix C. It should be noticed that the resultant from the proposed surface model reveals anisotropy of induced magnetic field

in the x-y plane due to the square shape of current loop. This anisotropy should be removed while a circular domain is considered in a plane with infinite size. In Sec. 3.3.3, however, we mentioned that an anisotropic magnetization in the surface plane is found (see Fig. 3.3.11). A granular structure found in surface scanning should be responsible for it. We should keep it in mind that the measured magnetic properties are originated from the whole film. A further confirmation of the surface anisotropy is unavailable due to the lack of surface scanning technique with high resolution. Nevertheless, we speculate that the finite size of thin film in the direction of surface normal is responsible for the larger anisotropy of magnetization in the meridian plane, the x-z plane for example, as shown in Fig. 3.3.9.

Figure 3.3.36 (b) and (c) show the two-dimensional dependent magnetic field strength $H_m(x, y)$ at different z positions. As we know, a torque given by the magnetic field on the LC molecule can be written as $\boldsymbol{\Gamma} = \chi_a(\mathbf{n} \cdot \mathbf{H})\mathbf{n} \times \mathbf{H}$ [1]. Therefore, the field-induced orientation effect on LC molecule is undistinguishable for fields in up or down direction. This is the reason why the saturation magnetization is essential even none of the residual magnetization is found. The z-dependent field strength $H_m(z)$ at different positions in the x-y plane is plotted in Fig. 3.3.36(d). The four x-y positions selected for simulation are marked on the contour plot by dots with the same color as that for the corresponding curves. As we can see from Fig. 3.3.36(d), the field is high near the surface and decays rapidly with distance, especially for points near domain boundaries.

According to this model, the estimation on the PAS is determined. For simplicity, we assume the orientations of the LC directors are uniform in a considered near-surface region with depth ξ . That means the elastic energy of LCs does not contribute to the polar anchoring energy confined in the nearby region of surface. Therefore, only the magnetic free energy F_{H_m} induced by magnetic surface is considered and written as

$$F_{H_m} = -\frac{1}{2}\chi_a \int_0^\xi H_m^2(z) \cos^2\theta_0 dz \quad (1)$$

where χ_a is the anisotropy of magnetic susceptibility of LC molecules and θ_0 is the deviation angle of LC director from the field direction of H_m . According to the principle of torque balance, we simply let $F_{H_m}/d\theta_0 = F_{W_p}/d\theta_0$ where F_{W_p} could

approximately be

$$F_{W_p} = \frac{1}{2} W_p \sin^2 \theta_0, \quad (2)$$

and then obtain the equivalent W_p :

$$W_p = \chi_a \int_0^\xi H_m^2(z) dz. \quad (3)$$

Taking the $H_m(z)$ at point iv into account, a W_p of 5.33×10^{-10} J/m² is obtained by using χ_a of 1.047×10^{-7} cgs unit for 5CB and ξ of 20 nm. Even if the value of magnetization 16.5 emu/g is used, a result of 1.64×10^{-7} J/m² is still much smaller than the measured value, 2.0×10^{-4} J/m². The significant differences are probably due to the following reasons. Firstly, the theories of deducing the PAS from the experimental results are built without the detail descriptions of surface structures from a microscopic point of view. Secondly, the lack of the information about the properties of the granular film composed of the magnetic nanoparticles makes the resultant underestimated. In Appendix D, estimation more complex on the required magnetic field is carried out basing on the measured polar anchoring strength. An incredibly large magnetic field is found in supporting the alignment of LC which is capable of being detected by MFM.

We have surveyed the surface of sputtered γ -Fe₂O₃ film with thickness of 212 nm by SPM. As shown in Fig. 3.3.37 (a), the AFM image reveals that the synthesized γ -Fe₂O₃ particle size is dispersive. This may be due to the variation of intensity of plasma giving rise to different oxidation rates of Fe [13]. However, no domain pattern is found on the MFM image, as shown in Fig. 3.3.37 (b). This is probably because the spatial resolution of the MFM cannot be better than 50 nm. Besides, the simulated field strengths decay rapidly in the depth of several nanometers. Even though the resolution is high enough, it is still difficult to extract the magnetic force distribution from the signals convoluted with the Van der Waals force information.

Again, it should be noticed that this simple model is for qualitative analyses only because the real surface structure is much more complicated than what we have proposed. For example, the surface bonding due to the molecular-orbital interactions between the metal atoms and cyanobenzene of 5CB might also be involved [14]. The acid-base interaction occurs on several kinds of inorganic surfaces reported by Uchida et al. is probably responsible for the primary mechanism as well [15]. Besides, the

magnetic properties of the dc-sputtered γ -Fe₂O₃ nanoparticles in this work are not well understood either. Recently, the influences of particle size on the magnetic properties have been carried out for γ -Fe₂O₃ nanoparticles by several groups [16-18]. Different magnetic properties have been observed with the same materials having similar grain sizes but produced by different methods. Therefore, more studies on the relation between the nanostructures and the revealed magnetic properties are required in the future.

3.4 Concluding remarks

We unambiguously demonstrate that ITO coated glass substrates, after HEIB bombardments using the diode-type dc sputter with HEIB and current density of 255 $\mu\text{A}/\text{cm}^2$, can achieve excellent homeotropic alignment of the NLCs. The polar anchoring strength of γ -Fe₂O₃ films with thickness less than 424 nm are larger than that of DMOAP film. The comparison between the surface polar anchoring strength and magnetization of the γ -Fe₂O₃ films with different thicknesses seems to indicate their interrelation from the microscopic point view. Both the measured saturation and net magnetizations decrease with increasing thickness. Additionally, we also observe the magnetization anisotropy of the sputtered γ -Fe₂O₃ film and it becomes larger as the film thickness decreases. The analyzed mean size of the particles composed of γ -Fe₂O₃ material is 30 ± 5 nm. And it cannot be effectively controlled by the coating time and beam energy. Even the ferrite films are thermally treated, no significant change in size of particle is found either. However, a clear growth of net and saturation magnetizations are found. Finally, we propose a simple model to explain how the magnetic field is induced and affect the orientation of NLC near the surface. However, the theories of deducing the polar anchoring strength from the experimental results built without the detail descriptions of surface structures from a microscopic point of view and the lack of the information about the properties of the amorphous film formed with the magnetic nanoparticles lead to that the resultant is underestimated. More investigations on the relation between the nanostructures and the revealed magnetic properties are required in the future. In addition, verification of both dipole-dipole and acid-base interactions is

also essential for the understanding of fundamental alignment mechanism.



References

1. P. G. deGennes and J. Prost, *The Physics of Liquid Crystals*, 2nd ed. (Oxford, New York, 1993), pp. 117-139.
2. T. J. Scheffer and J. Nehring, *J. Appl. Phys.* 48 (5), 1783 (1977).
3. K. H. Yang and Charles Rosenblatt, *Appl. Phys. Lett.* 43 (1), 62 (1983).
4. X. Nie, Y. H. Lin, Thomas X. Wu, H. Wang, Z. Ge, and S. T. Wu, *J. Appl. Phys.* 98 (1), 013516 (2005).
5. A. P. Grosvenor, B. A. Kobe, M. C. Biesinger, and N. S. McIntyre, *Surf. Interface Anal.* 36, 1564 (2004).
6. Y. S. Kang, D. K. Lee, and C. S. Lee, *J. Phys. Chem. B* 106, 9341 (2002).
7. B. Z. Tang, Y. Geng, J. W. Y. Lam, B. Li, X. Jing, X. Wang, F. Wang, A. B. Pakhomov, and X. X. Zhang, *Chem. Mater.* 11, 1581 (1999).
8. J. D. Desai, H. M. Pathan, S. K. Min, K. D. Jung, and O. S. Joo, *Appl. Surf. Sci.* 252, 2251 (2006).
9. V. Goossens, J. Wielant, S. Van Gils, R. Finsy, and H. Terryn, *Surf. Interface Anal.* 38, 489 (2006).
10. P. P. Vaishnava, U. Senaratne, E. C. Buc, R. Naik, V. M. Naik, G. M. Tsoi, and L. E. Wenger, *Phys. Rev. B* 76 (2), 024413 (2007).
11. S. Foner, *Magnetism*, ed. T. Rado and H. Suhl (Academic Press, New York, 1963) Vol. I, Chap. 9, pp. 415-419.
12. R. M. Cornell and U. Schwertmann, *The Iron Oxides: Structures, Properties, Reactions, Occurrences, and Uses*, 2nd ed. (Wiley-VCH, Weinheim, 2003), Chap. 1, pp. 1-7.
13. I. Banerjee, Y. B. Kholam, C. Balasubramanian, R. Pasricha, P. P. Bakare, K. R. Patil, A. K. Das, and S. V. Bhoraskar, *Scripta Materialia* 54, 1235 (2006).
14. P. N. Sanda, D. B. Dove, H. L. Ong, S. A. Jansen, and R. Hoffmann, *Phys. Rev. A* 39, 2653 (1989).
15. T. Uchida, M. Ohgawara, and Y. Shibata, *Mol. Cryst. Liq. Cryst.* 98, 149 (1983).
16. K. Simeonidis, S. Mourdikoudis, M. Moulla, I. Tsiaoussis, C. Martinez-Boubeta, M. Angelakeris, C. Dendrinou-Samara, and O. Kalogirou, *J. Magn. Magn. Mater.* 316, e1 (2007).
17. H. Zhu, D. Yang, L. Zhu, H. Yang, D. Jin, and K. Yao, *J. Mater. Sci.* 42, 9205 (2007).
18. A. Millan, A. Urtizberea, N. J. O. Silva, F. Palacio, V. S. Amaral, E. Snoeck, and V. Serin, *J. Magn. Magn. Mater.* 312, L5 (2007).

Figures

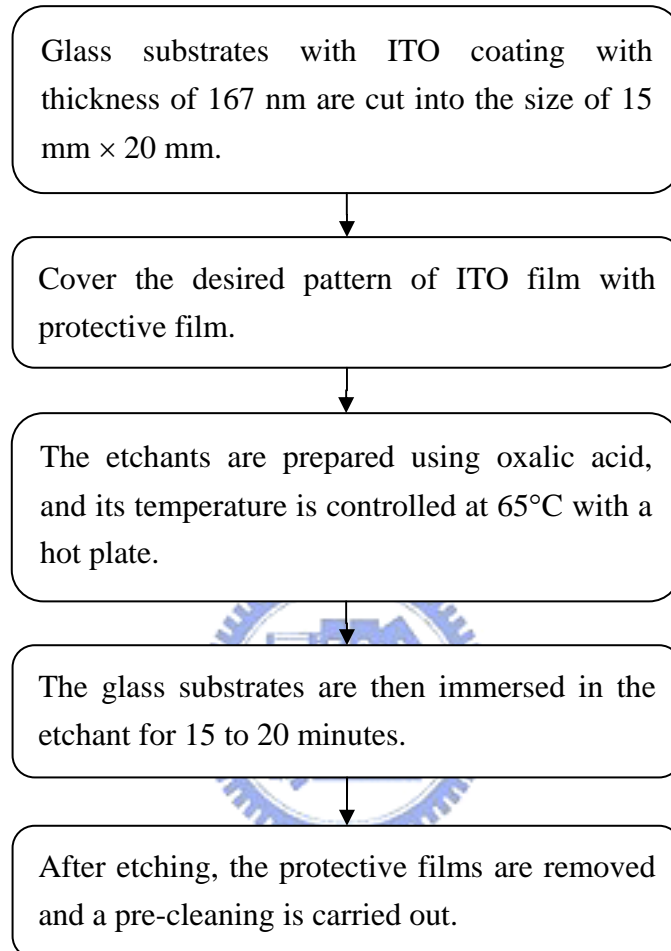


Figure 3.2.1 Procedures of etching process for the patterned-ITO.

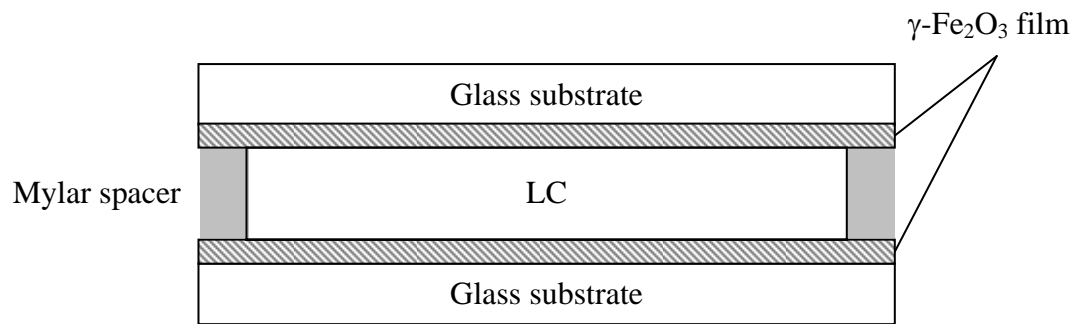


Figure 3.2.2 Schematic structure of a LC cell.



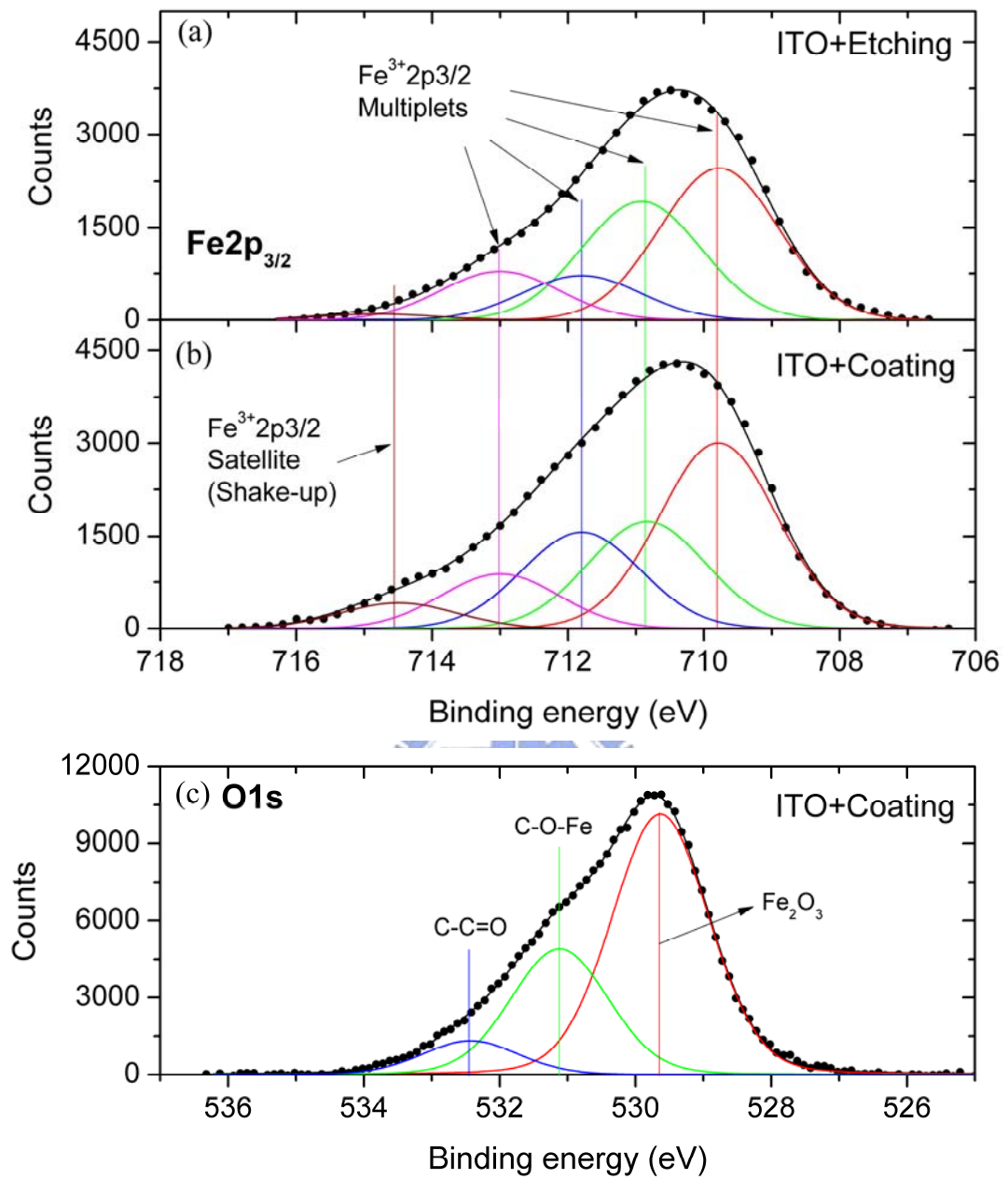


Figure 3.3.1 Deconvolution of the Fe 2p_{3/2} spectra of ITO-coated substrates treated in (a) etching mode and (b) coating mode with ion beam condition: $V_b=1120$ V, $J_{ion}=255$ $\mu\text{A}/\text{cm}^2$, incidence angle of (a) 60° and (b) 0° , and treating time of 5 min. (c) Deconvolution of the O 1s spectrum of ITO-coated substrates treated in coating mode with the same energy, current density, and treating time. The incidence angle is 0° .

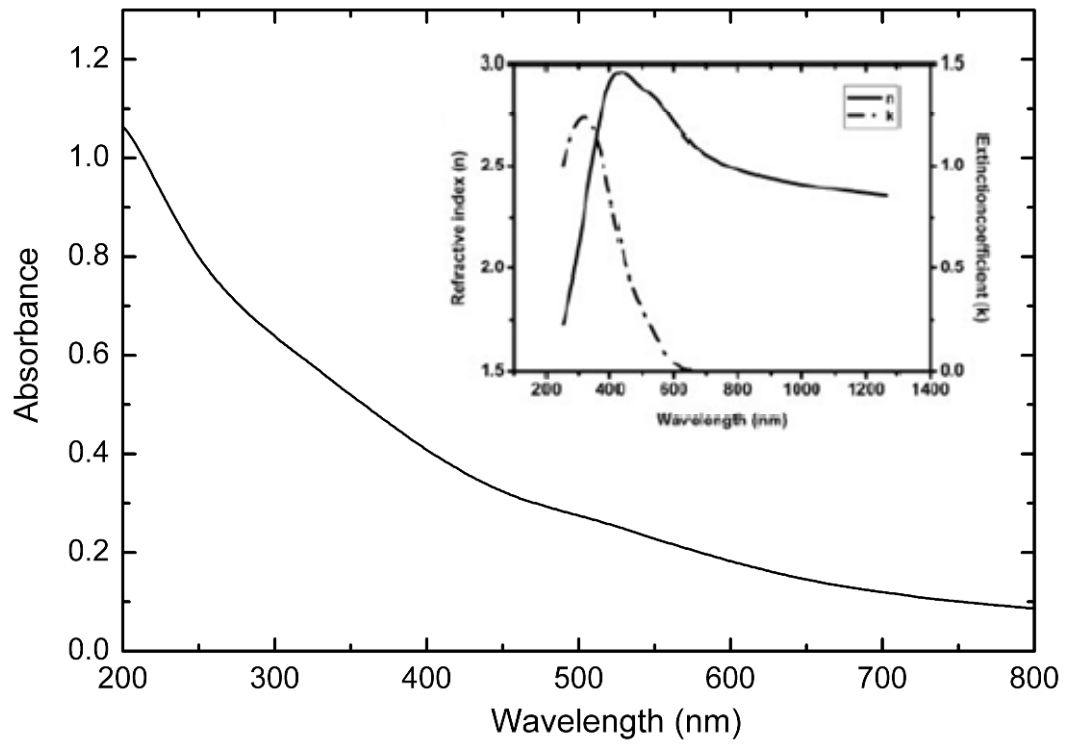


Figure 3.3.2 The UV/VIS absorbance spectrum of iron oxide thin film with ion condition: $V_b=1120$ V, $J_{ion}=255$ $\mu\text{A}/\text{cm}^2$, incidence angle of 0° , and coating time of 20 min. Inset: the optical constants of hematite ($\alpha\text{-Fe}_2\text{O}_3$).

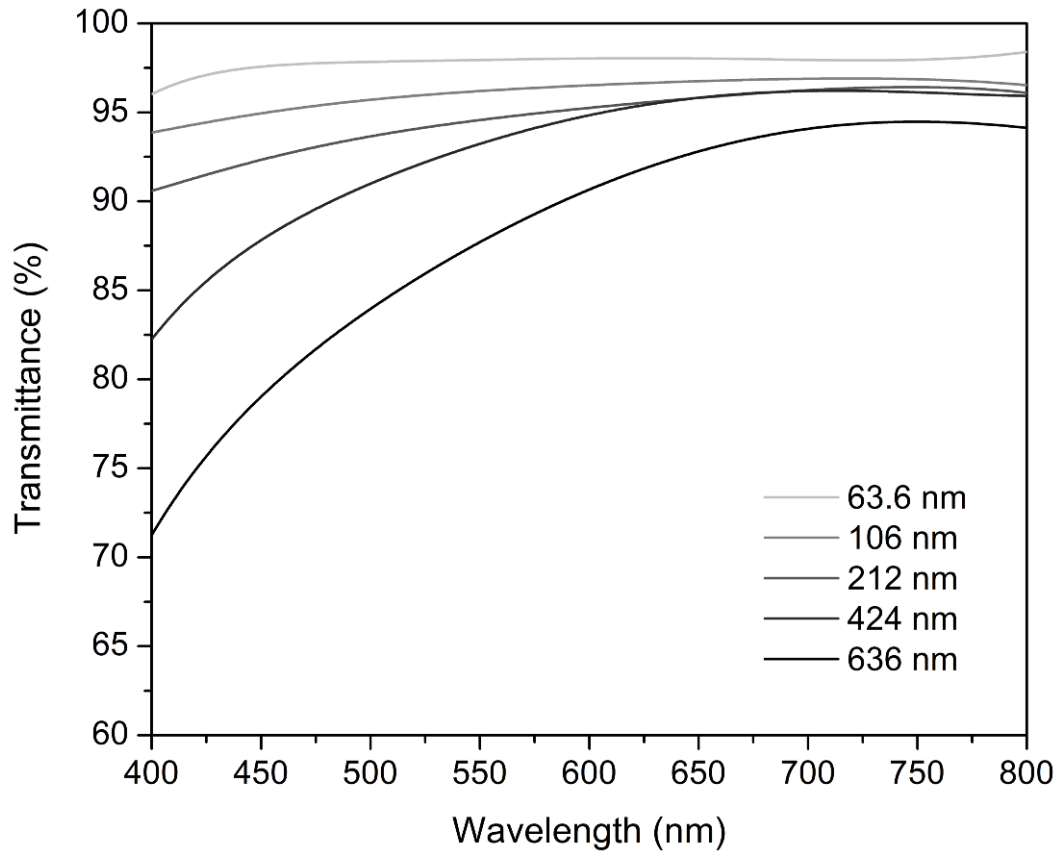


Figure 3.3.3 The UV/VIS transmittance spectra of γ -Fe₂O₃ films with different thickness of 63.6, 106, 212, 424, and 636 nm.

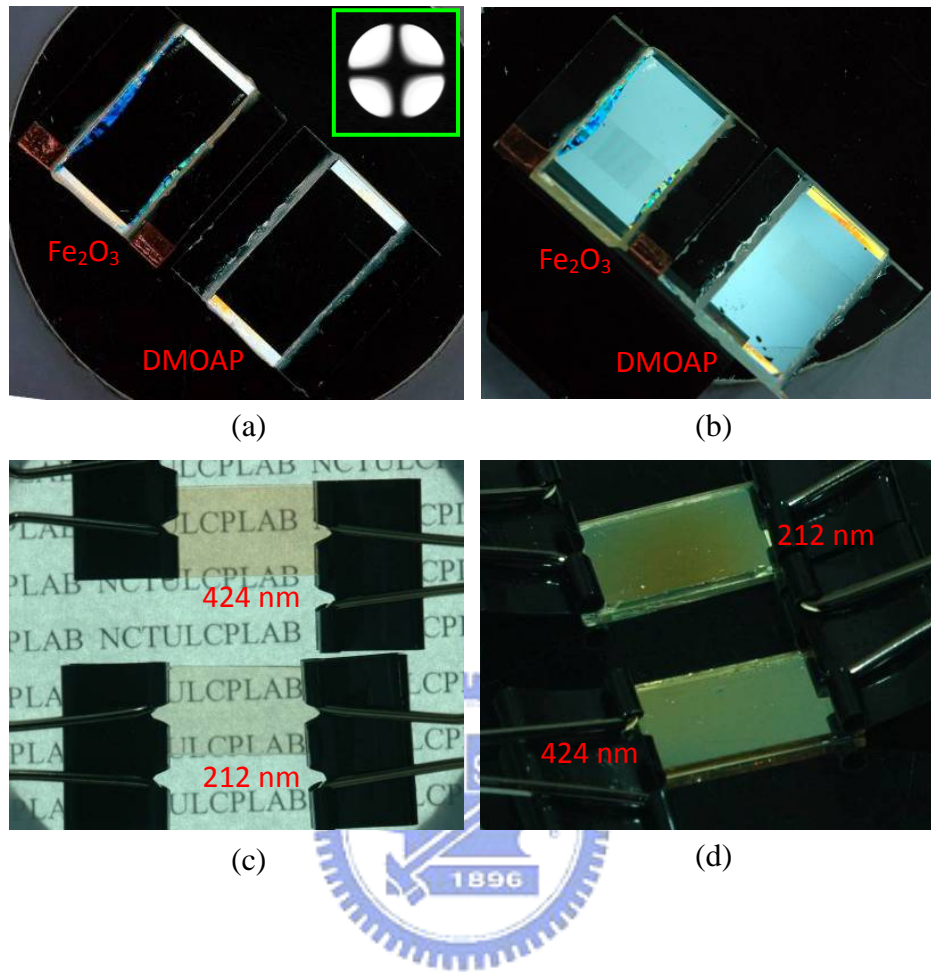


Figure 3.3.4 (a) Top-view and (b) tilt-view of the MLC-6608 cells with $\gamma\text{-Fe}_2\text{O}_3$ and DMOAP coating under crossed-polarizers; (c) top-view (without polarizers) and (d) tilt-view of the 5CB cells coated with different thickness of $\gamma\text{-Fe}_2\text{O}_3$ films. Inset: the conoscopic pattern of the MLC-6608 cells with $\gamma\text{-Fe}_2\text{O}_3$ coating.

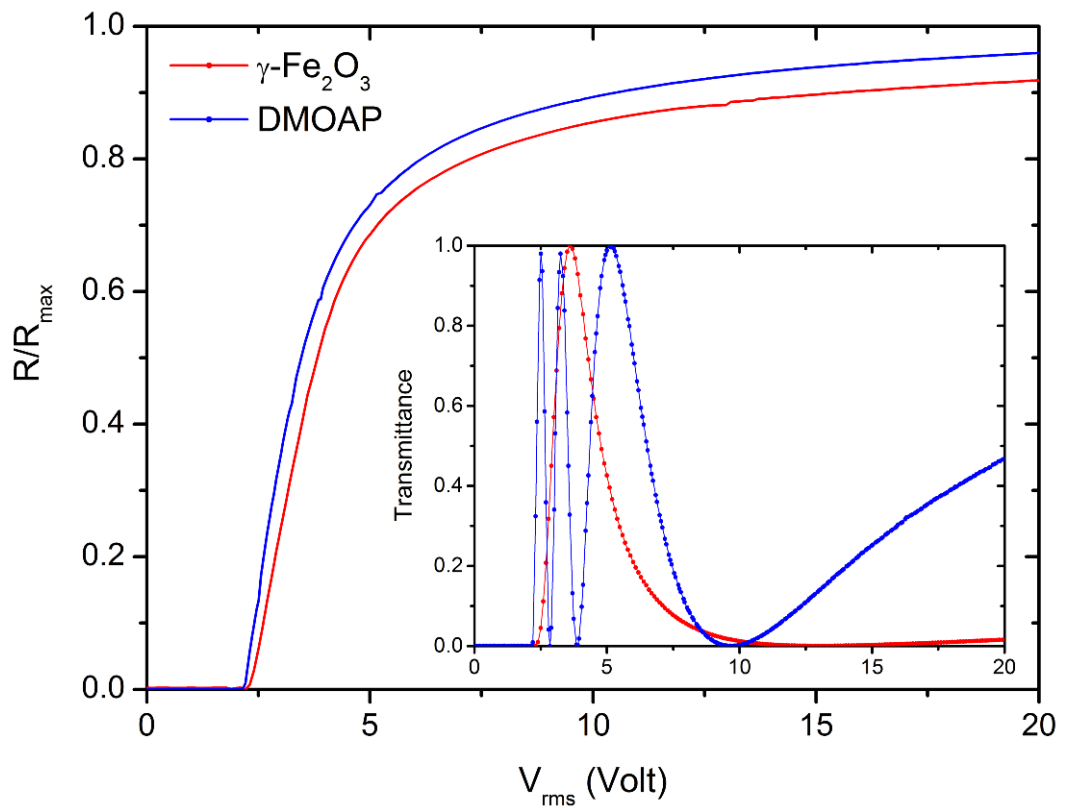


Figure 3.3.5 Normalized phase retardation of MLC-6608 cells at different applied voltage. Inset: the measured curves of transmittance versus applied voltage.

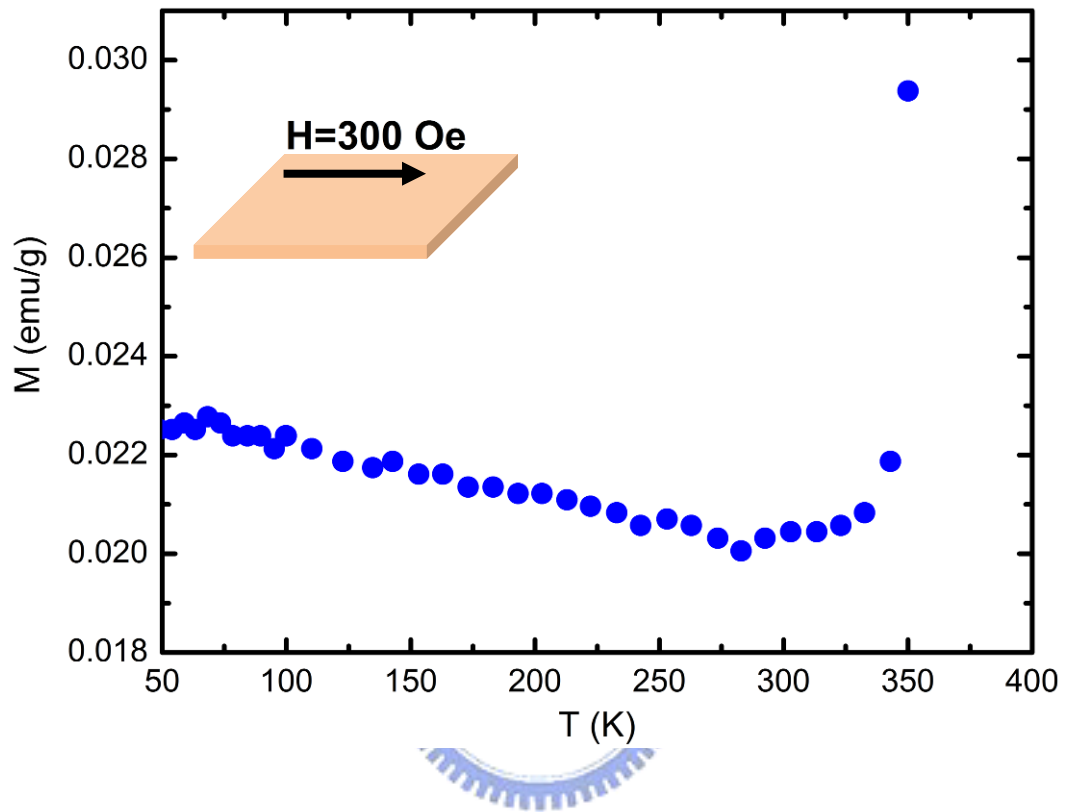


Figure 3.3.6 Temperature dependence of the magnetization measured in the direction parallel to the surface for the iron oxide film with thickness of 636 nm in an applied field of 300 Oe.

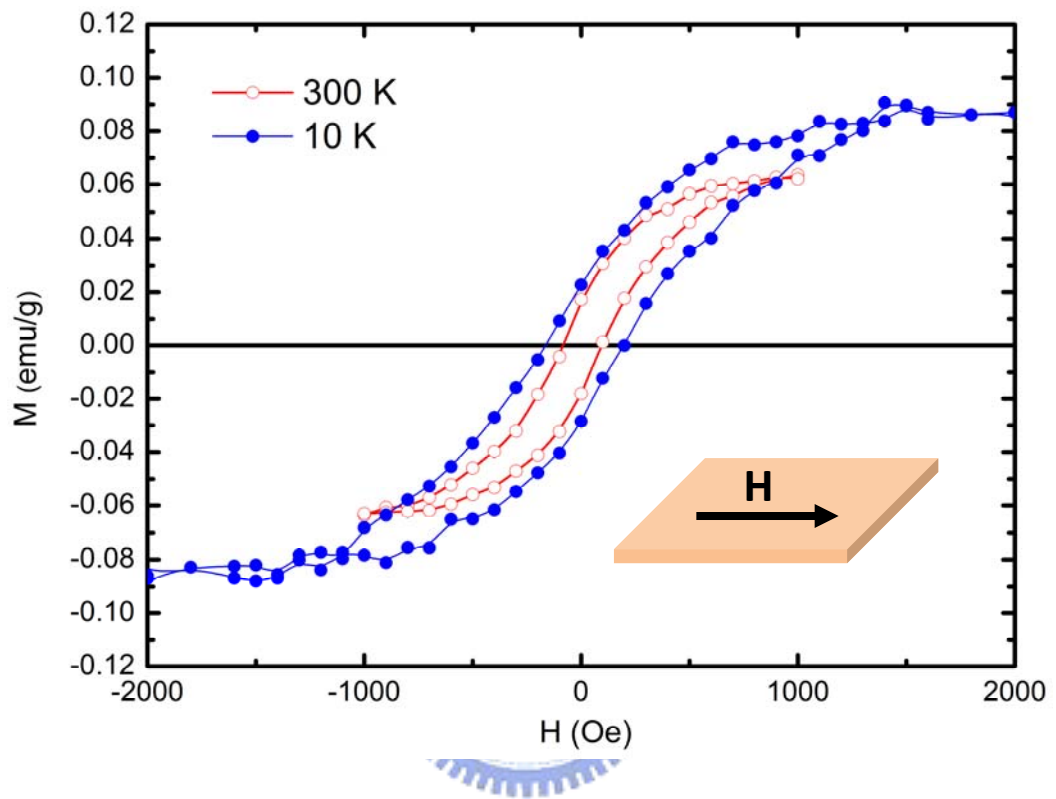


Figure 3.3.7 Magnetization curves for a $\gamma\text{-Fe}_2\text{O}_3$ film with thickness of 636 nm at $T=10$ K and 300 K in the magnetic field parallel to the film surface.

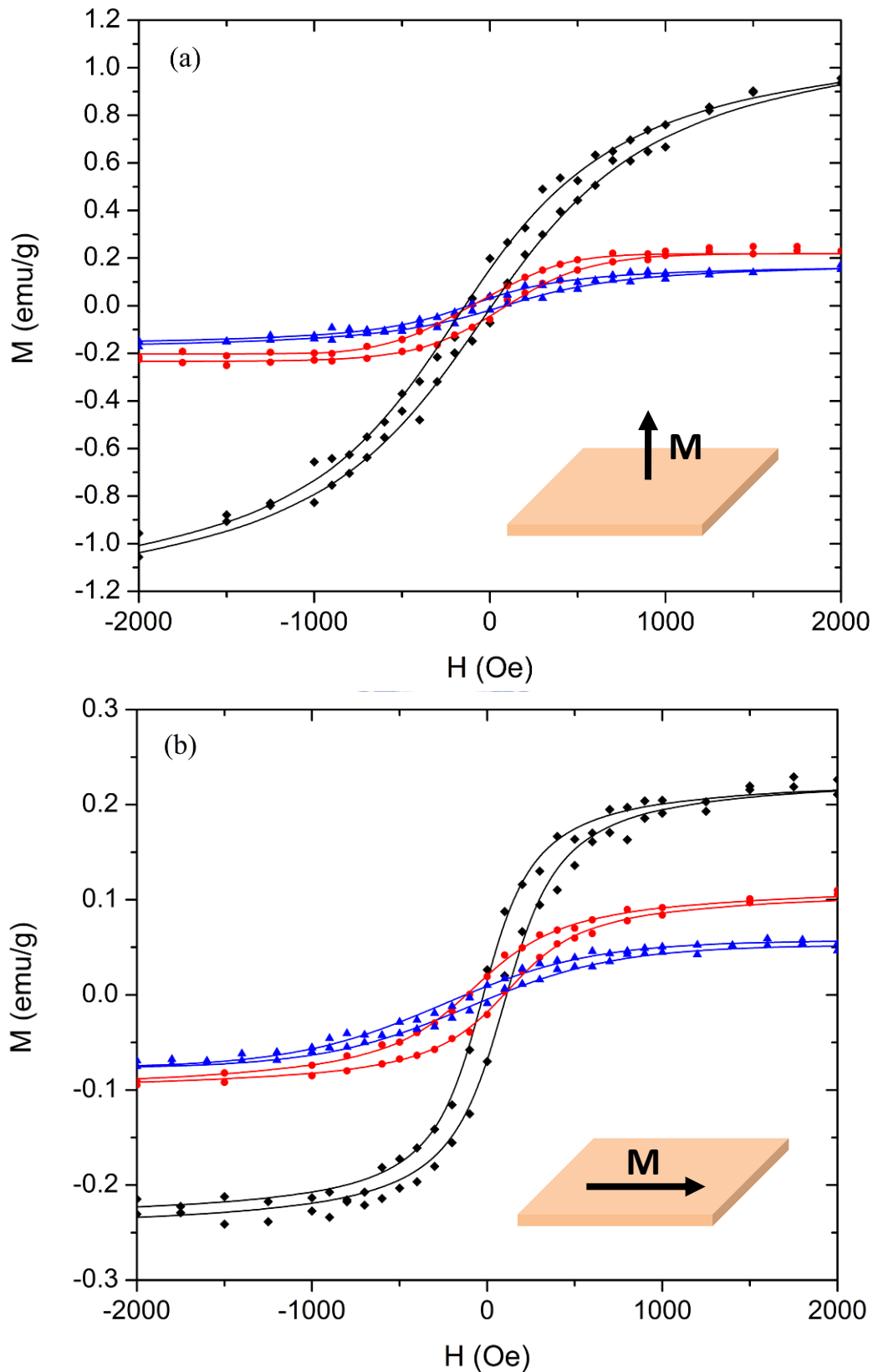


Figure 3.3.8 Hysteresis loops measured in the direction (a) perpendicular and (b) parallel to the surfaces for sputtered γ - Fe_2O_3 films with thickness of 212 nm (\blacklozenge), 424 nm (\bullet), and 636 nm (\blacktriangle).

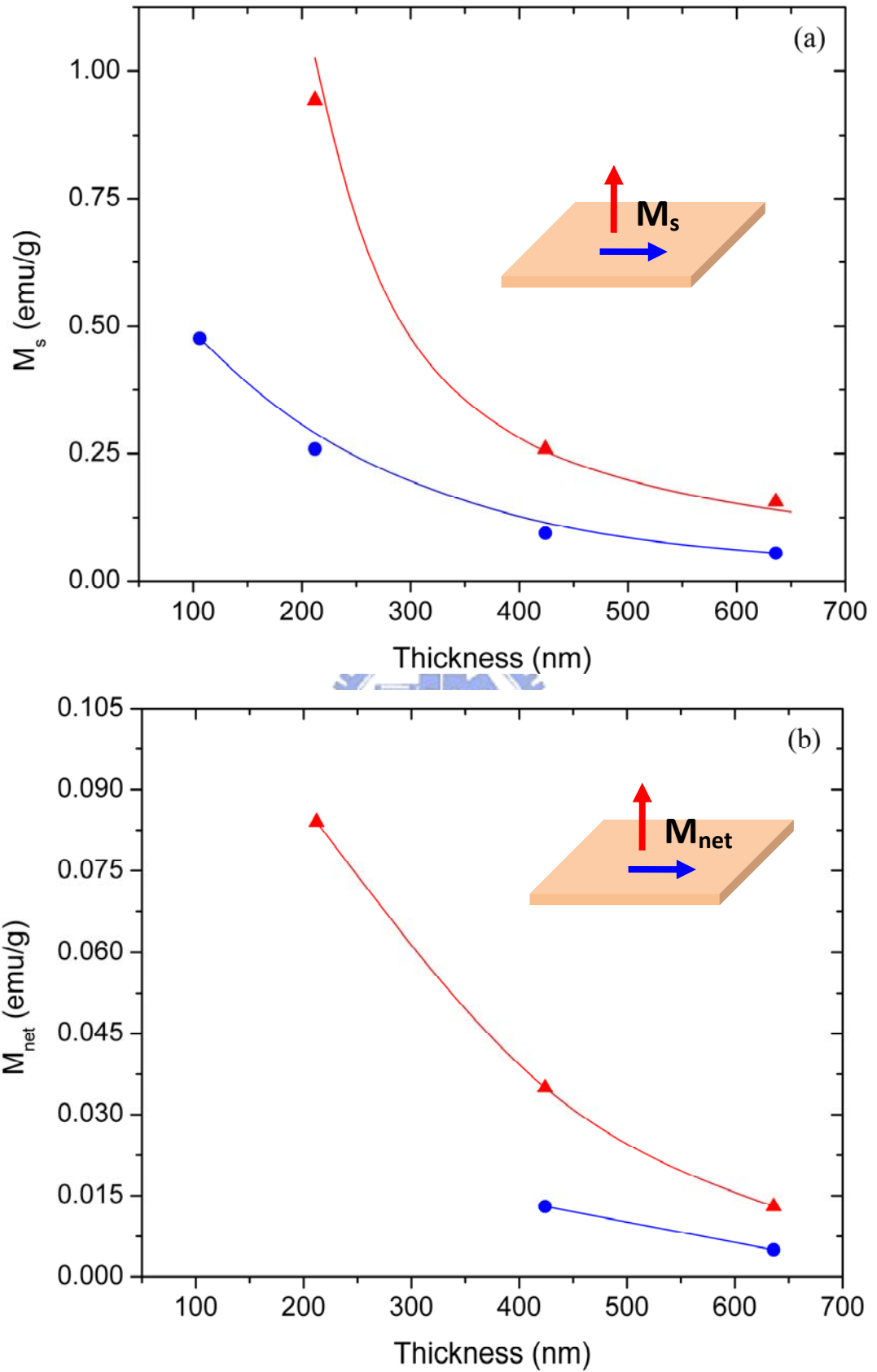


Figure 3.3.9 Thickness-dependence on (a) M_s and (b) M_{net} of the $\gamma\text{-Fe}_2\text{O}_3$ films. The vertical and horizontal components of M are labeled as (\blacktriangle) and (\bullet), respectively.

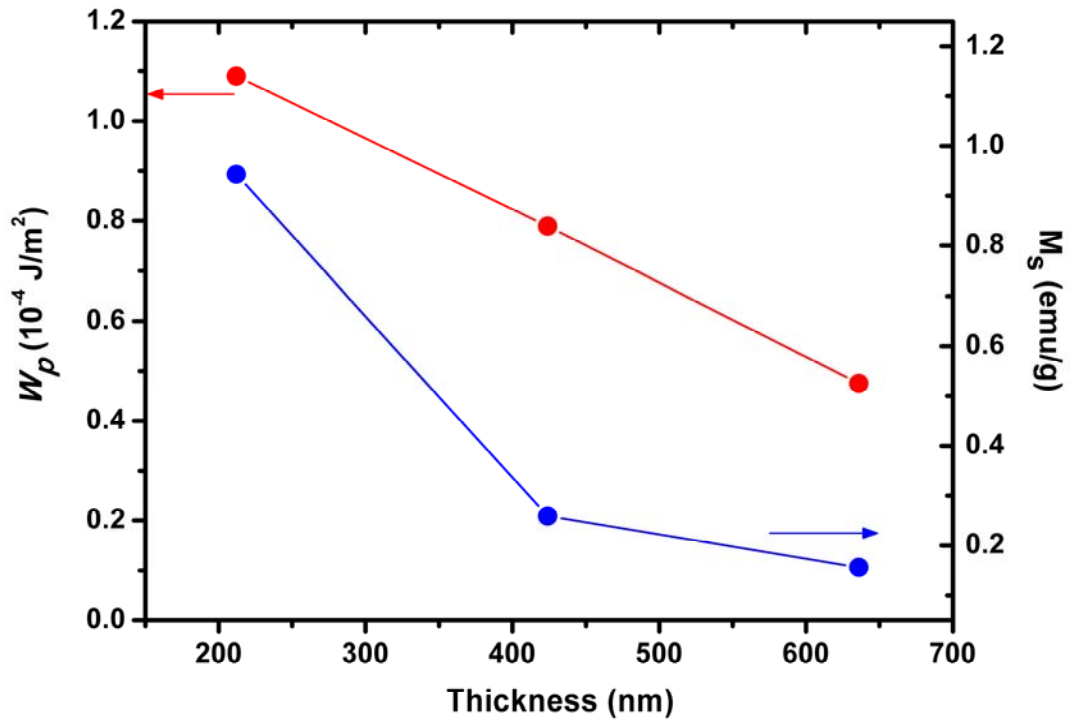


Figure 3.3.10 Polar anchoring strength W_p and the saturation magnetization M_s as a function of γ - Fe_2O_3 film thickness.

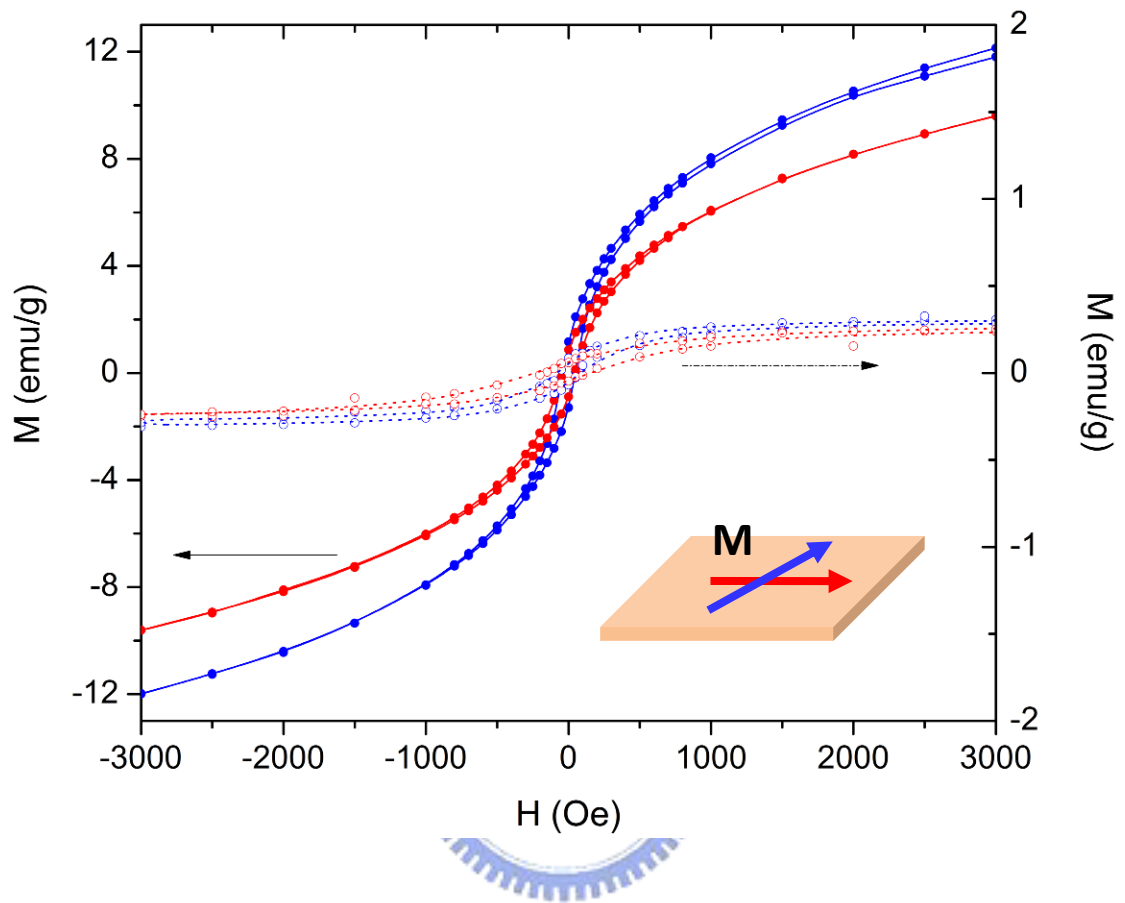


Figure 3.3.11 Hysteresis loops measured for an as-sputtered $\gamma\text{-Fe}_2\text{O}_3$ film (—○—) and a thermally-treated $\gamma\text{-Fe}_2\text{O}_3$ film (—●—) with thickness of 212 nm. Two randomly directions on each film are selected for measurements.

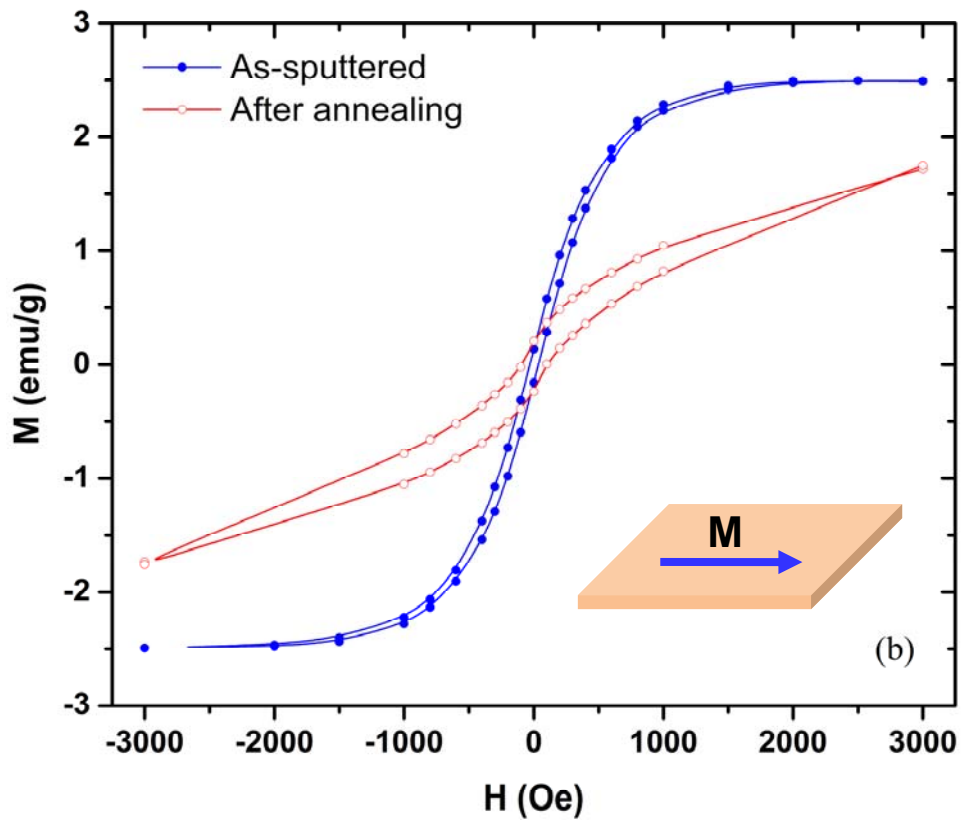
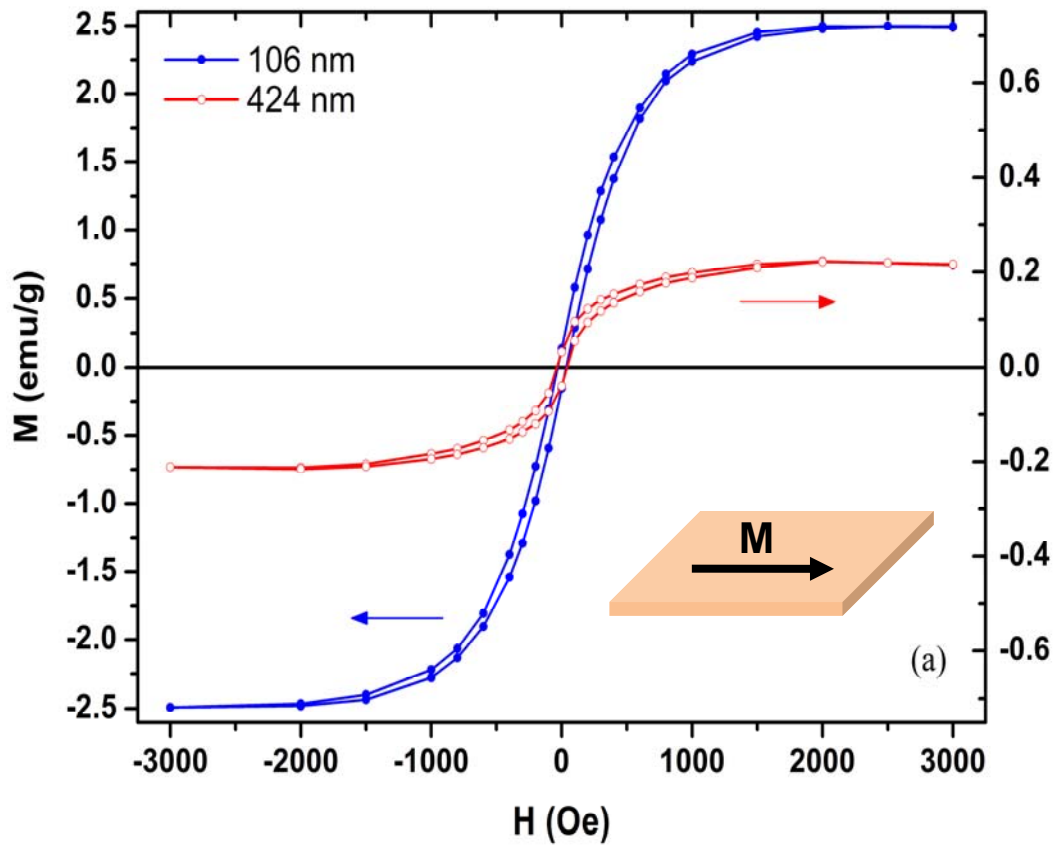


Figure 3.3.12 Hysteresis loops measured in the direction parallel to the surface (a) for as-sputtered $\gamma\text{-Fe}_2\text{O}_3$ films with thickness of 106 and 424 nm and (b) a 106 nm-thick $\gamma\text{-Fe}_2\text{O}_3$ film with thermal treatment at 573 K for 2 hours.

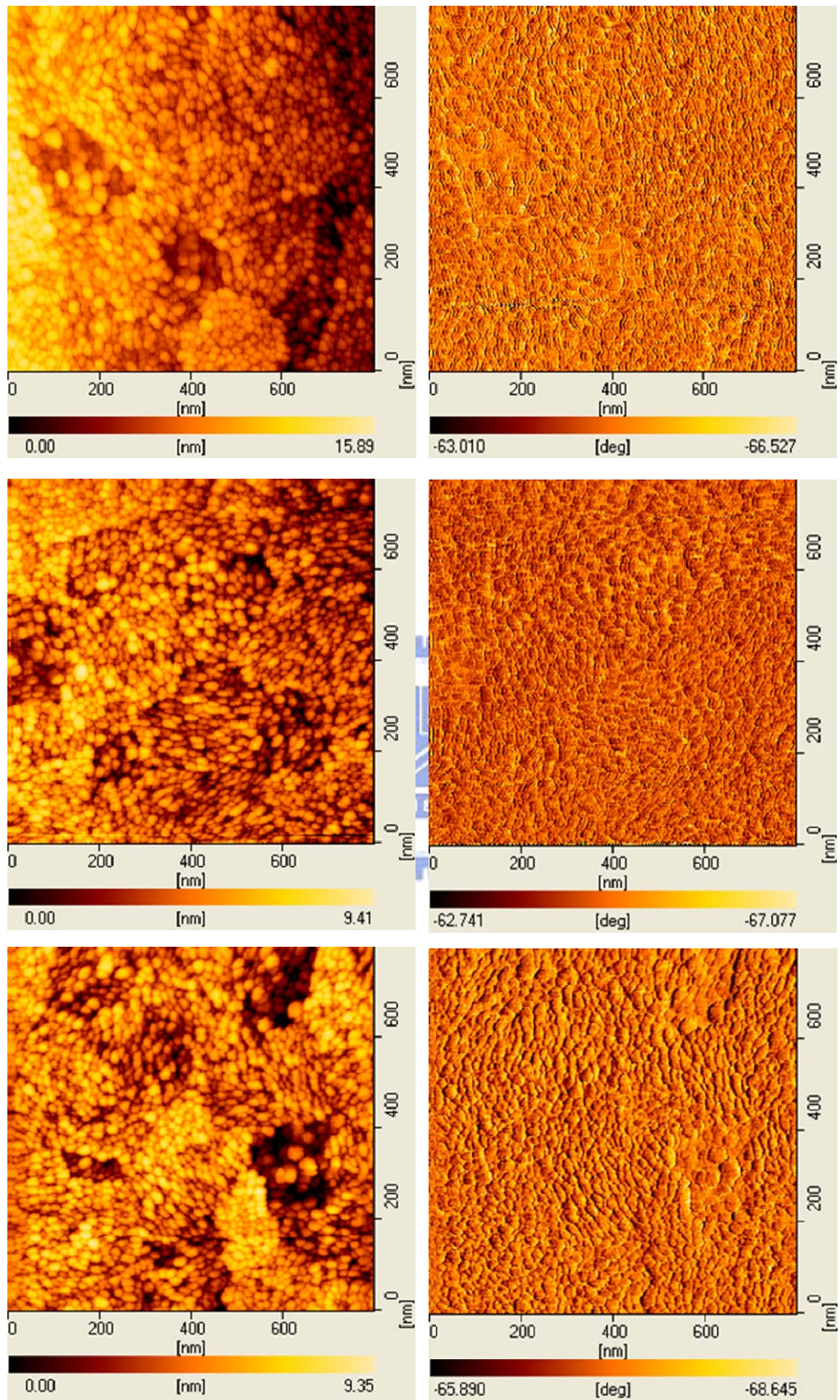


Figure 3.3.13 AFM images taken at three different positions on the γ -Fe₂O₃ film surface with thickness of 42.4 nm.

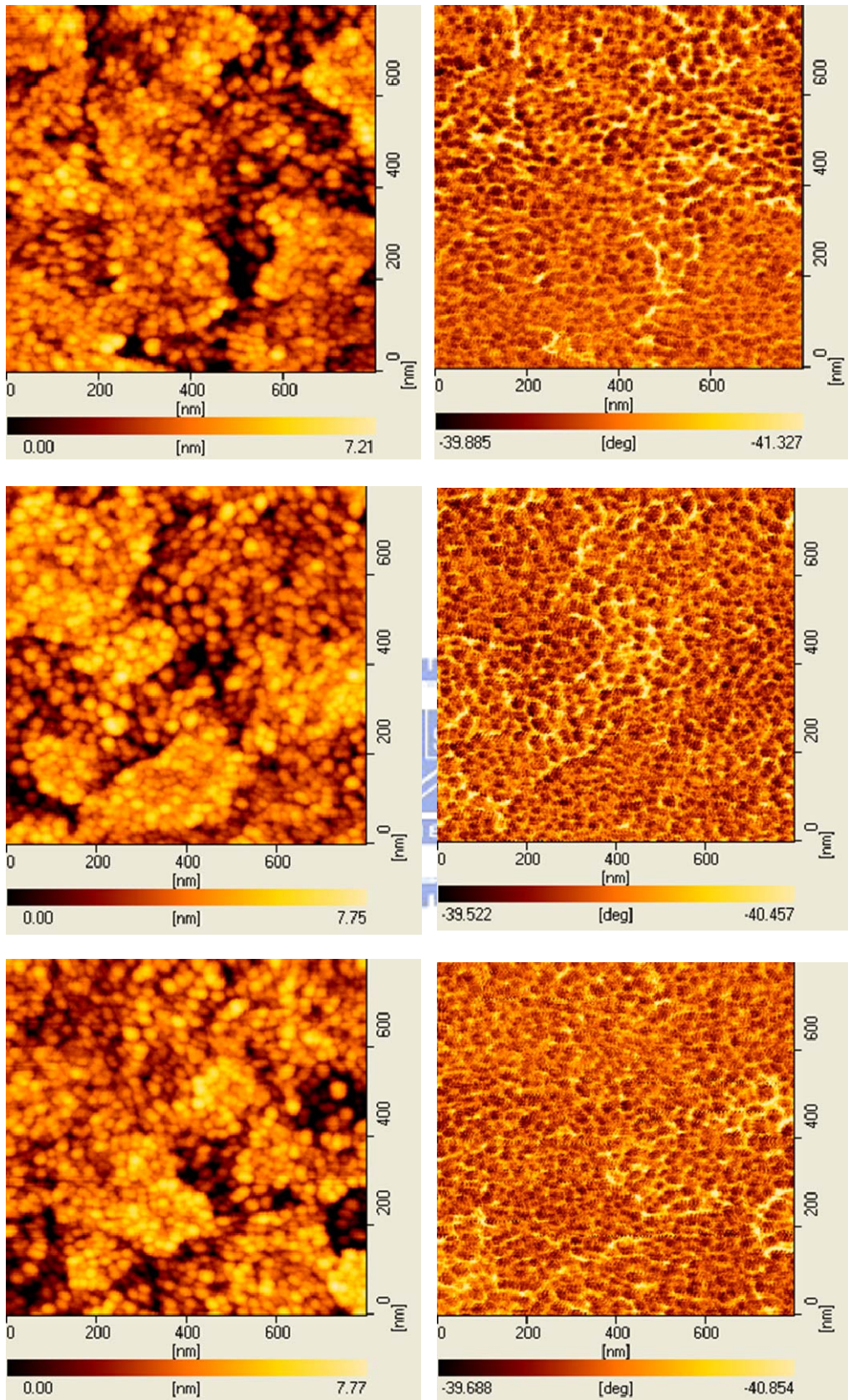


Figure 3.3.14 AFM images taken at three different positions on the γ -Fe₂O₃ film surface with thickness of 106 nm.

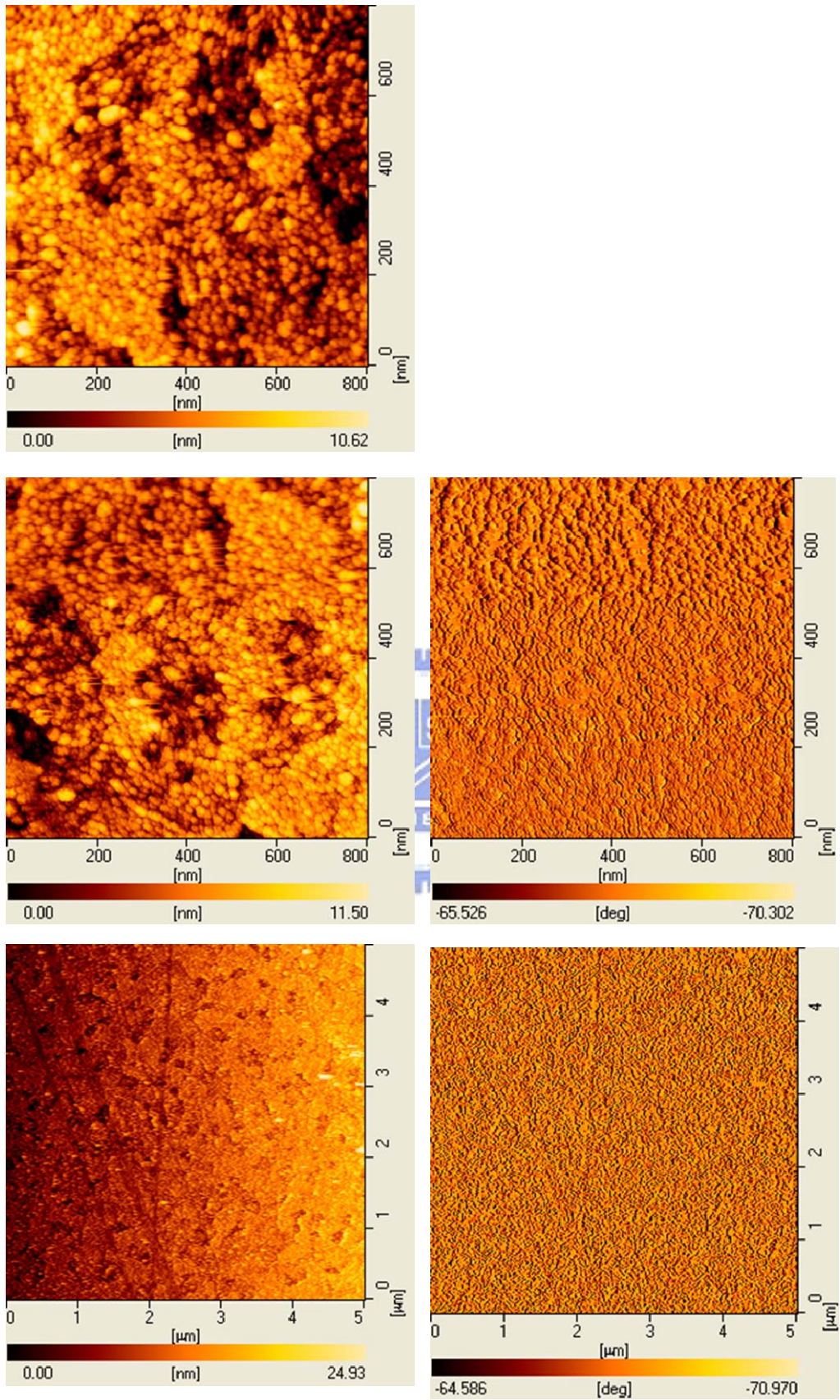


Figure 3.3.15 AFM images taken at three different positions on the γ -Fe₂O₃ film surface with thickness of 212 nm.

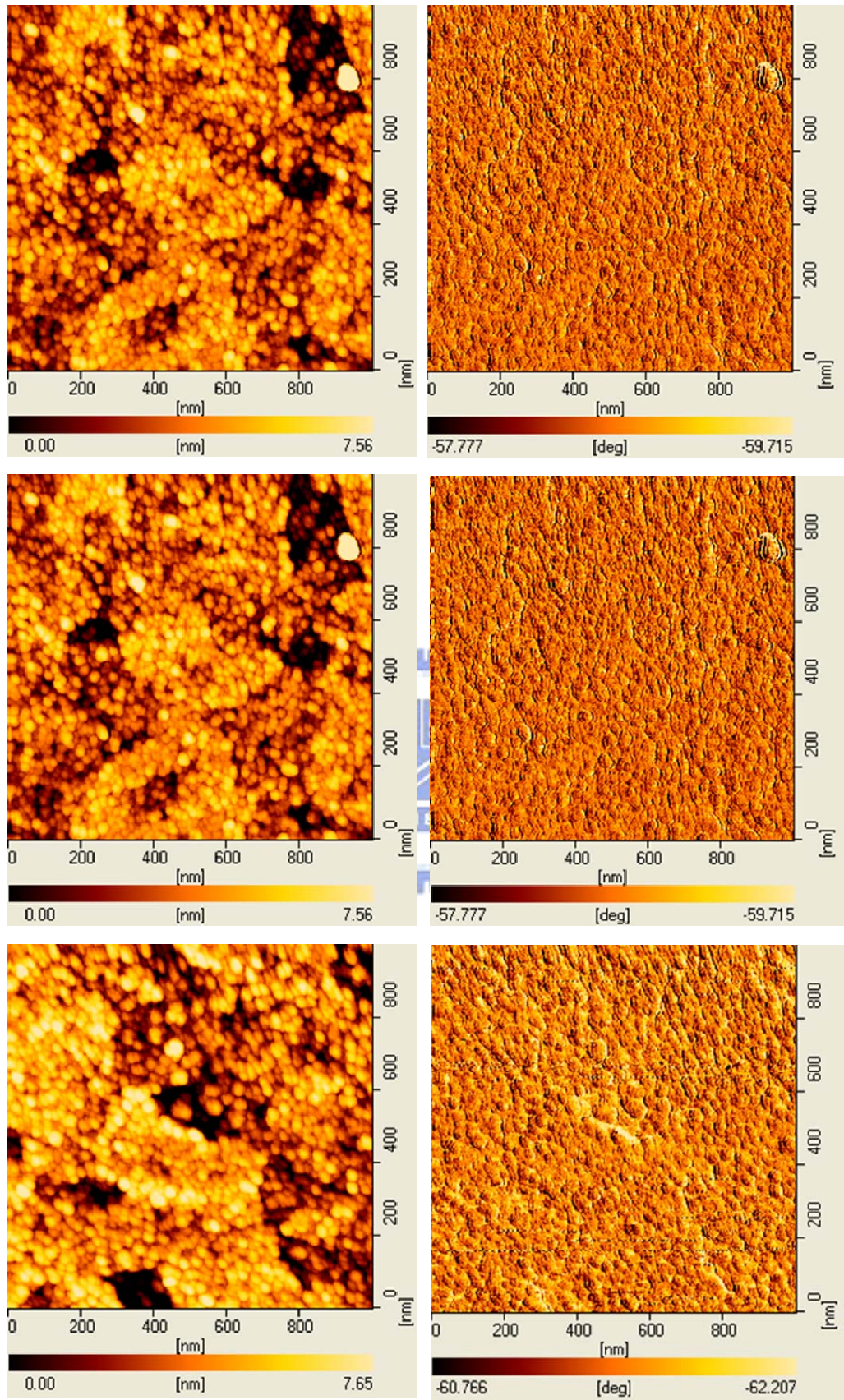


Figure 3.3.16 AFM images taken at three different positions on the $\gamma\text{-Fe}_2\text{O}_3$ film surface with thickness of 424 nm.

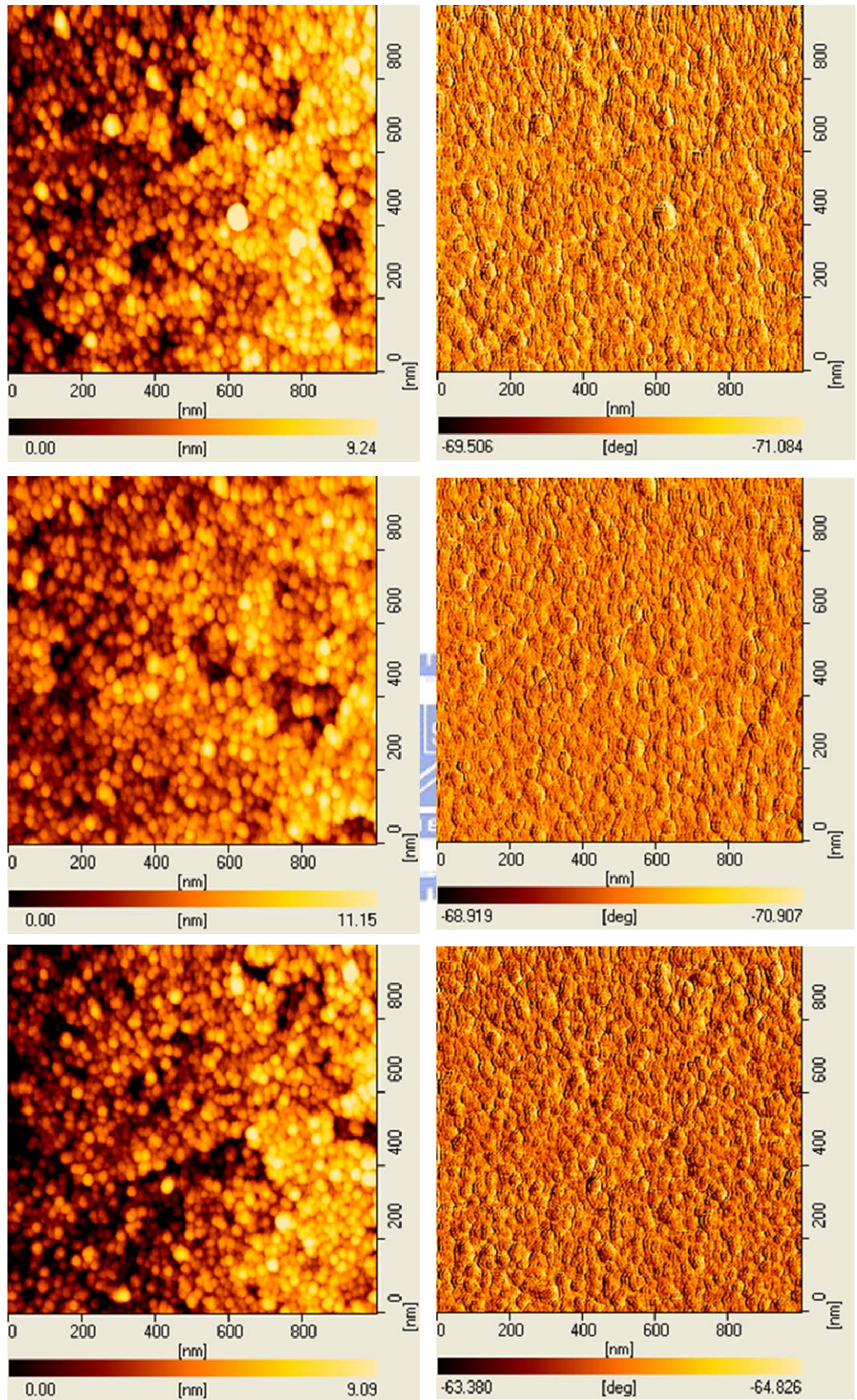


Figure 3.3.17 AFM images taken at three different positions on the $\gamma\text{-Fe}_2\text{O}_3$ film surface with thickness of 848 nm.

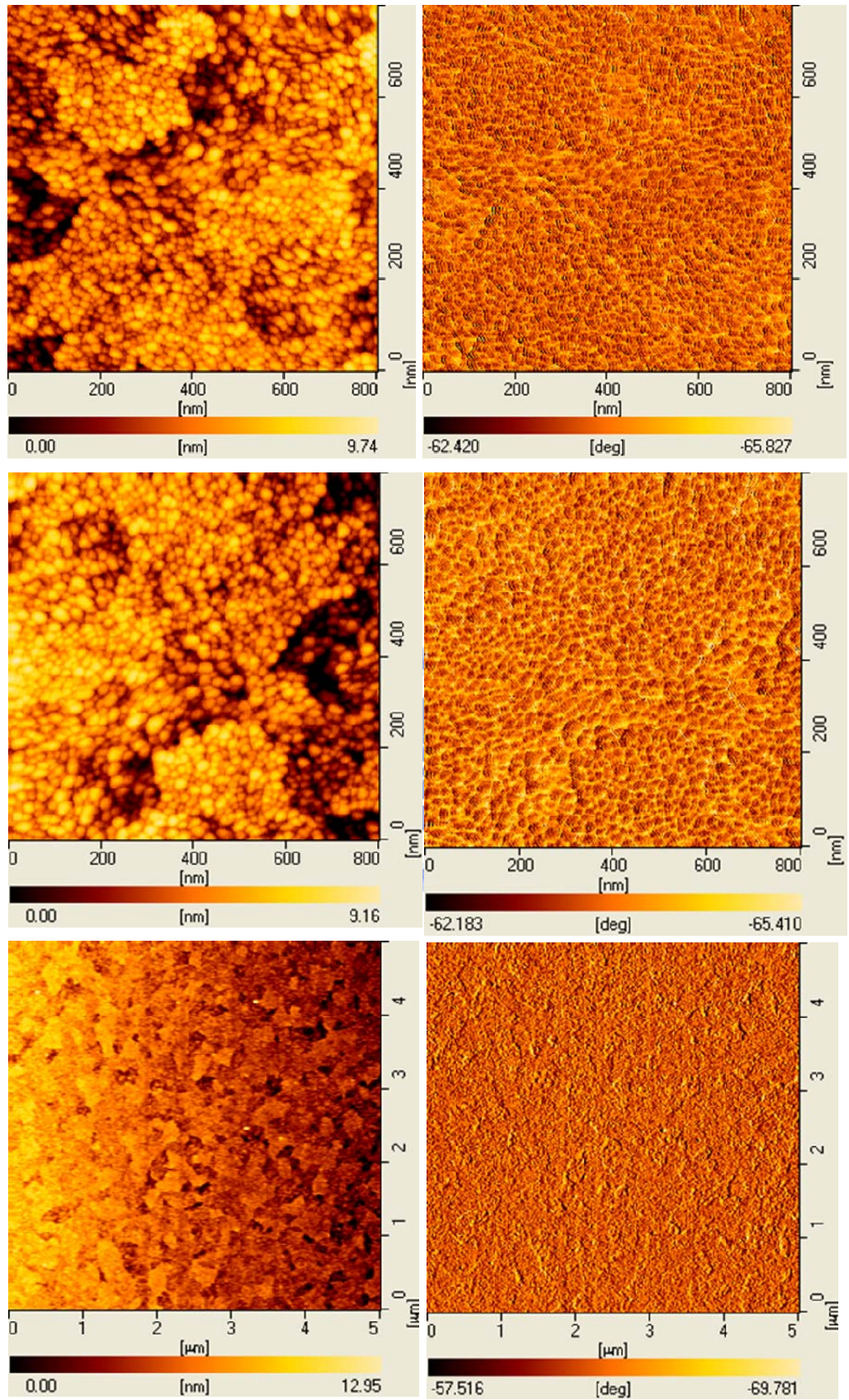


Figure 3.3.18 AFM images taken at three different positions on the annealed $\gamma\text{-Fe}_2\text{O}_3$ film surface with thickness of 42.4 nm.

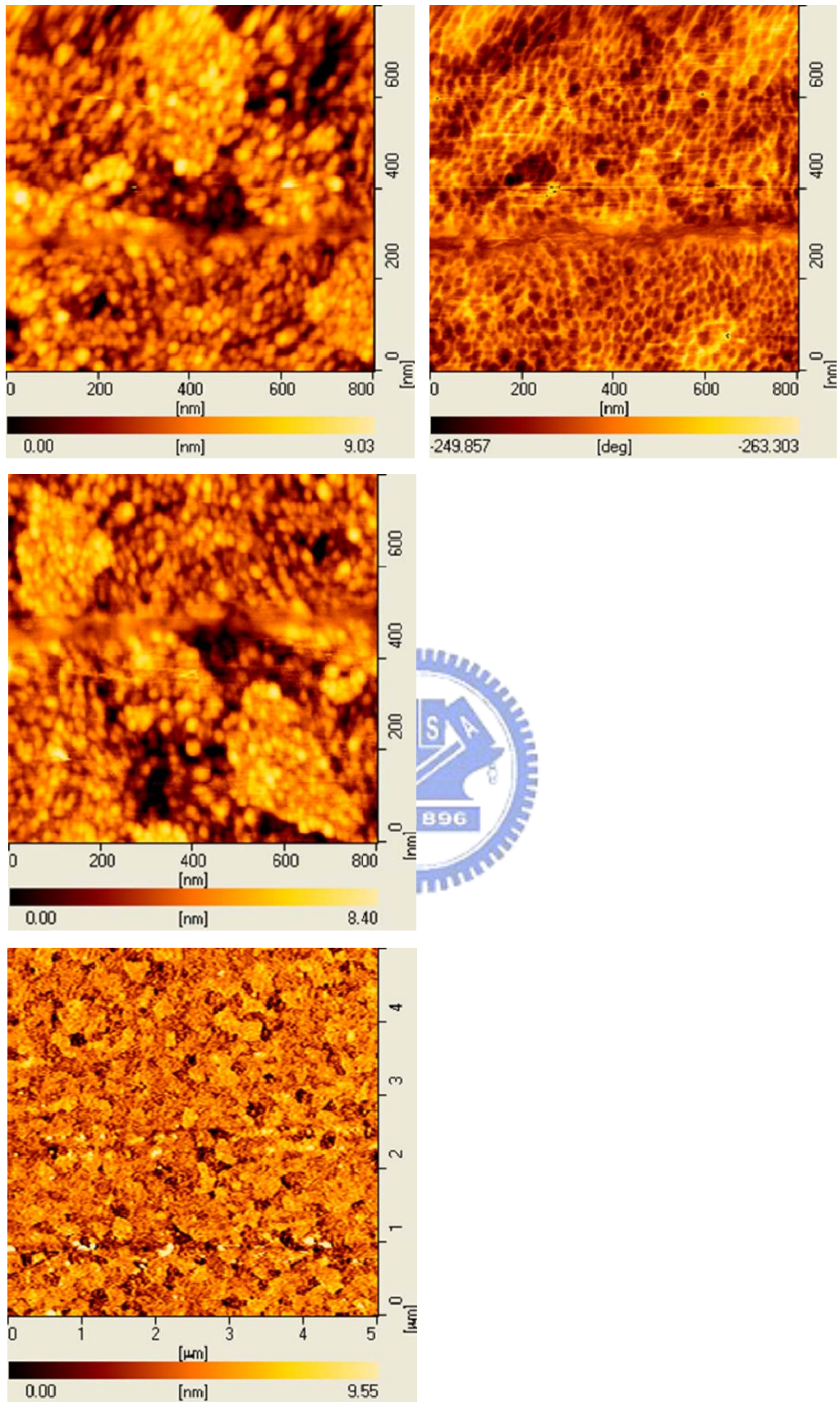


Figure 3.3.19 AFM images taken at three different positions on the annealed $\gamma\text{-Fe}_2\text{O}_3$ film surface with thickness of 106 nm.

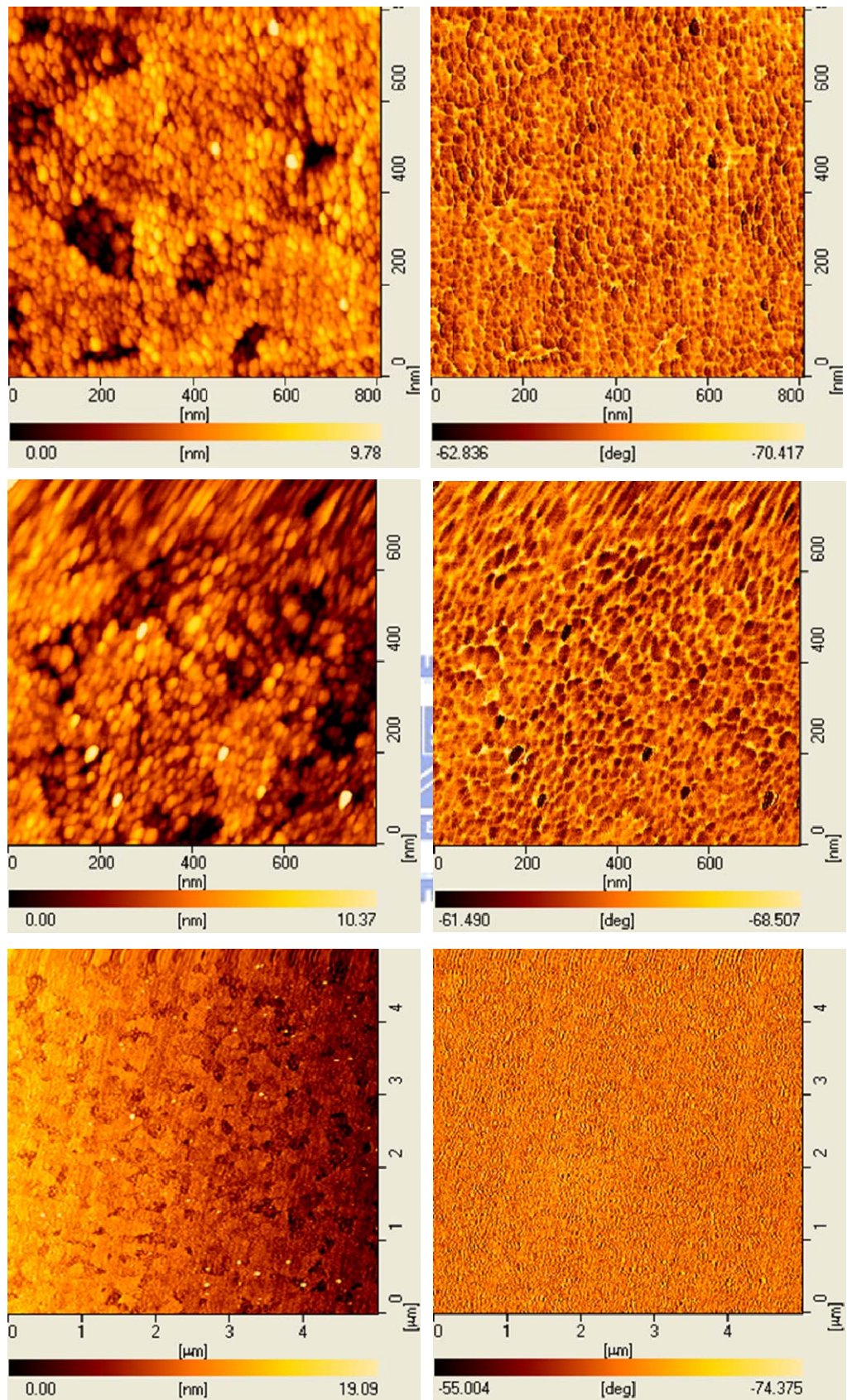


Figure 3.3.20 AFM images taken at three different positions on the annealed $\gamma\text{-Fe}_2\text{O}_3$ film surface with thickness of 212 nm.

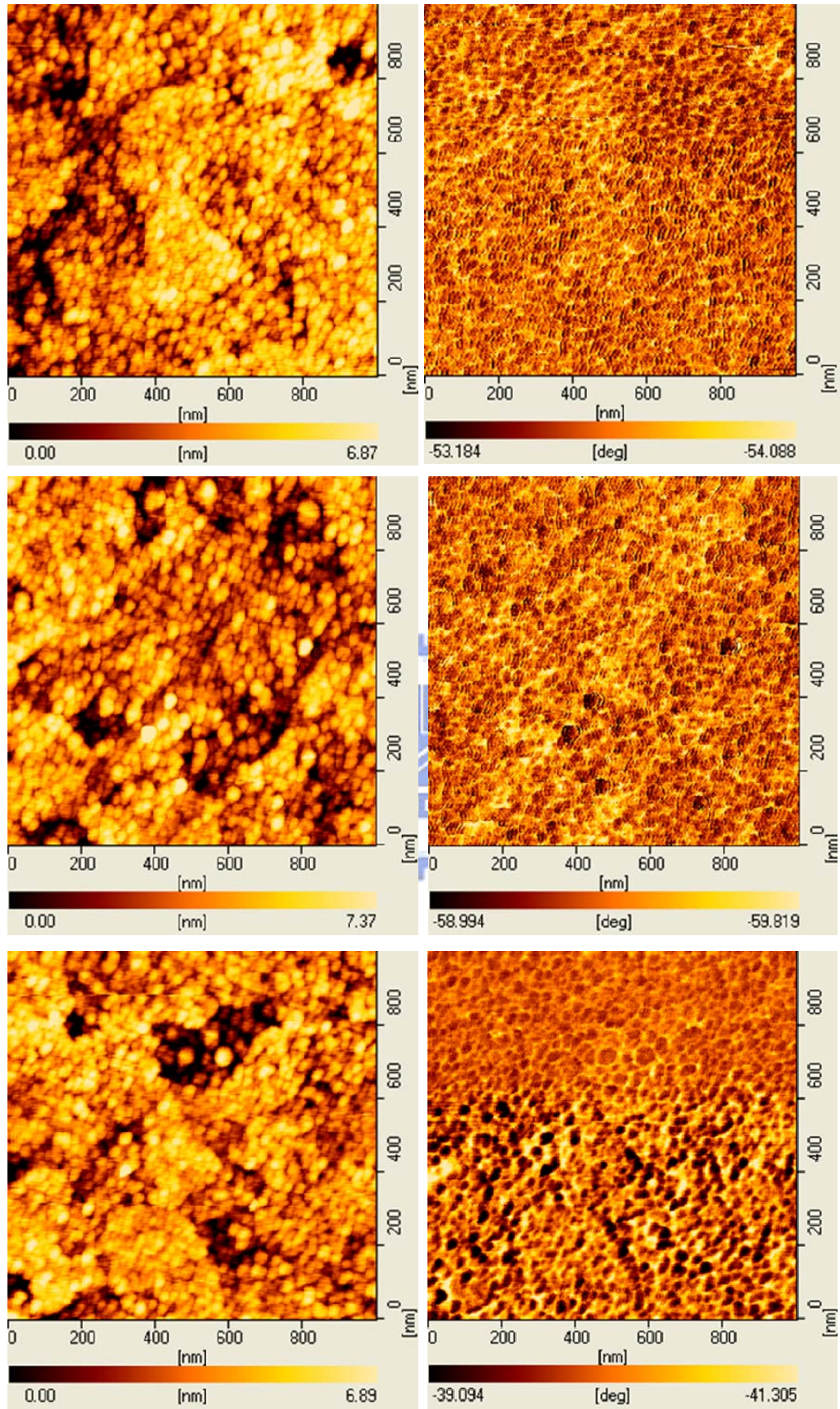


Figure 3.3.21 AFM images taken at three different positions on the annealed $\gamma\text{-Fe}_2\text{O}_3$ film surface with thickness of 424 nm.

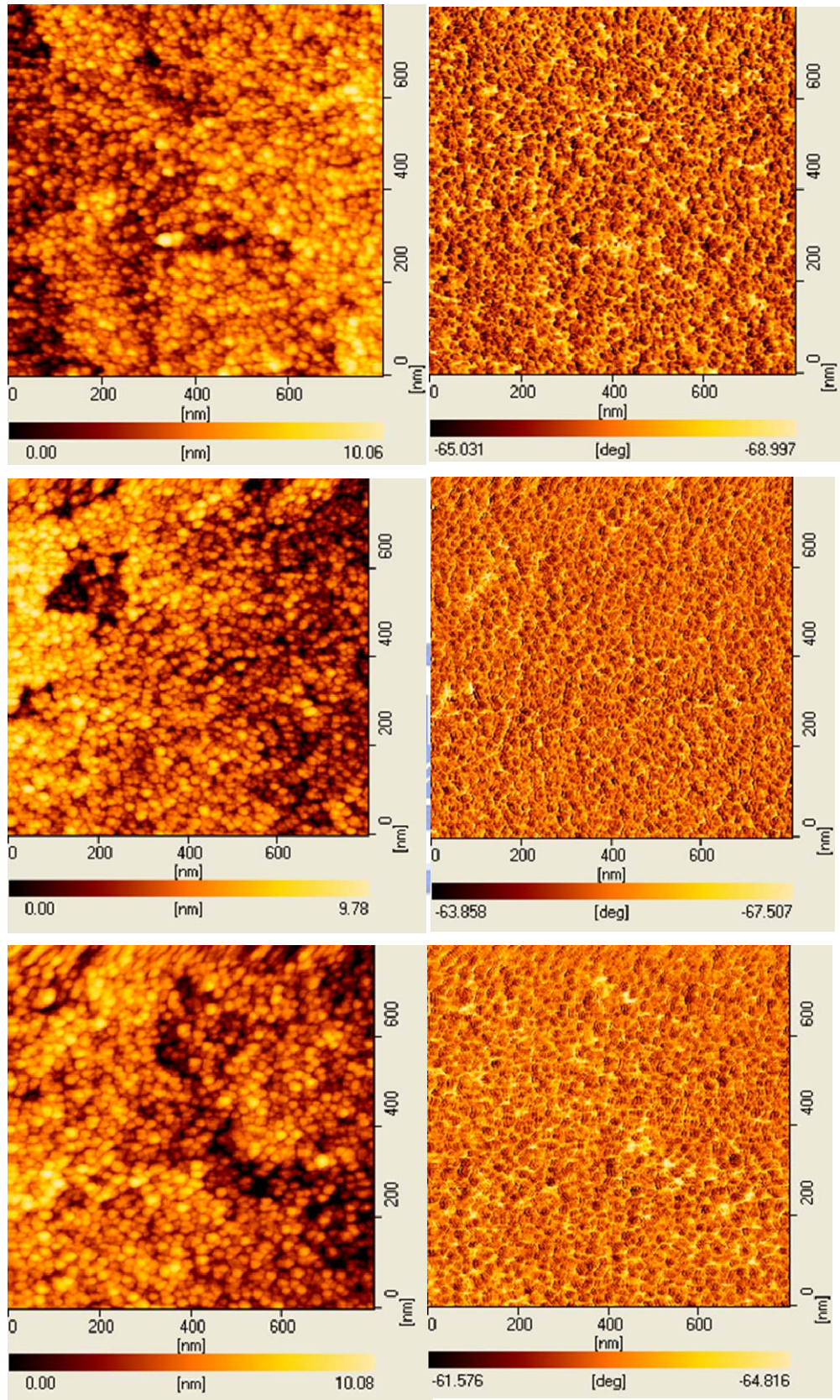
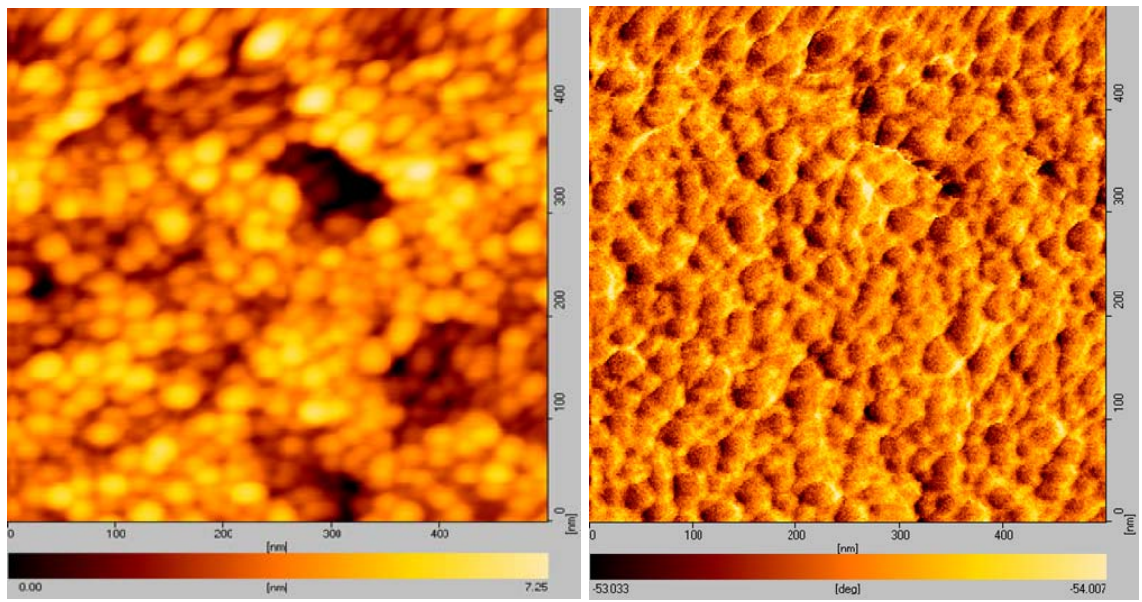
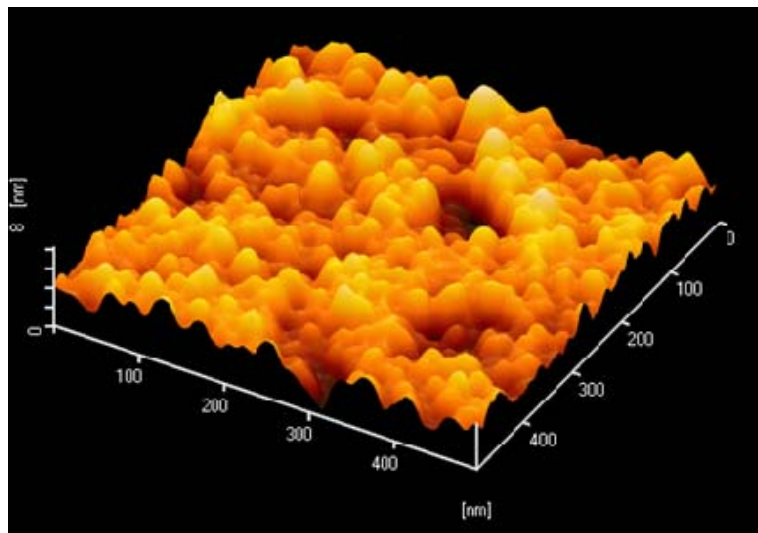


Figure 3.3.22 AFM images taken at three different positions on the annealed γ -Fe₂O₃ film surface with thickness of 848 nm.



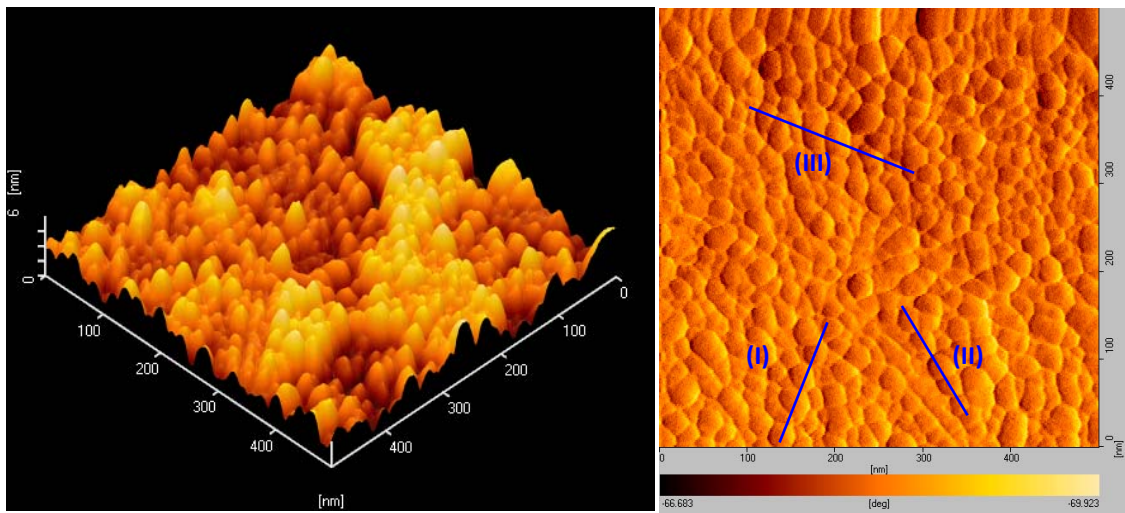
(a)

(b)



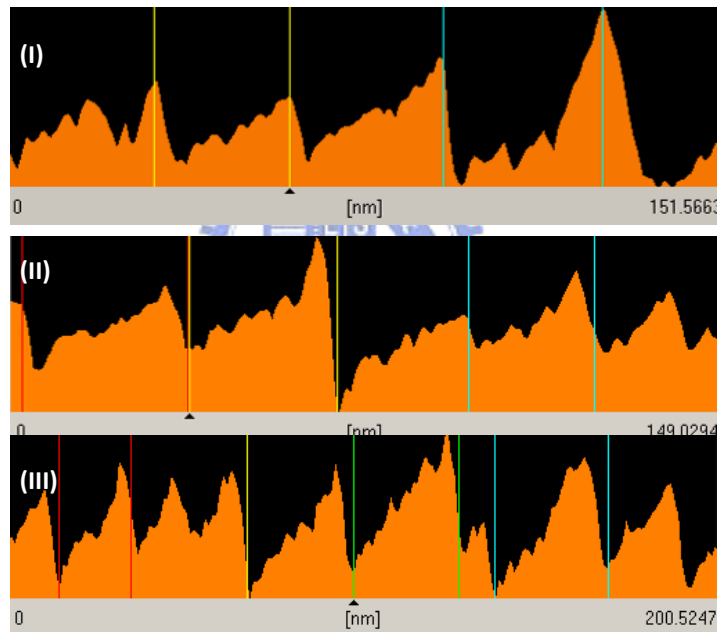
(c)

Figure 3.3.23 Surface morphology image of as-sputtered $\gamma\text{-Fe}_2\text{O}_3$ film with thickness of 169.6 nm: (a) Top-view image; (b) top-view phase image; (c) three-dimensional image.



(a)

(b)



(c)

Figure 3.3.24 Surface morphology of a γ -Fe₂O₃ film with thickness of 169.6 nm: (a) Three-dimensional image; (b) top-view phase image; (c) surface profiles for particle size analyses.

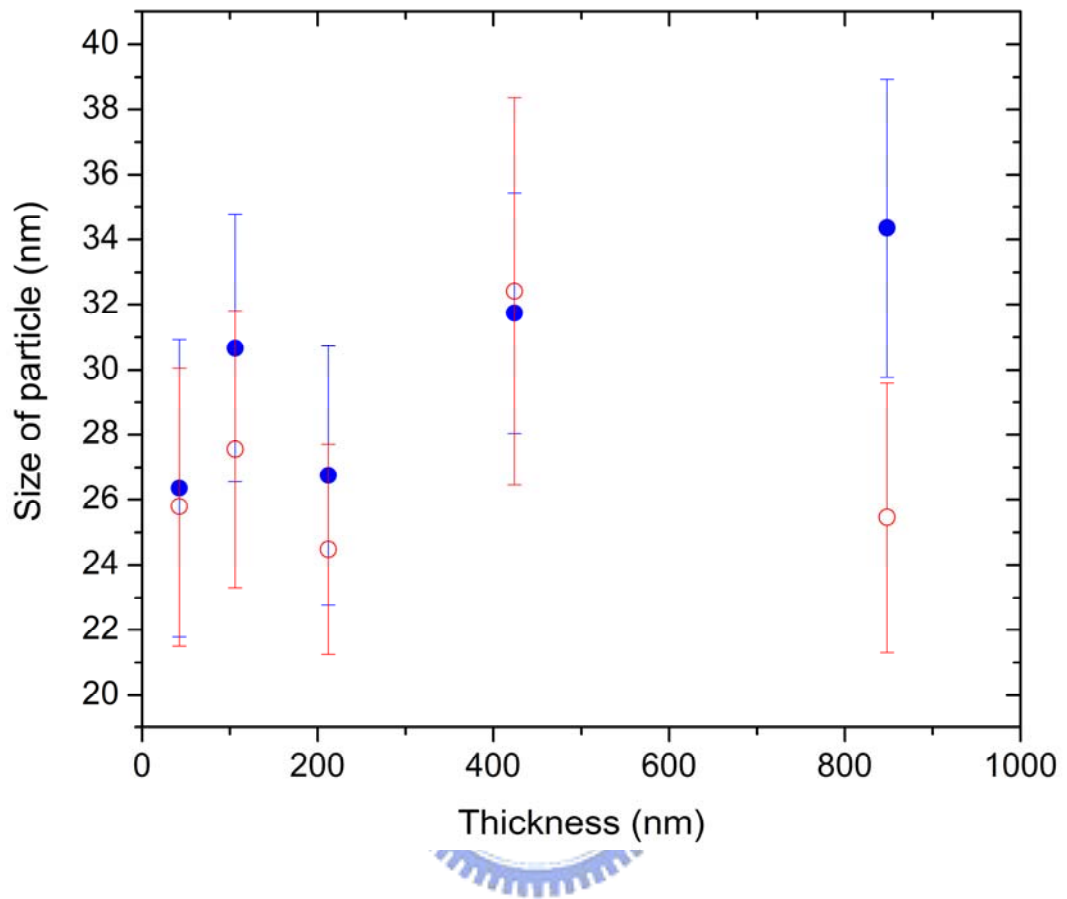


Figure 3.3.25 Thickness-dependence of particle size for as-sputtered (●) and annealed (○) γ -Fe₂O₃ films.

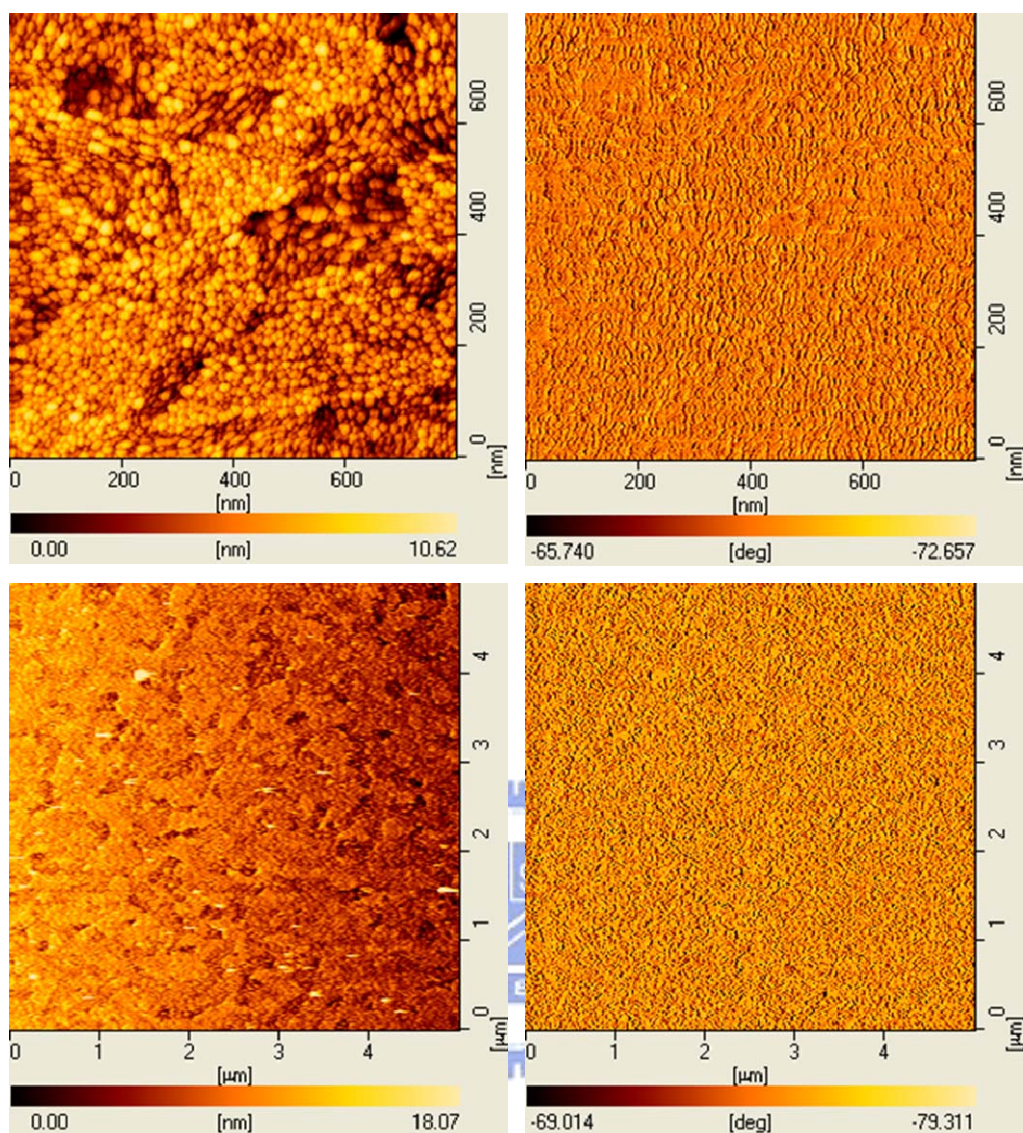


Figure 3.3.26 AFM images taken at two different positions on the γ -Fe₂O₃ film surface with coating time of 2 min and beam energy of 840 V.

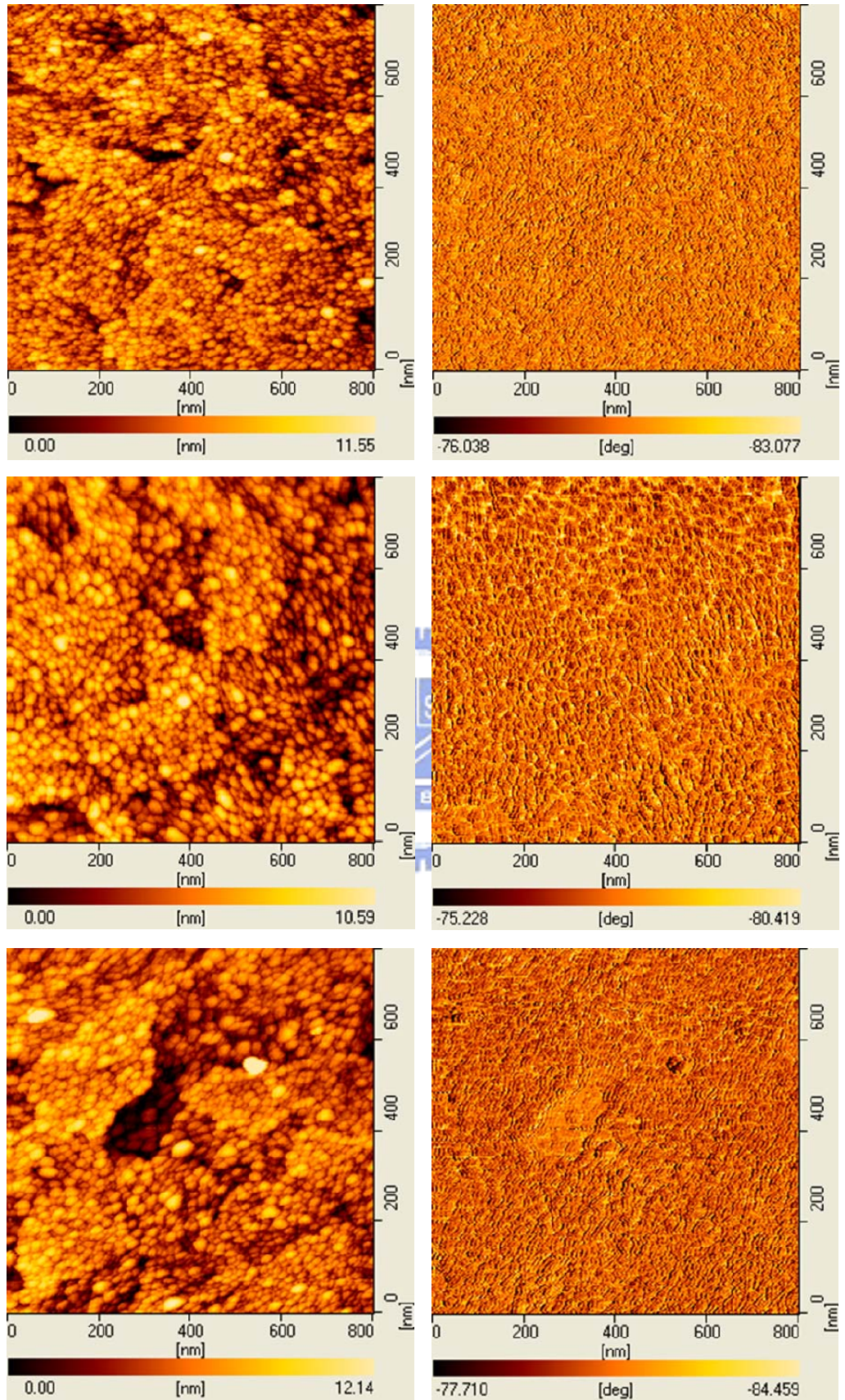


Figure 3.3.27 AFM images taken at three different positions on the γ -Fe₂O₃ film surface with coating time of 10 min and beam energy of 840 V.

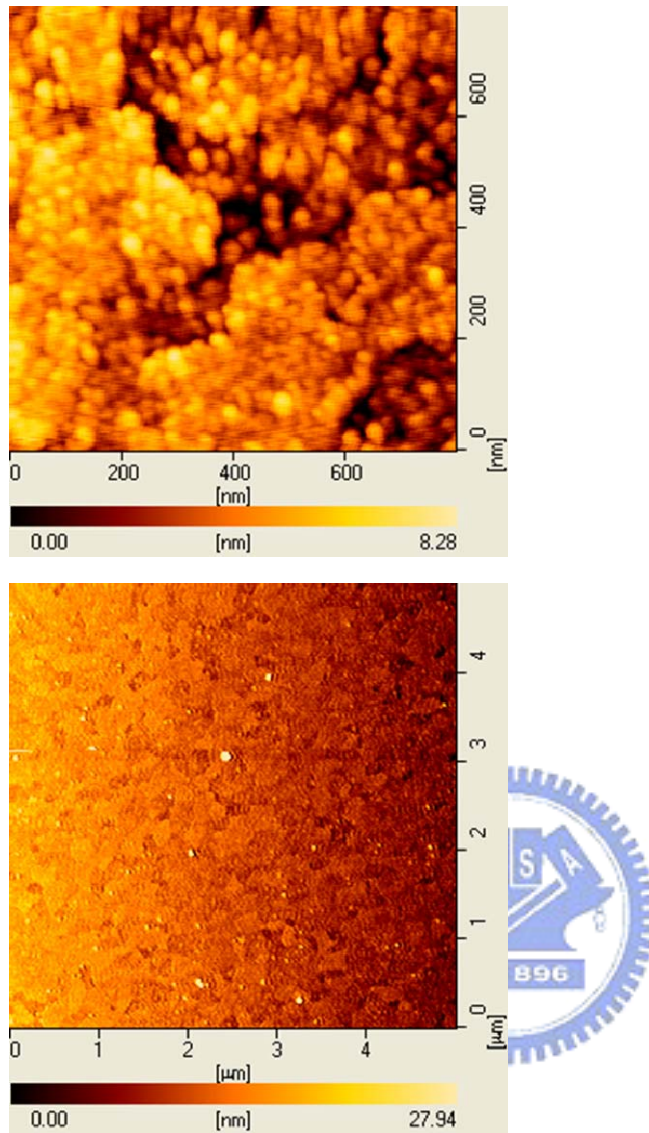


Figure 3.3.28 AFM images taken at two different positions on the annealed $\gamma\text{-Fe}_2\text{O}_3$ film surface with coating time of 2 min and beam energy of 840 V.

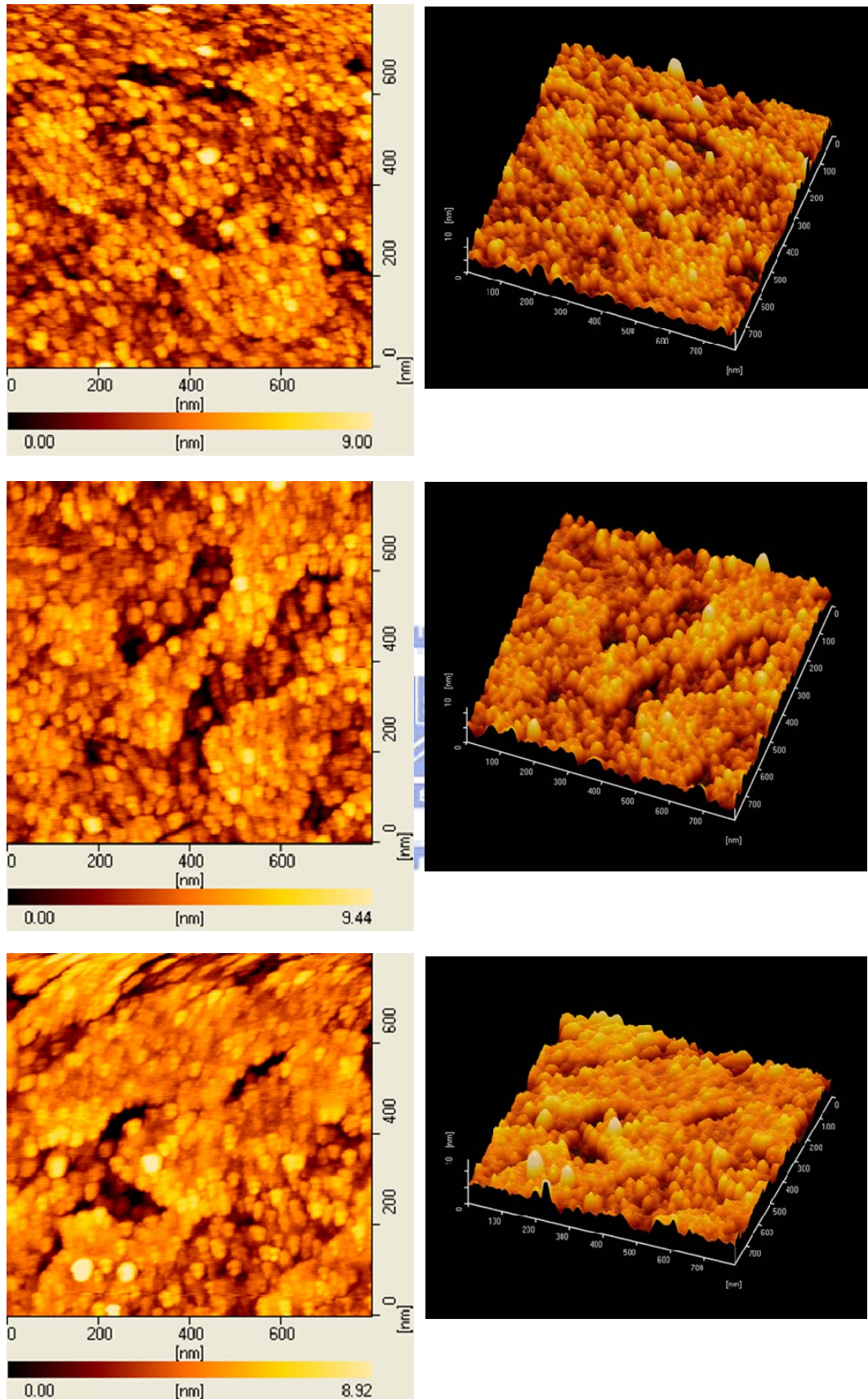


Figure 3.3.29 AFM images taken at three different positions on the annealed $\gamma\text{-Fe}_2\text{O}_3$ film surface with coating time of 10 min and beam energy of 840 V.

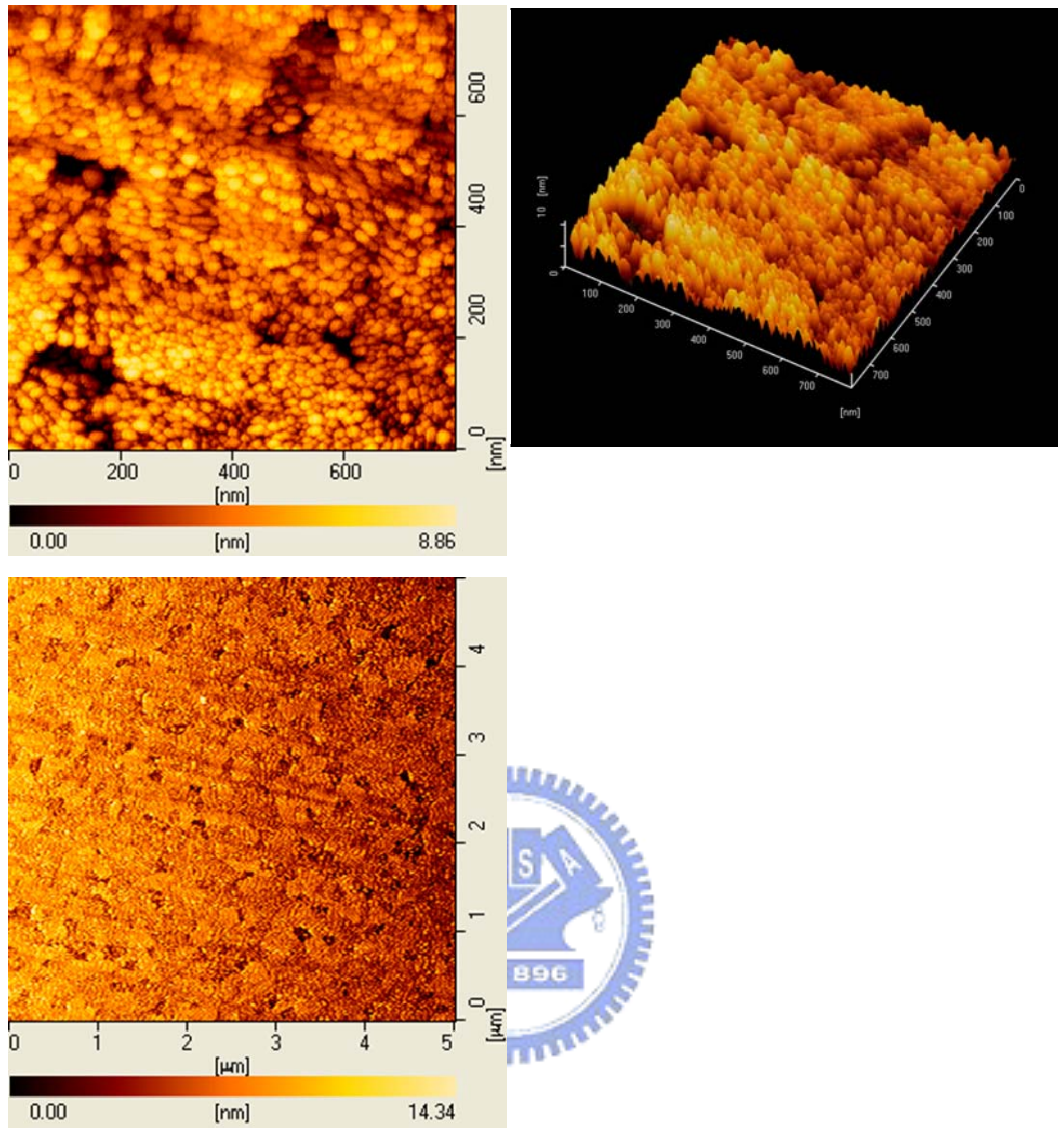


Figure 3.3.30 AFM images taken at two different positions on the $\gamma\text{-Fe}_2\text{O}_3$ film surface with coating time of 2 min and beam energy of 1400 V.

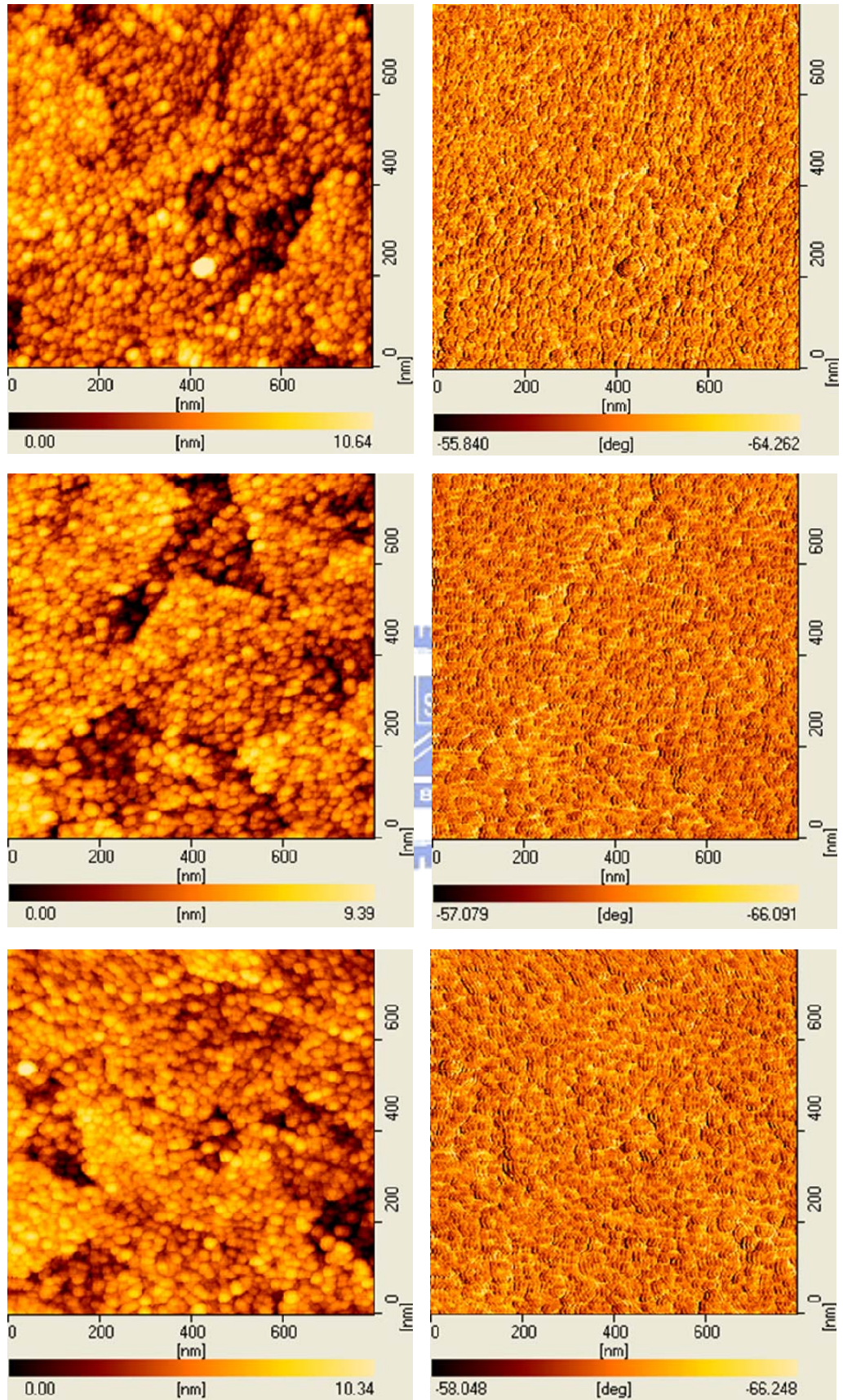


Figure 3.3.31 AFM images taken at three different positions on the γ -Fe₂O₃ film surface with coating time of 10 min and beam energy of 1400 V.

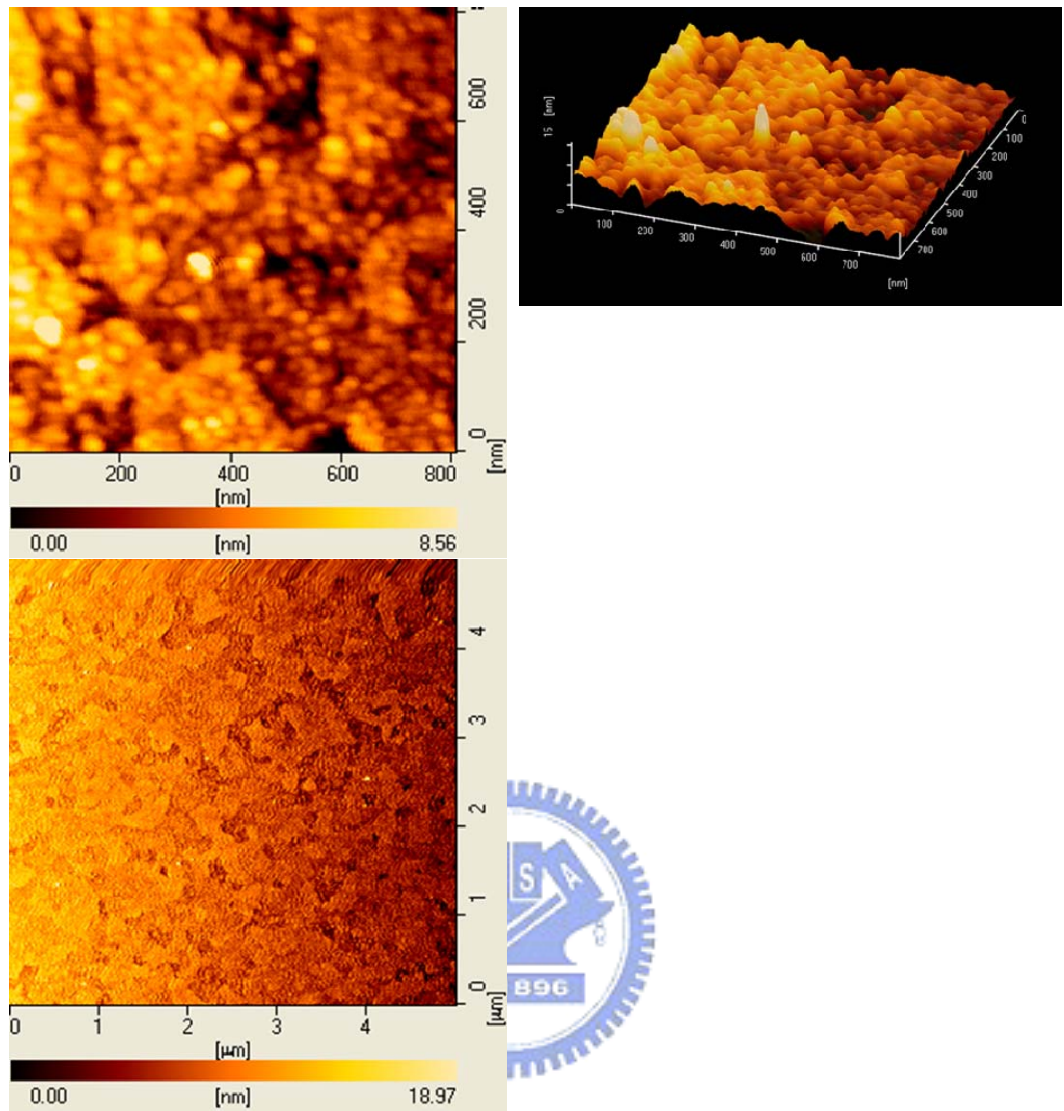


Figure 3.3.32 AFM images taken at two different positions on the annealed $\gamma\text{-Fe}_2\text{O}_3$ film surface with coating time of 2 min and beam energy of 1400 V.

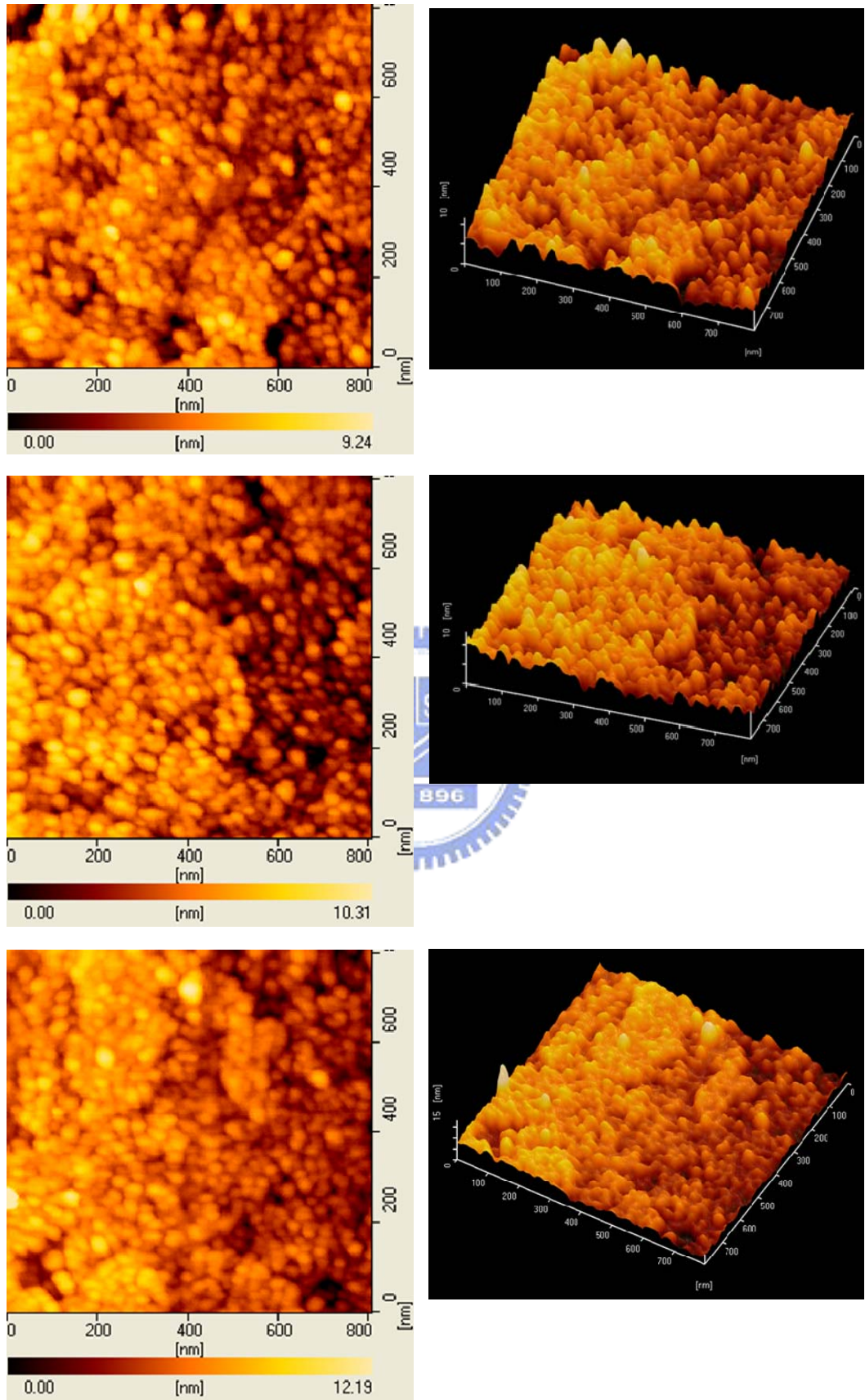


Figure 3.3.33 AFM images taken at three different positions on the annealed $\gamma\text{-Fe}_2\text{O}_3$ film surface with coating time of 10 min and beam energy of 1400 V.

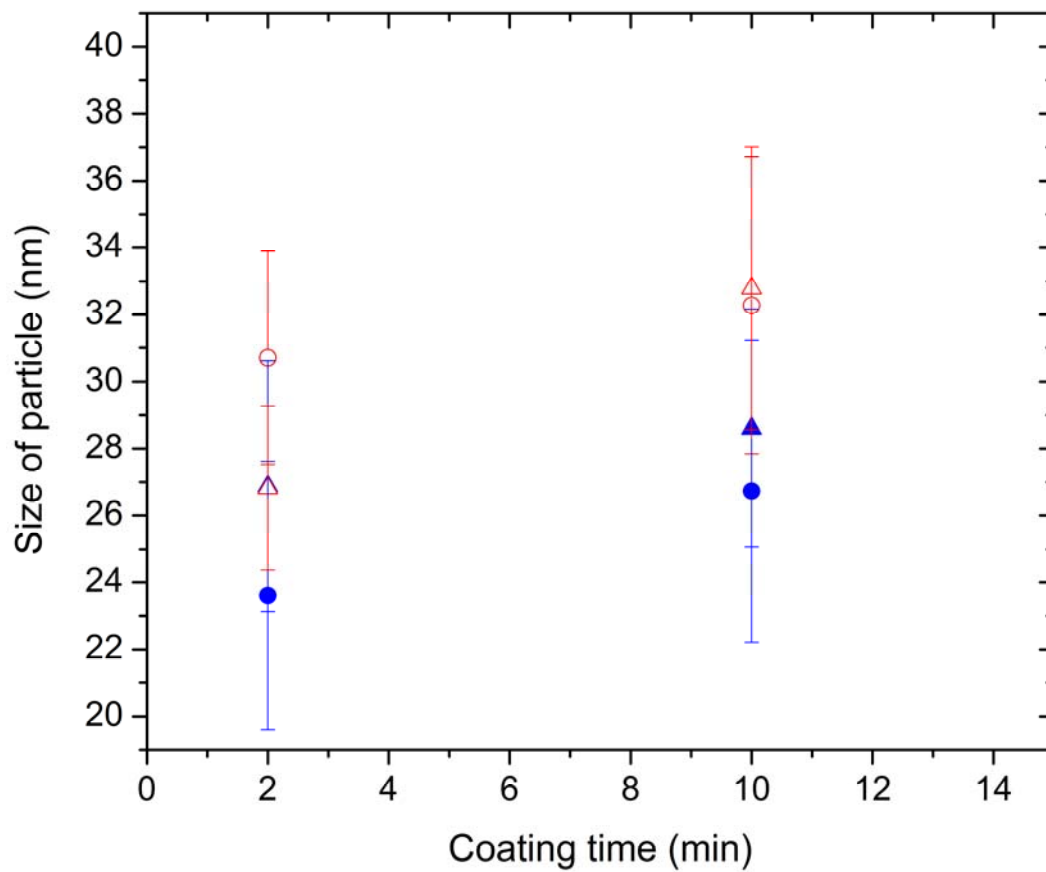
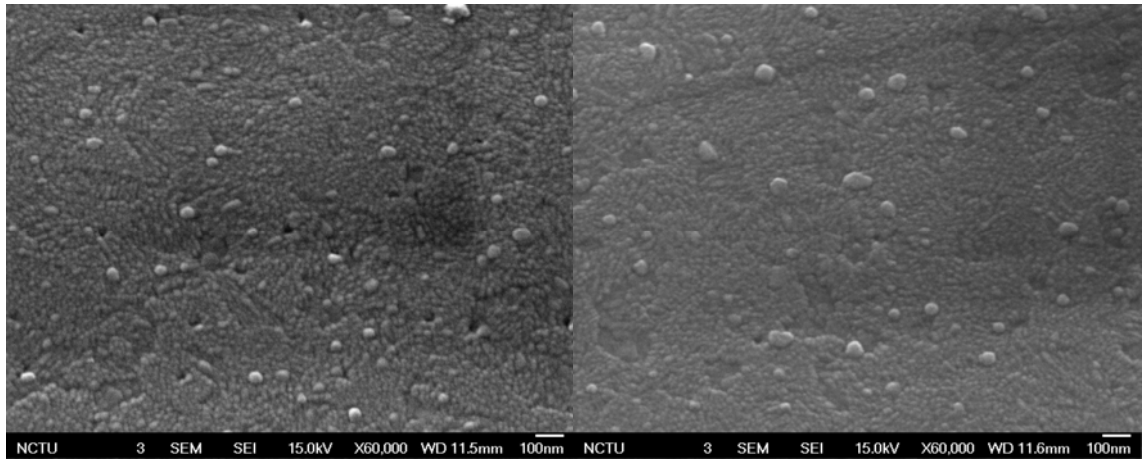
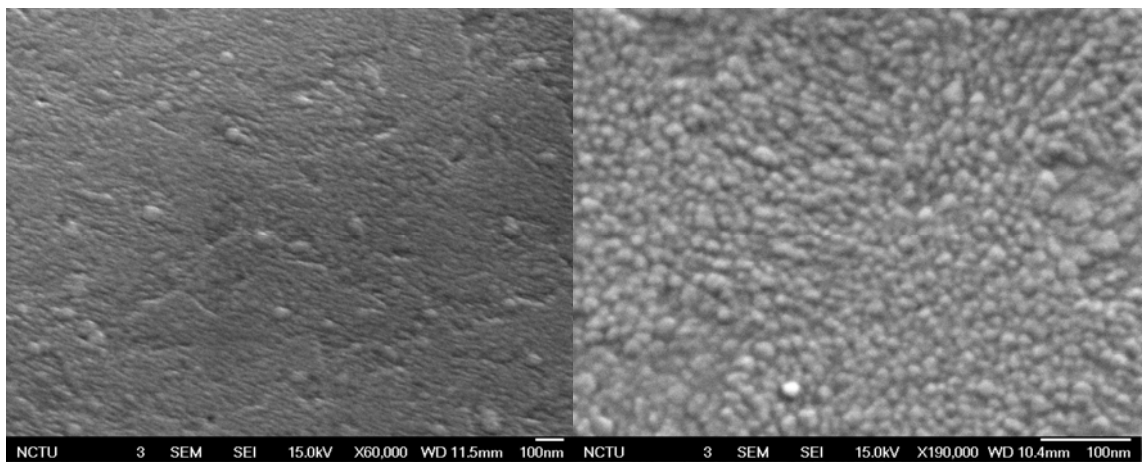


Figure 3.3.34 Thickness-dependence of size of particle for as-sputtered (solid) and annealed (open) γ -Fe₂O₃ films coated by beam energies of 840 V (circle) and 1400 V (triangle).



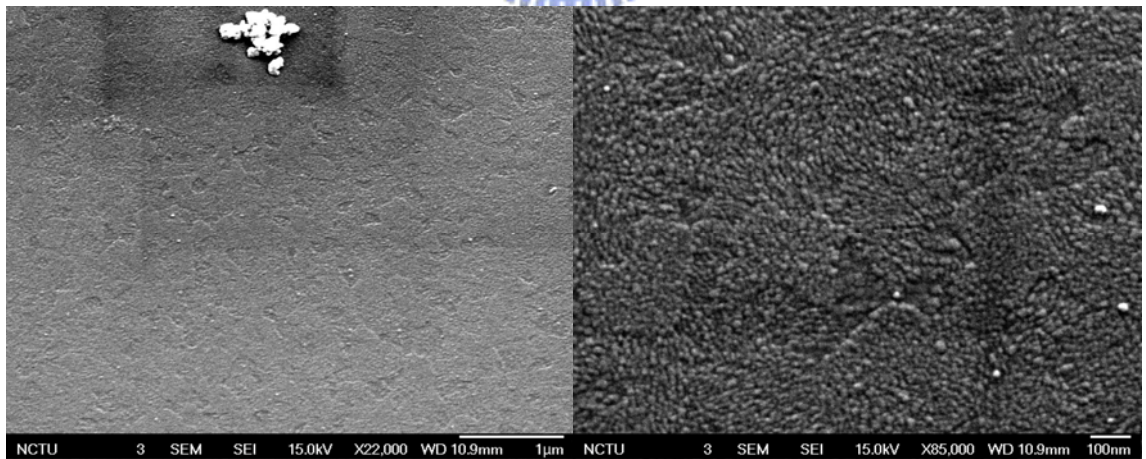
(a)

(b)



(c)

(d)



(e)

(f)

Figure 3.3.35 SEM images taken for $\gamma\text{-Fe}_2\text{O}_3$ films with thickness of (a) 106 nm (60,000X), (b) 318 nm (60,000X), and (c) 636 nm (60,000X), and $\gamma\text{-Fe}_2\text{O}_3$ films with thickness of (d) 212 nm (190,000X), (e) 424 nm (22,000X) and (f) 424 nm (85,000X) for 60-second thermal annealing.

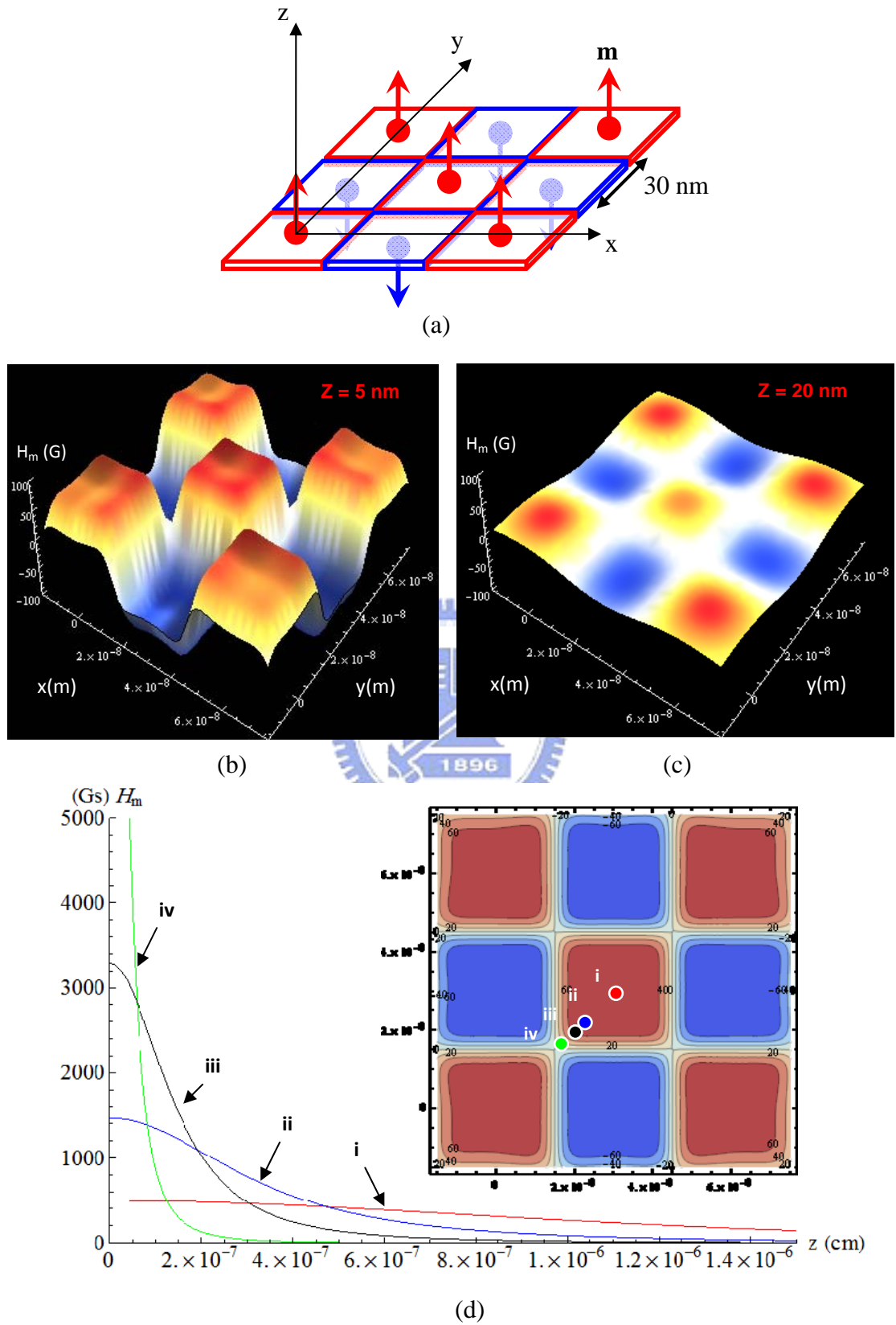


Figure 3.3.36 A simple model describing the spatial distribution of the induced magnetic field by the $\gamma\text{-Fe}_2\text{O}_3$ film: (a) imaginary surface structure; (b) $H_m(x, y)$ at $z = 5$ nm; (c) $H_m(x, y)$ at $z = 20$ nm; (d) $H_m(z)$ at different (x, y) .

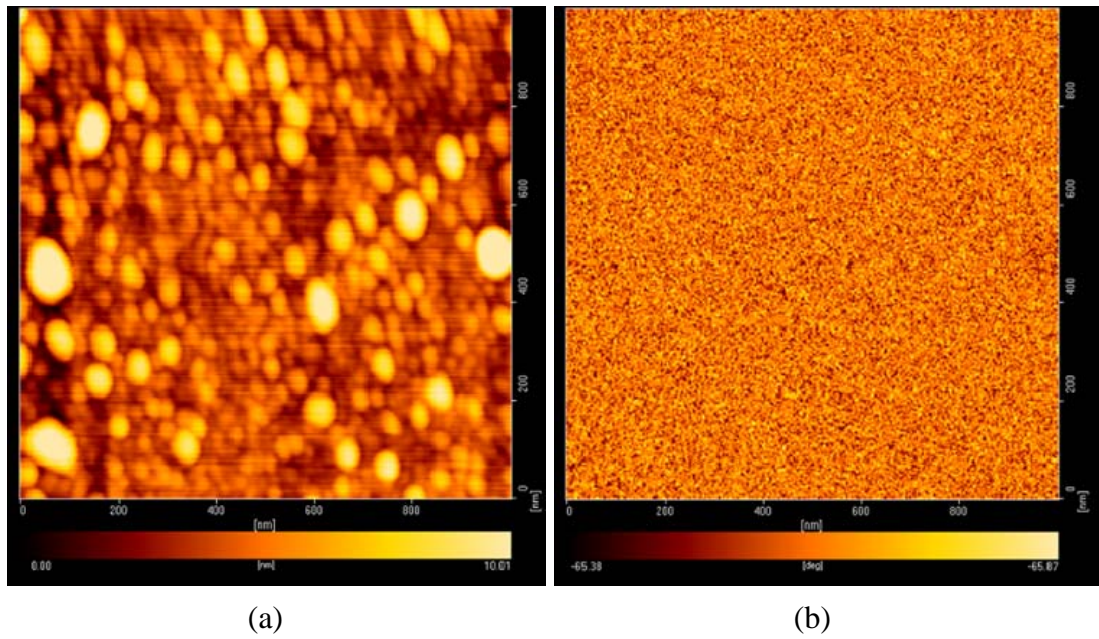


Figure 3.3.37 Surveyed images for $\gamma\text{-Fe}_2\text{O}_3$ film with 212 nm thick by (a) AFM and (b) MFM.



Tables

Table 3.3.1 Comparison of polar anchoring strength of the $\gamma\text{-Fe}_2\text{O}_3$ and DMOAP films.

| Liquid crystal | W_p (J/m ²) | | | |
|---|---------------------------|--|--|--|
| | DMOAP | $\gamma\text{-Fe}_2\text{O}_3$ 212 nm | $\gamma\text{-Fe}_2\text{O}_3$ 424 nm | $\gamma\text{-Fe}_2\text{O}_3$ 636 nm |
| MLC-6608 ($\Delta\varepsilon < 0$) | 7.1×10^{-5} | 1.1×10^{-4} | 7.9×10^{-5} | 4.8×10^{-5} |
| K15 ($\Delta\varepsilon > 0$) | 3.4×10^{-5} | 2.0×10^{-4} | – | – |

Table 3.3.2 Horizontal and vertical components of the magnetization induced by the $\gamma\text{-Fe}_2\text{O}_3$ films with different thickness. (Unit: emu/g)

| Thickness (nm) | M_{net} (\perp) | M_s (\perp) | M_{net} (\parallel) | M_s (\parallel) |
|----------------|------------------------------|-------------------|----------------------------------|-----------------------|
| 106 | – | – | 0.004/0.006 | 0.433/0.476 |
| 212 | 0.084 | 0.943 | – | 0.259 |
| 424 | 0.035 | 0.259 | 0.013 | 0.094 |
| 636 | 0.013 | 0.156 | 0.005 | 0.055 |

Table 3.3.3 Magnetization of the $\gamma\text{-Fe}_2\text{O}_3$ films with or without thermal annealing. (Unit: emu/g)

| Thickness (nm) | Before annealing | | After annealing | |
|-------------------|-----------------------|----------------------------------|------------------------------|----------------------------------|
| | M_s (\parallel) | M_{net} (\parallel) | M_s (\parallel) | M_{net} (\parallel) |
| 106 | 2.505 | 0.026 | unsaturated (1.731) | 0.066 |
| 212 | 0.298/0.246 | 0.009/0.036 | unsaturated (9.610/12.16) | 0.216/0.594 |
| 424 | 0.226 | 0.015 | – | – |

Chapter 4

Liquid Crystal Alignments on the Fluorinated Copolymer Films Treated by Ion Beam Bombardment and Ultraviolet Irradiation

4.1 Overview

Recently, a copolymer 4-(N-methacryloylamino)phenyl methacrylate with 2,2,3,3,-4,4,5,5-octafluoropentylmethacrylate (MAPhM-F8) with a structure as shown in Fig. 4.1.1 was developed jointly by the Syromyatnikov's group from Taras Shevchenko Kyiv National University of Ukraine, Yaroshchuk's group from Institute of Physics of NASU of Ukraine, and Lee's group from the Industrial Technology Research Institute, Taiwan [1,2]. A good photo-stability is found due to its high transparency in the visible and near ultraviolet (UV) spectral range. The 4-(N-methacryloylamino)phenyl methacrylate containing O- and NH-methacryloyl groups leads this compound to be thermally stable and capable of photo-crosslinking. A gradual change of pretilt angle from planar to vertical alignment is promoted by copolymerization of methacrylic monomers with fluorinated fragments of different concentrations or lengths in polymer. In this study, we study the alignment properties of nematic liquid crystal (NLC) on this fluorinated copolymer films treated by two different noncontact methods using the linearly polarized UV light (LPUVL) irradiation and argon ion beams (IB) bombardment. The surface-sensitive x-ray photoemission spectroscopy (XPS) studies have been carried out to evaluate the chemical compositions of the film surfaces. Furthermore, the surface energies of the treated films measured by using contact angle method are compared with the results from XPS analyses to find out the underlying mechanism.

4.2 Experiments

To understand the mechanism dominating the influence of the fluorinated carbonyl groups on the growth of pretilt angle, three MAPhM films copolymerized with different

mole fraction of F8 side chain including 0, 1/2, and 2/3 are used in this work and labeled as X_0 , $X_{1/2}$, and $X_{2/3}$, respectively. Before polymer coating, each substrate have to be cleaned using a standard process shown in the flowchart of Fig. 2.3.1. The indium-tin-oxide coated glass substrates with size of 20 mm \times 10 mm are spin coated with these copolymer MAPHM-F8 after cleaning process. The spin rate is 500 rpm for the first 5 seconds and 2000 rpm for the 20 seconds afterward. The substrates are then pre-baked at 90°C for 10 minutes and cured at 150°C for another half hour.

4.2.1 Surface treatments

After the thermal treatment, the copolymer films are then treated by the LPUVL irradiations and IB bombardments separately. For photo-alignment, the LPUVL is obtained from a 1000W Xenon arc lamp (Model 6269 Oriel) through a liquid filter, a convex lens and a Glan-Taylor prism in sequence. The schematic view of the setup is shown in Fig. 4.2.1. The liquid filter is designed to absorb the infrared radiation lying below the red end of visible spectrum. The intensity of the LPUVL irradiation is enhanced by focusing the light beam on the sample area using the convex lens. The photo-induced alignment is accomplished with a two-step irradiation process, which includes a linearly-polarized exposure with intensity of 2.4 mW/cm² at first and then an unpolarized UV light exposure with intensity of 12.7 mW/cm² for another 1 min to remove the degeneracy of the pretilt angle. The incidence angle of UV light is 45° throughout the process.

For ion beam bombardment, we employ a direct-current (dc) diode-type ion beam sputter (model IB-2 from EIKO Engineering Co., Ltd.) as described in Chap. 2 (see Figs. 2.2.1 and 2.2.2). The sputter is operated with etching mode, the bottom electrode acts as the cathode. The substrates are etched by ion beams from induced glow discharge near the top electrode. With an attached sample holder, the incidence angle, bombarding time, current density and the energy of ions are all controllable parameters in our system. The parameters such as the incidence angle θ_{ion} , the ion current density J_{ion} and the direct-current bias V_b between the electrodes are fixed at 60°, 255 μ A/cm², and 560 V, respectively. Before starting the ion-beam process, the chamber is pumped down to a base pressure of 30 mTorr and then the argon gas is fed to a target pressure of 120

mTorr.

4.2.2 Sample preparation

For the alignment characterization, two equally treated substrates are assembled with a 23 μm Mylar spacer in between with anti-parallel alignment direction to form an empty cell. The NLC 4'-n-pentyl-4-cyanobiphenyl (5CB, Merck) with a nematic range between 24.0°C and 35.3°C is then filled into the empty cell.

4.2.3 Alignment characterization

After annealing of the LC cells, the alignment direction and uniformity of each cell is checked by looking with a pair of crossed polarizers. The pretilt angle of 5CB molecules near the surface is measured by using the crystal rotation method [3].

4.2.4 Surface analyses

To clarify the relation between the surface energy and the induced alignment properties of the treated films, the contact angle measurements have also been carried out. The polar, dispersive, and total surface energy are evaluated according to the Owens-Wendt method [4]. In this method, the surface energy of a solid γ_s can be resolved into a dispersion and a polar component denoted as γ_s^d and γ_s^p , respectively, by

$$1 + \cos\theta = \frac{2}{\gamma_l} \left(\sqrt{\gamma_l^d \gamma_s^d} + \sqrt{\gamma_l^p \gamma_s^p} \right),$$

where θ is the contact angle, γ_l is the surface tension of the liquid which is in contact with the solid surface, $\gamma_l = \gamma_l^d + \gamma_l^p$ and $\gamma_s = \gamma_s^d + \gamma_s^p$. Two liquids, water and glycerol, are used in the contact angle measurements and their surface energies, $\gamma_{water}^d = 21.8 \text{ mJ/m}^2$, $\gamma_{water}^p = 51.0 \text{ mJ/m}^2$, $\gamma_{glycerol}^d = 37.0 \text{ mJ/m}^2$, $\gamma_{glycerol}^p = 26.4 \text{ mJ/m}^2$ are obtained from the literature [5].

The surface-sensitive x-ray photoemission spectroscopy (XPS, PHI-1600 from Physical Electronics, Inc.) studies have been carried out to evaluate the chemical compositions of the treated film surfaces. More description about the XPS we used has been given in Sec. 2.3.3. Only the Mg K α line is used in this work.

4.3 Results and discussion

The effect of treating time for LPUVL irradiation and IB bombardment on the MAPHM-F8 films with different concentrations of fluorinated carbonyl group will be discussed in this section.

4.3.1 Alignment characterization

Figure 4.3.1 shows the photographs of 5CB cells taken with crossed polarizers in the dark state. Those cells are aligned by X_0 , $X_{1/2}$, and $X_{2/3}$ films treated with LPUVL irradiation and IB bombardment. Effective alignments of LCs are given by both UV and IB treated surfaces. However, a significant amount of defects is shown up in the UV-treated cells. The amount of defect seems to be related to the concentration of fluorinated carbonyl group F8. Also, a higher dosage can largely decrease the defects.

According to the measured pretilt angles, as plotted with the exposure time in Fig. 4.3.2, remarkably, the highest pretilt angle induced by IB treatment is still much smaller than that induced by the LPUVL-irradiated surfaces. The pretilt angle also increases with the fluorine content of polymer film. The results also show that the largest pretilt angle is achieved in about 5 min for both alignment methods. Longer treatment time will reduce the pretilt angle. The error bar in Fig. 4.3.2 is obtained by averaging the measured values over different positions on the surface.

4.3.2 XPS analyses

In the XPS studies for the treated films, we first survey scan over all the spectrum range with a step size of 1 eV and the analyzer pass energy of 117.4 eV. Figures 4.3.3 and 4.3.4 show the survey spectra of the IB-treated and LPUVL-treated $X_{2/3}$ surfaces, respectively. The analysis for each involved element reveals that the fluorine (F) content on the IB-treated surface is drastically decreased no matter how short the treatment takes. For both the $X_{1/2}$ and $X_{2/3}$ films, as shown in Fig. 4.3.5, the reaction between oxygen and dangling bond induced by ion beam bombardment causes the significant increasing to oxygen content. However, no apparent change in the content of fluorine

and oxygen is found on the LPUVL-irradiated surface, which suggests that the photo-crosslinking dominates the photoreaction mechanism as mentioned in Vretik et al.'s work [1]. In addition, a small amount of iron element appears on the treated surface. It has been confirmed in Chap. 2 that they are sputtered from the electrode if the IB energy is high enough [6].

For the $X_{2/3}$ film, the further scan with multiplex mode about C_{1s} and F_{1s} peaks are accomplished with a step size of 0.2 eV and the analyzer pass energy of 46.95 eV, as shown in Fig. 4.3.6. Notice that the intensity of the peak at 290.9 eV corresponding to the CF_2 bond decreases after surface treatments. Figure 4.3.6(a) shows that the significant reduction of intensity is not observed until the LPUVL treatment lasts over 10 min (2.52 J/cm^2). Contrarily, the grafted fluorinated groups in the F8 monomer are mostly destroyed in the IB treatment even though the treatment duration is only 2 min, as shown in Fig. 4.3.6(b). The same behavior is also found in the F_{1s} spectrum, as shown in Fig. 4.3.6(c). The contribution of CF bond at 687.6 eV to the overall signal becomes significant for 10 min LPUVL treatment.

For core-level C_{1s} spectrum, it is convoluted by six main signals, C-C/C-H (284.56 eV), C-N (285.68 eV), C-O-C (286.29 eV), N-C=O (288.6 eV), O-C=O (287.7 eV), and F-C-F (290.7 eV) before surface treatment. Once the surface is treated by IB bombardment or a long-term LPUVL irradiation, the C-F (289.5 eV) bond is then formed due to the destruction of the CF_2 bond. The deconvoluted intensity of each signal for X_0 , $X_{1/2}$, $X_{2/3}$ films has been summarized in Tables 4.3.1, 4.3.2, and 4.3.3, respectively.

Furthermore, we plot the pretilt angle against CF_2/C ratio for all the samples with various treating times and mole fraction of fluorinated side chain, as shown in Fig. 4.3.7. Linear variation is found approximately in the logarithm-scaled pretilt angle as a function of CF_2/C ratio for the LPUVL-irradiated surfaces. The points for IB-treated surfaces basically follow this line only a little lower. The difference is possibly due to the drastic destruction to the photoactive group MAPHM by IB bombardments and the following re-oxidization of dangling bonds. This speculation will be further verified later. Despite the possibility of other mechanisms in determining the pretilt angle has not been excluded yet, we still can make sure that the role of CF_2 group for high pretilt

angle is essential.

4.3.3 Surface free energy

The results of our surface energy measurement are plotted against the exposure time as shown in Fig. 4.3.8. Without the surface treatments, the surface energies of X_0 , $X_{1/2}$, and $X_{2/3}$ polymer films are given as 45.4, 33.1, and 29.1 mJ/m^2 , respectively. As expected, a lower surface energy corresponding to a higher pretilt angle is owing to a higher content of fluorinated fragment in a polymer film. After surface treatments, an apparent increase of the surface energy is found for the IB-treated films, while it is unchanged for the LPUVL-treated films. These results also suggest that the IB treatment reduces the fluorine content in the films. It is also worth to notice that no significant anisotropy of surface energy is found in our samples treated by either method.

It is known that the LC alignment mode is ascribed to the competition between the surface tension of solid surface γ_s and LC molecules γ_{LC} mentioned in Creagh et al.'s work [7]. They concluded that a homeotropic alignment of LC is obtained if $\gamma_{LC} > \gamma_s$, otherwise, a homogeneous alignment occurs. Even though this conception is suitable for our case, this model is not absolutely correct without exceptions demonstrated by Uchida et al. [8].

We have plotted the pretilt angle as a function of surface energy in Fig. 4.3.9. The open and solid circles represent the samples treated by LPUVL irradiation and IB bombardment, respectively. The surface energy of an as-deposited X_0 film is marked with a dash line. As described in the literature, the incorporation of fluorine in a polymer film generally causes the polymer to have a lower surface energy [9]. Considering the fluorine effect only, the reduction of fluorine element cannot cause the surface energy to be higher than 45.4 mJ/m^2 of an as-deposited X_0 film. However, a remarkable increase of oxygen content after IB bombardment is also deduced, which can explain the extra increase of surface energy. In Fig. 4.3.9, the oxygen content is also plotted, an increasing linear relation with the surface energy is observed. Since the bond-breaking process is dominant in the IB treatments, it is expected that many dangling bonds are created. Then, the content of C=O carbonyl group increases due to the re-oxidization of these dangling bonds. These newly formed polar groups can cause

an increase on surface energy particularly in the dipole-dipole interaction.

The polar and dispersion components of surface energy are plotted in Fig. 4.3.10 as a function of pretilt angle in logarithm scale. The decreasing in surface energy with the pretilt angle is obvious, while the dispersion surface energy γ_s^d is essentially unchanged. We can conclude that the polar force contribution to the surface tension plays a dominant role in determining the pretilt angle. This relation had previously been described by Ban et al. in their work [10]. Therefore, the speculation through XPS analyses is further confirmed by surface energy measurements.

4.3.4 Depth-dependence of fluorine content

Furthermore, depth analyses of XPS have also been accomplished for 1 min, 10 min LPUVL-treated and as-deposited X_{2/3} films. The measured atomic ratio for C, O, N, and F are 37.0, 18.0, 3.3, and 41.7 %, respectively, for an as-deposited X_{2/3} film. However, compare with the calculated values, more fluorine content about 9.0 % is found on the surface. It reveals that the fluorine side chains predominantly move to the film surface.

The depth-dependencies of C, O, N, and F content in the LPUVL-irradiated X_{2/3} films with treating time of 1 min and 10 min are shown in Fig. 4.3.11(a) and Fig. 4.3.11(b), respectively. It reveals that the film surface is stacked with an excess amount of fluorinated group F8. This phenomenon especially occurs in the as-deposited MAPHM-F8 film. However, the fluorine content on the surface decreases after 10 min irradiation and additionally the depth-dependence is reduced. The excess CF₂ grafted side chain seems to move away from the surface. The depth-dependence of fluorine contents for 1 min- and 10 min-treated X_{2/3} films are plotted together in Fig. 4.3.12(a) for comparison. The black dash dot line points out the ideal content of fluorine in as-deposited X_{2/3} film. The content averaged over the whole measuring depth is also marked by the blue and red dash dot lines for 1 min- and 10 min-treated films, respectively. It should be noticed that the signals are acquired in only four depths by XPS measurement. Therefore, the fitted curve shown in Fig. 4.3.12(a) is used to calculate the mean content of the LPUVL-treated film. Two mean values of 24.7 and 27.1 are obtained and indicated by the blue and red dash dot lines. An approach to the

ideal value of F content is found in extending the irradiation time of LPUVL. Figure 4.3.12(b) shows the depth-dependence of CF_2 content for the same considered films. It reveals a similar variation with depth.

We have carried out a calculation basing on a straightforward idea mentioned above to explain the measured result. Different amount of F8 monomer with depth-dependence is assumed for each MAPHM-F8 film with treating time of 0 min, 1 min, and 10 min, as shown in Fig. 4.3.13(a), but the total amount in each film remains the same. That means the fluorinated carbonyl groups are diffused back into the film after LPUVL irradiation. For simplicity, we only consider five layers here. Figure 4.3.13(b) shows the resultant F content in each layer. A similarity between the simulated and experimental results suggests that the preliminary idea is workable.

According to the results about LC alignment presented in Sec. 4.3.1, a better quality but smaller pretilt are obtained from the reduction of fluorine content on the surface, as shown in Fig. 4.3.1. Obviously, the dosage of LPUVL by 10 min-irradiation is still not enough for stabilizing the aligning ability of fluorinated surface. It has been confirmed that a major peak of LPUVL at wavelength of 256 nm shown in the absorption spectrum of MAPHM-F8 film has a power density as small as $9.8 \mu W/cm^2$. The observation of pretilt angle for each LC cell has been carried out over 1 month to confirm this speculation, as shown in Fig.4.3.14. As a result, we deduce that an additional dosage is required for the MAPHM-F8 film with higher mole fraction of F8 group to accomplish the photo-crosslinking of MAPHM groups. The crosslinking process can reasonably enhance the uniformity and stability of chemical structure and further reduce the depth-dependence of chemical composition.

It is also worthy to be noticed that no depth-dependence is found in ion beam treatment even for 2 min duration, which suggests the re-coverage of sputtered materials on the surface.

4.4 Concluding remarks

The alignments properties and the mechanism related to high pretilt angle of a newly developed fluorinated copolymer film MAPHM-F8 treated by LPUVL irradiation

and IB bombardment are demonstrated in this work. A saturated pretilt angle about 34° is achieved on the LPUVL-irradiated $X_{2/3}$ film surface with dosage of 0.9 J/cm^2 . The photodecomposition becomes significant in the LPUVL treatments with dosage approximately higher than 1.6 J/cm^2 . However, the ion beam treatment reduces both fluorine content and the pretilt angle drastically. This is because that the bond-breaking reaction still dominates in the ion beam bombardments. The newly formed C=O carbonyl groups due to the re-oxidization cause a dramatic increase of polar surface energy. For MAPHM-F8 copolymer, the photo-crosslinking, through the XPS analysis, has been found dominating in the LPUVL irradiation. Furthermore, we have confirmed that the content of fluorinated groups CF_2 grafted in the F8 side chains plays a dominant role in determining the pretilt angle. The polar component of the surface tension in turn dominates the pretilt angle in this study. It is also observed that the fluorinated carbonyl side chains are preferentially clustered at the surfaces. The fluorine content on the surface decreases after 10 min irradiation and additionally the depth-dependence is reduced. That is, the excess CF_2 grafted side chain seems to be diffused back into the film. It is expected that the depth-dependence of F content should be eliminated and an approach to the ideal amount without depth issue is observed after a long-term irradiation of LPUVL. Finally, we deduce that an additional dosage is required for the MAPHM-F8 film with higher mole fraction of F8 group to accomplish the photo-crosslinking of MAPHM groups. The crosslinking process can reasonably enhance the uniformity and stability of chemical structure and further reduce the depth-dependence of chemical composition.

References

1. L. Vretik, V. Syromyatnikov, V. Zagniy, L. Paskal, O. Yaroshchuk, L. Dolgov, V. Kyrychenko, and C.-D. Lee, *Mol. Cryst. Liq. Cryst.* 479, 121 (2007).
2. L. Vretik, L. Paskal, V. Syromyatnikov, V. Zagniy, O. Savchuk, L. Dolgov, O. Yaroshchuk, and C.-D. Lee, *Mol. Cryst. Liq. Cryst.* 468, 173 (2007).
3. T. J. Scheffer and J. Nehring, *J. Appl. Phys.* 48, 1783 (1977).
4. D. K. Owens and R. C. Wendt, *J. Appl. Polym. Sci.* 13, 1741 (1969).
5. H. J. Busscher and J. Arends, *J. Colloid Interface Sci.* 81, 75 (1981).
6. H. Y. Wu and R. P. Pan, *Appl. Phys. Lett.* 91, 074102 (2007).
7. L. T. Creagh and A. R. Kmetz, *Mol. Cryst. Liq. Cryst.* 24, 59 (1973).
8. T. Uchida, K. Ishikawa, and M. Wada, *Mol. Cryst. Liq. Cryst.* 60, 37 (1980).
9. B. Ameduri and B. Boutevin, *Well-Architected Fluoropolymers: Synthesis, Properties and Applications*, (Elsevier, Amsterdam, 2004).
10. B. S. Ban and Y. B. Kim, *J. Appl. Polym. Sci.* 74, 267 (1999).



Figures

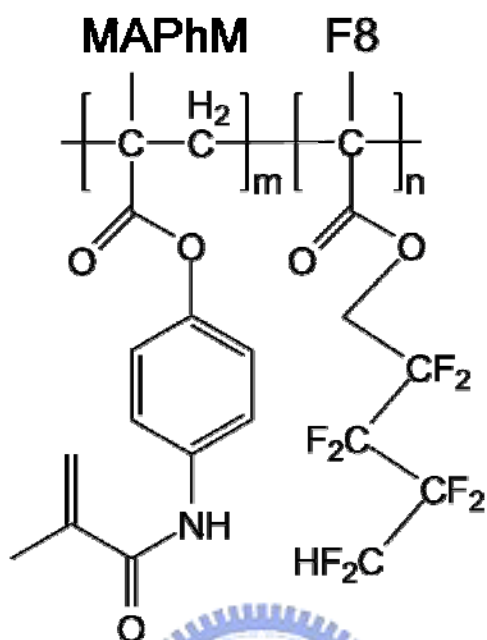


Figure 4.1.1 Chemical structure of the fluorinated polymer MAPHM-F8.

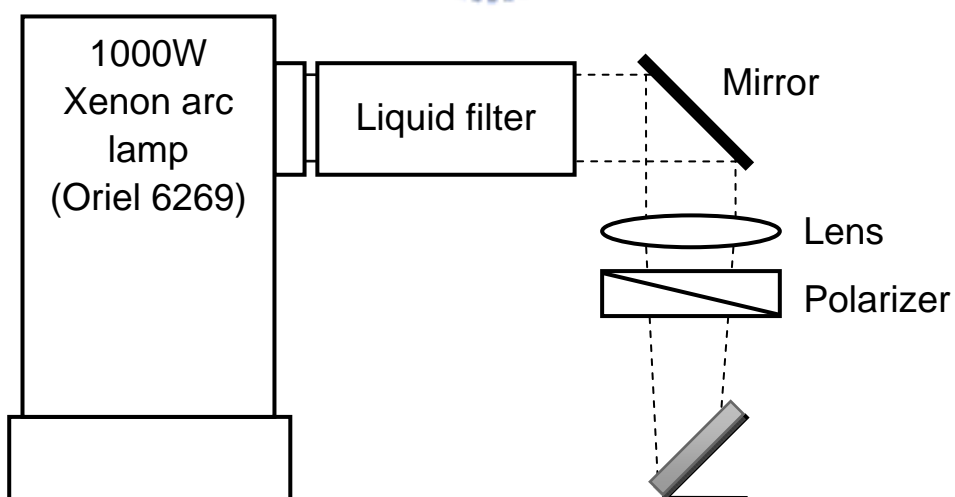


Figure 4.2.1 Schematic diagram of the LPUVL irradiation system.

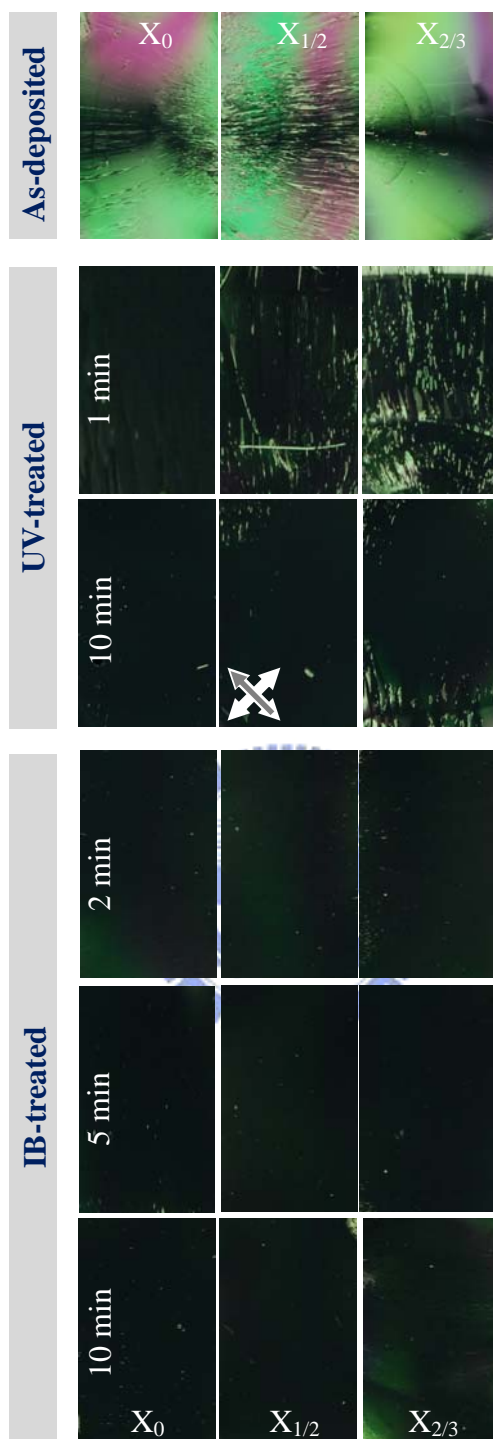


Figure 4.3.1 Photographs of 5CB cells taken with crossed polarizers in the dark state. The cells are aligned with surface-treated x_0 , $x_{0.5}$, and $x_{0.67}$ films by LPUVL irradiation and IB bombardment.

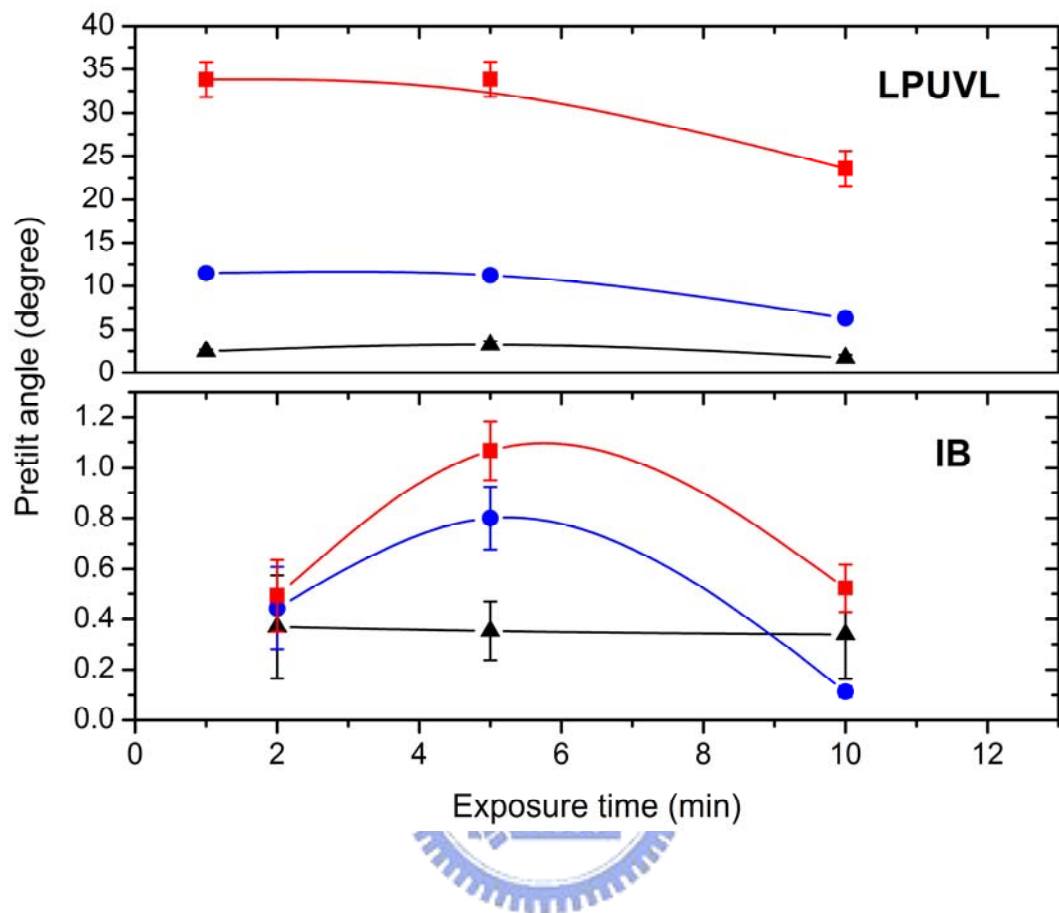


Figure 4.3.2 Pretilt angle of LC cells with MAPHM-F8 films, X_0 (▲), $X_{1/2}$ (●), and $X_{2/3}$ (■), treated by LPUVL irradiations and IB bombardments for different exposure times.

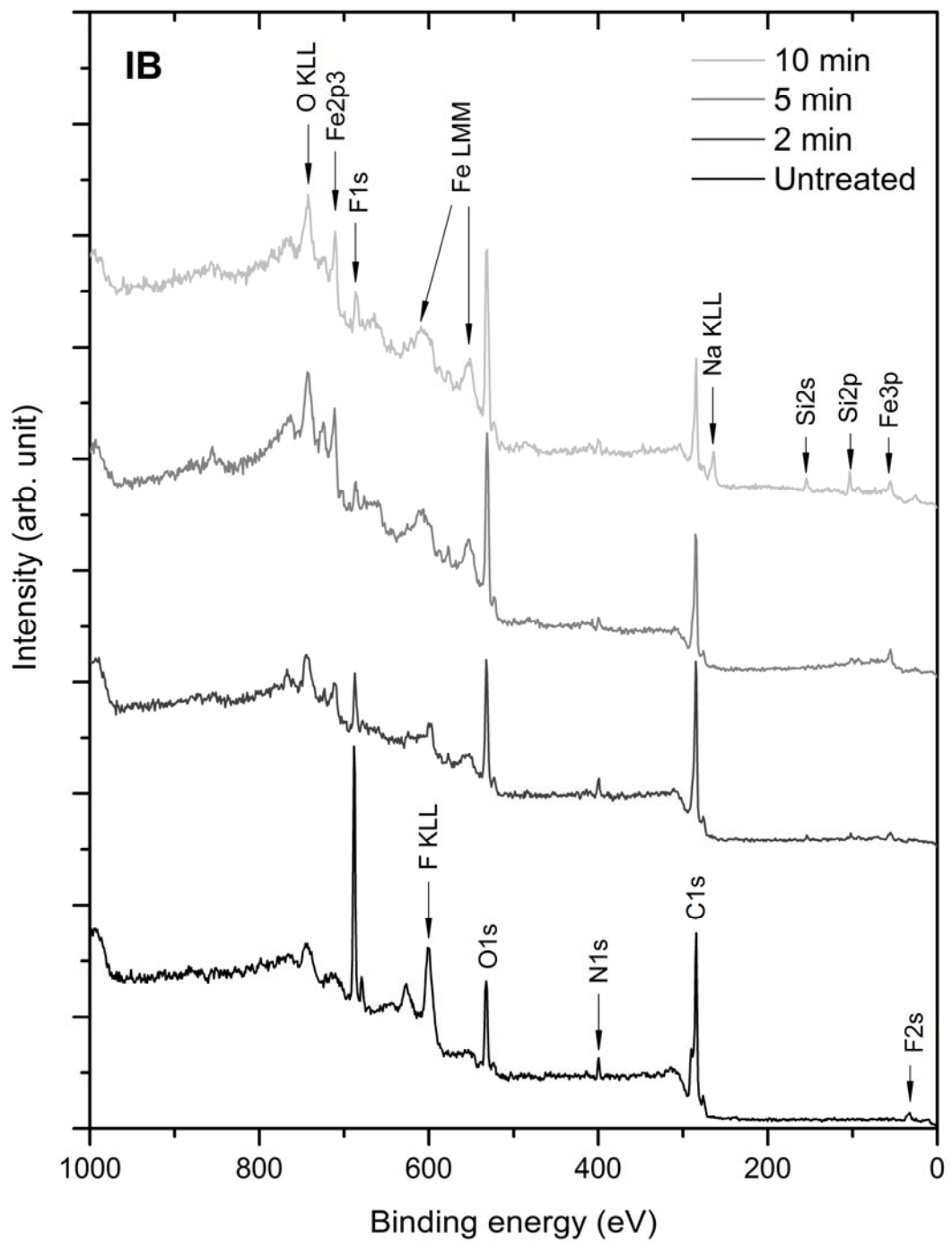


Figure 4.3.3 Survey spectra for the untreated and IB-treated $X_{2/3}$ films with different bombarding times.

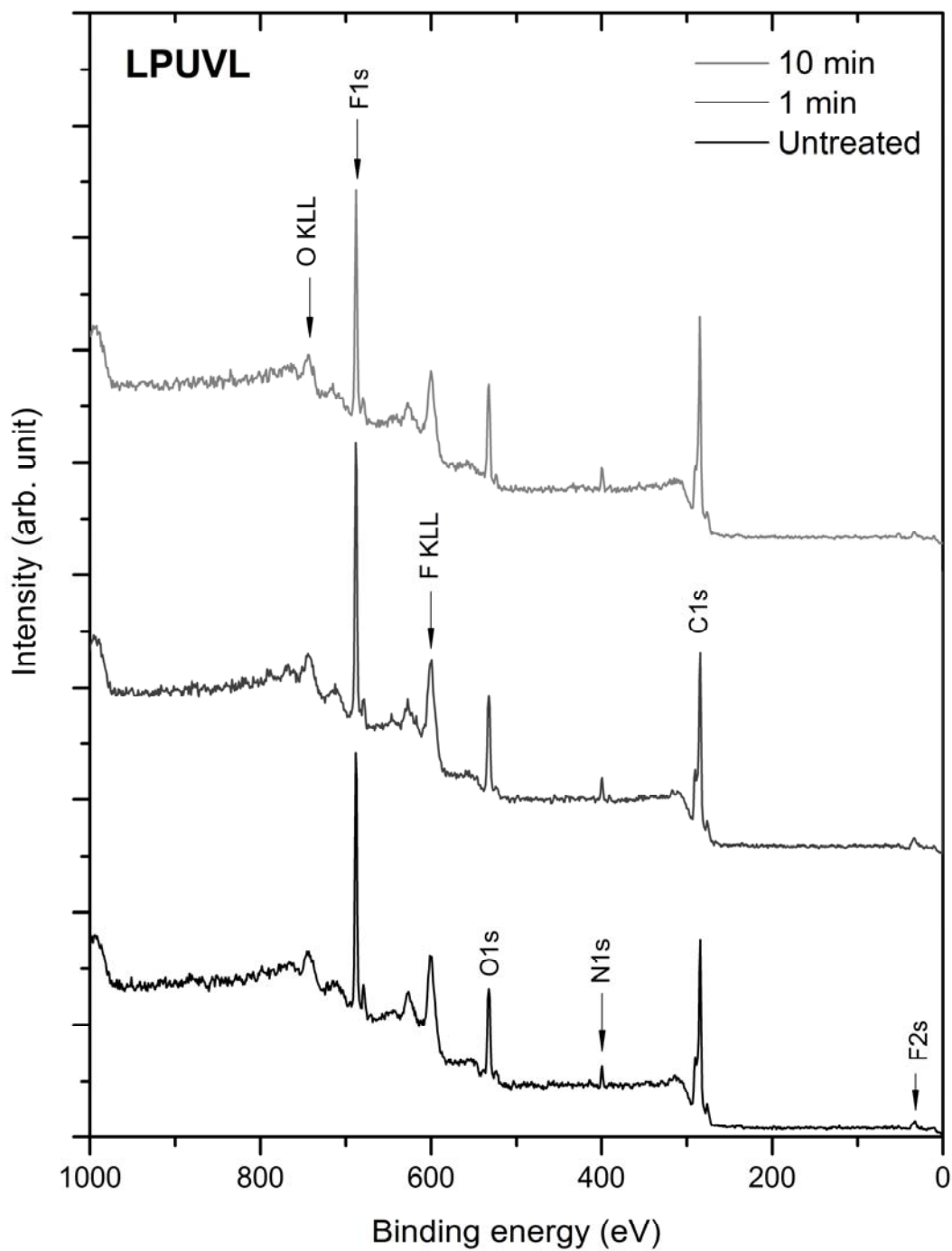


Figure 4.3.4 Survey spectra for the untreated and LPUVL-irradiated X_{2/3} films with different exposure times.

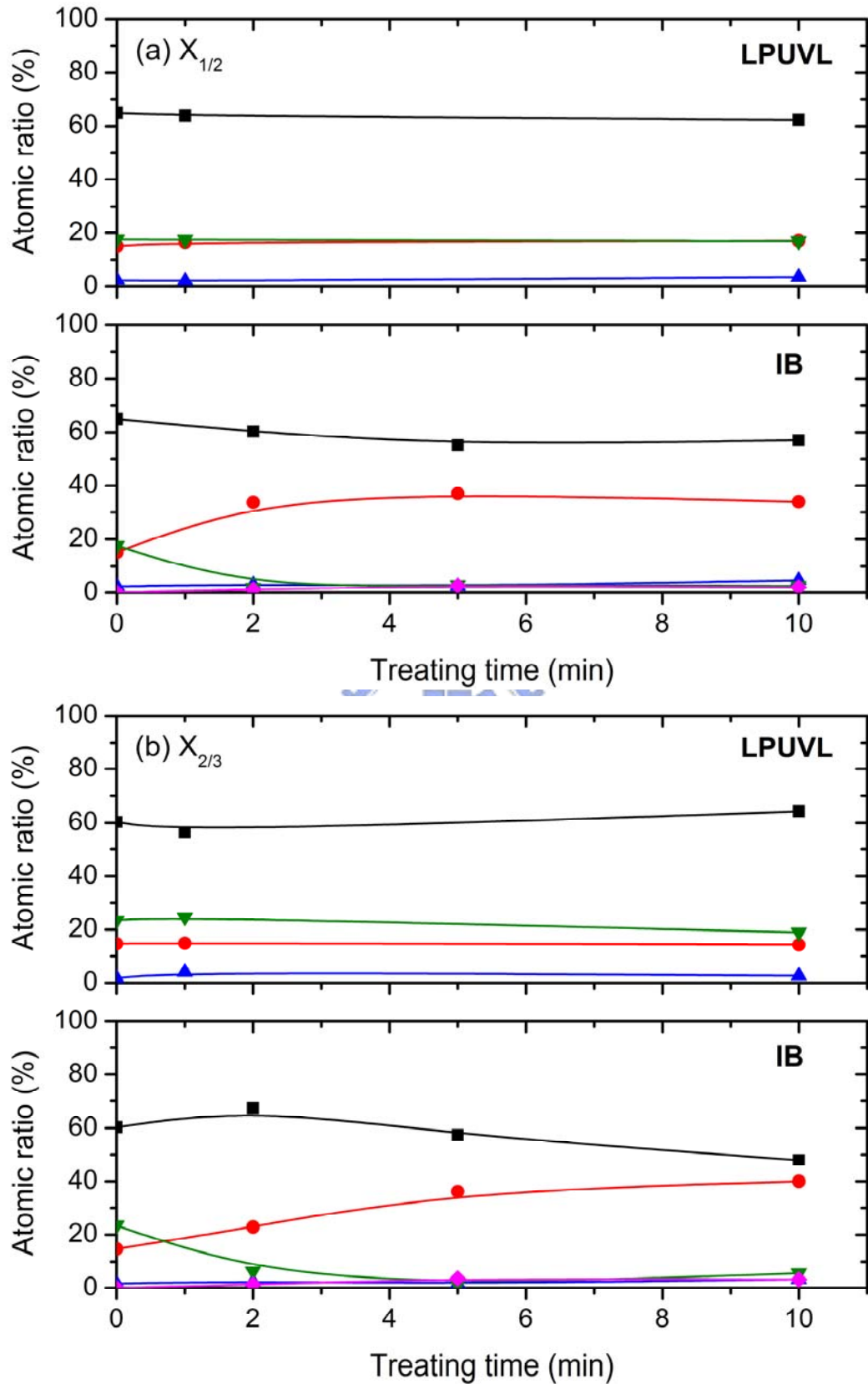


Figure 4.3.5 Variation of chemical composition of the (a) $X_{1/2}$ and (b) $X_{2/3}$ film surfaces treated by LPUVL irradiation and IB bombardment with respect to the treating time for elements: C (■), O (●), N (▲), F (▼), and Fe (◆).

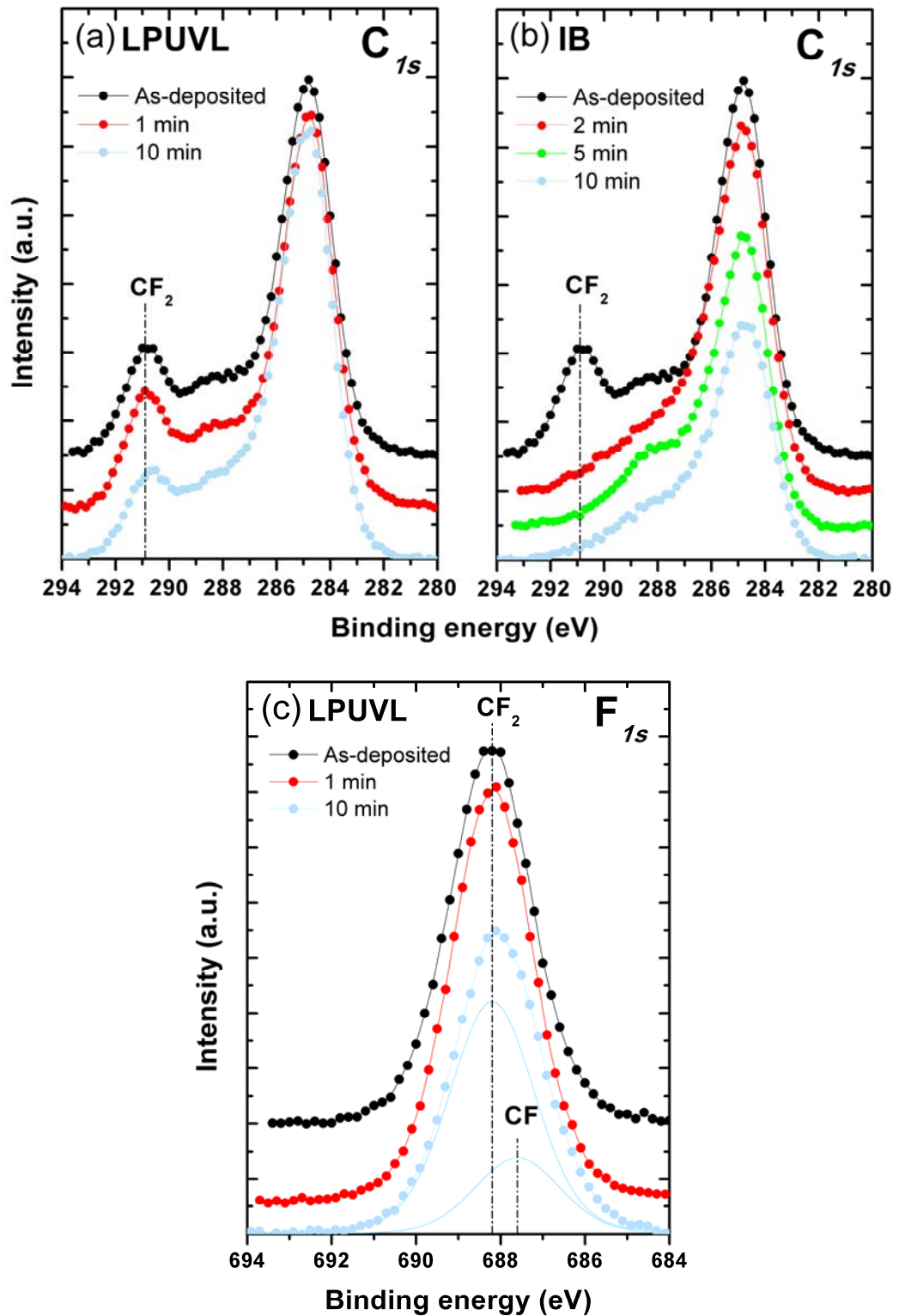


Figure 4.3.6 XPS spectra for $X_{2/3}$ films treated by both noncontact methods with different exposure times. The C_{1s} spectra for (a) LPUVL-irradiated films and (b) IB bombarded films and (c) the F_{1s} spectrum for LPUVL-irradiated films.

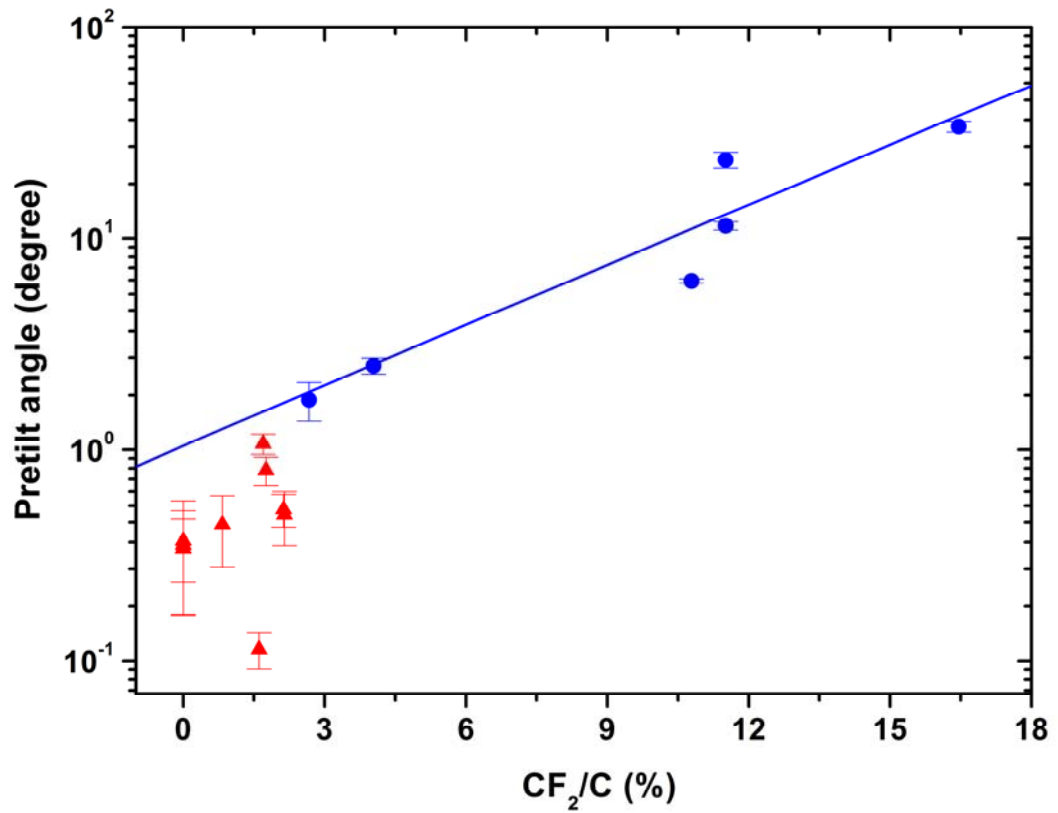


Figure 4.3.7 Logarithm scaled pretilt angle as a function of CF₂/C ratio for the LPUVL (●) and IB (▲) treatments.

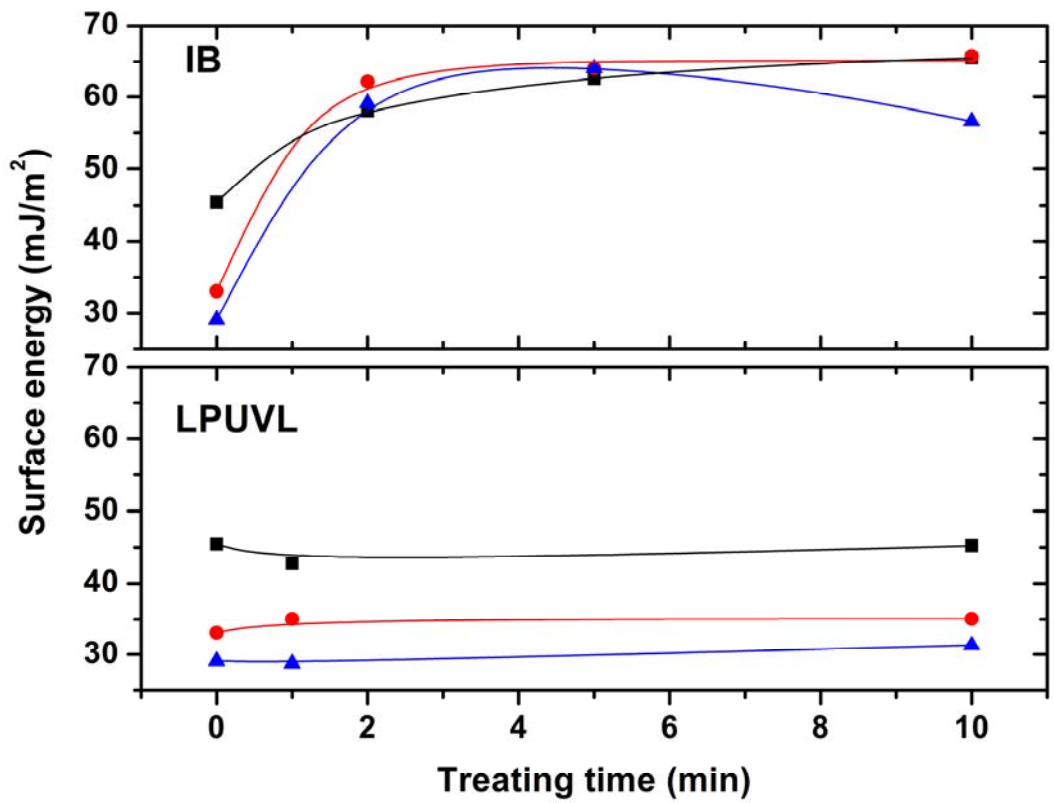


Figure 4.3.8 Surface energies of MAPHM-F8 films including X₀ (■), X_{1/2} (●), and X_{2/3} (▲) treated by LPUVL irradiations and IB bombardments for different treating times.

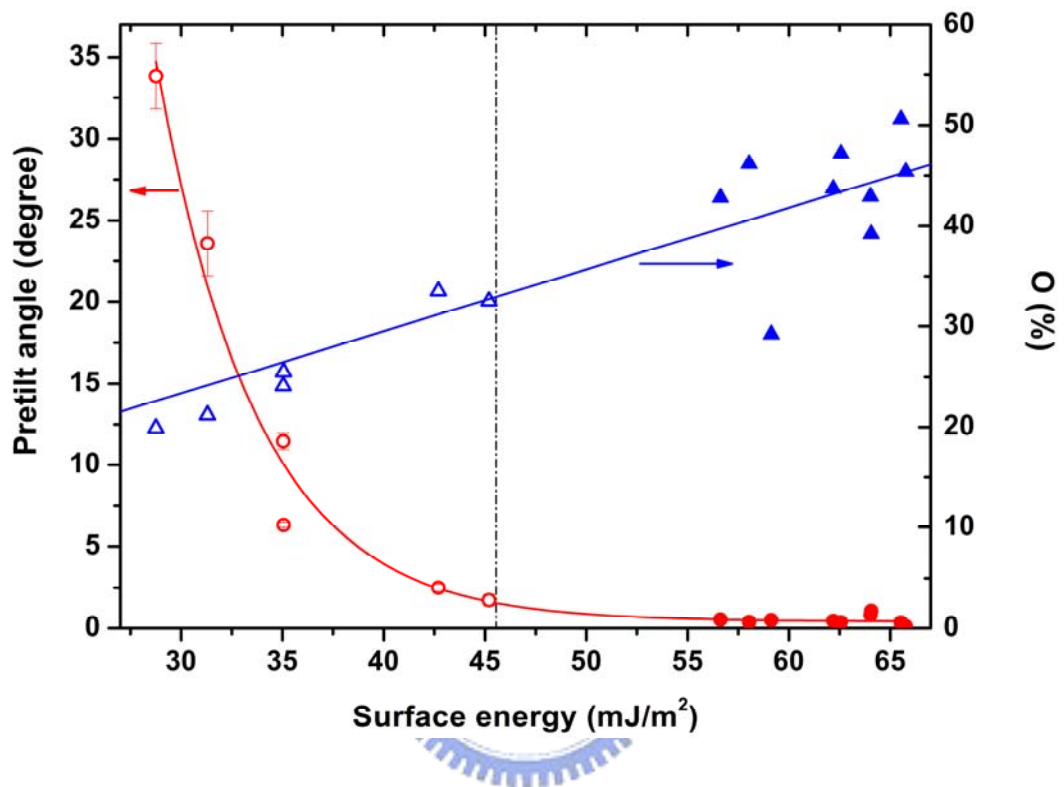


Figure 4.3.9 Pretilt angle (circle) and atomic ratio of oxygen content (triangle) as a function of surface energy for all the samples treated by LPUVL irradiation (open) and IB bombardment (solid) with different treating times.

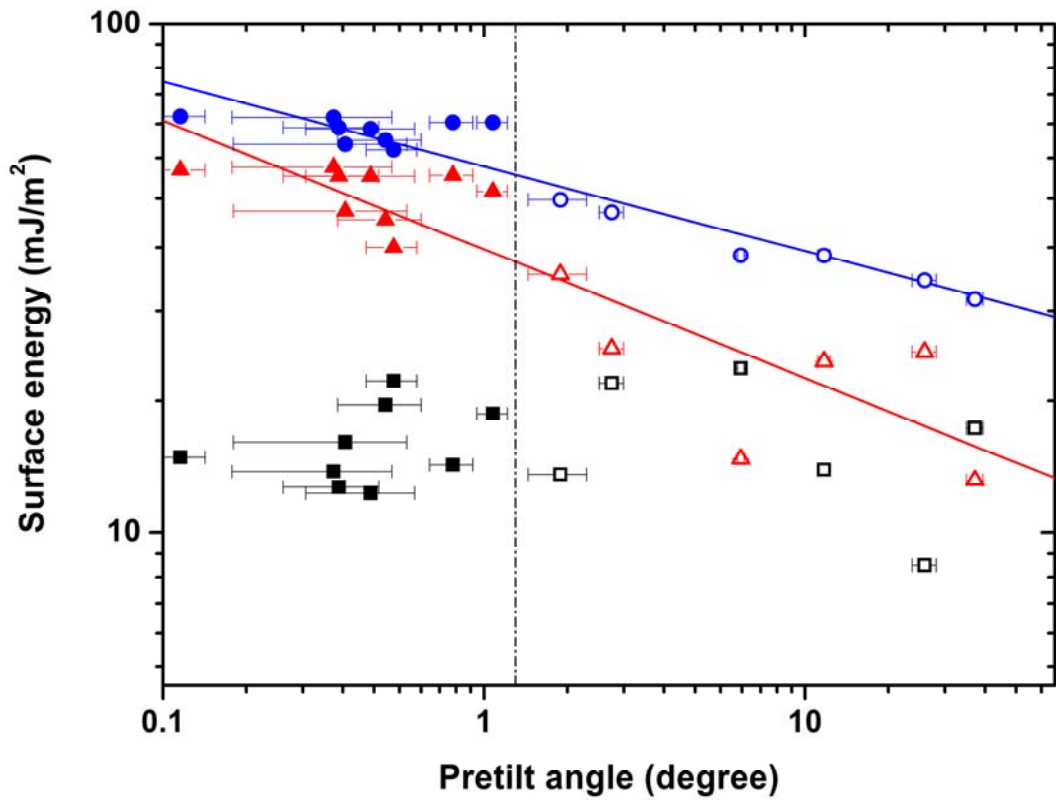


Figure 4.3.10 Total surface energy γ_s (circle), polar surface energy γ_s^p (triangle), and dispersion surface energy γ_s^d (square) are plotted as a function of pretilt angle in logarithm scale for all the samples treated by LPUVL irradiation (open) and IB bombardment (solid) with different treating times.

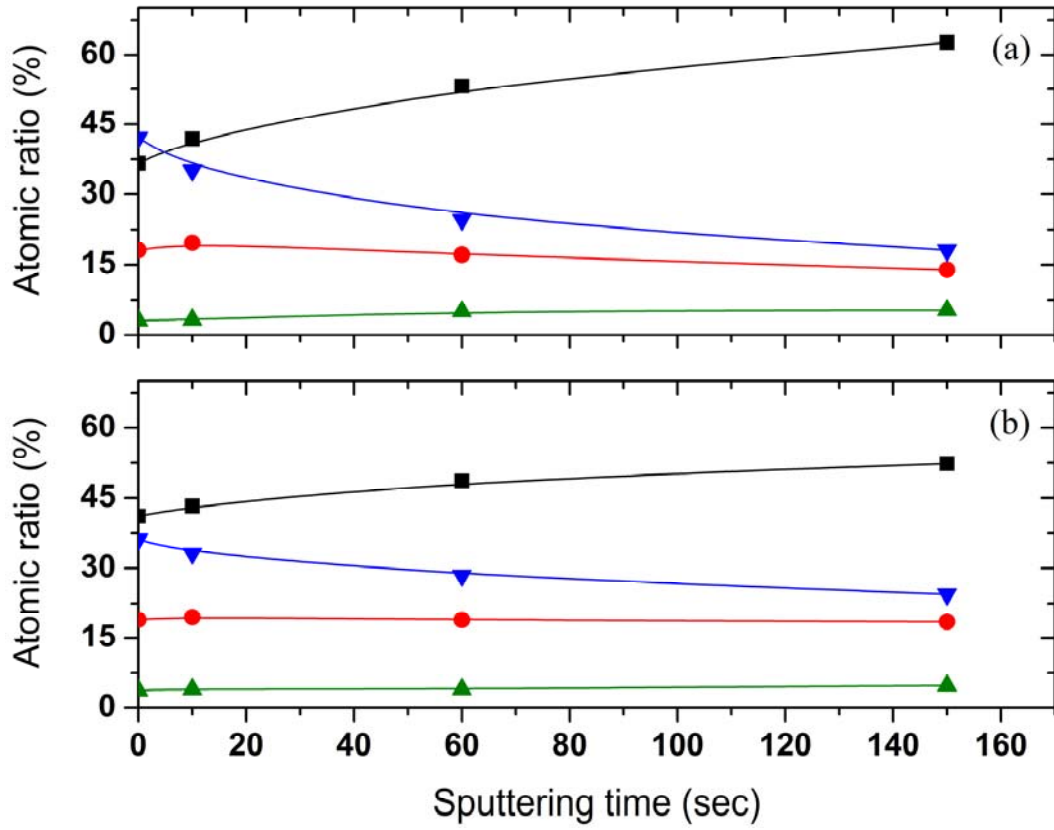


Figure 4.3.11 Depth-dependencies of C (■), O (●), N (▲) and F (▼) contents in the LPUVL-irradiated $X_{2/3}$ films with treating time: (a) 1 min and (b) 10 min.

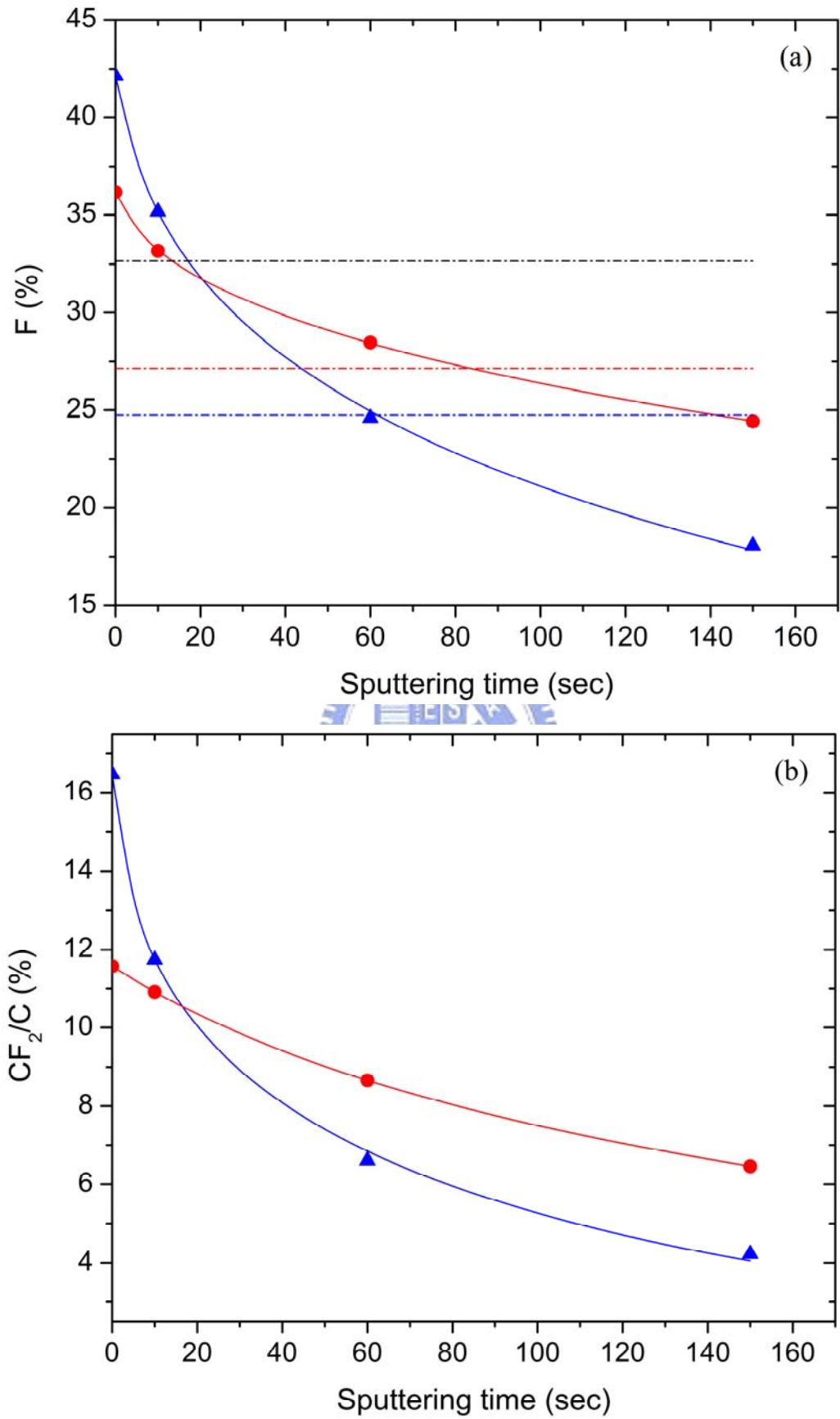


Figure 4.3.12 Depth-dependencies of (a) F and (b) CF₂ contents in the LPUVL-irradiated X_{2/3} films with treating time of 1 min (▲) and 10 min (●).

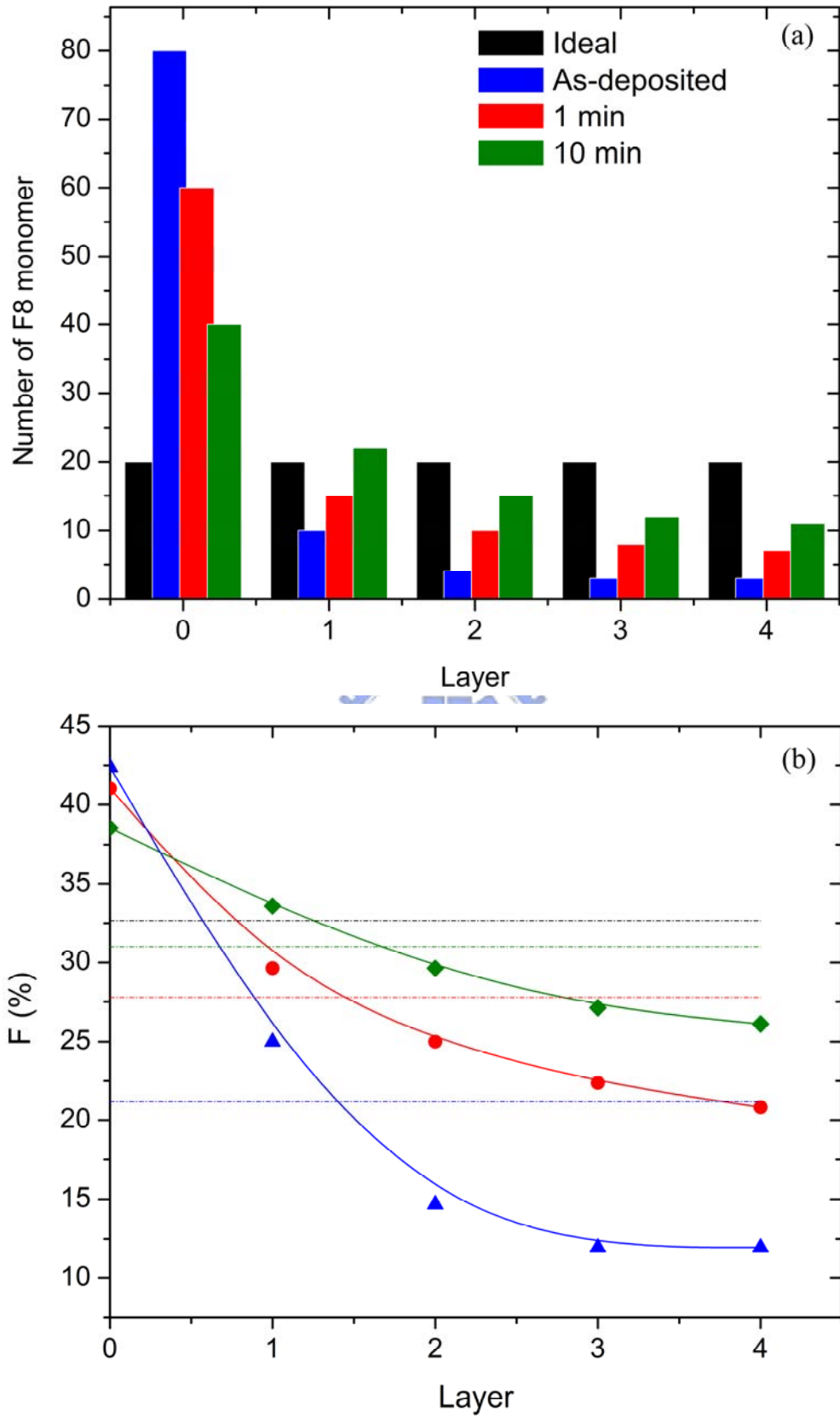


Figure 4.3.13 (a) Number of F8 monomer assumed in each layer and (b) the evaluated fluorine content for the as-deposited film (▲) and films treated by LPUVL-irradiation for 1 min (●) and 10 min (◆).

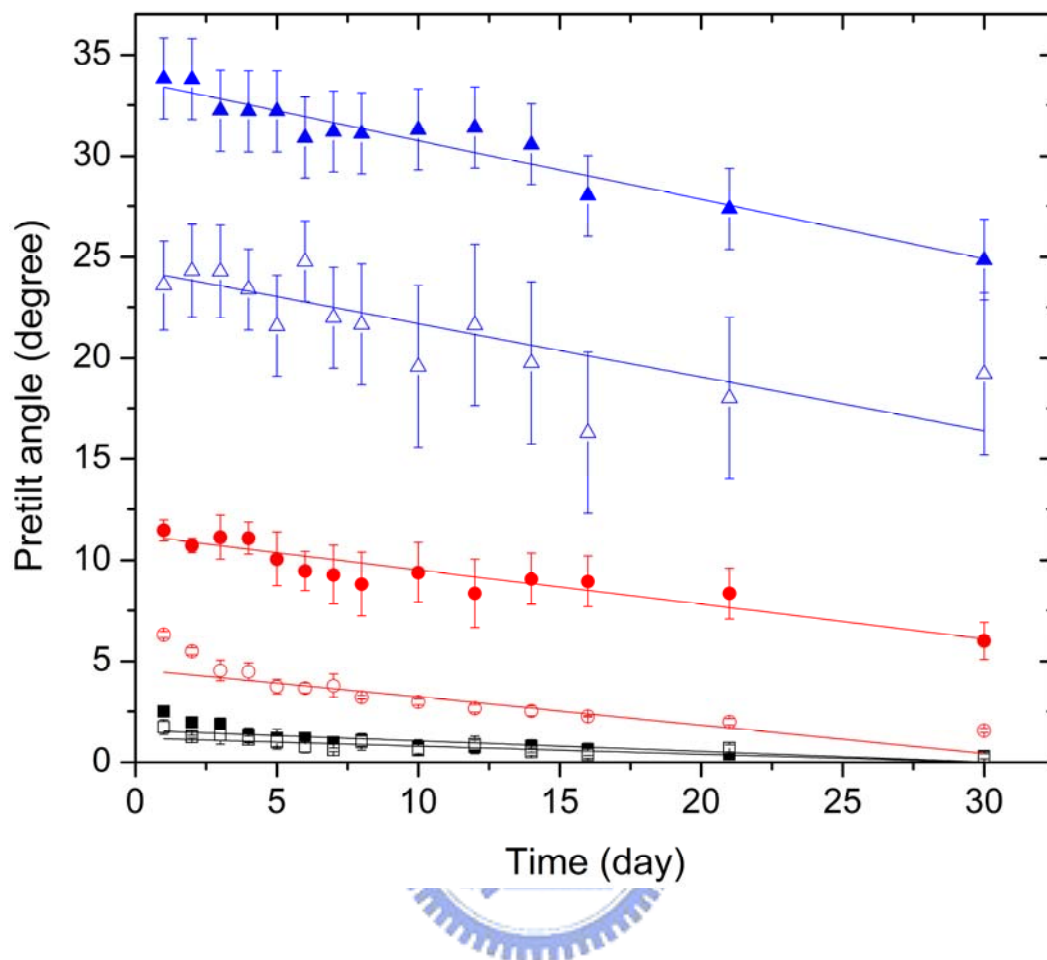


Figure 4.3.14 Stability of pretilt angle on the X_0 (square), $X_{1/2}$ (circle), $X_{2/3}$ (triangle) films treated by LPUVL-irradiation for 1 min (solid) and 10 min (open).

Tables

Table 4.3.1 Intensities a_0 of chemical bonds convoluted to the C_{1s} spectrum of X_0 surfaces treated by LPUVL irradiations and IB bombardments.

| | Untreated | LPUVL | | IB | | |
|---------|-----------|---------|---------|---------|---------|---------|
| | | 1 min | 10 min | 2 min | 5 min | 10 min |
| a_2 | 1.7752 | 1.7899 | 1.8427 | 1.9015 | 1.9459 | 1.7761 |
| a_3 | 0.7703 | 0.7180 | 0.7878 | 0.8855 | 0.9462 | 0.7810 |
| C-C/C-H | 19640 | 17710 | 19270 | 13550 | 13620 | 10950 |
| C-N | 5626.1 | 5351.7 | 5518.9 | 2032.0 | 1139.1 | 2675.8 |
| C-O-C | 1308.8 | 1085.1 | 1214.7 | 3309.5 | 3514.9 | 2226.6 |
| N-C=O | 1870.3 | 1377.2 | 1576.6 | 2219.2 | 2266.6 | 1900.1 |
| O-C=O | 1495.3 | 1633.8 | 1717.5 | 2323.0 | 2047.3 | 1789.6 |
| C-F | 0 | 0 | 0 | 0 | 0 | 0 |
| F-C-F | 0 | 0 | 0 | 0 | 0 | 0 |
| Total | 29940.5 | 27157.8 | 29297.7 | 23433.7 | 22588.1 | 19542.1 |

Table 4.3.2 Intensities a_0 of chemical bonds convoluted to the C_{1s} spectrum of $X_{1/2}$ surfaces treated by LPUVL irradiations and IB bombardments.

| | Untreated | LPUVL | | IB | | |
|---------|-----------|---------|---------|---------|---------|---------|
| | | 1 min | 10 min | 2 min | 5 min | 10 min |
| a_2 | 1.8985 | 1.8524 | 1.9376 | 1.8705 | 1.8447 | 1.9255 |
| a_3 | 0.8687 | 0.8021 | 0.7849 | 0.8805 | 0.8930 | 0.9092 |
| C-C/C-H | 22890 | 22910 | 24710 | 18720 | 15270 | 17140 |
| C-N | 6012 | 9774.2 | 4557.4 | 3794.6 | 4816.9 | 2360.0 |
| C-O-C | 1054.3 | 30.29 | 2243.5 | 3980.1 | 3147.6 | 3953.6 |
| N-C=O | 2087.3 | 2425.8 | 2160.1 | 2324.2 | 2089.2 | 2663.3 |
| O-C=O | 2920.1 | 3476.5 | 2949.2 | 3709.5 | 3310.8 | 2628.3 |
| C-F | 0 | 0 | 4.8 | 711.3 | 1269.8 | 547.7 |
| F-C-F | 4532.3 | 5025.2 | 4428.6 | 278.7 | 534.6 | 479.3 |
| Total | 39496.0 | 43642.1 | 41053.6 | 33518.3 | 30438.9 | 29772.3 |

Table 4.3.3 Intensities a_0 of chemical bonds convoluted to the C_{1s} spectrum of $X_{2/3}$ surfaces treated by LPUVL irradiations and IB bombardments.

| | Untreated | LPUVL | | IB | | |
|---------|-----------|---------|---------|---------|---------|---------|
| | | 1 min | 10 min | 2 min | 5 min | 10 min |
| a_2 | 1.9262 | 1.9297 | 1.9278 | 1.9988 | 1.9442 | 2.1685 |
| a_3 | 0.7370 | 0.6897 | 0.8115 | 0.8798 | 0.9363 | 0.9039 |
| C-C/C-H | 22210 | 23650 | 23970 | 21020 | 16240 | 15730 |
| C-N | 5081.5 | 5552.0 | 6816.0 | 3576.0 | 2223.1 | 0 |
| C-O-C | 1196.6 | 1407.6 | 2389.5 | 4192.0 | 3650.2 | 4133.6 |
| N-C=O | 2279.4 | 2471.2 | 2768.6 | 871.0 | 1857.6 | 1202.2 |
| O-C=O | 3090.9 | 3205.6 | 3214.6 | 3182.5 | 2806.2 | 2217.2 |
| C-F | 0 | 6.4 | 1515.6 | 1434.5 | 724.1 | 819.5 |
| F-C-F | 6575.7 | 7148.4 | 5093.8 | 752.8 | 474.7 | 524.8 |
| Total | 40434 | 43434.7 | 44252.6 | 35028.8 | 27975.9 | 24627.3 |



Chapter 5

Tilt Alignment of Liquid Crystals on the Polyimide Surface Treated by Plasma Irradiation with Simultaneous Coating of Magnetic Nanoparticles

5.1 Overview

In this chapter, a method to obtain the liquid crystal (LC) alignment with controllable pretilt angle is demonstrated. The polyimide (PI) films are treated by the plasma beam with simultaneous coating of maghemite nanoparticles in a diode-type ion-beam system. The influences of treating time and plasma energy on the alignment effect are discussed. To find out the alignment mechanism, the surface roughness and the size of coated nanoparticles have been characterized by using scanning electron microscope (SEM) and atomic force microscope (AFM). The surface energy has been investigated through the contact angle measurement. Furthermore, the composition of chemical bonds on the treated surfaces has been studied by using x-ray photoelectron spectroscopy (XPS). The results are also compared with the surface energies evaluated by contact angle measurements.

5.2 Experiments

The indium-tin-oxide coated glasses with size of 20 mm × 10 mm are used as the substrates. Before polymer coating, each substrate have to be cleaned out using a standard process shown in the flowchart of Fig. 2.3.1.

5.2.1 Plasma treatment

For plasma beam treatment, we employ a direct-current (dc) diode-type ion beam sputter (model IB-2 from EIKO Engineering Co., Ltd.) as described in Chap. 2 (see Figs. 2.2.1). The sputter is operated with coating mode, the bottom electrode acts as the anode. Due to the clearance between the electrodes is 35 mm only. The size of substrates has to

be controlled such that they can be totally immersed in the region of negative glow discharge, as shown in Fig. 5.2.1. The incidence angle of plasma beams is also fixed at 60° throughout this work. Before each plasma treatment, the chamber is pumped down to a base pressure of 30 mTorr and then argon gas is fed into the chamber to a target pressure. To keep the beam current density of 255 $\mu\text{A}/\text{cm}^2$ unchanged, the ultimate pressure of the chamber is adjusted between 45 and 160 mTorr depending on the applied dc bias V_b .

5.2.2 Sample preparation

After cleaning, the substrates are spin coated with the polyimide SE-130B (Nissan Chemical Industries, Ltd.), which is commonly used as an alignment agent in super twisted nematic liquid crystal display (LCD). The spin rate is 2000 rpm for the first 15 seconds and 4000 rpm for the 25 seconds afterward. The substrates are then pre-baked at 80°C for 15 minutes and cured at 170°C for another one hour. Each two substrates are then treated by plasma beam simultaneously and combined with a 23 μm Mylar spacer in between with anti-parallel alignment direction to form an empty cell. The nematic liquid crystal 4'-n-pentyl-4-cyanobiphenyl (5CB, Merck) with a nematic range between 24.0°C and 35.3°C is filled into the empty cell for alignment characterization.

5.2.3 Alignment characterization

After annealing, the alignment modes of the LC cells are characterized by using the polarizing optical microscope (POM). The pretilt angle of 5CB molecules near the surface is measured by using the “crystal rotation method” [1].

5.2.4 Surface analyses

In addition, the morphology on the film surface are investigated by the scanning probe microscope (SPM) unit system (SPA-300HV, SII NanoTechnology Inc.) operated in dynamic force mode AFM (DFM/AFM). To clarify the relation between the surface energy and the induced alignment properties of the treated films, the contact angle measurements have also been carried out. The detail has already been described in Sec. 4.2.4. To evaluate the chemical compositions of the treated film surfaces, the

surface-sensitive x-ray photoemission spectroscopy (XPS, PHI-1600 from Physical Electronics, Inc.) has been used. More description about the XPS we used has been given in Sec. 2.3.3. Only the Mg K α line is used in this work.

5.3 Results and discussion

After annealing, the alignment of LC cell is characterized by using a POM equipped with charge-coupled-display (CCD) device.

5.3.1 Alignment characterization

The photographs of LC cells with surfaces treated by plasma for 20 min with applied bias of 420 V and 560 V are shown in Fig. 5.3.1. Good quality of the alignment is obtained for each LC cell except those with treating time τ smaller than 2 min. The reliability and reproducibility have also been confirmed by observing the alignment properties over 3 months.

Furthermore, Fig. 5.3.2(a) shows the measured pretilt angle θ_p as a function of τ for plasma treatments with V_b of 420 V, 560 V, and 700 V. An increase of pretilt angle has been found with the treating time. The treatment with higher energy of plasma beam offers a higher pretilt angle. This trend is more obvious between the cells with a longer treating duration. In addition, the pretilt angle is measured as a function of the V_b , as plotted in Fig. 5.3.2(b). A sudden fall in pretilt angle at voltage of 840 V has been checked four times for its correctness. However, it should be noticed that the homeotropic alignments are eventually obtained in the cells with V_b higher than 700 V.

5.3.2 Surface morphologies

To find out the mechanism causes the increase of pretilt angle, the surface morphologies of plasma treated PI films are characterized. The measured mean surface roughness R_m is plotted as a function of τ and shown in Fig. 5.3.3(a). As the treating time is long enough similar tendencies toward a saturated roughness are found for both treating energies. Compare with the corresponding pretilt angle for each condition, it seems that no exact connection is found despite a similar trend is found for both of them with τ shorter than 20 min. Figure 5.3.3(b) reveals that treatment with higher energies of

plasma will decrease the surface roughness.

Besides, the SEM photographs with amplification factor of 100,000X for the PI surfaces treated by different conditions are taken at the angle of 30° from surface normal. Figure 5.3.4(a) shows the surface morphologies of the PI surfaces treated with different plasma energies. The film surface becomes more flat as the treating energy increases. As described in Chap. 3, the surface should be efficiently covered with a large amount of maghemite nanoparticles, especially when running the diode plasma system in coating mode. On the contrary, the surface treated with V_b lower than 700 V reveals a totally different morphology, as shown in Fig. 5.3.4(b). There exist lots of aggregations on the treated surfaces. No matter the energy we use in the treatment, a less dense distribution is found on the surface with a longer treating time. It is also worth noticing that the size of aggregation S_A increases with τ for both treating energies. Different rates of size growth are found, as shown in Fig. 5.3.5. A larger size of aggregation is obtained for plasma treatment with $V_b=420$ V if τ is longer than 10 min.

Further comparison between the pretilt angle and the size of aggregation shows a positive trend that a higher pretilt angle is obtained on the surface with a larger size of aggregation, as shown in Fig. 5.3.6. However, the different slopes of linear fit for 420 V and 560 V indicate that there are other mechanisms contribute to the generation of pretilt angle. As mentioned before, the measured surface roughness shows a minor influence on the induction of pretilt angle. As seen in Fig. 5.3.4(b), moreover, we deduce that the amount of pretilt angle is also related to the density of aggregation on the surface. This speculation has been confirmed through a further study by XPS.

5.3.3 Surface energy

The results of our surface energy measurement are plotted against the treating time as shown in Fig. 5.3.7. Without the surface treatments, the surface energy γ_s of PI SE-130B film is given as 45.8 mJ/m², which can be resolved into a polar component γ_s^p of 43.5 mJ/m² and a dispersion component γ_s^d of 2.3 mJ/m². That is, the dispersion forces are the major contribution to the surface energy of as-deposited film. After plasma beam treatments, a drastic growth of total surface energy is found for both treatments with V_b of 420 V and 560 V, as shown in Figs. 5.3.7(a) and 5.3.7(b),

respectively. The large variation in γ_s^p , according to our previous conclusion, is probably due to the bond-breaking effect and the followed re-oxidization of dangling bonds created by ion-beam/plasma-beam bombardments. However, the acid-base reactions usually happen on the iron oxide surface responsible for it have also been deduced from XPS results. Despite the growth of γ_s^d is not as much as that of γ_s^p , it should not be ignored. We will give more discussion on that by XPS analyses. It is also worth noticing that the γ_s , γ_s^d , and γ_s^p approach to the values of 76.3 mJ/m², 48.1 mJ/m², and 28.2 mJ/m², respectively, which are approximately the surface energies of a pure γ -Fe₂O₃ coating. As a result, it suggests that the treated PI film surface is covered with the maghemite nanoparticles. Figure 5.3.8 shows the surface energies of the films treated with V_b from 420 V to 1400 V for 10 min, which lead to a similar remark. The origin of the increase of surface energy will be discussed through XPS analyses.

5.3.4 XPS analyses

For the PI surfaces treated with $V_b=560$ V for different τ , their content of each element is measured in Fig. 5.3.9(a). It is contrary to the C and N content that the O and Fe content are increasing with τ . Similarly, a gradual growth of O and Fe content is also found with increasing V_b , as shown in Fig. 5.3.9(b). The N content is almost gone after treatment with $V_b=700$ V. Further analyses of the O1s composition reveal that γ -Fe₂O₃ and C-O-Fe bonds contribute to the large increase of O content and the polar surface energy γ_s^p . The intensity of each deconvoluted signal is listed in Table 5.3.1 and Table 5.3.2. Figure 5.3.10(a) shows the variation of O1s composition on the surfaces treated with $V_b=560$ V for different τ . A significant decrease of N-C=O and C-O-C bonds indicates that the polyimide structure is either destroyed in the plasma irradiation and/or covered with the maghemite nanoparticles according to the increasing signal of γ -Fe₂O₃ and C-O-Fe bonds. Besides, the compositions of O1s core level on the surfaces treated for 20 min are measured as a function of V_b in Fig. 5.3.10(b). The same remark can be obtained as well. It shows that these two iron-oxide-related bonds increase with plasma energy. A higher content of C-O-Fe bond compared to the γ -Fe₂O₃ bond indicates that the sputtered iron ion preferentially reacts with the PI surface in a treatment with the plasma energy lower than 700 V. Once the coating rate of γ -Fe₂O₃ nanoparticle is high

enough, it is difficult to react with the PI surface to form the C-O-Fe bond for iron ion.

Although the bond of C-O-Fe appears in a pure γ -Fe₂O₃ film as well, its XPS signal shows that the amount is much less than that of γ -Fe₂O₃ bonds, as mentioned in Sec. 3.3.1. As a result, it still could indicate a possibility of that the intensity of C-O-Fe bond measured from the treated PI surface represent the area of PI surface uncovered from γ -Fe₂O₃ nanoparticles. In Fig. 5.3.4, we have seen that the cluster structure extends to a larger aggregation. And so does the rest of the area uncovered from the clustered nanoparticles. For example, the size of aggregation for the surface treated by V_b of 420 V and 560 V for 40 min is measured as 53.2 ± 2.8 nm and 44.5 ± 3.1 nm, respectively, as shown in Fig. 5.3.5. However, a higher pretilt angle is obtained for 560 V-treated PI surface. It could be expected because a loose spread of aggregation is formed on the surface treated by $V_b=420$ V.

In addition, there is no significant difference between the surface energies for both surfaces. An almost the same result compared to that of a pure γ -Fe₂O₃ film is obtained, as shown in Fig. 5.3.7, no matter what the surface topology is. It is probably due to the surface energy represent a surface property resulting from a microscopic point of view.

Furthermore, the XPS results are also compared with the surface energy of each corresponding treating condition. We found a strong connection between the dispersive surface energy γ_s^d and the content of C-O-Fe bond. As seen in Fig. 5.3.11, the results measured from the surfaces treated by different beam energies and treating times have been put together for comparison. A linear relation is surprisingly found among them. Although a variety of species including mononuclear monodentate, mononuclear bidentate and binuclear mono or bidentate complexes can be formed through absorption of simple ligands such as the carbonyl groups including the types of RCHO (Aldehyde) and RCOOH (Carboxylic acid) on iron oxides, as shown in Fig. 5.3.12 [2]. That means a high polarity is usually found on the iron oxide surface, which reflects the increase of polar surface energy γ_s^p as confirmed in Sec. 5.3.3.

Nevertheless, the linear relation between dispersive surface energy and content of C-O-Fe bond indicates a possibility of linkage between the iron oxide and aromatic chains. As the typical chemical structure of PI drawn in Fig. 2.4.7, large amount of aromatic compounds like benzene ring and pyrrolidine are contained. These chemical

structures could raise the dispersive surface energy which is due to the van der Waals interaction. It is well known that the dipole-dipole interaction between the π orbital of liquid crystals and the alignment material contributes to the alignment effect of LC. We deduce that the anisotropy of alignment on the surface plane is caused by anisotropic destruction of benzene rings by plasma beam bombardment. The dangling bond reacts with the iron ion to form the iron-oxide-related bond like C-O-Fe. That means the benzene rings left unbroken offer ability for aligning LC; moreover, the newly-formed C-O-Fe bonds could increase the surface polarity and/or the dispersive surface energy.

Accordingly, we could speculate that the pretilt angle is determined by not only the size but also the distribution density of the aggregation. As mentioned in Chap. 3, a uniform γ -Fe₂O₃ coating can cause a homeotropic alignment of LC. Therefore, we could expect that a competition of intermolecular interaction between the treated PI surface and coated iron-oxide nanoparticles can lead to the resultant pretilt angle.

More studies on the surface and magnetic properties by using XPS and a superconducting quantum interference device are required to verify this speculation in the future.

5.4 Concluding remarks

A surface alignment method by using the plasma irradiation on the polyimide surface with simultaneous coating of maghemite nanoparticles has been demonstrated. The homogeneous alignments of LC with good quality and reliability are obtained on the PI surfaces treated with V_b lower than 700 V. The pretilt angle can be controlled by different applied bias and treating time. The alignment mechanism has also been discussed according to the results from AFM, SEM, and XPS. The pretilt angle is determined by not only the size but also the distribution density of the aggregation. The newly-formed bonds of C-O-Fe and γ -Fe₂O₃ are deduced responsible for the increase of polar surface energy after plasma treatment. In addition, the C-O-Fe bond could also increase the dispersive surface energy by bonding with the aromatic rings. Consequently, we deduce that the competition of intermolecular interactions between the plasma-treated PI surface and the coated iron-oxide nanoparticles leads to the resultant

pretilt angle.



References

1. T. J. Scheffer and J. Nehring, *J. Appl. Phys.* 48, 1783 (1977).
2. R. M. Cornell and U. Schwertmann, *The Iron Oxides: Structure, Properties, Reactions, Occurrences and Uses*, 2nd ed. (WILEY-VCH, Weinheim, 2003), pp. 265-267.



Figures

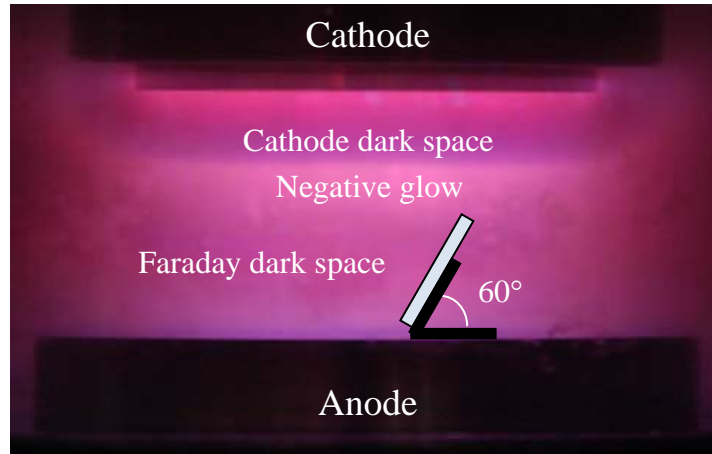


Figure 5.2.1 Spatial distribution of glow discharge in the diode-type ion beam system operated in the coating mode.

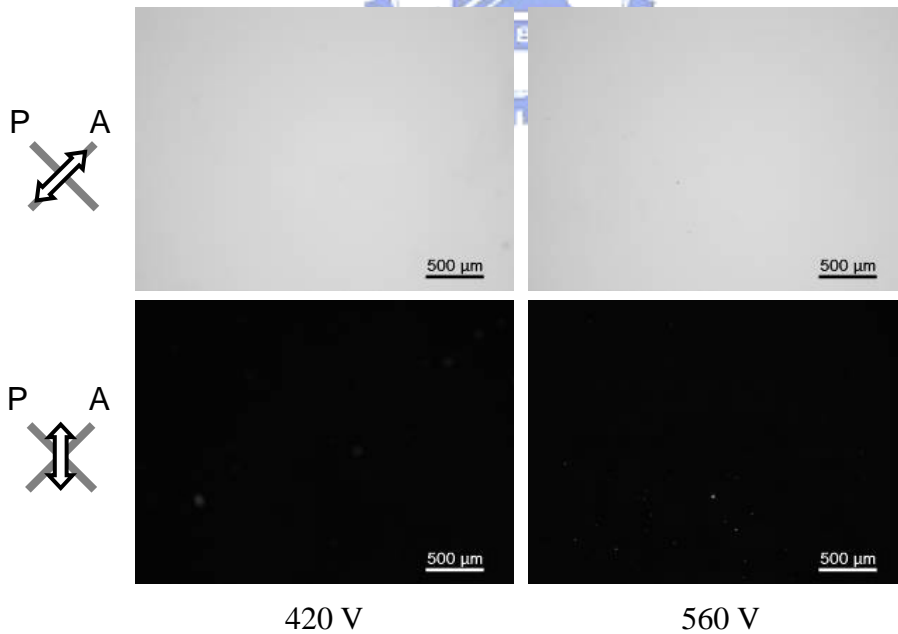


Figure 5.3.1 The POM photographs of LC cells treated by different V_b : 420 V and 560 V for 20 min.

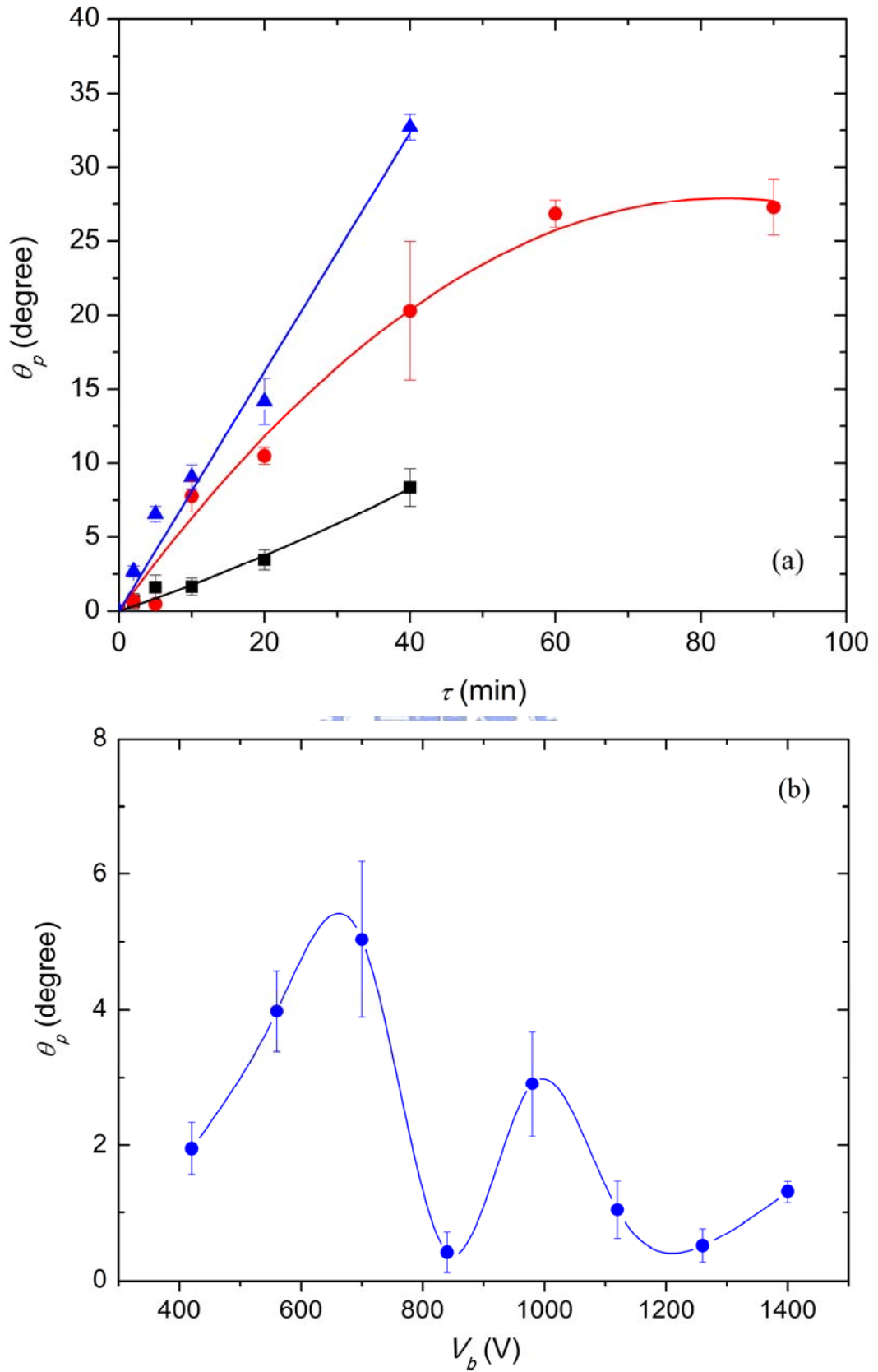


Figure 5.3.2 Pretilt angle θ_p is plotted as a function of (a) τ for 5CB cells with surfaces treated by plasma with different V_b : 420 V (■), 560 V (●), and 700 V (▲) and (b) V_b for 10 min treatments.

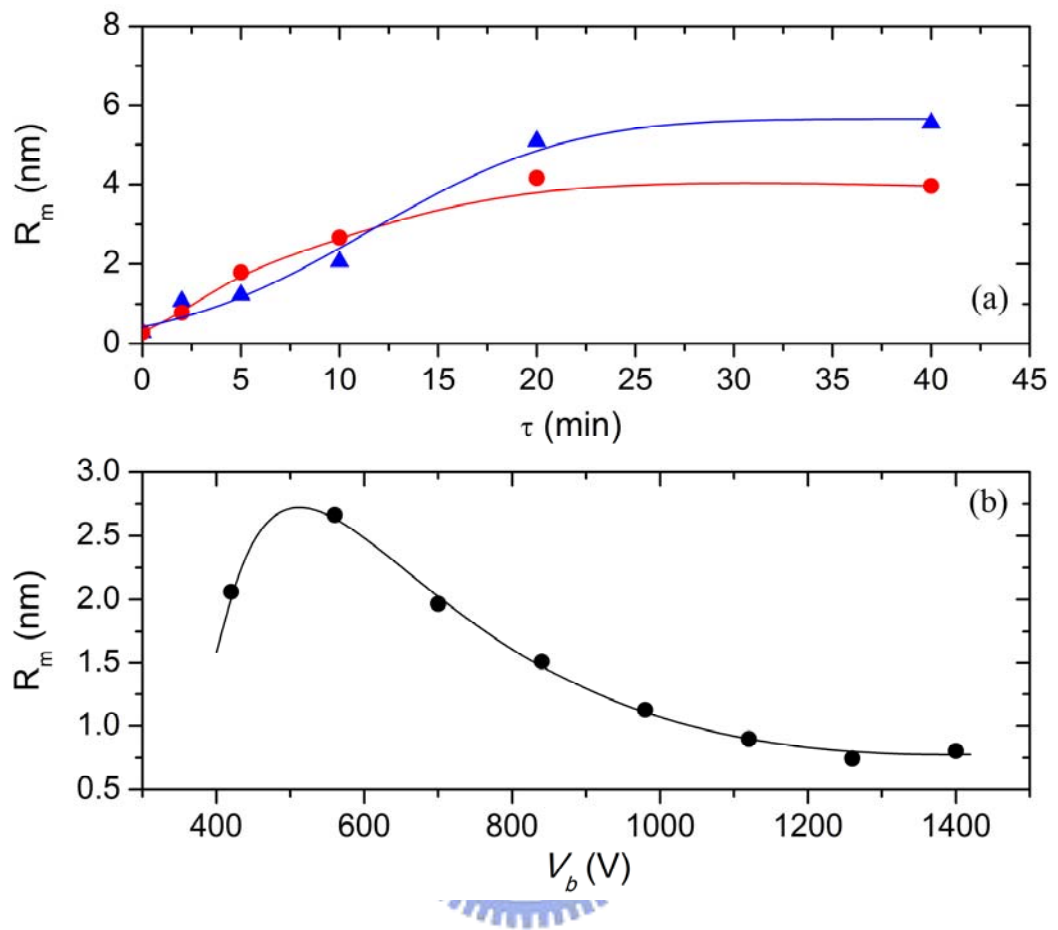


Figure 5.3.3 Surface roughness R_m of the PI films treated with different (a) τ with V_b of 420 V (▲) and 560 V (●), and (b) V_b with $\tau=10$ min.

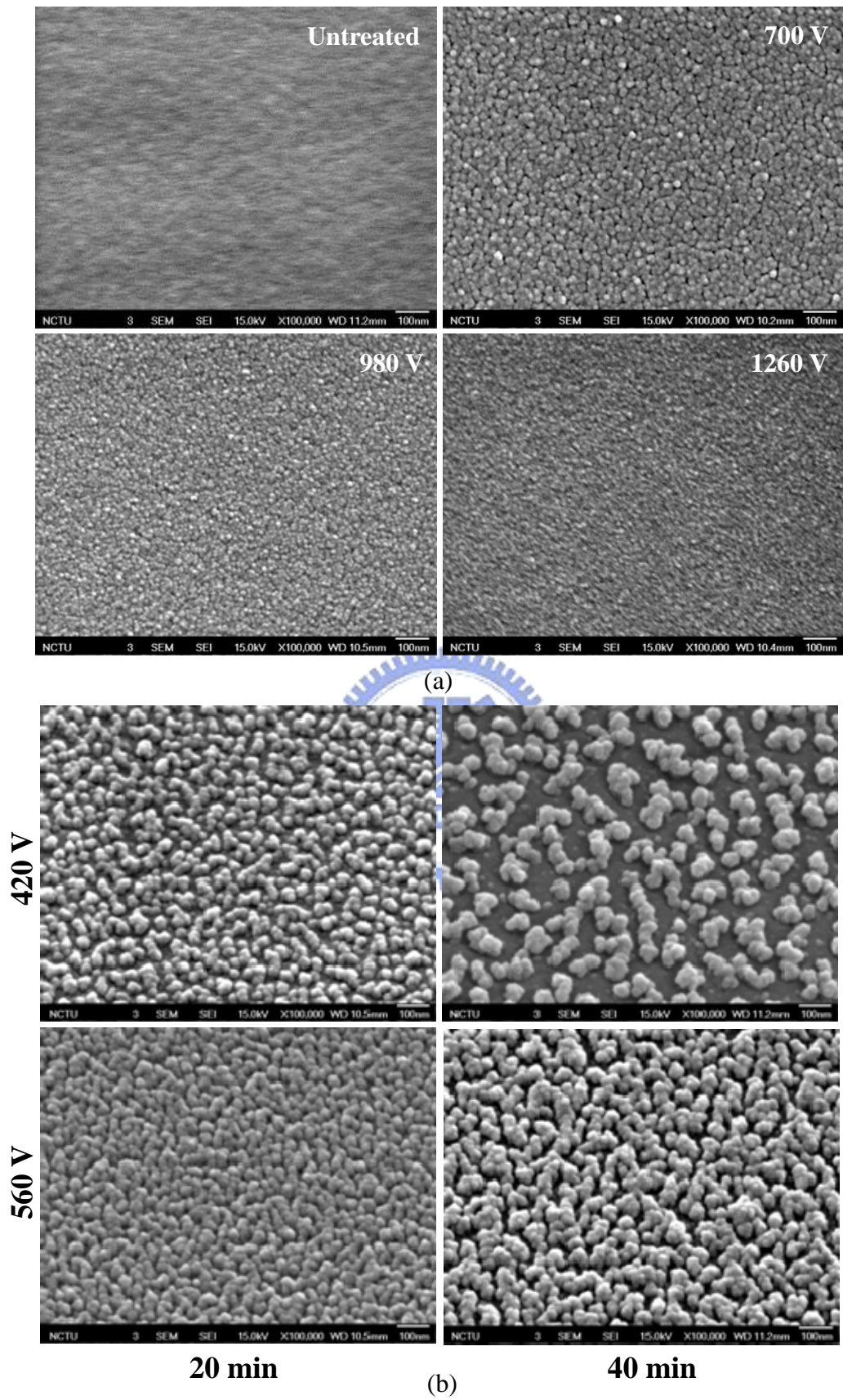


Figure 5.3.4 SEM photographs of the PI film surfaces treated with different (a) V_b for $\tau=10$ min and (b) τ for V_b of 420 V and 560 V.

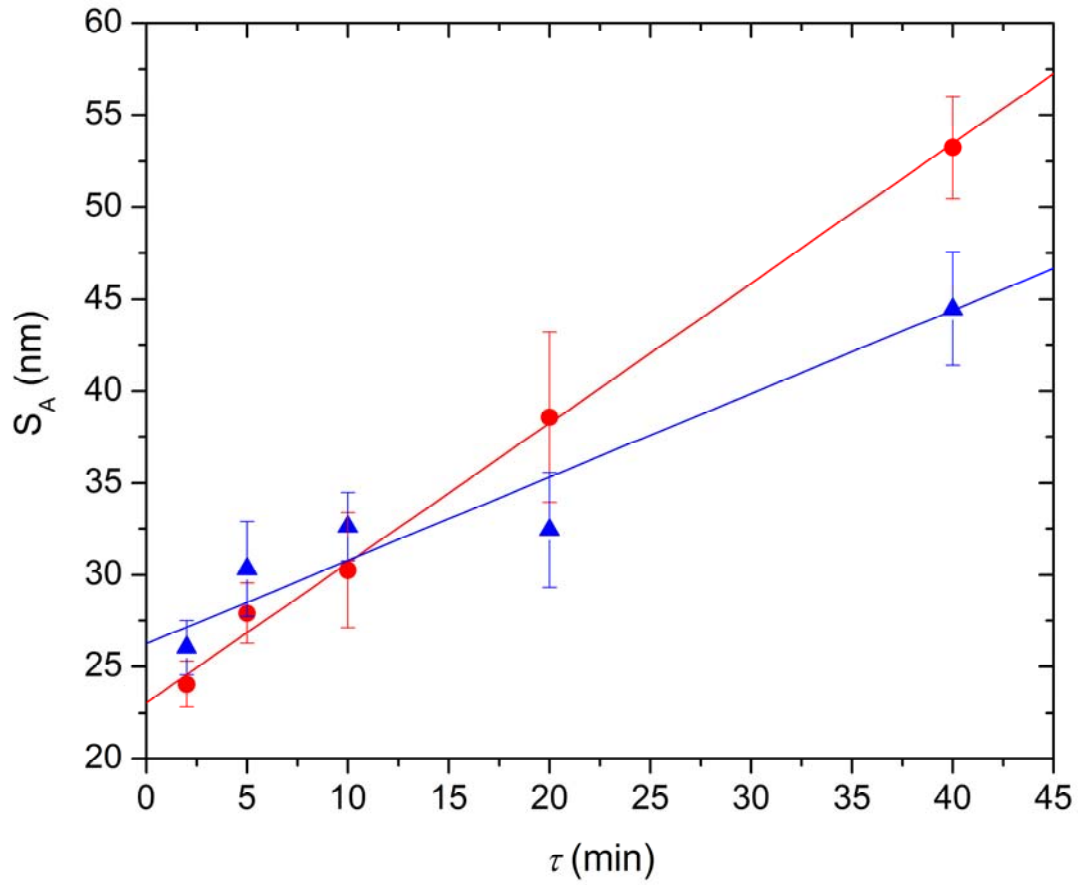


Figure 5.3.5 Size of aggregation S_A on the PI surfaces treated by V_b of 420 V (●) and 560 V (▲) is plotted as a function of τ .

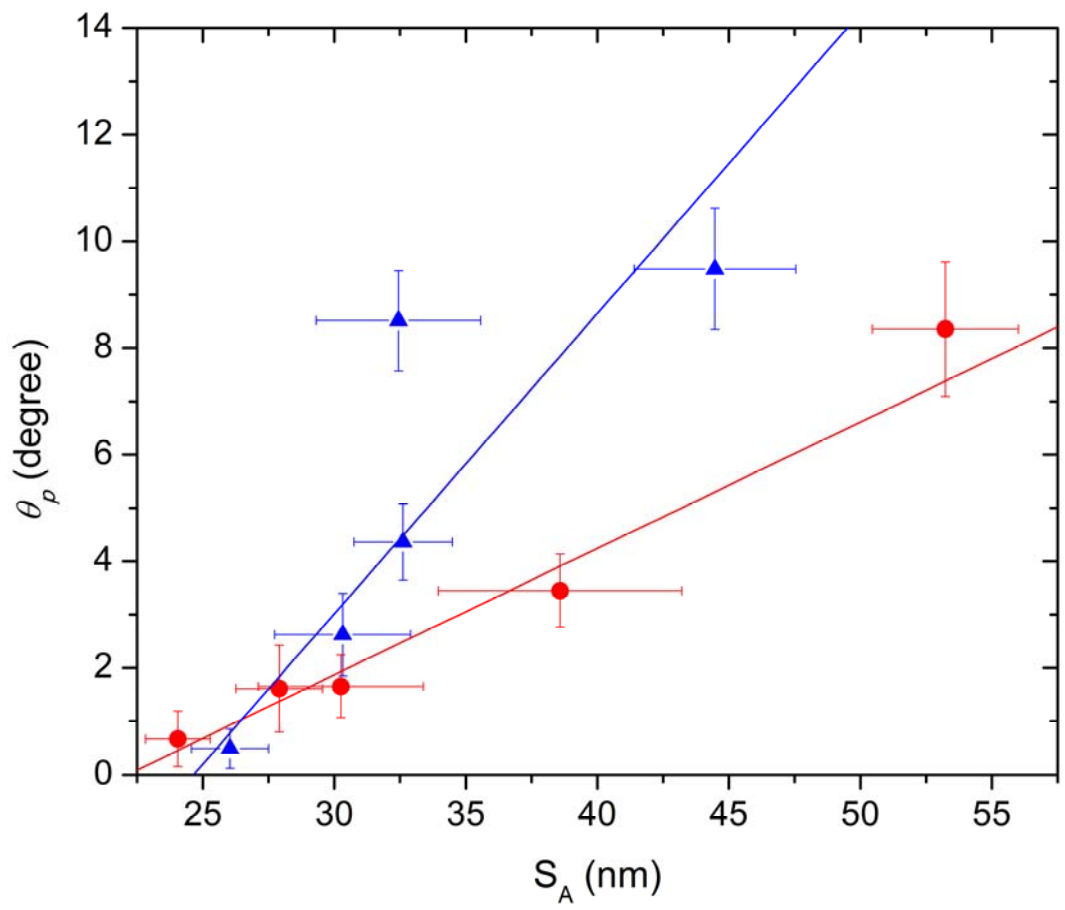


Figure 5.3.6 Pretilt angle θ_p is plotted as a function of the size of aggregation S_A for V_b of 420 V (●) and 560 V (▲).

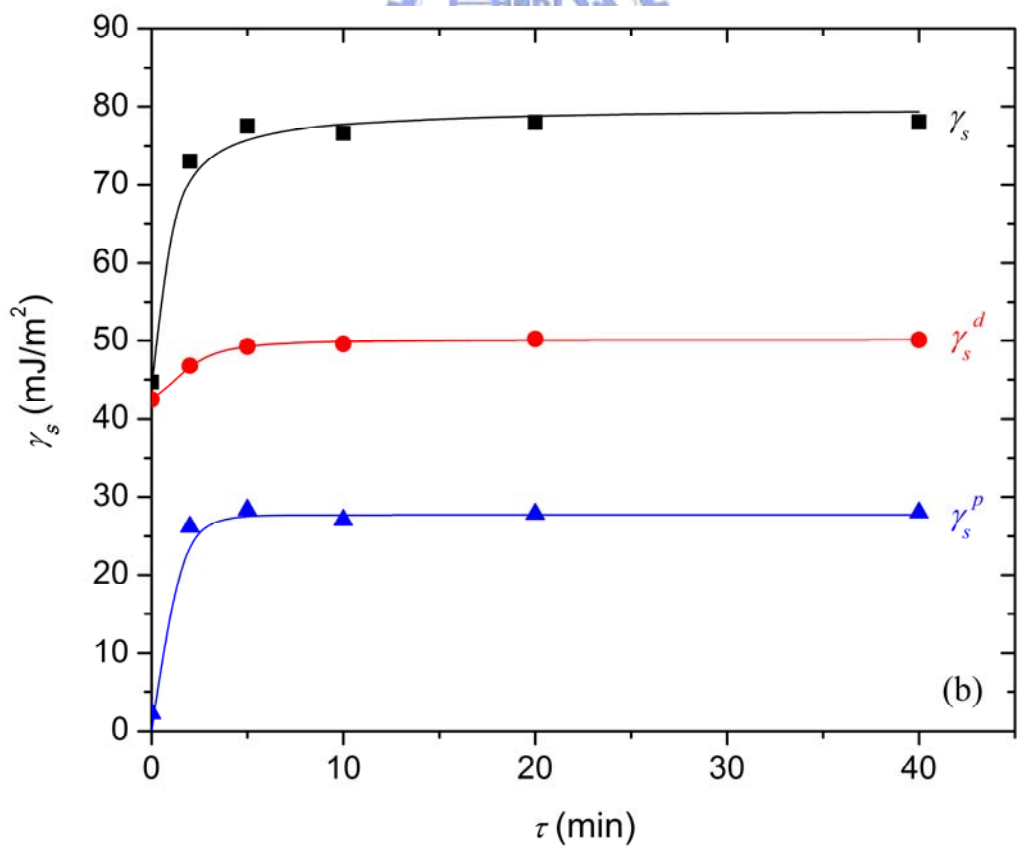
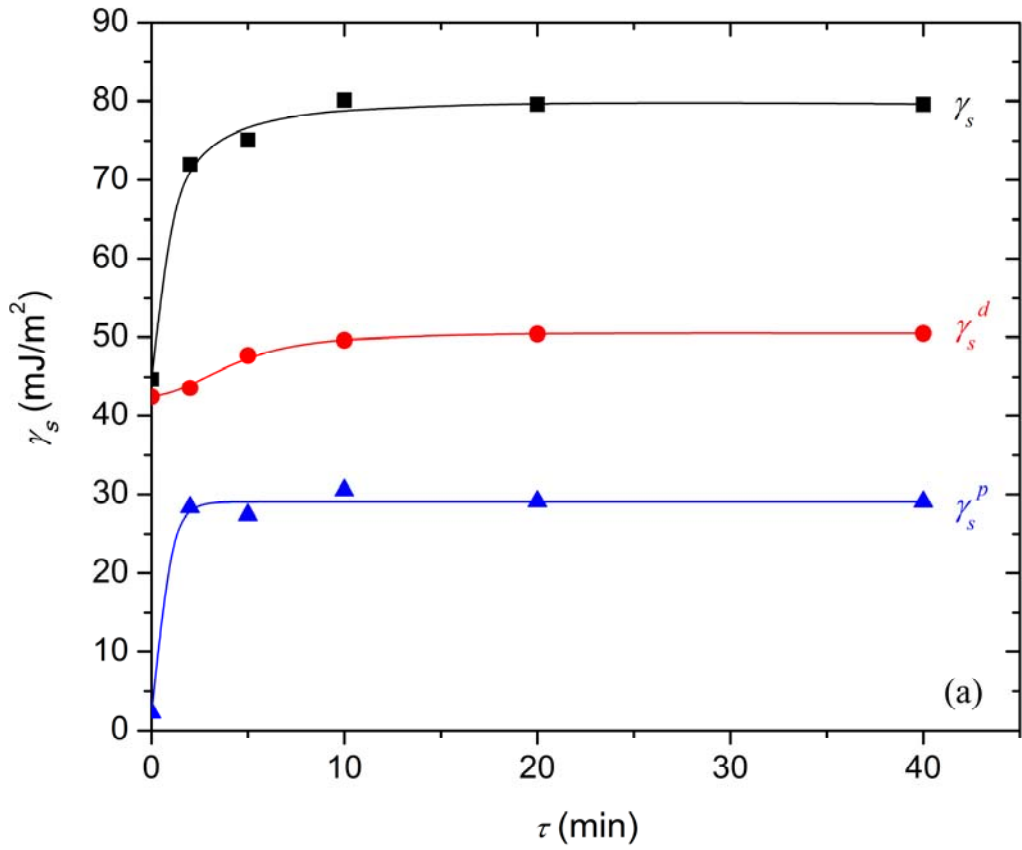


Figure 5.3.7 Surface energy γ_s is plotted with treating time τ for V_b of (a) 420 V and (b) 560 V.

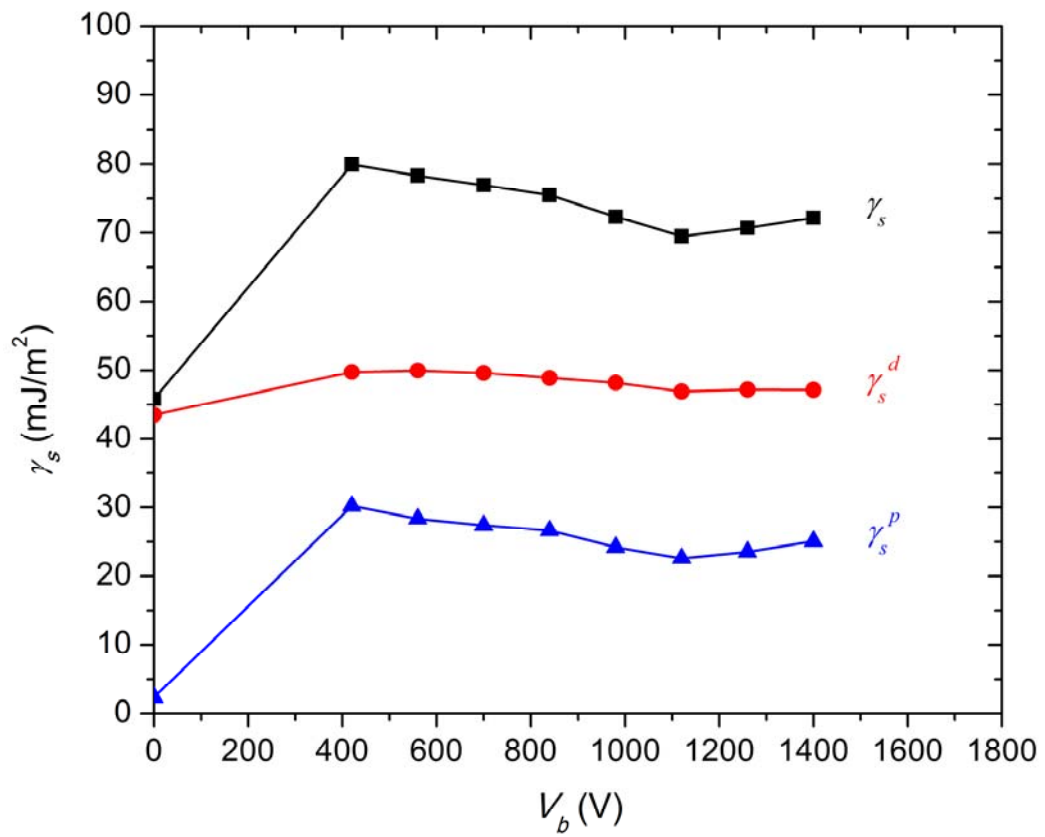


Figure 5.3.8 Surface energies γ_s of the PI films treated with different V_b for 10 min.

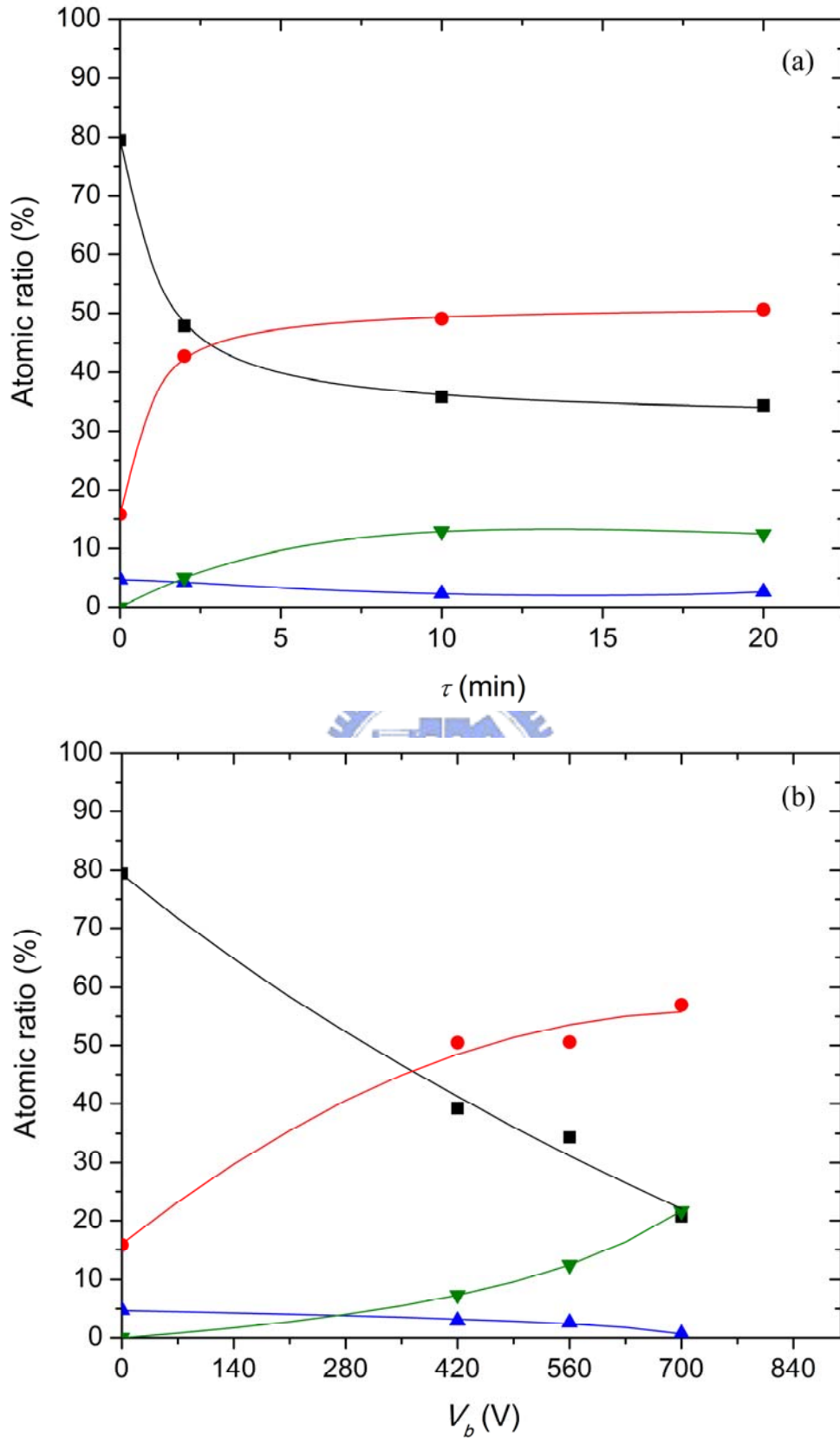


Figure 5.3.9 Content of C (■), O (●), N (▲), and Fe (▼) are plotted as a function of (a) τ with the bias of 560 V and (b) V_b for 20 min irradiation.

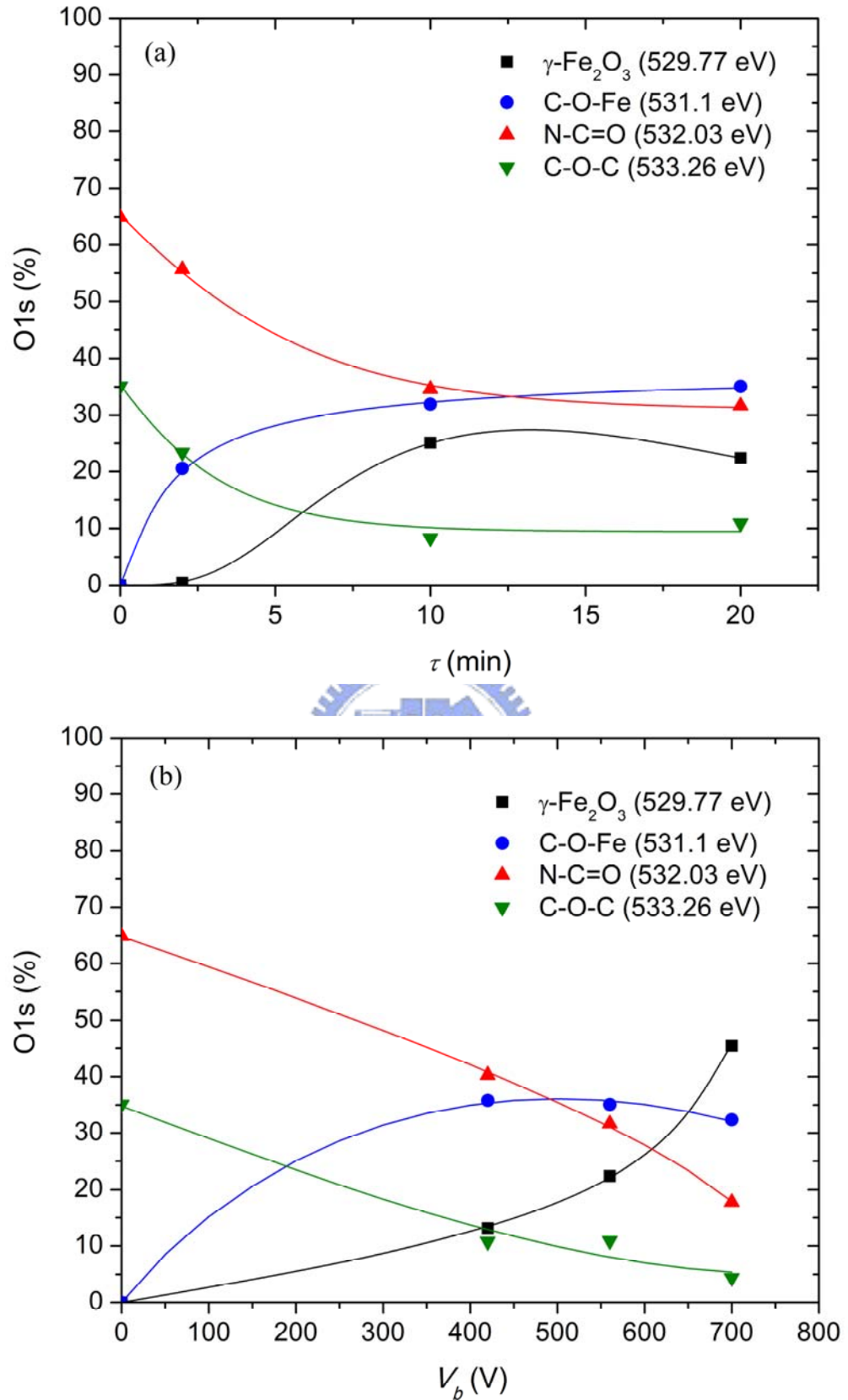


Figure 5.3.10 Composition of O1s core level signal as a function of (a) τ with the bias of 560 V and (b) V_b for 20 min irradiation.

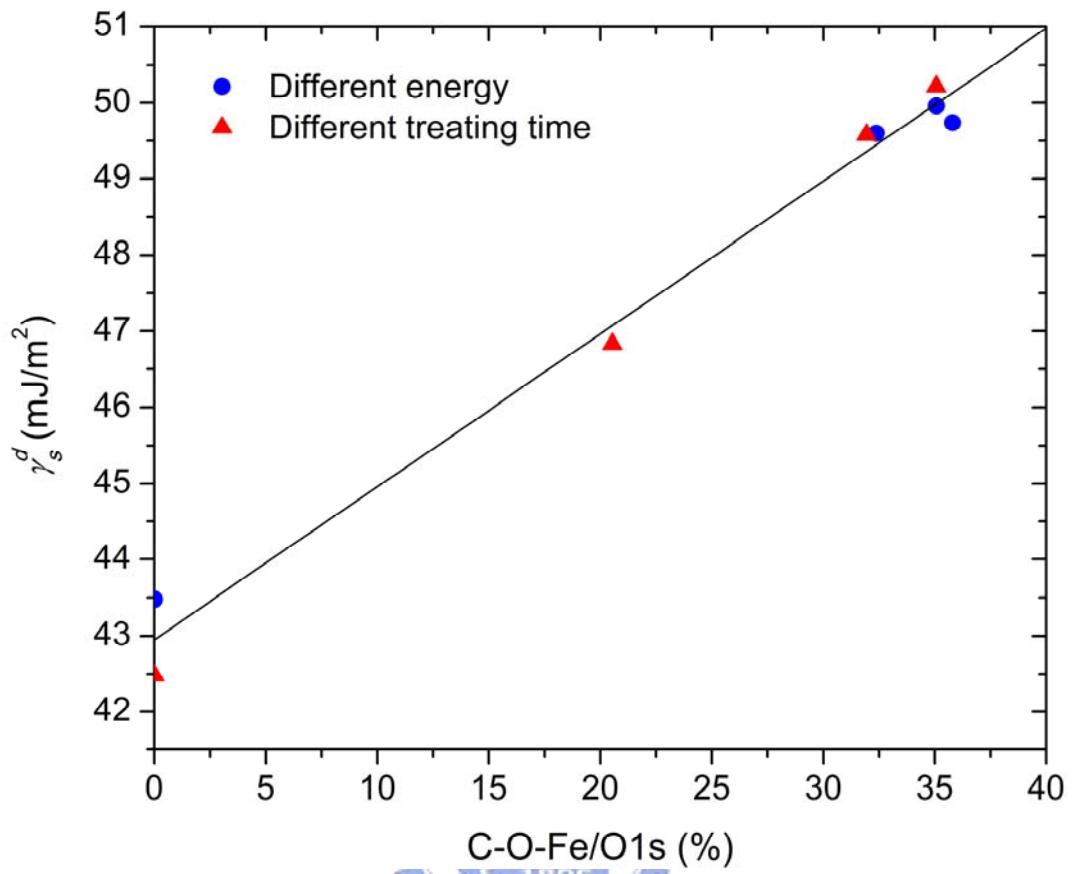


Figure 5.3.11 Relation between the dispersive surface energy and the content of C-O-Fe bond for surfaces treated by different V_b and τ .

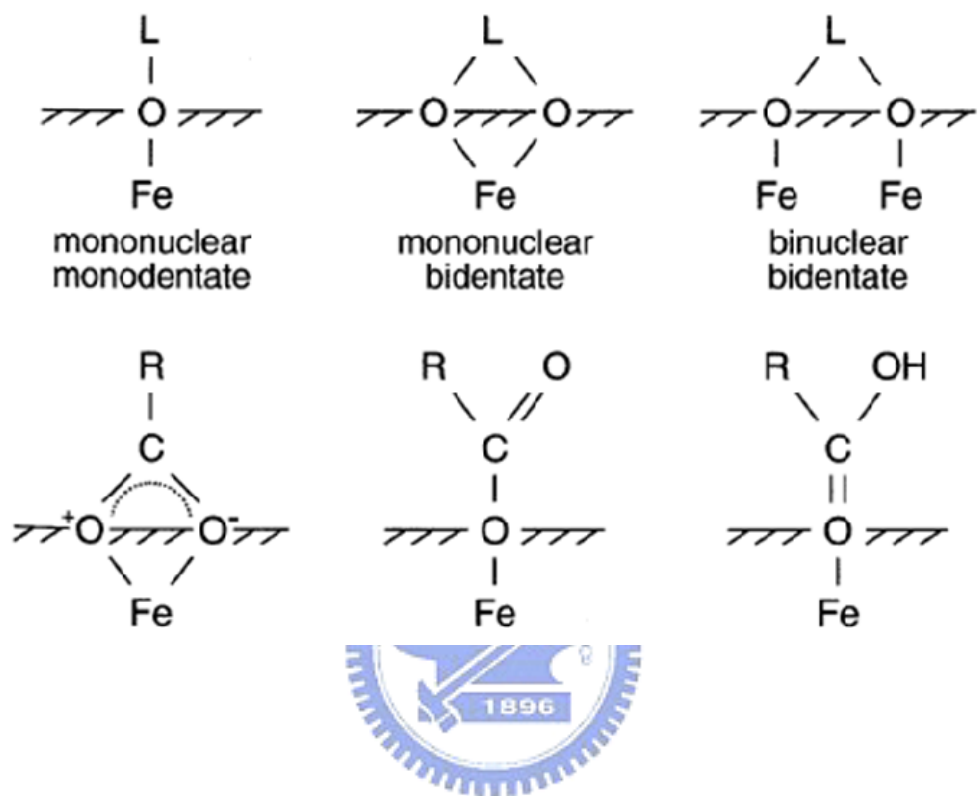


Figure 5.3.12 Modes of ligand coordination to the iron oxide surface and modes of coordination through COOH groups.

Tables

Table 5.3.1 Intensities a_0 of chemical bonds convoluted to the O_{1s} spectrum of surfaces treated by diode plasma with $V_b=560$ V for various τ .

| | Untreated | 2 min | 10 min | 20 min |
|--------------------------------|-----------|---------|---------|---------|
| a_2 | 2.4417 | 2.1913 | 2.1651 | 1.8080 |
| a_3 | 0.9357 | 0.8819 | 0.9450 | 0.8835 |
| N-C=O | 6800.6 | 6764.0 | 5146.1 | 4819.8 |
| C-O-C | 3677.0 | 2840.4 | 1239.9 | 1658.8 |
| C-O-Fe | 0 | 2496.4 | 4747.1 | 5339.1 |
| Fe ₂ O ₃ | 0 | 51.8 | 3731.7 | 3405.3 |
| Total | 10477.6 | 12152.6 | 14864.8 | 15223.0 |



Table 5.3.2 Intensities a_0 of chemical bonds convoluted to the O_{1s} spectrum of surfaces treated by different V_b for 20 min.

| | Untreated | 420 V | 560 V | 700 V |
|--------------------------------|-----------|---------|---------|---------|
| a_2 | 2.4417 | 2.0168 | 1.8080 | 1.5954 |
| a_3 | 0.9357 | 0.8592 | 0.8835 | 0.8121 |
| N-C=O | 6800.6 | 5970.3 | 4819.8 | 2995.5 |
| C-O-C | 3677.0 | 1595.9 | 1658.8 | 742.2 |
| C-O-Fe | 0 | 5305.1 | 5339.1 | 5453.3 |
| Fe ₂ O ₃ | 0 | 1946.4 | 3405.3 | 7649.7 |
| Total | 10477.6 | 14817.7 | 15223.0 | 16840.7 |

Chapter 6

Concluding Remarks

6.1 Looking back

We began this thesis by introducing a way to obtain a controllable alignment mode in a direct-current ion beam sputter equipped with diode-type electrodes. The polyimide SE-130B surfaces bombarded with ion-beam energies of 560 V and 1120 V result in a homogeneous alignment and a homeotropic alignment of liquid crystals, respectively. We found the main structures including the C-N, C-O-C bonds, and the aromatic rings of polyimide films are significantly destroyed in the ion beam bombardments and the formation of N-C=O bonds is considered as the neutralization of dangling bonds when exposed to the air. We deduced that, as summarized in Stöhr et al.'s work, the anisotropic destruction to the aromatic groups of polyimide film dominate the alignment mechanism. The alignment effects are attributed to the intermolecular interactions between the liquid crystals and the unbroken polyimide chains, or more precisely, the π orbital of benzene rings. The possibility of ultraviolet light induced alignment effect has been excluded in our ion beam treatment process.

In addition, for beam energy higher than 560 V, an unexpected coating of iron element on the bombarded polyimide surface lead to an interesting discovery that an excellent homeotropic alignment of liquid crystals is even achieved without any polyimide coating on the substrate. We have confirmed that the coated material is an iron oxide of γ -Fe₂O₃ which has intrinsic magnetism. The saturation magnetization, net magnetization and magnetic anisotropy have been found to be related to the thickness of γ -Fe₂O₃ film. All of them become raised as the film thickness decreases. Besides, the polar anchoring strength is measured against the film thickness. A polar anchoring strength larger than that of a DMOAP film is obtained by controlling the film thickness less than 424 nm. We found a thickness-dependence as well as that of the magnetic properties, which implies an interrelation between them from a microscopic point view. Meanwhile, we addressed an issue of what will happen to the magnetic properties of

films after annealing. The analyzed mean size of the particles composed of $\gamma\text{-Fe}_2\text{O}_3$ material is 30 ± 5 nm. And it cannot be effectively controlled by the coating time and beam energy. Even the ferrite films are thermally treated, no significant change in size of particle is found either. However, the saturation and net magnetizations are greatly improved. Accordingly, we speculate that the magnetic field induced by $\gamma\text{-Fe}_2\text{O}_3$ or/and the intermolecular interaction at the liquid-crystalline-maghemite interface give rise to the resultant homeotropic alignment of liquid crystal. To verify the former speculation, we proposed a simple model to explain how the magnetic field is induced and affect the orientation of nematic liquid crystal near the surface. However, the theories of deducing the polar anchoring strength from the experimental results built without the detail descriptions of surface structures from a microscopic point of view and the lack of the information about the properties of the amorphous film formed with the magnetic nanoparticles lead to that the resultant is underestimated. More investigations on the relation between the nanostructures and the revealed magnetic properties are required in the future. In addition, verification of both dipole-dipole and acid-base interactions is also essential for the understanding of fundamental alignment mechanism.

In the subsequent chapters, two methods are proposed to induce the liquid crystal alignment with high pretilt angle. Their mechanisms of determining the pretilt angle were also discussed.

Firstly, newly developed copolymer films MAPHM-F8 with different concentration of fluorinated carbonyl groups have been used in photo-irradiation and ion beam treatments. We found that the pretilt angle is controllable by the content of the fluorinated groups CF_2 grafted in the F8 side chains. A pretilt angle of 34° is achieved on the LPUVL-irradiated $X_{2/3}$ film surface. The crosslinking reaction is confirmed dominant in the treatment by LPUVL irradiations. Besides, an additional dosage has found to be required for the MAPHM-F8 film with higher mole fraction of F8 group to accomplish the photo-crosslinking of MAPHM groups. It is also observed that the fluorinated carbonyl side chains are preferentially clustered at the surfaces. The fluorine content on the surface decreases after 10 min irradiation and the depth-dependence is reduced as well, which means that the excess CF_2 grafted side chain seems to be diffused back into the film. It is expected that the depth-dependence of F content should

be eliminated and an approach to the ideal amount without depth issue is observed after a long-term irradiation of LPUVL.

On the contrary, the ion beam bombardment reduces the fluorine content drastically, which leads to a much smaller pretilt angle. This is because that the bond-breaking reaction still dominates in the ion beam bombardments. The newly formed C=O carbonyl groups due to the re-oxidization cause a larger increase of polar surface energy. We found that the polar component of the surface tension in turn dominates the pretilt angle.

Secondly, a surface alignment method by using the plasma beam irradiation on the polyimide SE-130B surface with simultaneous coating of maghemite nanoparticles is demonstrated. The homogeneous alignments of liquid crystals with good quality and reliability are obtained on the polyimide surfaces treated with plasma energy lower than 700 V. The pretilt angle can be controlled by different plasma energies and treating time. The determination of pretilt angle should be related to the size and the distribution density of the aggregation. In addition, the C-O-Fe bond could also increase the dispersive surface energy by bonding with the aromatic rings. Accordingly, we deduce that the competition of intermolecular interactions between the plasma-treated polyimide surface and the coated iron-oxide nanoparticles leads to the resultant pretilt angle.

The polyimide surfaces treated by ion beams show no microgroove structure but only with roughness changing with bombarding time and ion-beam energy. There is no strong connection between the measured pretilt angle and the roughness for the polyimide surfaces treated by the ion-beam and plasma-beam bombardments.

6.2 Looking forward

Until now, we have gone through several applications of a diode-type ion sputter for the liquid crystal alignment. The most attractive part is not only pursuing high quality of liquid crystal alignment but making the underlying mechanism well understood. To achieve a goal like this, each link between the results should be taken into consideration carefully. However, several issues are still unresolved. For example,

the dominant interaction between the γ -Fe₂O₃ film surface and liquid crystal molecule is still unknown due to the lack of information about the distribution of magnetization. What is the primary component of the aggregation shown on the plasma-beam treated polyimide film? How does the cluster structure get formed? These topics are interesting from application and academic point of view. Further studies should be carried out to clearly understand the mechanism of determining the pretilt angle in the future.

Acknowledgement

I would like to thank my colleagues Mr. Chih-Yu Wang and Ms. Meng-Chiou Huang first for doing the part of experiments. We would also like to thank Prof. Wen-Bin Jian and his students, Mr. Chin-Lun Lin, Mr. Yi-Jan Chen and Mr. Chau-Jen Hou, from Electrophysics department of National Chiao Tung University for help with the SQUID measurement, SPM and SEM surveys, Dr. Chein-Dhau Lee from Material and Chemical Research Laboratories of Industrial Technology Research Institute for the offer of copolymer MAPHM-F8, and Prof. Chwung-Shan Kou from Physics department of National Tsing Hua University for the use of equipment for measuring contact angle. Finally, I would like to thank Prof. Jenn-Chang Hwang for valuable suggestion in XPS analyses. This dissertation cannot be done without all of your generous support.

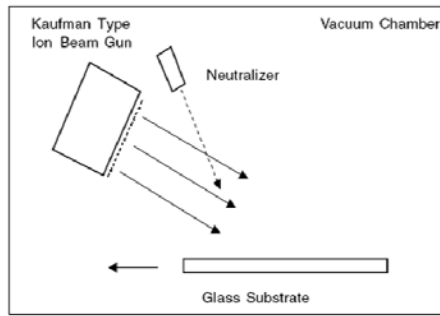
Appendix A

Ion Sources

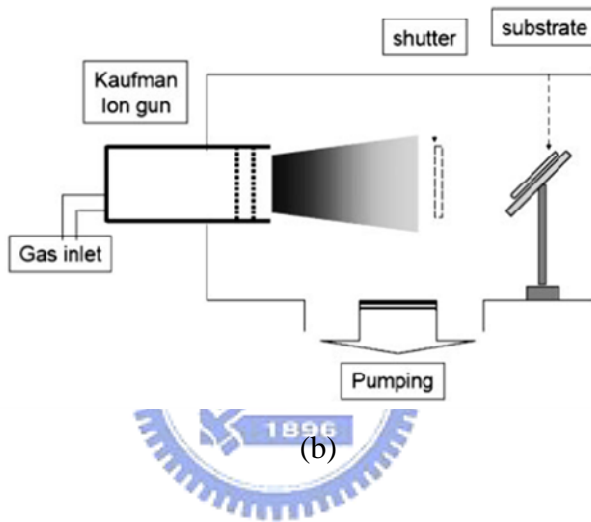
For sputtering, there are two classes of systems used to generate ions: plasmas and ion beams. The only real difference is that in the plasma source, the target surface is immersed in the plasma, and in the ion beam case, an independent plasma source is utilized and an ion beam is extracted to bombard the target surface. In the following, a description about ion beam system is addressed first.

Kaufman-type ion sources are typically considered to be a gridded broad beam ion source of permanent magnet design, with thermionic cathode filament to provide a source of electrons to support a magnetically confined plasma discharge. Compared to the conventional plasma diode, it offers a high degree of independent control for background pressure, ion current density, and ion energy and direction [1,2]. The pressure of the etching or deposition region is also substantially independent of discharge-chamber requirement. All of these advantages associated with spatial and electrical isolation of the ion production region from the target or substrate have resulted in greatly increased use of broad-beam ion sources in a variety of sputtering and thin-film applications. Typically, the working gas would be argon, and a two or three grid optic system being used to extract the ion beam. An additional source of electrons, usually being required for ion beam neutralization, is provided by tungsten filament, hollow cathode electron source, or plasma bridge neutralizer.

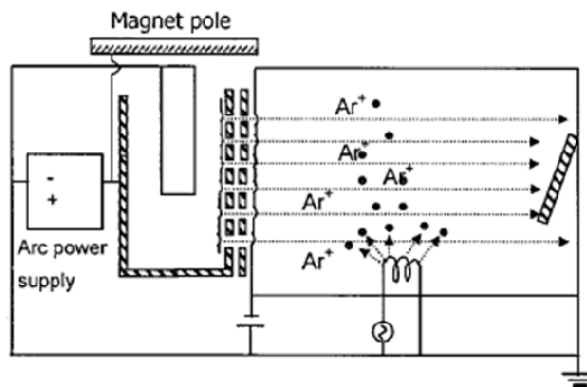
Until now, ion beam treatment for surface alignment of liquid crystals has been reported by several research groups. Kaufman-type ion source is mostly adopted for producing the collimated beam of ions in their works. In 1998, Chaudhari *et al.* firstly demonstrated the surface alignment using this type of ion source [3,4]. Ions are created using the direct-current (dc) plasma and accelerated using a dual grid configuration. In order to prevent the ion beam from diverging due to the repulsion of positively charged ions, a neutralizer filament on the outside of the ion source provides electrons to the ion beam through thermionic emission, as showing in Fig. A1(a). In 2002, Hwang et al. also used a Kaufman-type ion gun to treat a diamond-like carbon thin film [5]. Their



(a)



(b)



(c)

Fig. A1 Schematic drawing of ion beam system utilized in (a) Chaudhari *et al.*'s, (b) Hwang *et al.*'s, and (c) Gwag *et al.*'s works.

configuration of ion beam system is drawn in Fig. A1(b). After that, in 2004, Gwag *et al.* utilized an ion source of cold hollow cathode (CHC) type to obtain the ion beam [6]. Figure A1(c) plots its configuration, only the CHC is fed with argon gas. A discharge ignition takes place in the cathode chamber at nominal values of voltage. The extracted ions are collimated using the two perforated grids as electro-focusing lenses. Although the Kaufman-type ion source has been successfully applied to surface alignment of liquid crystals, the complexity of configuration and high cost cannot make itself an alternative in replacing the conventional rubbing method.

A **diode-type** dc sputter with planar electrodes is, therefore, adopted to offer the ion source for surface treatments due to its simplicity of configuration and low cost in this thesis. It is the simplest kind of plasma device composed of an anode and a cathode inside a vacuum system. Under the appropriate condition with adequate voltage across the electrodes and the gas pressure, the gas will breakdown into plasma discharge which

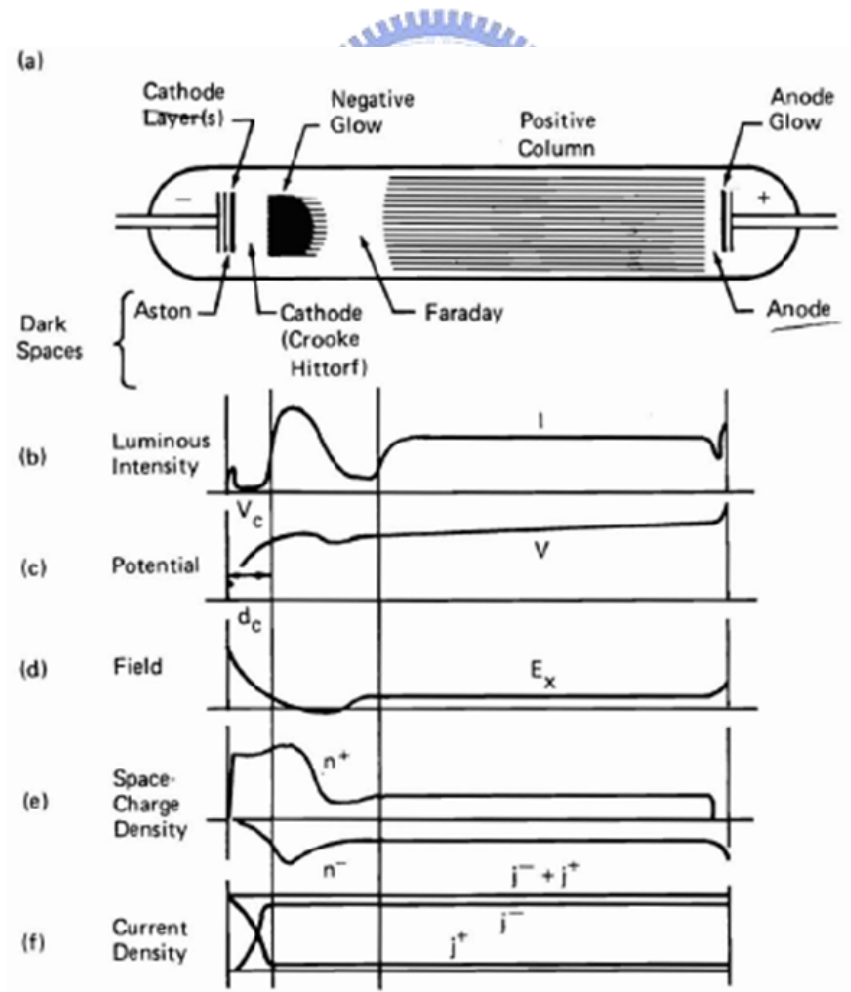


Fig. A2 The normal glow discharge in neon in a 50 cm tube at pressure of 1 torr.

is schematic represented in Fig. A2 [7].

In this discharge, a dark space or sheath occurs near the cathode in which there is a very large electric field. Its thickness is typically 1 to 4 cm, depending on the pressure and current density [8]. Ions are accelerated rapidly across the cathode dark space and strike the cathode. As part of collisions which cause sputtering, the secondary electrons are emitted from the sputtered surface. These electrons are very important to maintaining the plasma discharge. They are accelerated back across the cathode sheath. The energy gains of secondary electrons are used to form more ions in negative glow through collisions with gas atoms. Negative glow has the brightest intensity of the discharge and, however, the relatively low electric field, as shown in Fig. A2. The positive column is the region of the discharge which most nearly resembles a plasma, and most of the classic probe studies have been made on positive columns which is quasi-neutral [9]. The positive column is characterized by a region of uniform field, zero gradient of the plasma density and zero net space-charge. Electrons are accelerated across this region. It is found that, when the two electrodes are brought together, the cathode dark space and negative glow are unaffected while the positive column shrinks. This process continues so that eventually the positive column, and then the Faraday dark space, is consumed, leaving only the negative glow and dark spaces adjacent to each electrode. This last situation is the usual case in glow discharge processes where the inter-electrode separation is just a few times the cathode dark space thickness, as sketched in Fig. A3 [10]. The minimum separation is about twice the dark space

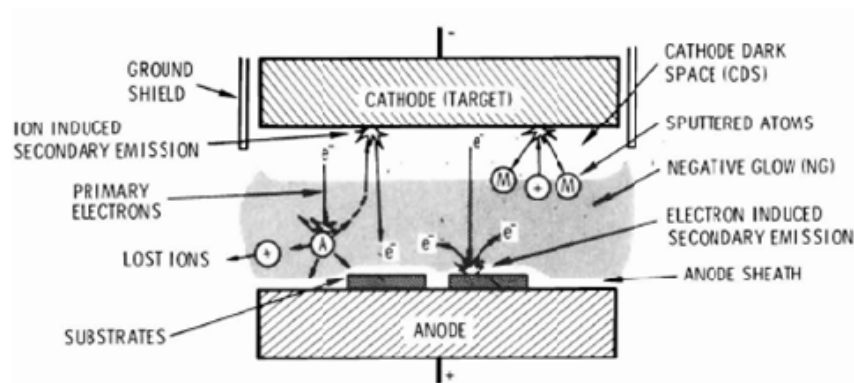


Fig. A3 Schematic representation of self-sustained plasma induced in a planar diode.

thickness; at less than this, the cathode dark space is distorted and then discharge is extinguished. Figure A4 plots the potential distribution of three basic regions, negative glow and two dark spaces adjacent to each electrode, in a dc glow discharge process [11]. The plasma is virtually field-free, so it has the same potential V_p adjacent to the sheath at the cathode. Some peculiarities should be noticed: Firstly, the plasma does not take a potential intermediate between electrodes. Secondly, the electric fields in the system are restricted to sheaths at each of electrodes. Thirdly, the sheath fields are such as to repel electrons trying to reach either electrode. Since current must be continuous in this discharge system, that means the currents at each of electrodes have to be equal. Therefore, all of these peculiarities follow from the mass of electron being so much less than that of ion.

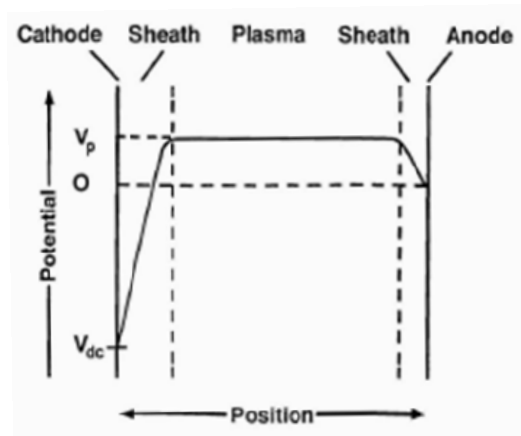


Fig. A4 Potential distribution in a dc glow discharge process.

However, in this thesis, the utilized dc sputter also shows the Faraday dark space in the operation with a lower dc bias. An increase of bias will cause the extension of cathode dark space and elimination from discharge system if the bias is high enough. It should be addressed that both operating modes are used in this thesis. In Chap. 2, the etching mode is selected to treat the polyimide film immersed in cathode region by bombarding of accelerated ions. On the contrary, in Chap. 5, the treatment is conducted in coating mode. The polyimide films are set in the region of negative glow and/or Faraday dark space. As shown in Fig. A2(e), the strong density gradient of electrons in the Faraday dark space causes them to diffuse toward the anode region.

References

1. H. R. Kaufman, *J. Vac. Sci. Technol.* 15(2), 272 (1978).
2. H. R. Kaufman, J. M. E. Harper, and J. J. Cuomo, *J. Vac. Sci. Technol.* 21(3), 764 (1982).
3. P. Chaudhari, J. A. Lacey, S. C. Lien and J. L. Speidell, *Jpn. J. Appl. Phys.* 37, L55 (1998).
4. J. P. Doyle et al., *Nuclear Instruments and Methods in Physics Research B* 206, 467 (2003).
5. J. Y. Hwang, Y. M. Jo, D. S. Seo, S. J. Rho, D. K. Lee, and H. K. Baik, *Jpn. J. Appl. Phys.* 41, L654 (2002).
6. J. S. Gwag, C. G. Jhun, J. C. Kim, T. H. Yoon, G. D. Lee, S. J. Cho, *J. Appl. Phys.* 96, 257 (2004).
7. E. Nasser, *Fundamental of Gaseous Ionization and Plasma Electronics*, (Wiley-Interscience, New York, 1971).
8. W. D. Westwood and R. Boynton, *J. Appl. Phys.* 43, 2691 (1972).
9. B. Chapman, *Glow Discharge Processes: Sputtering and Plasma Etching*, (Wiley, New York, 1980), Chap. 4, pp. 77-82.
10. J. L. Vossen and J. J. Cuomo, *Thin Film Processes*, ed. J. L. Vossen and W. Kern (Academic Press, New York, 1978), pp. 1-73.
11. F. D. Egitto and L. J. Matienzo, *Polyimides: Fundamental and Applications*, ed. M. K. Ghosh and K. L. Mittal (Marcel Dekker, New York, 1996), pp. 391-397.

Appendix B

Polar Anchoring Strength Measurement

In the past few decades, the liquid crystal (LC) has been widely used in the field of information display. The surface treatment that orients the liquid crystal director (the unit vector presenting the thermal average of LC molecular orientations) at the boundaries contacting with substrates plays an important role in these devices. As a result, understanding the surface phenomenon of LC is of prime important. The surface anchoring strength holding the director at the surface is one of the important parameters to characterize the alignment properties and simple methods for experimental determining this quantity are demanded.

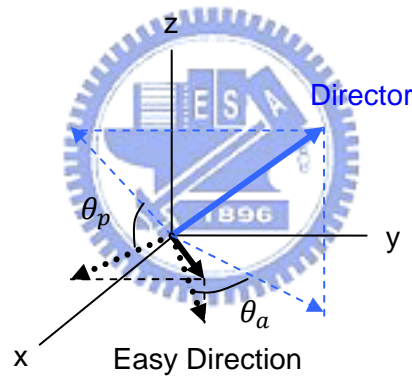


Fig. B1 Schematic representation of the displacement of component angles

The lowest order approximation for orientational surface energy of LC on a solid surface with an alignment treatment can be written as

$$f = \frac{1}{2} (W_a \sin^2 \theta_a + W_p \sin^2 \theta_p), \quad (1)$$

where θ_a and θ_p are the small displacement of azimuthal angle and polar angle, respectively, as shown in Fig. B1, when the director is rotated away from the original surface alignment direction. The two constants W_a and W_p are then defined as the azimuthal anchoring strength and the polar anchoring strength (PAS), respectively. In many of the liquid crystal display (LCD) modes such as twist-nematic (TN) mode,

vertical align (VA) mode and electrically controlled birefringence (ECB) mode, the driving field are applied in the direction perpendicular to the substrates. As a result, the polar (out of plane) anchoring strength becomes the major surface property critical to their operation.

Many techniques have been developed to measure the polar anchoring strength of cells with different alignment types such as planar [1], vertical (or homeotropic) [2,3] and hybrid [4] alignments. Each technique has its own limitations that often require specific material parameters or the direction of alignment [2]. Furthermore, these techniques may give values differ by two to three orders of magnitude on polar anchoring strength, even for the same pair of liquid crystal and substrate.

The high-electric-field (HEF) method [5] suggested by Yokoyama and van Sprang is a popular technique in external-field techniques [6-8] that measure the director deviations with respect to the applied field. The HEF technique measures the capacitance and optical phase retardation R simultaneously while varying the voltage applied to the nematic cell. Despite employing a small current-regulating capacitor connected in series with a LC cell is proposed by Yokoyama and SUN to remove the measurement of capacitance [9], a more powerful voltage source is needed in that technique. A very attractive feature of this technique is that in a certain range of applied voltage, the phase retardation is a linear function of inverse of the applied voltage. The PAS can be simply deduced from the intercept of this linear function with the R axis. However, the experimental data often do not follow the theoretical curves and significant differences exist among the values obtained by fitting data of different voltage ranges. Even negative values of PAS can be obtained sometimes by this method. Nastishin *et al.* have made a close study on this discrepancy of PAS [6]. Their results indicate that the behavior of liquid crystal at the substrate is intrinsically complicated and the in-plane inhomogeneities (such as variations of the anchoring energy, surface polarization, fracture in the patterned electrodes, etc.) should be considered in the theory. Moreover, since the intercept is very close to zero comparing to the measured data points, a small change in the slope of the linear fitting can result a very large change in the deduced PAS value. The discrepancies among different fitting range are partly due to this reason.

In the following, methods adopted in this thesis to obtain the PAS of a homogeneous and a homeotropic cells are introduced. We consider the planar case first using the analytical method proposed by Nastishin *et al.* in 1999 [8]. Instead of measuring the phase retardation R of the NLC cell as in the HEF method, we measure the transmittance of a polarized light passing through a pair of crossed polarizers and the NLC cell aligned in between. The transmittance T can be derived as [10]

$$T = \sin^2(2\Theta)\sin^2(R/2), \quad (2)$$

where Θ is the angle between the direction of polarizer and the e-ray direction of NLC cell. Besides, removal of capacitance measurement was achieved by a replacement of theoretical value.

In experiment, the transmittance T of LC cell is recorded against the applied voltage V . Figure B2 plots the experimental setup for measuring T - V curves. A pair of crossed polarizers is used and the LC cell is placed between these two polarizers such that the optical axis of the cell is at 45° with respect to the entrance polarizer. The chopper and lock-in amplifier are used to improve the sensitivity of our measuring system. The AC source consisting of a function generator and a power amplifier gives a 1 kHz square form of voltage into the LC cell. In order to remove the error caused by intensity variation of laser, the laser beam is divided into a probe beam and a reference

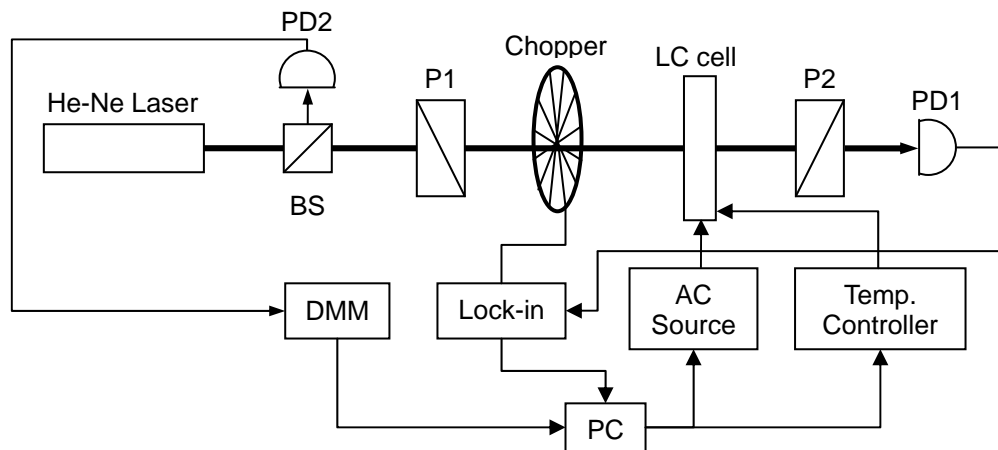


Fig. B2 Experimental setup for measuring the optical transmittance of the LC cell: P1 and P2, polarizers; PD1 and PD2, photo-detectors; BS, beam splitter; DMM, digital multi-meter; Lock-in, Lock-in amplifier. (The light source is a He-Ne laser with wavelength 632.8nm and the two polarizers are Glan-Thompson type).

beam. The intensities of these two beams are recorded simultaneously and a modified intensity given by $I = I_{pro}/I_{ref}$ is used through this work. The temperature is maintained at constant with a fluctuation less than 10 mK.

According to the Eq. (2), each local maximum or minimum of the transmittance should have the same values as one or zero, respectively. However, each extreme value is different from each other as plotted in Fig. B3. The small but nonzero minimum intensity comes from the misalignments of the two substrates, the small strain-induced birefringence in the glass, possible imperfections in the polarizers and scattering of LC. In order to get a more accurate polar anchoring strength, the residue intensity I_{res} , should be subtracted from the measured signal. We obtain I_{res} by measuring I with the cell heated to a temperature well above the clear point. We choose the peak intensity at the highest voltage as I_{max} , because the applied voltage is high enough to eliminate most of the effects just mentioned. Consequently, the real transmittance T can be obtained by $T = (I - I_{res})/(I_{max} - I_{res})$.

After the transformation of T into R , it is followed with that an analytical process is

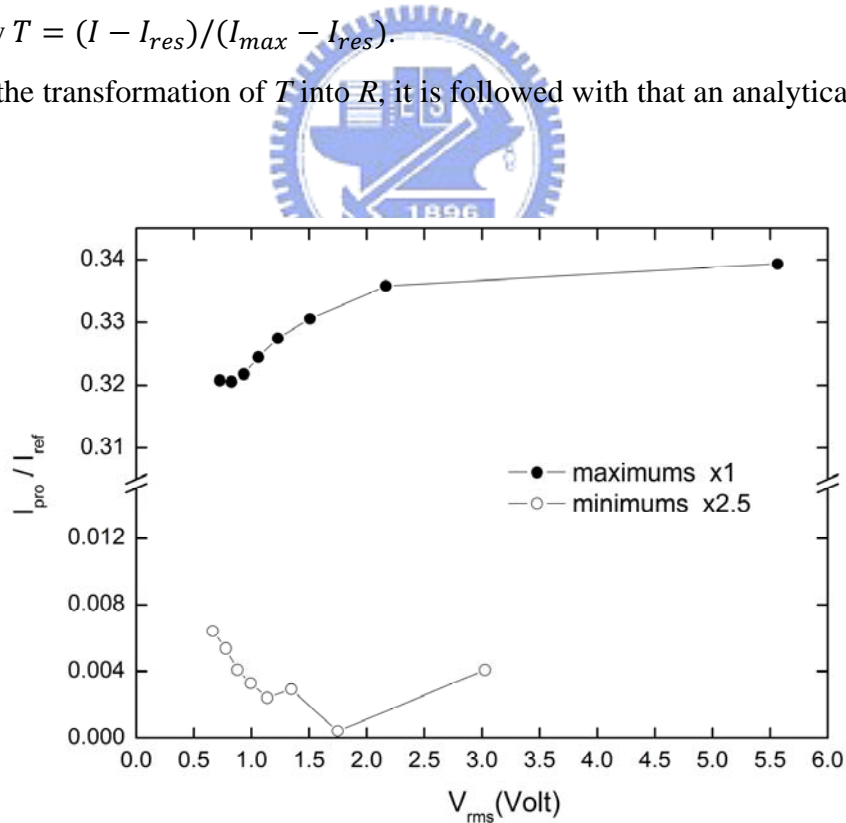
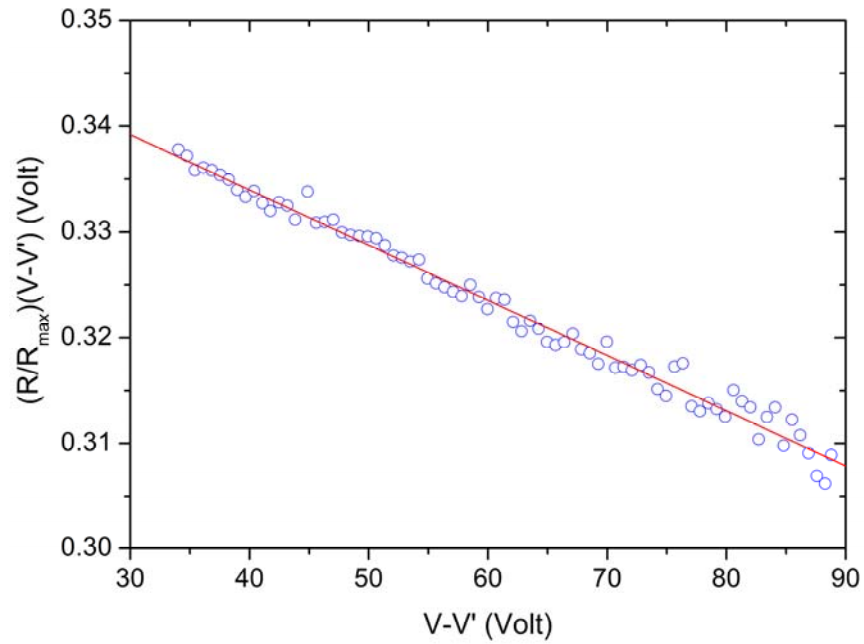
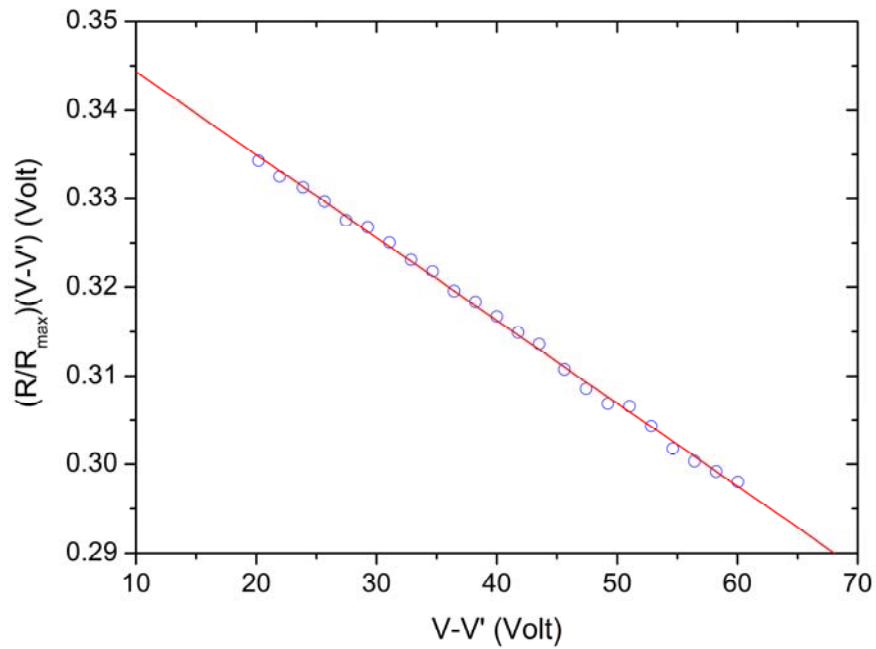


Fig. B3 The extreme values of intensity measured as a function of the applied voltage. The sample is IB-aligned (DC voltage of 560 V, current density of 255 $\mu\text{A}/\text{cm}^2$, irradiation time of 8 min, and angle of incidence of 60° with thickness of LC layer being 32.4 μm).



(a)



(b)

Fig. B4 Dependence of $(V - V')R/R_{max}$ plotted against $(V - V')$. The solid line represents the best linear fit to the data (a) from 34.0 V to 88.8 V and yields $W_p = 6.6 \times 10^{-4}$ J/m² of a rubbed 5CB cell and (b) 20.2 V to 60.0 V and yields $W_p = 3.2 \times 10^{-4}$ J/m² of an ion-beam bombarded 5CB cell with condition of 560 V, 255 μ A/cm², 60° and 90 sec for ion energy, current density, angle of incidence and treating time, respectively.

conducted to obtain the PAS according to Nastishin *et al.*'s proposal [8]. A further processing of the experimental R - V data is required to satisfy the mathematical form:

$$(V - V')R/R_{max} = \tilde{J}_0 - (1 + \kappa y_p)(V - V')2K_1/W_p d, \quad (3)$$

$$V' = \frac{1}{\epsilon_1} \sqrt{\frac{(\epsilon_1 - \epsilon_2)K_1}{\epsilon_0}} \int_{y_p}^1 \sqrt{\frac{(1+\gamma)(1+\kappa y)}{y(1+\gamma y)}} dy,$$

$$y_p = \sin^2 \theta_p, \kappa = (K_3 - K_1)/K_1, \text{ and } \gamma = (\epsilon_1 - \epsilon_2)/\epsilon_2$$

where \tilde{J}_0 is a constant associated with physical properties of LC, R_{max} is the retardation under no external field, θ_p is the pretilt angle of LC cell, K_1 and K_3 are splay and bend elastic constant, respectively, ϵ_1 and ϵ_2 are the components of dielectric tensor that are parallel and perpendicular to the director, respectively, and ϵ_0 is dielectric constant of vacuum. It should be noticed that the linear relation revealed in Eq. (3) is only valid within a certain range of applied voltage (V_{min}, V_{max}). This criterion is resulted from two assumptions [5] taken into the deduction of Eq. (3). In general, V_{min} is determined by $6V_{th}$ depending on the physical properties of LC. However, V_{max} is evaluated by $(0.2/\pi \cos \theta_p)(W_p d/K_1)V_{th}\sqrt{\epsilon_2/\epsilon_1}$ which includes the desirable W_p . That means the range of applied voltage chosen for fitting has to be self-consistent within that evaluated according to the fitted result.

Two 5CB cells, for example, aligned by rubbed and ion-beam bombarded polyimide surfaces are considered and linear fits of the processed data are shown in Fig. B4(a) and Fig. B4(b), respectively. For the rubbed cell, $W_p = 6.6 \times 10^{-4} \text{ J/m}^2$ obtained by fitting through the range from 34.0 V to 88.8 V gives a reasonable range of fit (4.60 V, 116.27 V). For the ion-beam treated cell, the fit range chosen from 20.2 V to 60.0 V results in $W_p = 3.2 \times 10^{-4} \text{ J/m}^2$ which suggests a consistent range of (4.59 V, 64.88 V).

Now, we turn to deal with the vertically-aligned LC cell in a similar way proposed by Nie *et al.* in 2005 [11]. Description of the equations deduced for vertical case will be skipped in the following due to a similar idea is used. We will compare the W_p obtained by different fitting processes with or without capacitance measurements instead. For accurate determination of PAS, capacitance measurement is essential. Figure B5 plots the voltage-dependent capacitance of a VA cell filled with negative LC mixture MLC-6608. The intercept extrapolation method proposed by Yokoyama *et al.* is

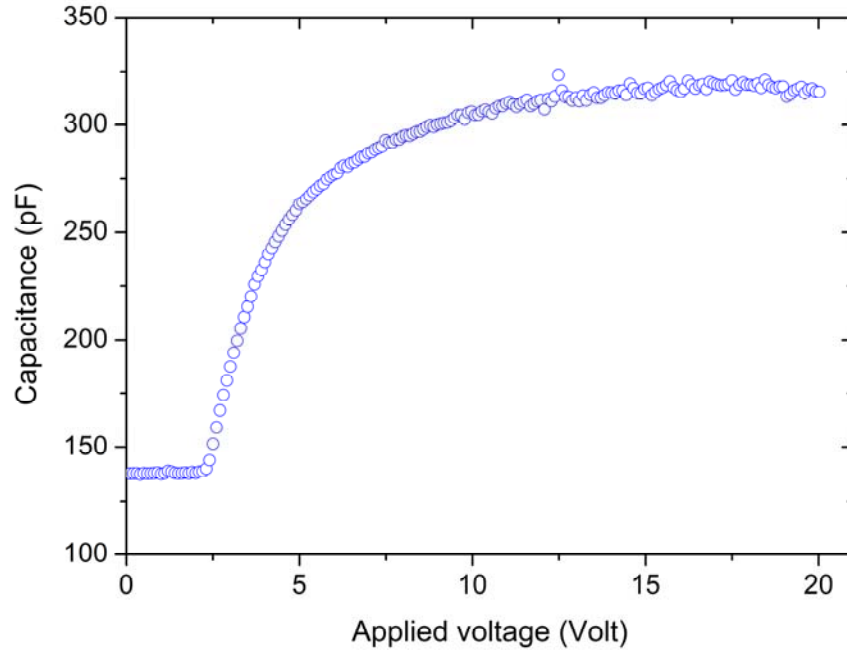


Fig. B5 Voltage-dependent capacitance of a VA cell filled with MLC-6608.

used [5] and a linear fit shown in Fig. B6(a) gives an intercept of 1.0404, moreover, a PAS of $1.2 \times 10^{-4} \text{ J/m}^2$ is evaluated. Without capacitance measurement, a less accurate W_p is obtained as $1.1 \times 10^{-4} \text{ J/m}^2$, as shown in Fig. B6(b). The difference between these two values is not significant, even the error due to the precision of measured LC-layer thickness is close to $0.1 \times 10^{-4} \text{ J/m}^2$. Nonetheless, we still could skip the capacitance measurement for convenience if comparison between a series of samples is required only. Finally, it should be addressed that accuracy of determining the PAS is also related to correctness of each LC parameter which is intrinsically temperature-sensitive. As a result, the clear point of LC should be accurately determined as well.

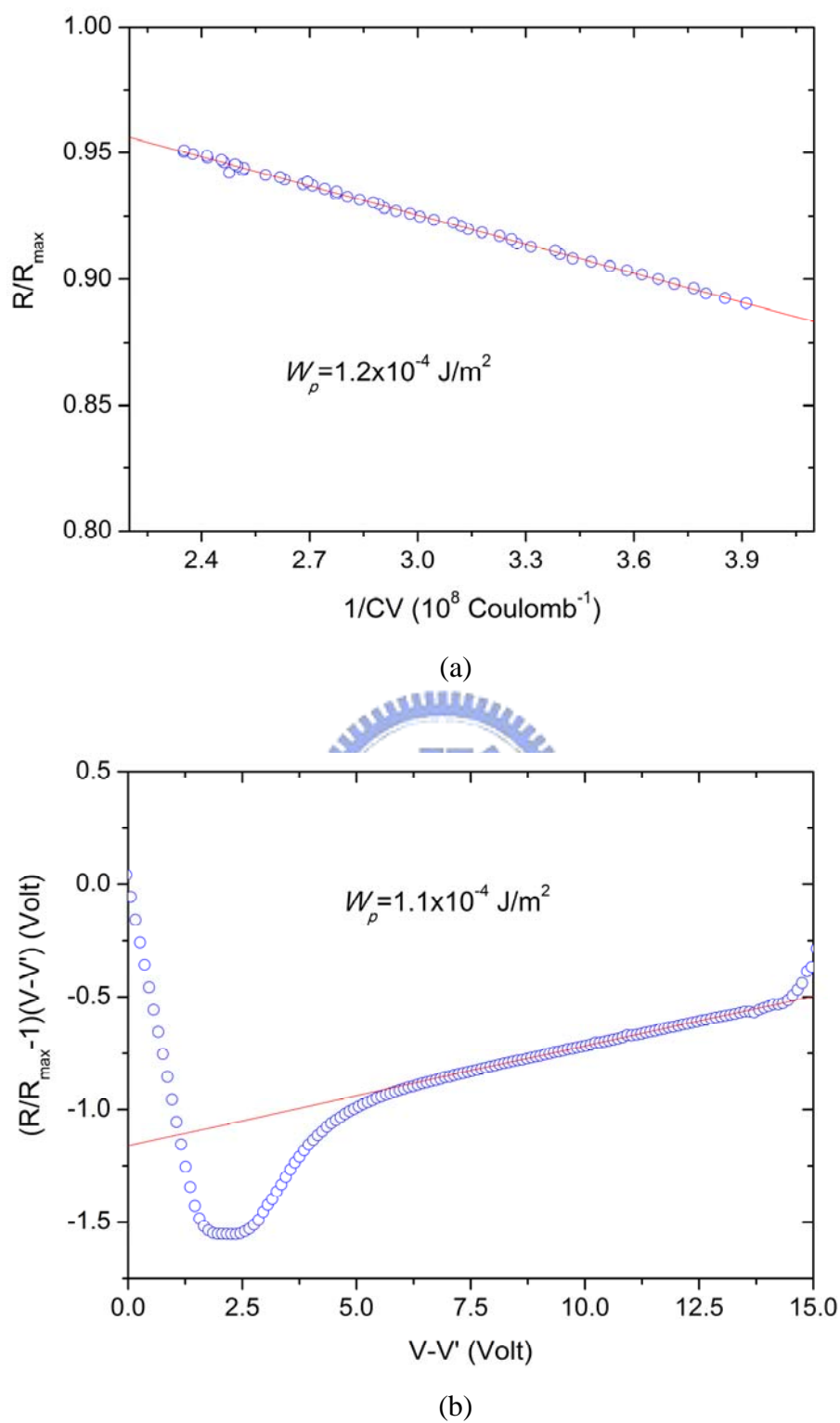


Fig. B6 Illustration of the (a) intercept extrapolation method and (b) slope fitting method. A MLC-6608 cell aligned by γ -Fe₂O₃ film with thickness of 212 nm is used as an example.

References

1. K. H. Yang, *J. Appl. Phys.* 53, 6742 (1982).
2. S. Naemura, *Appl. Phys. Lett.* 33, 1 (1978).
3. G. Carbone and C. Rosenblatt, *Phys. Rev. Lett.* 94, 057802 (2005).
4. L. T. Hung, O. Shinichirou, K. Munehiro and A. Tadashi, *Jpn. J. Appl. Phys.* 43, No. 5B, L649 (2004).
5. H. Yokoyama and H. A. van Sprang, *J. Appl. Phys.* 57, 4520 (1985).
6. Yu. A. Nastishin, R. D. Polak, S. V. Shiyanovskii, V. H. Bodnar, and O. D. Lavrentovich, *J. Appl. Phys.* 86, 4199 (1999).
7. D. F. Gu, S. Uran, and C. Rosenblatt, *Liq. Cryst.* 19, 427 (1995).
8. Yu. A. Nastishin, R. D. Polak, S. V. Shiyanovskii, and O. D. Lavrentovich, *Appl. Phys. Lett.* 75, 202 (1999).
9. H. Yokoyama and R. Sun, *Jpn. J. Appl. Phys.* 39, L45 (2000).
10. R. C. Jones, *J. Opt. Soc. A.* 31, 488 (1941).
11. X. Nie, Y. H. Lin, T. X. Wu, H. Wang, Z. Ge, and S. T. Wu, *J. Appl. Phys.* 98, 013516 (2005).



Appendix C

Simulation of Magnetic Field Distribution

Assume a short segment of wire $d\vec{l}'$ carrying current I is located at \vec{r}' . To obtain the spatial distribution of magnetic induction $\vec{B}(\vec{r})$ induced by a well-defined arrangement of magnetic moments, the Biot-Savart law is used and can be written as

$$\vec{B}(\vec{r}) = \frac{\mu_0}{4\pi} \int \frac{I d\vec{l}' \times (\vec{r} - \vec{r}')}{|\vec{r} - \vec{r}'|^3}. \quad (1)$$

Let us consider the surface structure composed of square domains with equal size and magnetization M , as shown in Fig. 3.3.36(a). It is well known that a magnetic moment m could be equivalently replaced by IS where S is the area enclosed by the route of current. Therefore, the hypothetic structure is equivalent to the squarely-arrayed current loops, as shown in Fig. C1. The red loops represent the magnetic moments oriented toward the z-direction while the blue ones oriented in the opposite direction. Assume the length of each side of square domain is L ; the spatial distribution of magnetic field $\vec{H}(x, y, z)$ induced by a surface composed of nine square domains is then evaluated using the Eq. (1). The resultant can be written as the following:

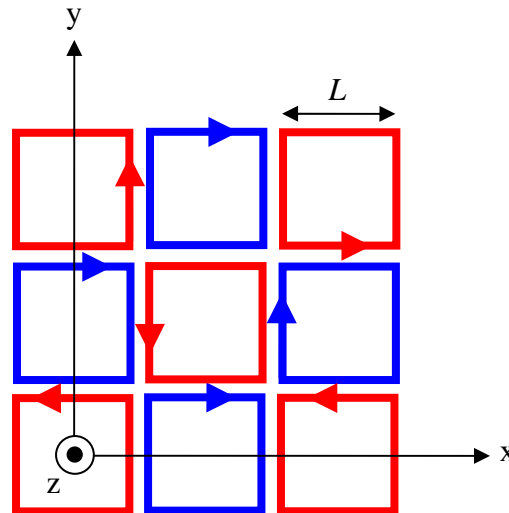


Fig. C1 Equivalent current-loops of squarely-arrayed magnetic domains

$$\vec{H}(x, y, z) = H_x(x, y, z)\hat{i} + H_y(x, y, z)\hat{j} + H_z(x, y, z)\hat{k}, \quad (2)$$

where \hat{i} , \hat{j} , and \hat{k} are the unit vectors along the x , y , and z axes, respectively, in the three-dimensional Cartesian coordinate system,

$$\begin{aligned} H_x(x, y, z) = & \frac{-m}{4\pi L^2} \left[\frac{z}{z^2+(x+L/2)^2} \left(\frac{2y-3L}{\sqrt{z^2+(y-3L/2)^2+(x+L/2)^2}} + \frac{y+L/2}{\sqrt{z^2+(y+L/2)^2+(x+L/2)^2}} - \right. \right. \\ & \left. \frac{y-5L/2}{\sqrt{z^2+(y-5L/2)^2+(x+L/2)^2}} - \frac{2y-L}{\sqrt{z^2+(y-L/2)^2+(x+L/2)^2}} \right) + \frac{2z}{z^2+(x-L/2)^2} \left(\frac{2y-L}{\sqrt{z^2+(y-L/2)^2+(x-L/2)^2}} - \right. \\ & \left. \frac{y+L/2}{\sqrt{z^2+(y+L/2)^2+(x-L/2)^2}} - \frac{2y-3L}{\sqrt{z^2+(y-3L/2)^2+(x-L/2)^2}} + \frac{y-5L/2}{\sqrt{z^2+(y-5L/2)^2+(x-L/2)^2}} \right) + \\ & \frac{2z}{z^2+(x-3L/2)^2} \left(\frac{y+L/2}{\sqrt{z^2+(x-3L/2)^2+(y+L/2)^2}} - \frac{2y-L}{\sqrt{z^2+(x-3L/2)^2+(y-L/2)^2}} + \right. \\ & \left. \frac{2y-3L}{\sqrt{z^2+(y-3L/2)^2+(x-3L/2)^2}} - \frac{y-5L/2}{\sqrt{z^2+(y-5L/2)^2+(x-3L/2)^2}} \right) + \\ & \left. \frac{z}{z^2+(x-5L/2)^2} \left(\frac{2y-L}{\sqrt{z^2+(x-5L/2)^2+(y-L/2)^2}} - \frac{y+L/2}{\sqrt{z^2+(x-5L/2)^2+(y+L/2)^2}} - \right. \right. \\ & \left. \left. \frac{2y-3L}{\sqrt{z^2+(y-3L/2)^2+(x-5L/2)^2}} + \frac{y-5L/2}{\sqrt{z^2+(y-5L/2)^2+(x-5L/2)^2}} \right) \right], \end{aligned}$$

$$\begin{aligned} H_y(x, y, z) = & \frac{-m}{4\pi L^2} \left[\frac{z}{z^2+(y+L/2)^2} \left(\frac{2x-3L}{\sqrt{z^2+(x-3L/2)^2+(y+L/2)^2}} + \frac{x+L/2}{\sqrt{z^2+(x+L/2)^2+(y+L/2)^2}} - \right. \right. \\ & \left. \frac{x-5L/2}{\sqrt{z^2+(x-5L/2)^2+(y+L/2)^2}} - \frac{2x-L}{\sqrt{z^2+(x-L/2)^2+(y+L/2)^2}} \right) + \frac{2z}{z^2+(y-L/2)^2} \left(\frac{2x-L}{\sqrt{z^2+(x-L/2)^2+(y-L/2)^2}} - \right. \\ & \left. \frac{x+L/2}{\sqrt{z^2+(x+L/2)^2+(y-L/2)^2}} - \frac{2x-3L}{\sqrt{z^2+(x-3L/2)^2+(y-L/2)^2}} + \frac{x-5L/2}{\sqrt{z^2+(x-5L/2)^2+(y-L/2)^2}} \right) + \\ & \frac{2z}{z^2+(y-3L/2)^2} \left(\frac{x+L/2}{\sqrt{z^2+(y-3L/2)^2+(x+L/2)^2}} - \frac{2x-L}{\sqrt{z^2+(y-3L/2)^2+(x-L/2)^2}} + \right. \\ & \left. \frac{2x-3L}{\sqrt{z^2+(x-3L/2)^2+(y-3L/2)^2}} - \frac{x-5L/2}{\sqrt{z^2+(x-5L/2)^2+(y-3L/2)^2}} \right) + \\ & \left. \frac{z}{z^2+(y-5L/2)^2} \left(\frac{2x-L}{\sqrt{z^2+(y-5L/2)^2+(x-L/2)^2}} - \frac{x+L/2}{\sqrt{z^2+(y-5L/2)^2+(x+L/2)^2}} - \right. \right. \\ & \left. \left. \frac{2x-3L}{\sqrt{z^2+(x-3L/2)^2+(y-5L/2)^2}} + \frac{x-5L/2}{\sqrt{z^2+(x-5L/2)^2+(y-5L/2)^2}} \right) \right], \end{aligned}$$

and

$$\begin{aligned} H_z(x, y, z) = & \frac{-m}{4\pi L^2} \left[\frac{y+L/2}{z^2+(y+L/2)^2} \left(\frac{x-5L/2}{\sqrt{z^2+(x-5L/2)^2+(y+L/2)^2}} + \frac{2x-L}{\sqrt{z^2+(x-L/2)^2+(y+L/2)^2}} - \right. \right. \\ & \left. \frac{x+L/2}{\sqrt{z^2+(x+L/2)^2+(y+L/2)^2}} - \frac{2x-3L}{\sqrt{z^2+(x-3L/2)^2+(y+L/2)^2}} \right) + \frac{2y-L}{z^2+(y-L/2)^2} \left(\frac{2x-3L}{\sqrt{z^2+(x-3L/2)^2+(y-L/2)^2}} + \right. \\ & \left. \frac{x+L/2}{\sqrt{z^2+(x+L/2)^2+(y-L/2)^2}} - \frac{x-5L/2}{\sqrt{z^2+(x-5L/2)^2+(y-L/2)^2}} - \frac{2x-L}{\sqrt{z^2+(x-L/2)^2+(y-L/2)^2}} \right) + \end{aligned}$$

$$\begin{aligned}
& \frac{2x-L}{z^2+(x-L/2)^2} \left(\frac{2y-3L}{\sqrt{z^2+(y-3L/2)^2+(x-L/2)^2}} + \frac{y+L/2}{\sqrt{z^2+(y+L/2)^2+(x-L/2)^2}} - \frac{y-5L/2}{\sqrt{z^2+(y-5L/2)^2+(x-L/2)^2}} - \right. \\
& \left. \frac{2y-L}{\sqrt{z^2+(y-L/2)^2+(x-L/2)^2}} \right) + \frac{x+L/2}{z^2+(x+L/2)^2} \left(\frac{2y-L}{\sqrt{z^2+(y-L/2)^2+(x+L/2)^2}} + \frac{y-5L/2}{\sqrt{z^2+(y-5L/2)^2+(x+L/2)^2}} - \right. \\
& \left. \frac{y+L/2}{\sqrt{z^2+(y+L/2)^2+(x+L/2)^2}} - \frac{2y-3L}{\sqrt{z^2+(y-3L/2)^2+(x+L/2)^2}} \right) + \\
& \frac{2x-3L}{z^2+(x-3L/2)^2} \left(\frac{2y-L}{\sqrt{z^2+(y-L/2)^2+(x-3L/2)^2}} + \frac{y-5L/2}{\sqrt{z^2+(y-5L/2)^2+(x-3L/2)^2}} - \right. \\
& \left. \frac{y+L/2}{\sqrt{z^2+(y+L/2)^2+(x-3L/2)^2}} - \frac{2y-3L}{\sqrt{z^2+(y-3L/2)^2+(x-3L/2)^2}} \right) + \\
& \frac{2y-3L}{z^2+(y-3L/2)^2} \left(\frac{2x-L}{\sqrt{z^2+(x-L/2)^2+(y-3L/2)^2}} + \frac{x-5L/2}{\sqrt{z^2+(x-5L/2)^2+(y-3L/2)^2}} - \right. \\
& \left. \frac{x+L/2}{\sqrt{z^2+(x+L/2)^2+(y-3L/2)^2}} - \frac{2x-3L}{\sqrt{z^2+(x-3L/2)^2+(y-3L/2)^2}} \right) + \\
& \frac{y-5L/2}{z^2+(y-5L/2)^2} \left(\frac{x+L/2}{\sqrt{z^2+(x+L/2)^2+(y-5L/2)^2}} + \frac{2x-3L}{\sqrt{z^2+(x-3L/2)^2+(y-5L/2)^2}} - \right. \\
& \left. \frac{2x-L}{\sqrt{z^2+(x-L/2)^2+(y-5L/2)^2}} - \frac{x-5L/2}{\sqrt{z^2+(x-5L/2)^2+(y-5L/2)^2}} \right) + \\
& \frac{x-5L/2}{z^2+(x-5L/2)^2} \left(\frac{y+L/2}{\sqrt{z^2+(y+L/2)^2+(x-5L/2)^2}} + \frac{2y-3L}{\sqrt{z^2+(y-3L/2)^2+(x-5L/2)^2}} - \right. \\
& \left. \frac{2y-L}{\sqrt{z^2+(y-L/2)^2+(x-5L/2)^2}} - \frac{y-5L/2}{\sqrt{z^2+(y-5L/2)^2+(x-5L/2)^2}} \right) \Big].
\end{aligned}$$

The z -dependence of H_z and H_x field components is shown in Fig. C2 and Fig. C3, respectively. Without exception, the mathematical form of H_y and H_x components should be similar to each other but composed of opposite variables (x and y). It is worth noticing that the H_z component is distributed over the most part of domain area and being eliminated eventually at the boundaries. On the contrary, the H_x and H_y components are mainly distributed in the nearby region of boundaries. Figures C4 and C5 show the x -dependence of H_x and H_z components at lines of ($y=L$, $z=2$ nm) and ($y=L$, $z=5$ nm), respectively.

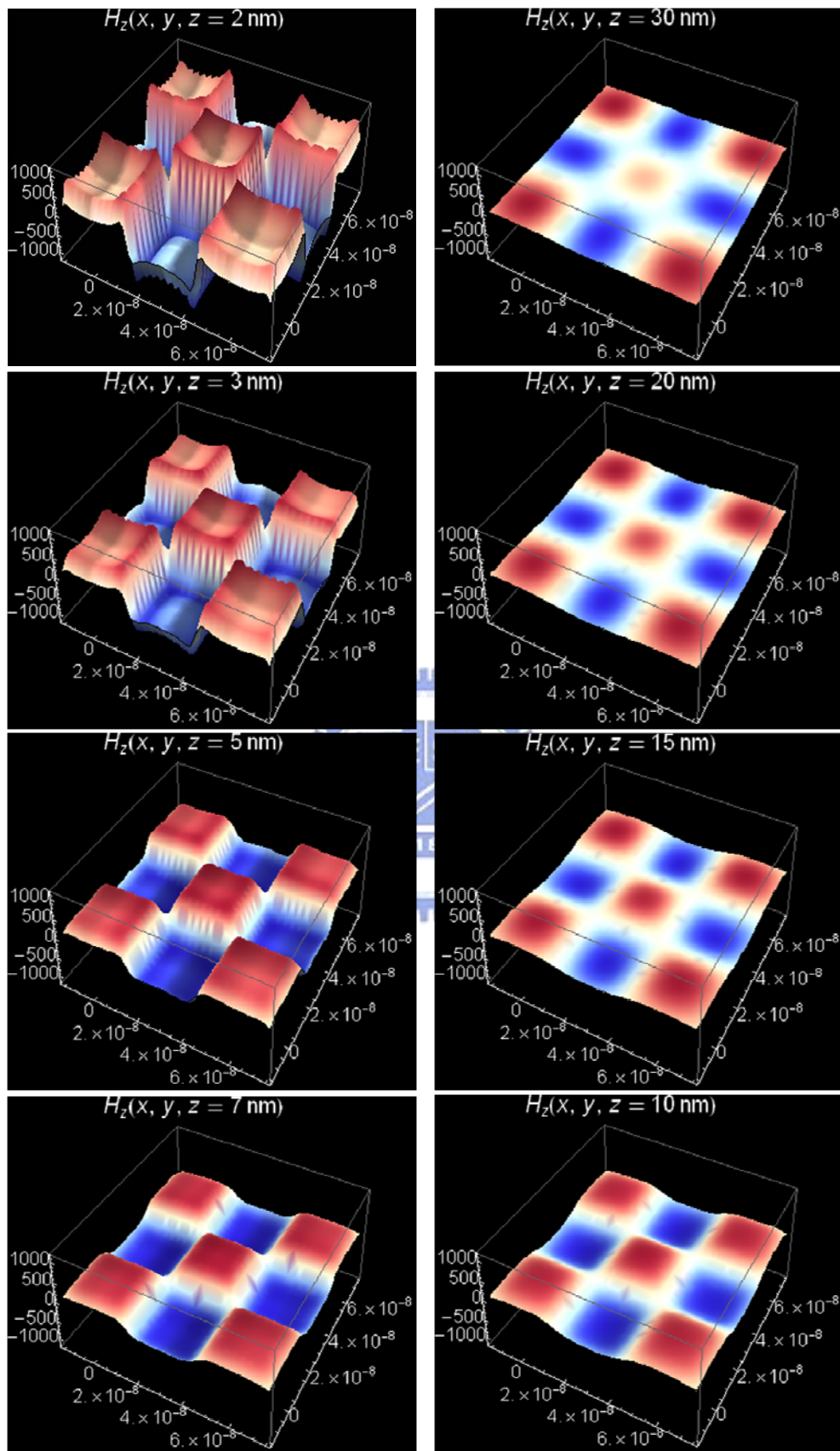


Fig. C2 Z-dependence of $H_z(x, y, z)$

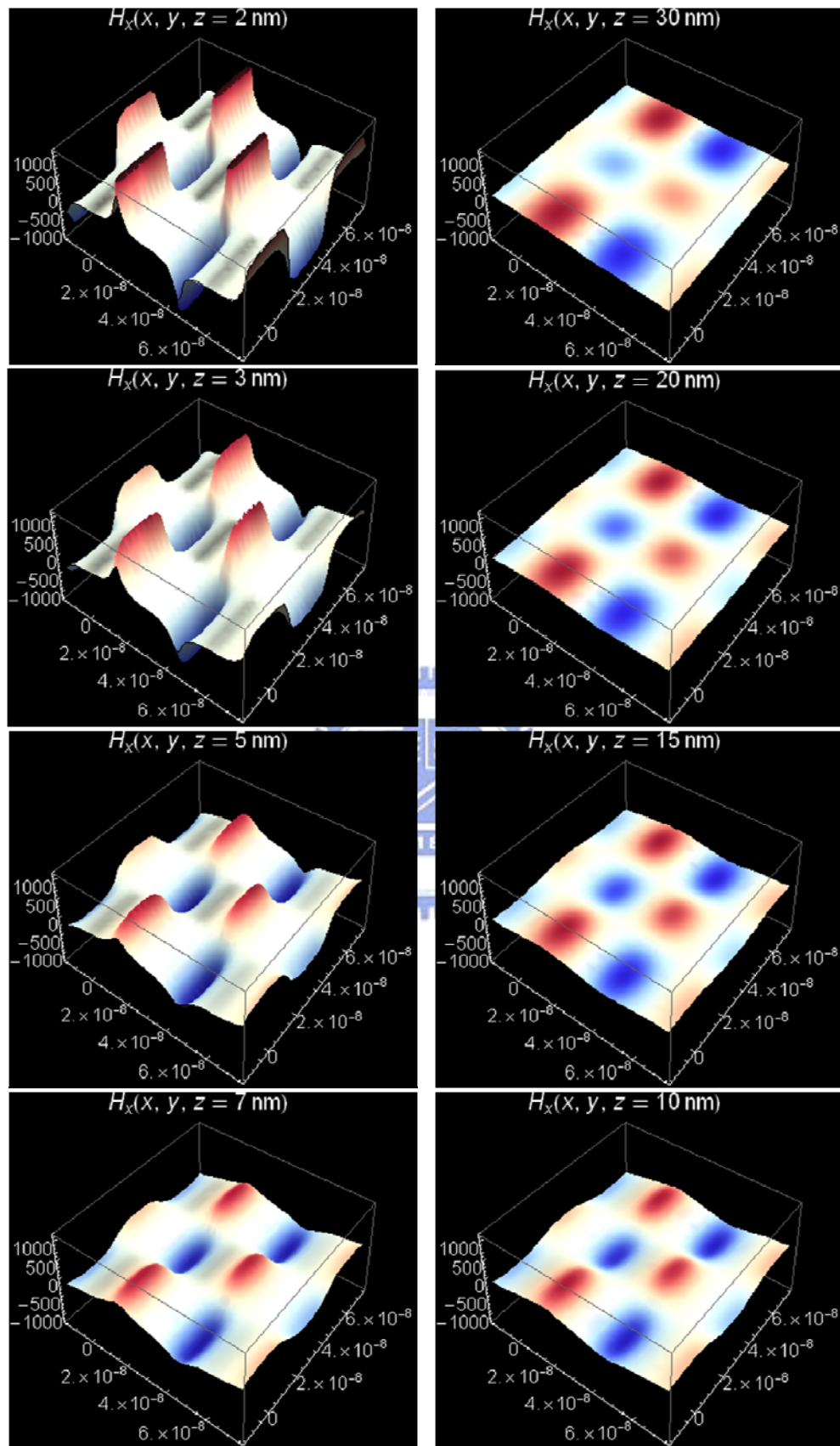
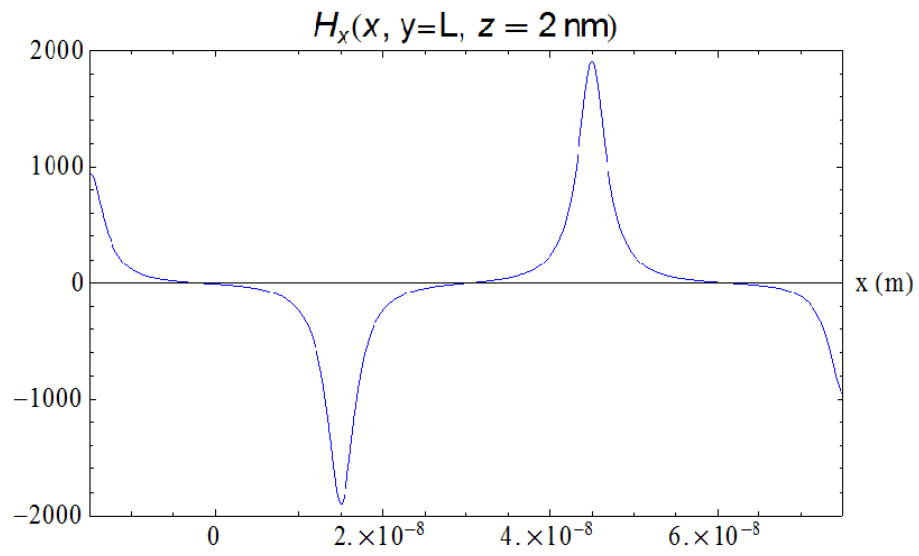
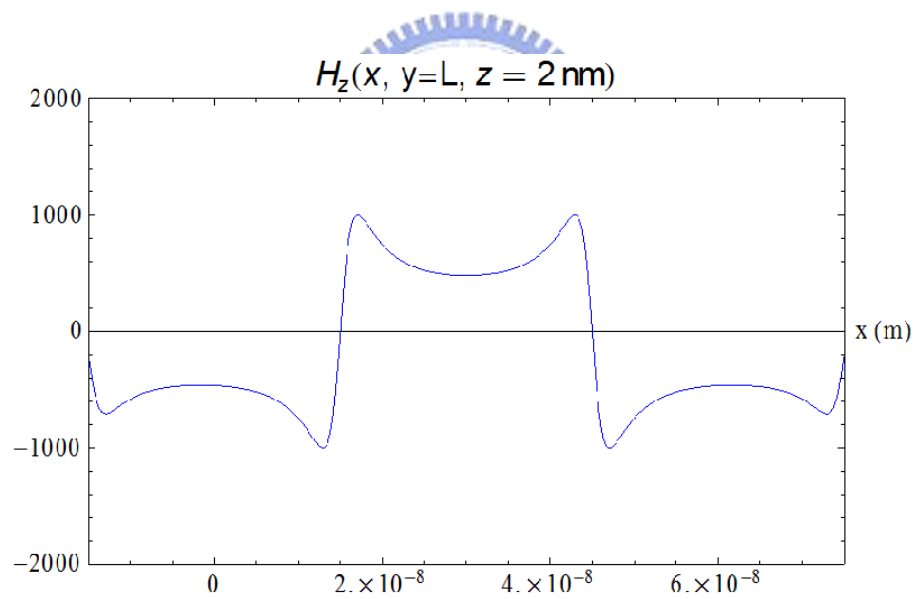


Fig. C3 Z-dependence of $H_x(x, y, z)$

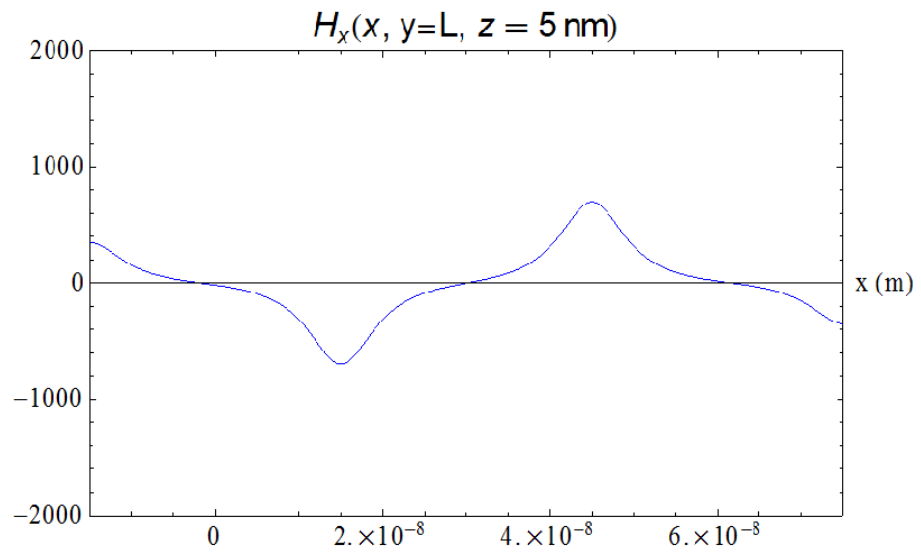


(a)

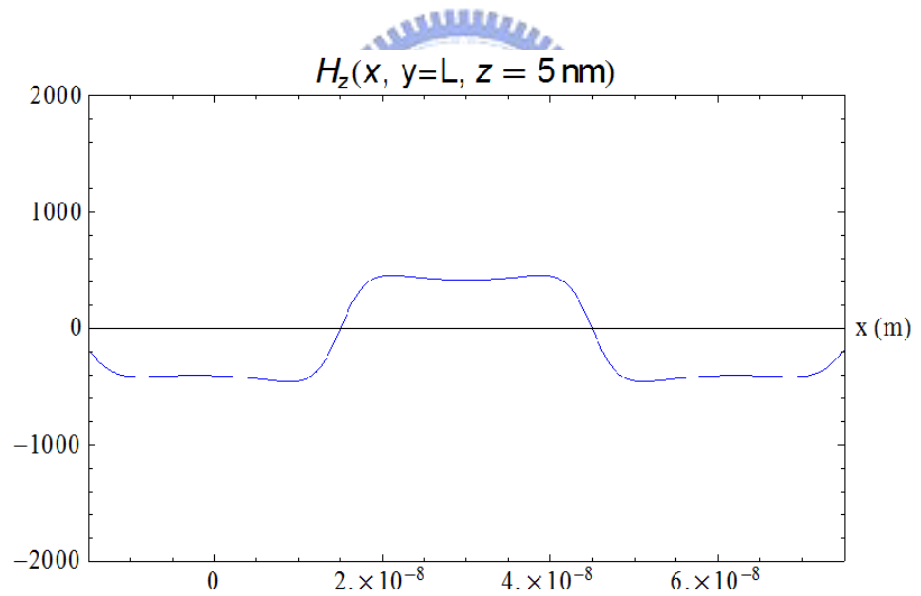


(b)

Fig. C4 X-dependence of (a) H_x and (b) H_z components at the position of ($y=L, z=2 \text{ nm}$)



(a)



(b)

Fig. C5 X-dependence of (a) H_x and (b) H_z components at the position of ($y=L, z=5 \text{ nm}$)

Appendix D

Estimation of the Magnetic Field Strength for Liquid Crystal Alignment

In Sec. 3.3.5, we have given a simple but rough estimation of polar anchoring strength without considering the elastic energy of liquid crystal (LC) molecules. It will be taken into account through the following steps. First, we have to obtain the spatial distribution of director \mathbf{n} confined by two boundaries with specific polar anchoring strength. Let us consider a vertically-aligned LC cell with thickness d and polar anchoring strength W_p of two identical surfaces.

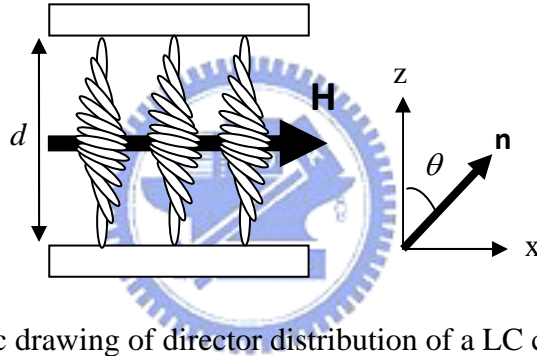


Fig. D1 Schematic drawing of director distribution of a LC cell

The total free energy density g can be described as:

$$g = \frac{1}{2}(K_{11}\sin^2\theta + K_{33}\cos^2\theta) \left(\frac{d\theta}{dz}\right)^2 - \frac{1}{2}\chi_a H^2 \sin^2\theta + \frac{1}{2}W_p \sin^2\theta_0 + \frac{1}{2}W_p \sin^2\theta_d \quad (1)$$

where K_{11} and K_{33} are the Frank elastic constants for splay and bend deformations of LC molecules, $\theta_0 = \theta(0)$ and $\theta_d = \theta(d)$, χ_a is the anisotropy of magnetic susceptibility of LC molecules, and H represents the applied magnetic field. Here θ_0 is equal to θ_d due to the identical surface layers are assumed. According to the Euler-Lagrange equation, the derivative of θ obtained by minimizing the total free energy of the discussed physical system is written as:

$$\left(\frac{d\theta}{dz}\right)^2 = \chi_a H^2 \frac{\cos^2\theta - \cos^2\theta_m}{K_{33}\cos^2\theta + K_{11}\sin^2\theta} \quad (2)$$

where $\theta_m = \theta(d/2)$. The boundary condition can be determined by the following equations:

$$H(\theta_m) = \frac{2}{d\sqrt{\chi_a}} \int_{\theta_0}^{\theta_m} \sqrt{\frac{K_{33}\cos^2\theta + K_{11}\sin^2\theta}{\cos^2\theta - \cos^2\theta_m}} d\theta \quad (3)$$

and

$$\theta_0(\theta_m) = \frac{\sin(\theta_m)}{\sqrt{K_{33} + W_p d/2\sqrt{K_{33}}}} \int_0^{\theta_m} \sqrt{\frac{K_{33}\cos^2\theta + K_{11}\sin^2\theta}{\cos^2\theta - \cos^2\theta_m}} d\theta. \quad (4)$$

To solve Eq. (2) with boundary conditions for $\theta(z)$ under certain field strength, the PDE solver embedded in Mathematica (Wolfram Research, Inc.) according to the finite different method has been adopted. Figure D2 shows the orientational distribution of LC in a surface-aligned cell with $d=24.8 \mu\text{m}$ and $W_p=2\times 10^{-4} \text{ J/m}^2$ applied with different strength of magnetic field. It should be mentioned that all the distribution profiles will intersect the z -axis at the same point with extrapolation length d_e of 35.4 nm. A strong

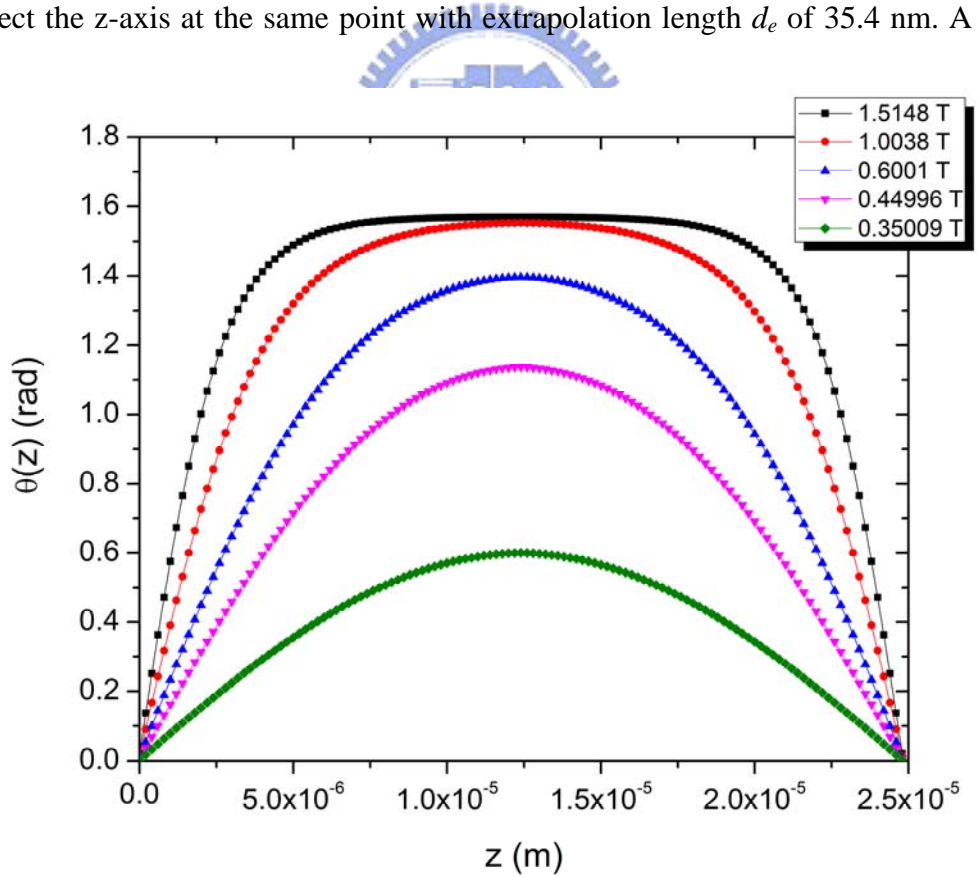


Fig. D2 Field-dependence of director distribution in a LC cell aligned with $W_p=2\times 10^{-4} \text{ J/m}^2$

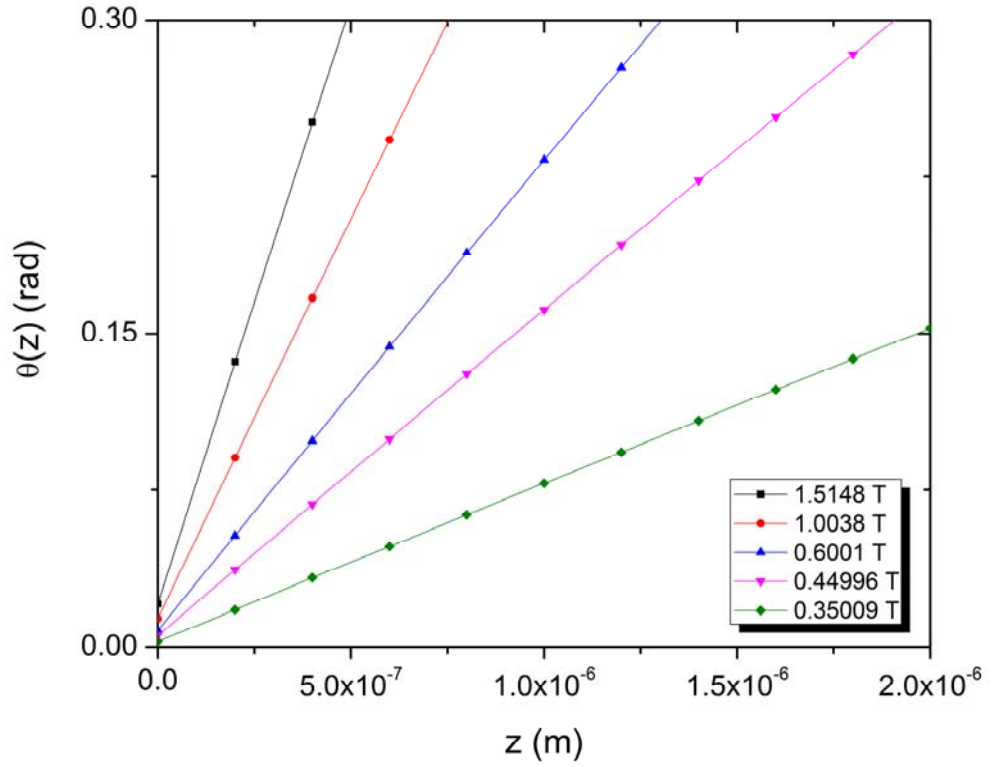


Fig. D3 A close look at director distribution in nearby region of surface in a LC cell aligned with $W_p=2 \times 10^{-4} \text{ J/m}^2$

anchoring effect will cause d_e approach to zero; moreover, d_e is equal to zero if $W_p \rightarrow \infty$ [1].

We should notice that the conventional theory, Rapini-Papoular and Frank Elastic theories, of measuring surface anchoring strength cannot yield the realistic orientational profile of LC director in the surface region (SR). As a result, to obtain a more real profile of director distribution shown in Fig. D4, we assume a voluminal anchoring strength $W_v(z)$ which is a function of z in SR. The total free energy F_{SR} of LC system specified above in SR is then written as

$$F_{SR} = \frac{1}{2} \int_0^\xi \left[(K_{11} \sin^2 \phi + K_{33} \cos^2 \phi) \left(\frac{d\phi}{dz} \right)^2 - \chi_a H^2 \sin^2 \phi - W_v(z) \sin^2 \phi \right] dz \quad (5)$$

according to the definition:

$$\frac{1}{2} \int_0^\xi W_v(z) \sin^2 \phi dz = \frac{1}{2} W_p \sin^2 \theta_0, \quad (6)$$

where ξ is the thickness of SR.

However, we have no idea about the explicit form of $W_v(z)$. So, for simplicity, we

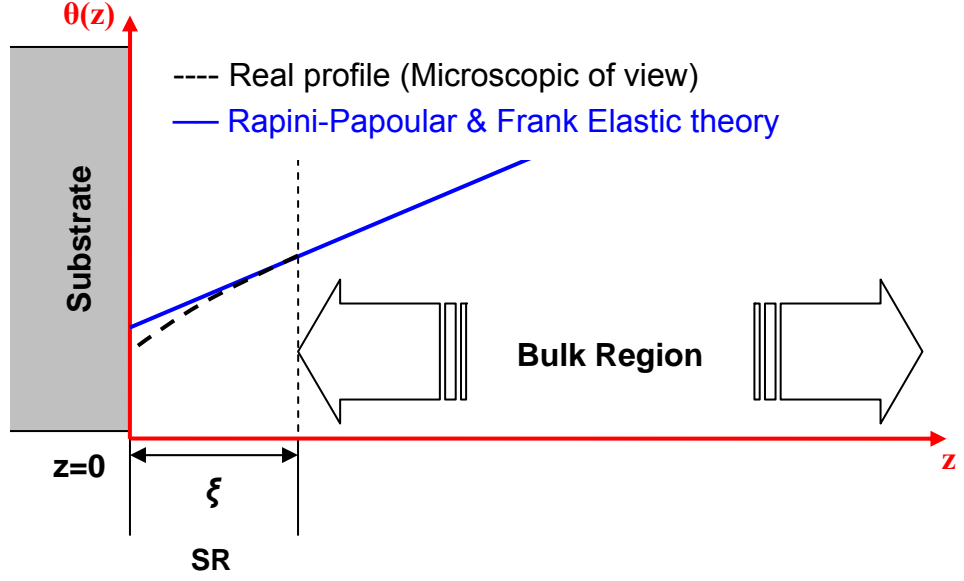


Fig. D4 Schematic drawing of LC director distribution in surface region

assume $W_v(z)\sin^2\theta(z)$ is constant for any $z \in [0, \xi]$. Then a simple form for $W_v(z)$ is obtained as

$$W_v(z) = \frac{W_p \sin^2 \theta_0}{\xi \sin^2 \phi} \quad (7)$$

Take the variation of the functional in Eq. (5) to obtain the following equation

$$(K_{11} - K_{33})\cos\phi\sin\phi \left(\frac{d\phi}{dz}\right)^2 + (K_{11}\sin^2\phi + K_{33}\cos^2\phi) \frac{d^2\phi}{dz^2} + \chi_a H^2 \cos\phi\sin\phi + \frac{W_p \sin^2 \theta_0}{\xi \tan\phi} = 0 \quad (8)$$

with boundary conditions $\phi(\xi) = \theta_0$ and $\phi'(\xi) = \theta_0'$. The required boundary conditions are determined by using the Eq. (3), Eq. (4) and $\theta(z)$ evaluated with $H=0.5$ T and listed in Table D1. According to the condition of $W_p=5 \times 10^{-5}$ J/m², $H=0.5$ T and $\xi=10$ nm, the Eq. (8) is solved with the corresponding boundary condition.

Table D1 Boundary condition θ_0 and θ_0' at $H=0.5$ T

| W_p (10^{-4} J/m ²) | 0.5 | 0.7 | 2.0 |
|--------------------------------------|---------|---------|---------|
| θ_m (rad) | 1.2656 | 1.2626 | 1.2576 |
| θ_0 (rad) | 0.0260 | 0.0185 | 0.0065 |
| θ_0' (rad/cm) | 1832.76 | 1831.28 | 1828.59 |

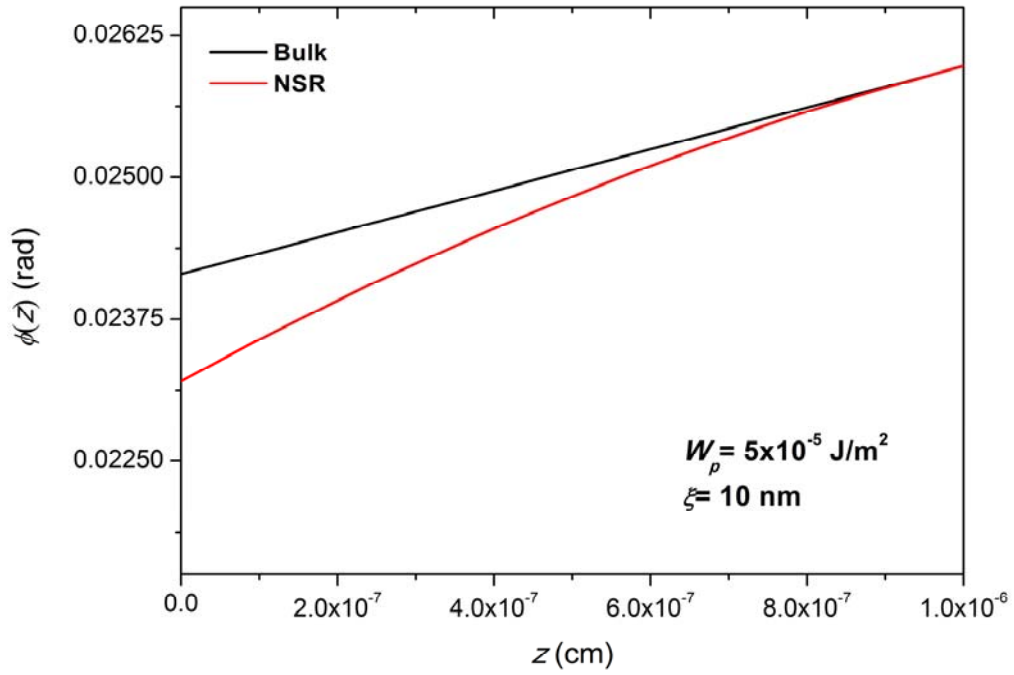


Fig. D5 Director distribution $\phi(z)$ in SR at $H=0.5$ T

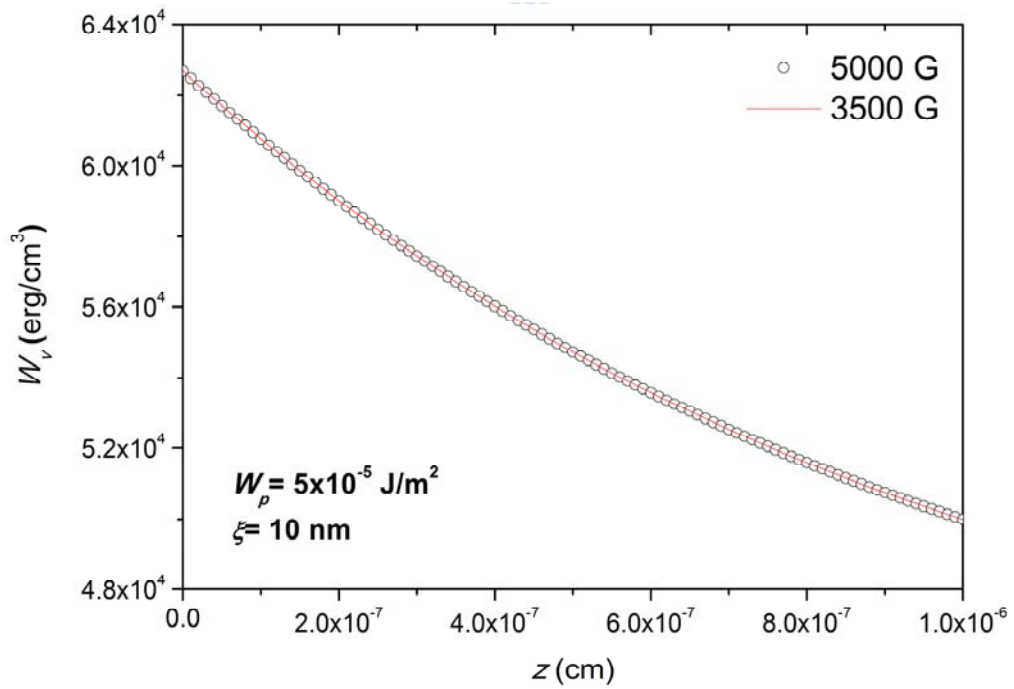


Fig. D6 $W_v(z)$ in SR evaluated for two strength of H : 0.35 and 0.50 T

Figure D5 shows the evaluated $\phi(z)$ and compared with the $\theta(z)$ obtained without $W_v(z)$ in SR. A nonlinear profile is obtained which is supposed to approximately be close to the real profile no matter what it is. Besides, we could expect that the $W_v(z)$ is independent of H and it has been confirmed in Fig. D6. Figure D7 shows the $W_v(z)$

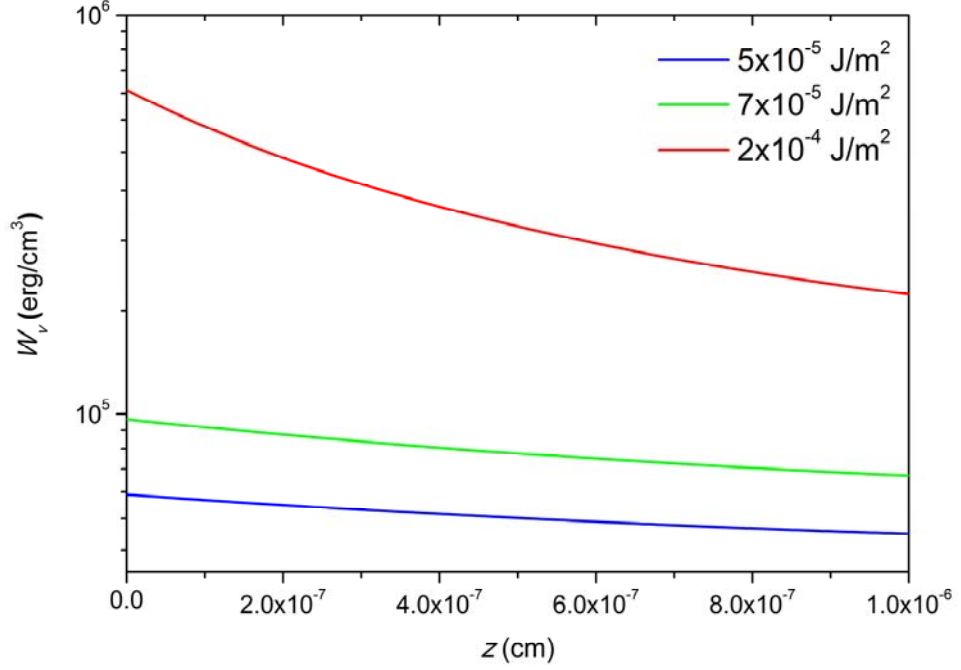


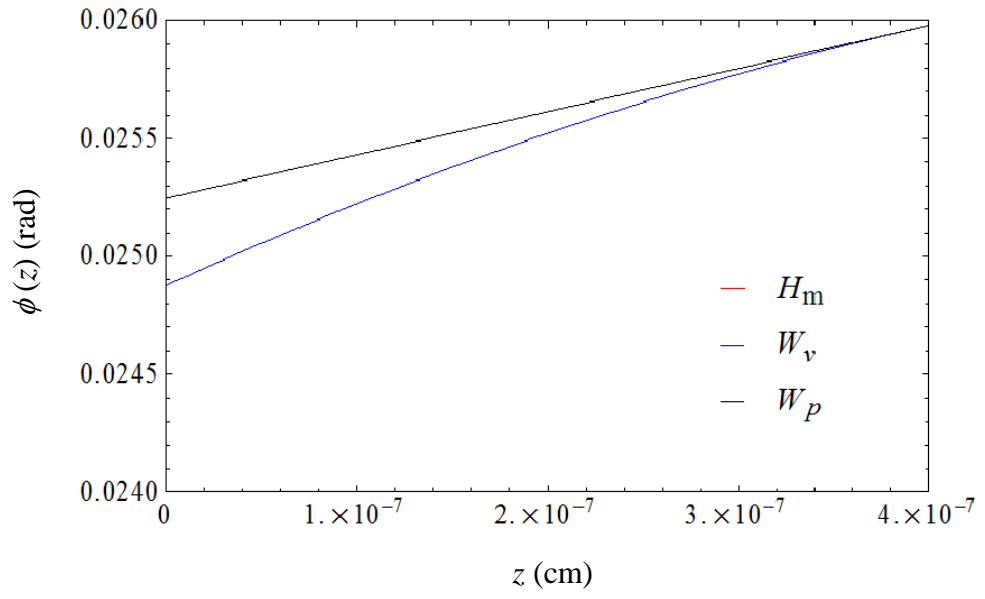
Fig. D7 $W_v(z)$ in SR at H=0.5 T with three different W_p

calculated for three different W_p without surprise.

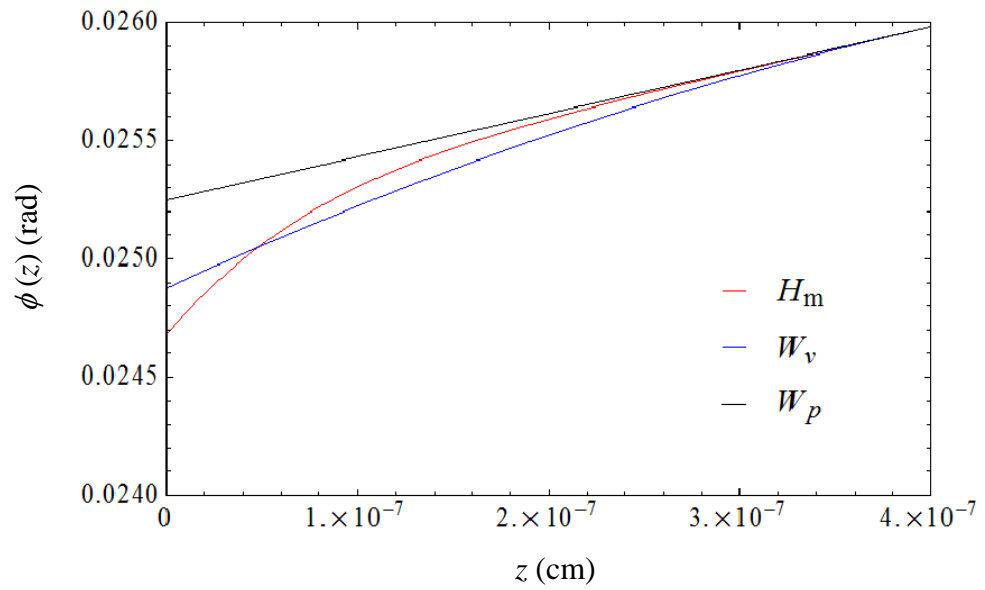
Now, let us replace the term $W_v(z)\sin^2\phi$ with surface induced magnetic energy $\chi_a H_m^2(z)\sin^2\phi$. After variational calculation, we obtain

$$\begin{aligned}
 (K_{11} - K_{33})\cos\phi\sin\phi \left(\frac{d\phi}{dz}\right)^2 + (K_{11}\sin^2\phi + K_{33}\cos^2\phi) \frac{d^2\phi}{dz^2} \\
 + \chi_a H^2 \cos\phi\sin\phi + \chi_a H_m^2(z)\cos\phi\sin\phi = 0
 \end{aligned} \quad (9)$$

The H-field distribution $H_z(x, y, z)$ simulated in Appendix C is taken as $H_m(z)$ where $x=y=5L/9$ in Fig. C1. Figure D8(a) shows the influence of $H_m(z)$ on the solved $\phi(z)$. No change is found. It indicates that the contribution of free energy caused by $H_m(z)$ to total free energy of system in SR could be ignored. So, how much field strength is required to let the $\phi(z)$ be closed to that solved with $W_v(z)$? Figure D8(b) reveals a result solved by considering a value being 1300 times the original $H_m(z)$. That means the simulated $H_m(z)$ from multiple magnetic moments is far smaller than the needed one in the conventional formalism.



(a)



(b)

Fig. D8 Director distribution $\phi(z)$ in SR with $\xi=4$ nm at $H=0.5$ T for (a) $H_m(z)$ and (b) $1300 \times H_m(z)$

References

1. P. G. deGennes and J. Prost, *The Physics of Liquid Crystals*, 2nd ed. (Oxford, New York, 1993), pp. 108-116.

